

BIO-BASED POLYMER COMPOSITE OF POLY (LACTIC
ACID)/TITANIUM SILICON OXIDE/SILK FIBROIN



A Thesis Submitted in Partial Fulfillment of the Requirements for the
Degree of Doctor of Philosophy in Polymer Engineering
Suranaree University of Technology
Academic Year 2020

พอลิเมอร์คอมพอลิทชีวภาพของพอลิแลคติกแอซิดกับออกไซด์ของ
ไทเทเนียม ซิลิคอนและไหมไฟโบรอิน



นางสาวอภาภรณ์ เทียมสินสังวร

วิทยานิพนธ์นี้เป็นส่วนหนึ่งของการศึกษาตามหลักสูตรปริญญาวิศวกรรมศาสตรดุษฎีบัณฑิต
สาขาวิชาวิศวกรรมพอลิเมอร์
มหาวิทยาลัยเทคโนโลยีสุรนารี
ปีการศึกษา 2563


BIO-BASED POLYMER COMPOSITE OF POLY (LACTIC ACID)/TITANIUM
SILICON OXIDE/SILK FIBROIN


Suranaree University of Technology has approved this thesis submitted in partial fulfillment of the requirements for the Degree of Doctor of Philosophy.

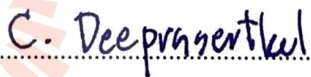
Thesis Examining Committee

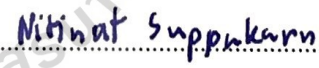

.....
(Assoc. Prof. Dr.Sittipong Amnuaypanich)

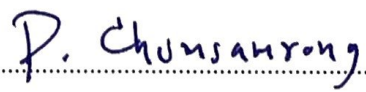
Chairperson



.....
(Assoc. Prof. Dr.Yupaporn Ruksakulpiwat)
Member (Thesis Advisor)


.....
(Assoc. Prof. Dr.Chaiwat Ruksakulpiwat)
Member (Thesis Co-Advisor)


.....
(Asst. Prof. Dr.Chantima Deeprasertkul)
Member


.....
(Asst. Prof. Dr.Nitinat Suppakarn)
Member


.....
(Assoc. Prof. Dr.Pranee Chumsamrong)
Member


.....
(Assoc. Prof. Dr.Chatchai Jothityangkoon)
Vice Rector for Academic Affairs and
Quality Assurance


.....
(Assoc. Prof. Dr.Pomsiri Jongkol)
Dean of Institute of Engineering

อภาภรณ์ เทียมสินสังวร : พอลิเมอร์คอมพอสิตชีวภาพของพอลิแลคติกแอซิดกับออกไซด์
ของไทเทเนียม ซิลิคอนและไหมไฟโบรอิน (BIO-BASED POLYMER COMPOSITE OF
POLY(LACTIC ACID)/TITANIUM SILICON OXIDE/SILK FIBROIN) อาจารย์ที่ปรึกษา :
รองศาสตราจารย์ ดร.ยุพาพร รักสกุลพิวัฒน์, 236 หน้า

คำสำคัญ : พอลิแลคติกแอซิด/ออกไซด์ผสมของไทเทเนียมและซิลิคอน/ไหมไฟโบรอิน/สมบัติการออก
ฤทธิ์ยั้งแบคทีเรีย

งานวิจัยนี้ได้ศึกษาผลของค่าความเป็นกรดเบส และอัตราส่วนโดยอะตอมของไทเทเนียมและ
ซิลิคอนในออกไซด์ผสมที่มีต่อการสังเคราะห์ออกไซด์ผสมของไทเทเนียม-ซิลิคอน (Ti_xSi_y) ด้วยวิธีโซล
เจลเพื่อใช้เป็นสารเติมเต็มสำหรับพอลิแลคติกแอซิดโดยมีไทเทเนียมไอโซพโรพอกไซด์ และเตตระ
เอทิลอโทซิลิเกตเป็นสารตั้งต้น โครงสร้างทางเคมีของออกไซด์ผสม Ti_xSi_y และถูกยืนยันด้วยเทคนิค
ซิลิคอน-29 นิวเคลียร์แมกเนติกเรโซแนนสเปกโตรสโกปีและฟูเรียรทรานสฟอร์มอินฟราเรดสเปกโตรส
โกปี จากการวิเคราะห์สมบัติทางโครงสร้างและทางกายภาพ พบว่าออกไซด์ผสมที่มีอัตราส่วนของ
อะตอมไทเทเนียมกับซิลิคอน 70/30 ($Ti_{70}Si_{30}$) มีขนาดเส้นผ่าศูนย์กลางของอนุภาคเฉลี่ยระหว่าง
131-150 นาโนเมตร พื้นที่ผิวจำเพาะเท่ากับ 569.70 ตารางเมตรต่อกรัม และมีปริมาตรรูพรุน 1.42
ลูกบาศก์เซนติเมตรต่อกรัม

ฟิล์มพอลิเมอร์คอมพอสิตระหว่างพอลิแลคติกแอซิดกับออกไซด์ผสมของไทเทเนียมและ
ซิลิคอน (PLA/ Ti_xSi_y) พอลิเมอร์คอมพอสิตระหว่างพอลิแลคติกแอซิดกับผงไหมไฟโบรอิน (PLA/SF)
และพอลิเมอร์คอมพอสิตระหว่างพอลิแลคติกแอซิดกับออกไซด์ผสมของไทเทเนียมและซิลิคอนกับผง
ไหมไฟโบรอิน (PLA/ Ti_xSi_y /SF) ถูกเตรียมเป็นฟิล์มจากสารละลาย ปริมาณของออกไซด์ผสมคือ 1 3
และ 5 เปอร์เซ็นต์โดยน้ำหนักสำหรับ PLA/ Ti_xSi_y ปริมาณของผงไหมไฟโบรอินคือ 1 3 และ 5
เปอร์เซ็นต์โดยน้ำหนักสำหรับ PLA/SF และ PLA/ Ti_xSi_y /SF ตรวจสอบสมบัติทางกล สมบัติทาง
สัณฐานวิทยา สมบัติทางความร้อน สมบัติในการย่อยสลาย และสมบัติการออกฤทธิ์ยั้งแบคทีเรีย
ของ PLA/ Ti_xSi_y PLA/SF และ PLA/ Ti_xSi_y /SF

การเติมออกไซด์ผสม $Ti_{70}Si_{30}$ ปริมาณ 3 เปอร์เซ็นต์โดยน้ำหนักในพอลิแลคติกแอซิดช่วย
เพิ่มค่าการทนต่อแรงดึงและค่ามอดุลัสของยังก์ของฟิล์มพอลิแลคติกแอซิด การเติมออกไซด์ผสม
 $Ti_{70}Si_{30}$ ที่ปริมาณ 5 เปอร์เซ็นต์โดยน้ำหนักจะลดอุณหภูมิการตกผลึกขณะให้ความร้อนและเพิ่ม
ปริมาณผลึกของพอลิแลคติกแอซิด นอกจากนี้ฟิล์ม $Ti_{70}Si_{30}$ ที่ปริมาณ 5 เปอร์เซ็นต์โดยน้ำหนัก
(97PLA/5 $Ti_{70}Si_{30}$) เพิ่มประสิทธิภาพในการย่อยสลายภายใต้แสงยูวีของฟิล์มพอลิแลคติกแอซิด
อนุภาคออกไซด์ผสมมีความสามารถในการป้องกันแสงยูวี(UV)ได้โดยเฉพาะอย่างยิ่งออกไซด์ผสมชนิด
 $Ti_{70}Si_{30}$ นอกจากนี้ฟิล์มพอลิเมอร์คอมพอสิตที่เติมออกไซด์ผสมของไทเทเนียมและซิลิคอนชนิด

Ti₇₀Si₃₀ มีสมบัติการออกฤทธิ์ยับยั้งแบคทีเรียที่ดีเยี่ยมต่อแบคทีเรียชนิดเอสเชอริเชีย โคลิ (*E. coli*) และแบคทีเรียชนิดสแตฟิโลค็อกคัส ออเรียส (*S. aureus*)

การศึกษาฟิล์มพอลิเมอร์คอมพอสิตระหว่างพอลิแลคติกแอซิดกับผงไหมไฟโบรอิน (PLA/SF) และ พอลิเมอร์คอมพอสิตระหว่างพอลิแลคติกแอซิดกับออกไซด์ผสมของไทเทเนียมและซิลิคอนกับผงไหมไฟโบรอิน (PLA/Ti_xSi_y/SF) ได้สกัดผงไหมด้วยสารละลายแคลเซียมคลอไรด์ที่อุณหภูมิ 100 องศาเซลเซียส ฟิล์มพอลิเมอร์คอมพอสิต PLA/SF แสดงค่าการยึดตัวสูงสุด ณ จุดขาด ที่ปริมาณผงไหม 3 เปอร์เซ็นต์โดยน้ำหนัก ในขณะที่ค่าการทนต่อแรงดึงและค่ามอดุลัสของยังก์ของต่ำกว่าพอลิแลคติกแอซิด อัตราการซึมผ่านของไอน้ำของฟิล์มพอลิเมอร์คอมพอสิตระหว่างพอลิแลคติกแอซิดกับผงไหมไฟโบรอินและฟิล์มพอลิเมอร์คอมพอสิตระหว่างพอลิแลคติกแอซิดกับผงไหมไฟโบรอินและออกไซด์ผสมของไทเทเนียมและซิลิคอนเพิ่มขึ้นอย่างมีนัยสำคัญ เมื่อเพิ่มปริมาณผงไหมไฟโบรอิน ค่าความทึบแสงของฟิล์มพอลิเมอร์คอมพอสิตระหว่างพอลิแลคติกแอซิดกับผงไหมไฟโบรอินและฟิล์มพอลิเมอร์คอมพอสิตระหว่างพอลิแลคติกแอซิดกับผงไหมไฟโบรอินและออกไซด์ผสมของไทเทเนียมและซิลิคอนเพิ่มขึ้นเมื่อเพิ่มปริมาณผงไหมและยังเพิ่มประสิทธิภาพในการป้องกันแสงยูวีและแสงอัลตราไวโอเล็ตอีกด้วย นอกจากนี้การผสมผงไหมไฟโบรอินยังเพิ่มประสิทธิภาพในการย่อยสลายให้กับพอลิแลคติกแอซิด

มหาวิทยาลัยเทคโนโลยีสุรนารี

สาขาวิชา วิศวกรรมพอลิเมอร์
ปีการศึกษา 2563

ลายมือชื่อนักศึกษา _____
ลายมือชื่ออาจารย์ที่ปรึกษา _____
ลายมือชื่ออาจารย์ที่ปรึกษาร่วม _____

ARPAPORN TEAMSINSUNGVON : BIO-BASED POLYMER COMPOSITE OF
POLY(LACTIC ACID)/TITANIUM SILICON OXIDE/SILK FIBROIN. THESIS ADVISOR :
ASSOC. PROF. YUPAPORN RUKSAKULPIWAT, Ph.D., 236 PP.

Keyword : Poly(Lactic Acid)/Titanium Silicon Oxide/Silk Fibroin/Antimicrobial Properties

In this research, the effects of pH and Ti/Si atomic ratio of titanium-silicon binary mixed oxide (Ti_xSi_y) on structural and physical properties of Ti_xSi_y mixed oxide were studied using sol-gel method. The Ti_xSi_y mixed oxide was used as filler for PLA. Titanium (IV)isopropoxide (TTIP) and tetraethylorthosilicate (TEOS) were used as Ti and Si precursor, respectively. The structural and physical properties were studied. The chemical structure of Ti_xSi_y mixed oxide was confirmed by ^{29}Si -NMR and FTIR. The averaged diameter of $Ti_{70}Si_{30}$ mixed oxide was in range of 131-150 nm. $Ti_{70}Si_{30}$ mixed oxide showed specific surface area, S_{BET} of $569.70\text{ m}^2\text{g}^{-1}$ and pore volume of $1.42\text{ cm}^3\text{g}^{-1}$ have been obtained.

PLA/ Ti_xSi_y , PLA/silk fibroin (SF), and PLA/ Ti_xSi_y /SF composite films were prepared by solution film casting method at 1, 3, and 5 wt.% of Ti_xSi_y mixed oxide for PLA/ Ti_xSi_y composites and 1,3, 5 wt.% of SF For PLA/SF and PLA/ Ti_xSi_y /SF composites. Mechanical, morphological, thermal, and degradation properties were investigated. And antimicrobial activity of all PLA/ Ti_xSi_y composites were evaluated as well.

The addition of 3 wt.% of $Ti_{70}Si_{30}$ mixed oxide into PLA film improved the tensile strength and Young's modulus of PLA. The incorporation of 5wt.% of $Ti_{70}Si_{30}$ decreased the cold crystallization temperature and increased degree of crystallinity of PLA. In addition, 97PLA/5 $Ti_{70}Si_{30}$ improved efficiency of photocatalytic activity of PLA. Ti_xSi_y nanoparticles were able to remove UV light, particularly $Ti_{70}Si_{30}$ enhanced a stronger higher UV-shielding potential. Furthermore, PLA with the addition of TiO_2 and $Ti_{70}Si_{30}$ exhibited excellent antibacterial effect on gram-negative bacteria (*E. coli*) and gram-positive bacteria (*S. aureus*) indicating the improved antimicrobial effectiveness of PLA nanocomposites.

To prepare PLA/SF and PLA/ Ti_xSi_y /SF composite, silk fibroin (SF) powder can be prepared in-house by re-dissolving in $CaCl_2$ solution at 100°C . All of PLA/SF and

composite showed the higher elongation at break than neat PLA, especially at 3wt.% of SF while the tensile strength and Young's modulus were lower than PLA. By adding SF and $Ti_{70}Si_{30}$, tensile strength and Young's modulus of PLA were increased. Water vapor transmission rate (wvtr) of PLA was significantly increased by incorporation of SF due to the hydrophilicity of SF. Moreover, opacity of PLA/SF, and PLA/ Ti_xSi_y composites increased with increasing SF content and exhibited good preventing against UV-Visible light. All of PLA composites incorporating with SF and $Ti_{70}Si_{30}$ exhibited much higher weight loss as a function of time than neat PLA. The weight loss of PLA/SF nanocomposite was also found to increase with increasing SF content.



School of Polymer Engineering

Academic Year 2020

Student's Signature Arpaporn T.
Advisor's Signature Nyapaporn
Co-advisor's Signature Chirist D.

ACKNOWLEDGEMENTS

I gratefully acknowledge the financial support from Suranaree University of Technology and Center of Excellence on Petrochemicals and Materials Technology.

First and foremost, I am deeply grateful and appreciation to my thesis advisor, Assoc. Prof. Dr. Yupaporn Ruksakulpiwat, for her valuable supervision, inspiring guidance, supporting information, advice and kindness throughout the period of study. I also special thank my thesis advisor for her tireless effort in encouraging me to complete my work. Sincere appreciation is also extended to the thesis co-advisor, Assoc. Prof. Dr.Chaiwat Ruksakulpiwat, for his valuable suggestions during my research work. In addition, I gratefully thank the chairperson, Assoc. Prof. Dr.Sittipong Amnuaypanich and the committee, Assoc. Prof. Dr.Chaiwat Ruksakulpiwat, Asst. Prof. Dr. Chantima Deeprasertkul, Asst. Prof. Dr.Nitinat Suppakarn, and Assoc. Prof. Dr.Pranee Chumsamrong for their valuable suggestion and encouragement.

My appreciation also goes to Dr. Penphittha Amonpattaratkit for her excellent descriptions in the experiment of X-ray absorption spectroscopy (XAS). Special thanks are extended to Synchrotron Light Research Institute (SLRI) for the facilities in the use of XAS at beamline 8. Moreover, I wish to thank all staff members, and all friends of the School of Polymer Engineering for their helps and supports throughout my work.

Finally, my graduation would not be achieved without best wish from my parents, Mr. Boontom and Mrs. Banyen Teamsinsungvon, my sisters, Miss Kullakarn and Miss Aemorn Teamsinsungvon, and Mr. Siwanat Lomchid who give me a valuable life with their unconditional love, encouragement, and supporting me in all situations in my whole life.

Arpaporn Teamsinsungvon

TABLE OF CONTENTS

	Page
ABSTRACT (THAI).....	I
ABSTRACT (ENGLISH).....	III
ACKNOWLEDGEMENTS.....	V
TABLE OF CONTENTS.....	VI
LIST OF TABLES.....	XI
LIST OF FIGURES.....	XIV
SYMBOLS AND ABBREVIATIONS.....	XX
CHAPTER	
I INTRODUCTION.....	1
1.1 General introduction.....	1
1.2 Research objectives.....	5
1.3 Scope and limitation of the study.....	5
II LITERATURE REVIEW.....	7
2.1 Biocomposites.....	7
2.2 Poly (lactic acid).....	8
2.3 The improvement of PLA properties.....	11
2.4 Improving interfacial adhesion of PLA composites.....	14
2.5 Titanium-Silicon oxide.....	17
2.5.1 Titanium dioxide (TiO ₂).....	18
2.5.2 Silicon dioxide (SiO ₂).....	20
2.5.3 Sol-gel process.....	22
2.5.4 Synthesis of TiO ₂ -SiO ₂ via sol-gel method.....	23
2.6 Silk fibroin (SF).....	31
2.7 PLA composites.....	36
2.7.1 PLA/TiO ₂ composites.....	36

TABLE OF CONTENTS (Continued)

	Page
2.7.2	PLA/SiO ₂ composites..... 40
2.7.3	PLA/natural fiber composites..... 43
III	EXPERIMENTAL..... 49
3.1	Materials..... 49
3.2	Experimental..... 49
3.2.1	Synthesis of titanium-silicon oxide (Ti _x Si _y) 49
3.2.2	Characterization of titania-silica oxide..... 52
3.2.2.1.	²⁹ Si Solid-state nuclear magnetic resonance spectroscopy (²⁹ Si solid-state NMR) 52
3.2.2.2.	Fourier transform infrared spectroscopy (FTIR) 52
3.2.2.3.	Field emission scanning electron microscope (FE-SEM)..... 53
3.2.2.4.	X-ray diffraction (XRD)..... 53
3.2.2.5.	X-ray absorption near-edge structure spectroscopy (XANES) and extended X-ray absorption fine structure Spectroscopy (EXAFS)..... 53
3.2.2.6.	X-ray fluorescence (XRF)..... 54
3.2.2.7.	Particle size distribution 54
3.2.2.8.	Specific surface area..... 54
3.2.3	Preparation of silk fibroin powder..... 54
3.2.4	Characterization of silk fibroin powder 56
3.2.5	Preparation of PLA/TiO ₂ , PLA/SiO ₂ and PLA/Ti _x Si _y oxide composites..... 57
3.2.6	Preparation of PLA/SF composites..... 57
3.2.7	Preparation of PLA/Ti _x Si _y /SF composites 58

TABLE OF CONTENTS (Continued)

	Page
3.2.8	Characterization of PLPLA/Ti _x Si _y , PLA/SF, and PLA/Ti _x Si _y /SF composites 58
3.2.8.1.	Mechanical properties 58
3.2.8.2.	Thermal properties..... 58
3.2.8.3.	Morphological property..... 59
3.2.8.4.	Water vapor transmission rate (WVTR) 59
3.2.8.5.	Photocatalytic degradation of methylene blue (MB) 60
3.2.8.6.	Light Transmittance and Opacity measurements..... 63
3.2.8.7.	Hydrolytic degradation 64
3.2.8.8.	<i>In vitro</i> degradation 64
3.2.8.9.	Antimicrobial activity..... 65
IV	RESULTS AND DISCUSSION..... 66
4.1	The effect of pH on structural and physical properties of titanium-silicon oxide 66
4.1.1	²⁹ Si Solid-state nuclear magnetic resonance spectroscopy (²⁹ Si solid-state NMR) 66
4.1.2	Fourier transform infrared spectroscopy (FTIR) 68
4.1.3	Field emission scanning electron microscope (FE-SEM) 70
4.1.4	X-ray diffraction (XRD)..... 71
4.1.5	X-ray absorption near-edge structure spectroscopy (XANES)..... 73
4.1.6	Extended X-ray absorption fine structure spectroscopy (EXAFS)..... 74

TABLE OF CONTENTS (Continued)

	Page
4.1.7 X-ray fluorescence (XRF)	78
4.1.8 Particle size distribution.....	79
4.1.9 Nitrogen adsorption-desorption isotherms.....	82
4.2 The effect of atomic ratio of Ti/Si ratio on structural and physical properties of titanium-silicon oxide.....	84
4.2.1 Fourier transform infrared spectroscopy (FTIR)	84
4.2.2 Field emission scanning electron microscope (FE-SEM)	85
4.2.3 X-ray diffraction (XRD).....	86
4.2.4 X-ray absorption near-edge structure spectroscopy (XANES)	87
4.2.5 Extended X-ray absorption fine structure spectroscopy (EXAFS).....	88
4.2.6 X-ray fluorescence (XRF)	92
4.2.7 Particle size distribution.....	92
4.2.8 Nitrogen adsorption-desorption isotherms.....	95
4.3 The effect of Ti_xSi_y oxide on properties of PLA/ Ti_xSi_y composites	96
4.3.1 Mechanical properties.....	96
4.3.2 Thermal properties.....	101
4.3.3 Morphological property	112
4.3.4 Water vapor transmission rate (WVTR)	114
4.3.5 Photocatalytic degradation of methylene blue (MB).....	115
4.3.6 Light transmittance and opacity measurements.....	118
4.3.7 Hydrolytic degradation.....	121
4.3.8 <i>In vitro</i> degradation	122

TABLE OF CONTENTS (Continued)

	Page
4.3.9	Antimicrobial activity..... 126
4.4	The effect of silk fibroin on properties of PLA/SF and PLA/Ti _x Si _y /SF composites..... 131
4.4.1	Characterization of silk fibroin (SF) powder..... 131
4.4.1.1.	Determination of %yield of SF..... 132
4.4.1.2.	Identification of SF..... 134
4.4.2	Mechanical properties of PLA/SF and PLA/ Ti _x Si _y /SF composites 144
4.4.3	Thermal properties of PLA/SF and PLA/Ti _x Si _y / SF composites 149
4.4.4	Morphological properties of PLA/SF and PLA/ Ti _x Si _y /SF composites 156
4.4.5	Water vapor transmission rate (WVTR) of PLA/SF and PLA/Ti _x Si _y /SF composites 160
4.4.6	Light Transmittance and Opacity Measurements of PLA/SF and PLA/Ti _x Si _y /SF composites 162
4.4.7	Hydrolytic degradation of PLA/SF and PLA/Ti _x Si _y /SF composites..... 164
4.4.8	In vitro degradation of PLA/SF and PLA/ Ti _x Si _y /SF composites 165
V	CONCLUSIONS..... 167
REFERENCES 169
APPENDIX 187
APPENDIX A	Publications 188
BIOGRAPHY 236

LIST OF TABLES

Table		Page
2.1	General characteristics of a commercial PLA, 3D Printing Monofilament – General Purpose Grade (Ingeo™ Biopolymer 4043D Technical data sheet, produced by NatureWorks LLC)	9
2.2	Physical and chemical properties of rutile, anatase, and brookite	19
2.3	Common silica and titania precursors and their chemical structures	25
2.4	Composition of silk fiber.....	33
2.5	Structure of silk fibers from Bombyx mori silkworm	35
3.1	Mole of component in the preparation of Ti_xSi_y oxide synthesized at various pH values.....	51
3.2	Mole of component in the preparation of Ti_xSi_y oxide at pH 9.0 at various ratio between Ti and Si	52
4.1	Structure parameter (obtained from fittings of Ti K-edge EXAFS data) of first two coordination shells around Ti atom of Ti_xSi_y oxide synthesized at various pH values	77
4.2	Percentage of atomic and atomic ratio of Ti and Si in TiO_2 , SiO_2 , and Ti_xSi_y oxide synthesized at various pH values.....	78
4.3	The particle sized of TiO_2 , SiO_2 , and Ti_xSi_y oxide synthesized at various pH values.....	81
4.4	Specific surface area, pore volume and mean pore size of TiO_2 , SiO_2 , and Ti_xSi_y oxide synthesized at various pH values.....	82
4.5	Structure parameter (obtained from fittings of Ti K-edge EXAFS data) of first two coordination shells around Ti atom of Ti_xSi_y oxide with different Ti/Si ratio.	91
4.6	Percentage of atomic and atomic ratio of Ti and Si in Ti_xSi_y oxide with different Ti/Si ratio, TiO_2 , and SiO_2	92

LIST OF TABLES (Continued)

Table	Page
4.7 The particle sized of TiO ₂ , SiO ₂ , and Ti _x Si _y oxide with different atomic ratio of Ti/Si ratio.....	93
4.8 Specific surface area, pore volume and average pore size of SiO ₂ , TiO ₂ , and Ti _x Si _y oxide with different Ti/Si ratio.....	95
4.9 Tensile properties of PLA, PLA/TiO ₂ , PLA/SiO ₂ , PLA/Ti _x Si _y , and PLA/TiO ₂ SiO ₂ composites at various filler contents.	98
4.10 Thermal characteristics of PLA and PLA/Ti _x Si _y composites (the second heating, heating rate 5°C/min).....	102
4.11 Thermal degradation temperature of PLA, PLA/TiO ₂ , PLA/SiO ₂ , PLA/Ti _x Si _y , and PLA/TiO ₂ SiO ₂ composites.....	111
4.12 Transmittance (%) and opacity values of PLA, PLA/TiO ₂ , PLA/SiO ₂ , PLA/Ti _x Si _y , and PLA/TiO ₂ SiO ₂ composites films in the visible, UV-A, UV-B, and UV-C regions.....	120
4.13 Antimicrobial activity of gram-negative bacteria (<i>Escherichia coli</i>) of PLA, PLA/TiO ₂ , and PLA/Ti _x Si _y composite films.....	128
4.14 Antimicrobial activity of gram-positive bacteria (<i>Staphylococcus aureus</i>) of PLA, PLA/TiO ₂ , and PLA/Ti _x Si _y composite films.....	129
4.15 %yield of silk fibroin extracted from <i>Bombyx mori</i> silkworm cocoons using Ajisawa's solution and CaCl ₂ solution with various temperature.	133
4.16 Typical absorption band of FTIR spectra of silk fibroin.	135
4.17 Tensile properties of PLA, PLA/SF, PLA/Ti ₇₀ Si ₃₀ , PLA/Ti ₇₀ Si ₃₀ /SF composite at various SF contents.....	149
4.18 Thermal characteristics of PLA, PLA/SF _y , PLA/3Ti ₇₀ Si ₃₀ and PLA/3Ti ₇₀ Si ₃₀ /SF composites film (the second heating, heating rate 5°C/min).....	152
4.19 Thermal degradation temperature of PLA, PLA/SF, PLA/Ti ₇₀ Si ₃₀ , PLA/Ti ₇₀ Si ₃₀ /SF composite at various SF contents.....	155

LIST OF TABLES (Continued)

Table	Page
4.20 Transmittance (%) and opacity values of PLA, PLA/SF, PLA/3Ti ₇₀ Si ₃₀ and PLA/3Ti ₇₀ Si ₃₀ /SF composites films in the visible. UV-A, UV-B and UV-C regions	163



LIST OF FIGURES

Figure		Page
2.1	Chemical structure of poly (lactic acid) (PLA).....	8
2.2	Chemical structure of PLA-g-GMA.....	15
2.3	Crystal structures of TiO ₂ (a) rutile (b) brookite and (c) anatase (Ti (blue); O (red)).....	20
2.4	Structure of (a) crystalline and (b) amorphous SiO ₂	21
2.5	Functionalization on the surface of silica particle with modifier.....	22
2.6	Schematic representation of primary and secondary particles in alkoxide gel.....	23
2.7	Proposed model for the formation process of mesostructured TiO ₂ -SiO ₂ materials through titanium-citric acid complexes.....	29
2.8	Overview of the origin and structures of silk fibroin.....	32
2.9	Silk structure. (a) Solution conformation of <i>Bombyx mori</i> silk, (b) 2D silk fibroin schematic, and (c) Primary structure of the <i>Bombyx mori</i> silk heavy chain.....	34
2.10	Schematic representation of the (a) surface-unmodified SiO ₂ and (b) surface-modified SiO ₂ aggregate.....	43
2.11	SEM images of SF/PLA blend films within (a) 20 μm bar and (b) 200 nm bar. (c) Schematic of the SF-PLA interaction mechanisms based on the SEM images.....	47
3.1	Experimental procedures for preparing Ti _x Si _y oxide particles.....	50
3.2	Sequential experimental procedure for silk fibroin extraction from <i>Bombyx mori</i> silk cocoon.....	56
3.3	Schematic illustration of the experimental setup for photocatalytic process.....	61
3.4	Wavelength-absorbance curves of methylene blue aqueous solutions.....	62

LIST OF FIGURES (Continued)

Figure	Page
3.5	Calibration curve of methylene blue aqueous solutions..... 63
4.1	²⁹ Si-NMR patterns of (a) SiO ₂ and (b) Ti ₅₀ Si ₅₀ oxide67
4.2	FTIR spectra of TiO ₂ , SiO ₂ , and Ti _x Si _y oxides synthesized at various pH values..... 69
4.3	Proposed the probable mechanism for Ti _x Si _y oxides synthesized. 70
4.4	SEM images of Ti _x Si _y oxides synthesized at various pH values: (a) SiO ₂ , (b) Ti _x Si _y pH 8.0, (c) Ti _x Si _y pH 9.0, (d) Ti _x Si _y pH 10.0. 71
4.5	XRD patterns of Ti _x Si _y oxide synthesized at various pH values..... 72
4.6	Ti K-edge XANES spectra of Ti _x Si _y oxide synthesized at various pH values..... 74
4.7	The experimental EXAFS data of Ti _x Si _y oxide synthesized at various pH values in <i>R-space</i> within the intermission of 1.1-3 Å..... 76
4.8	Particle size distributions measured on a Zetasizer Nano ZS of SiO ₂ and Ti _x Si _y oxide synthesized at various pH values; (a) SiO ₂ , (b) Ti _x Si _y pH 8.0, (c) Ti _x Si _y pH 9.0, (d) Ti _x Si _y pH 10.0. 80
4.9	Nitrogen adsorption-desorption isotherms of SiO ₂ , TiO ₂ , and Ti _x Si _y oxide synthesized at various pH values..... 83
4.10	FTIR spectra of TiO ₂ , SiO ₂ , and Ti _x Si _y oxides synthesized with different atomic ratio of Ti/Si ratio..... 84
4.11	SEM images of TiO ₂ and Ti _x Si _y oxides synthesized with different atomic ratio of Ti/Si ratio; (a) TiO ₂ , (b) Ti ₇₀ Si ₃₀ , (c) Ti ₅₀ Si ₅₀ , (d) Ti ₄₀ Si ₆₀ 86
4.12	XRD patterns of Ti _x Si _y oxide with different Ti/Si atomic ratio..... 87
4.13	Ti K-edge XANES spectra of oxide with different atomic ratio of Ti/Si ratio..... 88
4.14	The experimental EXAFS data of Ti _x Si _y oxide with different Ti/Si ratio in <i>R-space</i> within the intermission of 1.1-3 Å..... 90
4.15	Particle size distributions measured on a Zetasizer Nano ZS of TiO ₂

LIST OF FIGURES (Continued)

Figure	Page
and TiO ₂ -SiO ₂ oxide with different atomic ratio of Ti/Si ratio; (a) TiO ₂ , (b) Ti ₇₀ Si ₃₀ , (c) Ti ₅₀ Si ₅₀ , (d) Ti ₄₀ Si ₆₀	94
4.16 Nitrogen adsorption-desorption isotherms of SiO ₂ , TiO ₂ , and Ti _x Si _y oxide with different Ti/Si ratio.....	96
4.17 Stress-strain curves of PLA, PLA/TiO ₂ , PLA/SiO ₂ , PLA/Ti _x Si _y , and PLA/TiO ₂ SiO ₂ composites at various filler contents	97
4.18 Tensile strength of PLA, PLA/TiO ₂ , PLA/SiO ₂ , PLA/Ti _x Si _y , and PLA/TiO ₂ SiO ₂ composites at various filler contents	100
4.19 Elongation at break of PLA, PLA/TiO ₂ , PLA/SiO ₂ , PLA/Ti _x Si _y , and PLA/TiO ₂ SiO ₂ composites at various filler contents.	100
4.20 Young's modulus of PLA, PLA/TiO ₂ , PLA/SiO ₂ , PLA/Ti _x Si _y , and PLA/TiO ₂ SiO ₂ composites at various filler contents	101
4.21 DSC thermogram of PLA, PLA/TiO ₂ , PLA/SiO ₂ , PLA/Ti _x Si _y , and PLA/TiO ₂ SiO ₂ composites (first heating, heating rate 5°C/min).....	105
4.22 DSC thermogram of PLA, PLA/TiO ₂ , PLA/SiO ₂ , PLA/Ti _x Si _y , and PLA/TiO ₂ SiO ₂ composites (cooling, cooling rate 5°C/min).....	106
4.23 DSC thermogram of PLA, PLA/TiO ₂ , PLA/SiO ₂ , PLA/Ti _x Si _y , and PLA/TiO ₂ SiO ₂ composites (second heating, heating rate 5°C/min).....	107
4.24 TGA thermogram of DSC thermogram of PLA, PLA/TiO ₂ , PLA/SiO ₂ , PLA/Ti _x Si _y , and PLA/TiO ₂ SiO ₂ composites.....	109
4.25 DTG Thermogram of PLA, PLA/TiO ₂ , PLA/SiO ₂ , PLA/Ti _x Si _y , and PLA/TiO ₂ SiO ₂ composites.....	110
4.26 SEM micrographs of the fracture surface of PLA, PLA/TiO ₂ , PLA/SiO ₂ , PLA/Ti _x Si _y , and PLA/TiO ₂ SiO ₂ composites.....	112
4.27 SEM micrographs after tensile testing of PLA, PLA/TiO ₂ , PLA/SiO ₂ , PLA/Ti _x Si _y , and PLA/TiO ₂ SiO ₂ composites.....	114

LIST OF FIGURES (Continued)

Figure	Page
4.28 Water vapor transmission rate (WVTR) of PLA, PLA/TiO ₂ , PLA/SiO ₂ , PLA/Ti _x Si _y , and PLA/TiO ₂ SiO ₂ composites.....	115
4.29 Concentration of methylene blue (MB) due to absorption of PLA, PLA/TiO ₂ , PLA/SiO ₂ , PLA/Ti _x Si _y , and PLA/TiO ₂ SiO ₂ composites films under UV irrigation.....	116
4.30 Photographs of films prepared from PLA, PLA/TiO ₂ , PLA/SiO ₂ , PLA/Ti _x Si _y , and PLA/TiO ₂ SiO ₂ composites (250-300 μm thickness).....	119
4.31 Weight loss of hydrolytic degradation of PLA, PLA/TiO ₂ , PLA/SiO ₂ and PLA/Ti _x Si _y composite films as functions of degradation time.	122
4.32 Weight loss of PLA, PLA/TiO ₂ , PLA/SiO ₂ and PLA/Ti _x Si _y composite films after different periods of in vitro degradation.....	123
4.33 Tensile strength of PLA, PLA/TiO ₂ , PLA/SiO ₂ and PLA/Ti _x Si _y composite films after different period of in vitro degradation.....	124
4.34 Elongation at break of PLA, PLA/TiO ₂ , PLA/SiO ₂ and PLA/Ti _x Si _y composite films after different period of in vitro degradation.....	125
4.35 Young's modulus of PLA, PLA/TiO ₂ , PLA/SiO ₂ and PLA/Ti _x Si _y composite films after different period of in vitro degradation.....	125
4.36 Comparison of bacterial cell wall structure of gram-negative bacteria and gram-positive bacteria.....	126
4.37 The number of (a) bacteria <i>Escherichia coli</i> (b) bacteria <i>Staphylococcus aureus</i> on of PLA, PLA/TiO ₂ , and PLA/Ti _x Si _y composite films at time 0 h (at dilution 10 ⁻³) and 24 h (at dilution 10 ⁰).....	130
4.38 Products of silk extraction from <i>Bombyx mori</i> silkworm cocoons; (a) cocoons, (b) degummed silk, (c) silk fibroin and (d) sericin	132
4.39 FTIR Transmittance spectra of cocoon, degummed silk, silk fibroin and sericin.	136
4.40 FTIR Transmittance spectra of silk produced by Ajisawa's solution	137

LIST OF FIGURES (Continued)

Figure	Page
4.41 FTIR Transmittance spectra of silk produced by CaCl_2 solution.....	137
4.42 X-ray diffraction pattern of silk fibroin (SF) and sericin.....	138
4.43 SEM images (x5000, 10 kV) and EDS spectra of sericin	139
4.44 SEM images of Cocoon, degummed silk, silk fibroin and sericin	140
4.45 SEM images of degumsilk and silk fibroin prepared from Ajisawa's solution	141
4.46 SEM images of degummed silk and silk fibroin prepared from CaCl_2 solution	142
4.47 TGA curves of cocoon, degummed silk, silk fibroin, and sericin of <i>Bombyx mori</i> silk.....	143
4.48 DTG curves of cocoon, degummed silk, silk fibroin, and sericin of <i>Bombyx mori</i> silk.....	144
4.49 Stress-strain curves of PLA, PLA/SF, PLA/Ti ₇₀ Si ₃₀ , PLA/Ti ₇₀ Si ₃₀ /SF composite at various SF contents.....	145
4.50 Tensile strength of PLA, PLA/SF, PLA/Ti ₇₀ Si ₃₀ , PLA/Ti ₇₀ Si ₃₀ /SF composite at various SF contents.....	146
4.51 Elongation at break of PLA, PLA/SF, PLA/Ti ₇₀ Si ₃₀ , PLA/Ti ₇₀ Si ₃₀ /SF composite at various SF contents.....	147
4.52 Young's modulus of PLA, PLA/SF, PLA/Ti ₇₀ Si ₃₀ , PLA/Ti ₇₀ Si ₃₀ /SF composite at various SF contents.....	148
4.53 DSC thermograms of PLA and PLA/SF composite at various SF contents. (the second heating, heating rate 5°C/min).....	150
4.54 DSC thermograms of PLA/Ti ₇₀ Si ₃₀ and PLA/Ti ₇₀ Si ₃₀ /SF composite at various SF contents. (the second heating, heating rate 5°C/min).....	151
4.55 TGA thermogram of PLA, PLA/SF, PLA/Ti ₇₀ Si ₃₀ , PLA/Ti ₇₀ Si ₃₀ /SF composite at various SF contents.....	153

LIST OF FIGURES (Continued)

Figure	Page
4.56 DTG Thermogram of PLA, PLA/SF, PLA/Ti ₇₀ Si ₃₀ , PLA/Ti ₇₀ Si ₃₀ /SF composite at various SF contents.	154
4.57 SEM micrographs of PLA/SF composite at various SF contents (Fracture surface)	157
4.58 SEM micrographs of PLA/Ti ₇₀ Si ₃₀ /SF composite at various SF contents (Fracture surface).....	158
4.59 SEM micrographs of PLA/SF composite at various SF contents (after tensile test).....	159
4.60 SEM micrographs of PLA/Ti ₇₀ Si ₃₀ /SF composite at various SF contents (after tensile test).....	160
4.61 Water vapor transmission rate (WVTR) of PLA, PLA/SF, and PLA/Ti ₇₀ Si ₃₀ , and PLA/Ti ₇₀ Si ₃₀ /SF composite films.	161
4.62 Photographs of films prepared from PLA, PLA/SF, and PLA/Ti ₇₀ Si ₃₀ , and PLA/Ti ₇₀ Si ₃₀ /SF composite films (250-300 μm thickness).....	164
4.63 Weight loss of hydrolytic degradation of PLA, PLA/SF, PLA/Ti ₇₀ Si ₃₀ and PLA/Ti ₇₀ Si ₃₀ /SF composite films as functions of degradation time.	165
4.64 Weight loss of PLA, PLA/SF, PLA/Ti ₇₀ Si ₃₀ and PLA/Ti ₇₀ Si ₃₀ /SF composite films after different periods of in vitro degradation.....	166

SYMBOLS AND ABBREVIATIONS

°C	=	Degree Celsius
g	=	Gram
%w/v	=	Percent weight by volume
wt.%	=	Percent by weight
PLA	=	Poly (lactic acid)
TiO ₂	=	Titanium dioxide (Titania)
SiO ₂	=	Silicon dioxide (Silica)
Ti _x Si _y	=	Titanium-silicon mixed oxide
TEOS	=	Tetraethylorthosilicate
TTIP	=	Titanium (IV) isopropoxide
FTIR	=	Fourier transform infrared spectroscopy
SF	=	Silk fibroin
GPC	=	Gel permeation chromatography
²⁹ Si-NMR	=	²⁹ Silicon nuclear magnetic resonance spectroscopy
SEM	=	Scanning electron microscope
FE-SEM	=	Field emission scanning electron microscope
XRD	=	X-ray diffraction
XANES	=	X-ray absorption near-edge structure spectroscopy
EXAFS	=	Extended X-ray absorption fine structure spectroscopy
XRF	=	X-ray fluorescence
BET	=	Brunauer, Emmett, Teller
DSC	=	Differential scanning calorimetry
TGA	=	Thermogravimetric analysis
WVTR	=	Water vapor transmission rate
RVP	=	Relative vapor pressure
PBS	=	Phosphate buffered saline
χ_c	=	Degree of crystallinity

SYMBOLS AND ABBREVIATIONS (Continued)

ΔH_m	=	Melting enthalpy
ΔH_m^0	=	Melting enthalpy of an infinitely large crystal
<i>E.coli</i>	=	<i>Escherichia coli</i>
<i>S.aureus</i>	=	<i>Staphylococcus aureus</i>
CFU	=	Colony-forming unit
σ^2	=	Debye-Waller factor
CN	=	Coordination number
Å	=	Angstrom
MPa	=	Megapascal
GPa	=	Gigapascal

CHAPTER I

INTRODUCTION

1.1 General introduction

In recent year, biocomposites/green composites materials, a category of biocompatible and/or eco-friendly composites, are remarkable achievements to replace conventional nonbiodegradable petroleum-based materials (Singh, Afrin, and Karim, 2017). Generally, biocomposites are made up of biodegradable polymer (bio-based polymer) being obtained from renewable resources (algae, bacteria, microorganisms, plants, etc) and bio-based reinforcing agents (Nagalakshmaiah, Afrin, Malladi, Elkoun, Robert, Ansari, Svedberg, and Karim, 2019).

Bio-based polymers represent interesting areas of material science, in which chemical, medical, and environmental scientists are leading to human health care, improving ability of life, protecting environment from white pollution, and reducing fossil-fuels consumptions. There are widely used in the medical and packaging engineering fields. Meanwhile aliphatic polyesters contain flexible ester bonds and they can degrade into nontoxic matters in different pH solutions, they might be the most promising bio-based polymers for medical (Cheung, Lau, Tao, and Hui, 2008) and packaging applications (F. Wang, Liu, Yuan, Yang, Li, and Gao, 2016; H. Wang, Liu, Chu, She, Jiang, Zhai, Jiang, and Li, 2015). With their excellent biocompatibility, polylactic acid (PLA)(Aoki, Kinoshita, Miyazaki, Saito, Fujie, Iwaya, Takeoka, and Saitoh, 2013; Chitrattha and Phaechamud, 2016; Cui, Jiang, Yuan, Cao, Li, Tang, and Qin, 2020; Liu, Liang, Zhang, Lan, and Qin, 2017), polyglycolic acid (PGA)(Lee, Yoon, Woo, and Choi, 2003; Samantaray, Little, Haddleton, McNally, Tan, Sun, Huang, Ji, and Wan, 2020), and polycaprolactone (PCL)(Bai, Li, Duo, Hao, Zhang, Shi, Guo, Ren, and Feng, 2017; Lima, Sousa, Arruda, Almeida, and Canedo, 2019; Malikmammadov, Tanir, Kiziltay, Hasirci, and Hasirci, 2017), as well as their copolymers are becoming the most commonly used synthetic biodegradable polymers in the medical field.

Poly (lactic acid) (PLA) is an important bio-based polymer. It made up with repeated monomer unit, lactic acid (LA), with a long linear chain. PLA made from sustainable and renewable materials (corn, bagasse, starch, rice, etc.) and breaks up into water and carbon dioxide throughout simple hydrolysis. PLA has been viewed as one of the most favorable materials due to its excellent biodegradability, biocompatibility, composability, renewability, good transparency, good barrier properties, low toxicity, high strength, high modulus, and excellent process-ability. Thus, PLA has been extensively used in a variety of application. The product of PLA degradation are non-toxic making it an ordinary choice for medical applications (Athanasίου, Niederauer, and Agrawal, 1996). Moreover, PLA has been accepted by the food and drug administration (FDA) to be safe for apply in food packaging materials. However, its brittleness, poor toughness, slow crystallization rate, low degree of crystalline, poor thermal stability, low degradation rate, lack of reactive side-chain group and hydrophobicity are major drawbacks of PLA and limit its application (Burg, Holder, Culberson, Beiler, Greene, Loeb sack, Roland, Mooney, and Halberstadt, 1999; Rasal, Janorkar, and Hirt, 2010; Yeh, Huang, Chai, and Chen, 2009).

Consequently, to further increase PLA applications, some properties of PLA such as mechanical properties, thermal properties, crystallinity, degradability and antimicrobial properties need to be improved. Several modifications such as polymer blends, copolymerization, plasticization, and polymer composites have been applied for improving some PLA properties. Currently, the addition of selected nanofillers into PLA such as organomodified layered silicates (OMLS) (Huang, Hwang, Liu, and Lin, 2010), carbon nanotubes (CNTs) (Cui, Jiang, Yuan, Cao, Li, Tang, and Qin, 2020; Tang, Chen, Wang, Xu, Hsiao, Zhong, and Li, 2012), zinc oxide (Murariu, Paint, Murariu, Raquez, Bonnaud, and Dubois, 2015), modified organo-montmorillonite clay (OM-MMt) (Dintcheva and Al-Malaika, 2020), silica nanofillers (SiO_2) (Hakim et al., 2017; G. Wu, Liu, Jia, and Dai, 2016), titanium dioxide (TiO_2) (Luo, Lin, and Guo, 2019; Xiu, Qi, Bai, Zhang, and Fu, 2017), is identified as a modern technique that can lead to main enhancements of PLA characteristic features.

Two of the most interesting nanofiller which are widely used is titanium dioxide and silicon dioxide. Titanium dioxide (TiO_2) called as titania, is an important chemical

and environmental material. TiO_2 particles are interesting nanomaterial due to its favorable biological effects, attractive photocatalytic activity, excellent photostability, biocompatibility, antimicrobial biomaterials and high corrosion resistance (Fonseca, Ochoa, Ulloa, Alvarez, Canales, and Zapata, 2015; Luo, Lin, and Guo, 2019; Zapata, Palza, Cruz, Lieberwirth, Catalina, Corrales, and Rabagliati, 2013). It is also extensively used as pharmaceutical and food additive, as well as white pigment in cosmetic products and in the paper engineering. In addition, it exhibits antimicrobial properties with adding silver, remove odors, and presenting strong germicidal properties (Wist, Sanabria, Dierolf, Torres, and Pulgarin, 2002). It is considered non-toxic and has been accepted by the food and drug administration (FDA) to be safe for apply in human food, drugs, cosmetic, and food packaging materials. The nanoparticles suggestion a low release rate of titanium ions that have an antimicrobial properties and wound healing. The titanium ions released from nanoparticle prevents microbial production and thus it increases wound healing (Archana, Singh, Dutta, and Dutta, 2013).

Another one nanofiller is silicon dioxide (SiO_2) called as silica, is a chemical compound that contains oxygen and silicon. Within inorganic oxide fillers, the silica particles have admitted much concentration because of their well-defined ordered structure, the ease surface modification, high surface area, and cost-effective production (F. Wu, Lan, Ji, Liu, Yang, and Yang, 2013). The addition of SiO_2 into polymer material is acknowledged to improve strength, modulus of elasticity, wear resistance, heat and fire resistances, insulating properties, etc (Serenko and Muzafarov, 2016). In addition, SiO_2 has been widely applied in a food additive, drug delivery, bioimaging, gene delivery, and engineering. Additionally, SiO_2 is classified by the FDA as a “generally regarded as safe” (GRAS) agent, thus making it an ultimate candidate for biomedical applications (Ha, Weitzmann, and Beck Jr, 2013).

Titanium-silicon oxide (Ti_xSi_y) denotes a new class of materials that have fascinated much attention in current years. The metal oxide has been widely used as catalysts and supports for an extensive variety of reactions. It made out from TiO_2 and SiO_2 not only take advantage of TiO_2 , the photocatalytic properties and antimicrobial biomaterials, and SiO_2 , excellent mechanical strength and high thermal stability, but also extends their applications throughout the generation of new active sites of catalyst

because of chemical bond between two materials (Gao and Wachs, 1999). There are many different methods to synthesize the Ti_xSi_y oxide but method that is more promising for low cost-effective is the sol-gel methods. This method does not require expensive solvents. During sol-gel methods, titanium alkoxide (e.g. titanium isopropoxide, TTIP) is often used.

Furthermore, the tensile strength and crystallization rate of PLA can be improved by reinforced PLA with fibers (Li and Huneault, 2007). Especially, silk fibroin (SF) of silkworm is a normally obtainable natural biopolymer. This is because of their nanostructured surface morphology and notable properties derived from the combination of characteristics of distinct constituent elements (Haraguchi, 2021). SF is extracted from cocoons of *Bombyx mori* silkworm. Silk fibroin (SF) has been extensively applied for biomedical applications (tissue engineering and wound healing) because of its excellent mechanical properties, good oxygen and water vapor permeability, hemocompatibility, controlled proteolytic biodegradation, lower inflammatory response than collagen, and morphologic flexibility. Additionally, its capability to support stem cell adhesion, proliferation, and variation in vitro and promote tissue regeneration are well recognized (Vepari and Kaplan, 2007). Therefore, the PLA/silk fibroin membrane could be a good candidate for wound dressing applications.

Additionally, the ways to extend crystallization rate of PLA include adding nucleating agent, reducing the amount of D-lactide isomers in the L-lactide, adding plasticizer and playing with the molding conditions, respectively. The adding a nucleating agent is the effective and easily, so this way is applied to extend crystallization rate of PLLA (Y. Cai, Yan, Fan, Yu, Chen, and Yin, 2012). The crystallization behavior of polymer is affected by nucleating agent affect leading to related morphology of the polymer. They provide extra nucleation sites which are accountable for a closer crystallization rate.

The nucleating agents can be divided into two types: inorganic and organic. Inorganic nucleating agents include Titanium dioxide (TiO_2) (Buzarovska, 2013), barium sulfate ($BaSO_4$) (Liao, Yang, Yu, and Zhou, 2007), talc (Battezzore, Bocchini, and Frache, 2011; Xiao, Guo, and Bao, 2015), , mica (Souza, Andrade, and Dias, 2014), calcium carbonate ($CaCO_3$)(N. Shi and Dou, 2014; X. Shi, Zhang, Siligardi, Ori, and

Lazzeri, 2015), nanoclay, carbon nanotube, and silica (SiO_2) (Hakim et al., 2017). Inorganic ones are used to improve mechanical properties of polymer. There are generally solid particles and cannot be deformed. Another type of nucleating agents for polymer processing can be classified into organic agents, such as hydrazide (Qi, Yang, Xiong, Deng, Zhang, and Zhu, 2015; Xu, Zhang, Zhao, Han, and Xue, 2015), aromatic multiamide derivative (Y.-H. Cai and Zhao, 2016), sorbitol, metal aromatic carboxylates, derivatives, and organic phosphates. Then, Ti_xSi_y oxide and SF are expected to improve properties of PLA in this study.

1.2 Research objectives

The main objectives of this research are classified as followings:

- (i) To study the preparation and characterization of the chemical and physical properties of titanium-silicon oxide (Ti_xSi_y) nanoparticle to be used as filler in poly (lactic acid) (PLA).
- (ii) To study the effect of Ti_xSi_y oxide nanoparticle and its content on the physical properties of PLA/ Ti_xSi_y oxide nanocomposites.
- (iii) To study the preparation and characterization of silk fibroin (SF).
- (iv) To study the effect of silk fibroin (SF) and its content on the physical properties of PLA/SF composites and PLA/ Ti_xSi_y oxide/SF composites.
- (v) To study the effects of Ti_xSi_y oxide nanoparticle on antimicrobial properties of PLA composites.
- (vi) To study biodegradation ability of PLA/ Ti_xSi_y oxide and PLA/ Ti_xSi_y oxide/SF composites.

1.3 Scope and limitation of the study

Titanium-silicon oxide (Ti_xSi_y) was prepared via sol-gel method with three difference atomic ratio of Ti/Si from Titanium (IV) isopropoxide (TTIP) and Tetraethylorthosilicate (TEOS) using as Ti and Si precursor via sol-gel method. The structures of Ti_xSi_y oxide was characterized by ^{29}Si nuclear magnetic resonance spectroscopy (^{29}Si NMR), Fourier transform infrared spectroscopy (FT-IR), Field emission scanning electron microscope (FE-SEM), X-ray diffraction (XRD), X-ray absorption near-

edge structure spectroscopy (XANES), and extended X-ray absorption fine structure spectroscopy (EXAFS). The chemical composition was analyzed by energy dispersive X-ray fluorescence (EDXRF). Particle size distribution of Ti_xSi_y oxide was determined by dynamic light scattering method. The N_2 adsorption isotherm of Ti_xSi_y oxide was measured by volumetric gas absorption method and the specific surface area and pore size distribution were calculated by BET and BJH method, respectively.

Silk fibroin (SF) was used to improve the hydrophilicity, and biocompatibility of PLA. SF powder was prepared from cocoons of *Bombyx mori* silkworm by degumming and freeze-drying method.

Neat PLA and PLA composites with different percentages of Ti_xSi_y oxide (1, 3, 5 wt.%) were prepared by solution casting method for their mechanical, morphological, and thermal properties and crystalline behavior. Tensile properties of the composites were evaluated according to ASTM D882-18 and the mechanical properties of all composites were compared. The morphology of the composites was observed by scanning electron microscopy (SEM). Thermal properties of the composites were studied by differential scanning calorimetry (DSC) and thermogravimetric analysis (TGA). The rate of water passed through the PLA and PLA composites film at a particular time interval was evaluated according to a modified ASTM E96/E96M. The antimicrobial effect of the composites was determined using the JIS Z 2801:2006 method. In addition, the hydrolytic degradation and in vitro degradation of composites were done according to the standard BS EN ISO 10993-13:2010 and ASTM F1635-16.

Based on mechanical properties of PLA/ Ti_xSi_y oxide nanocomposites, the composite giving the optimum mechanical properties was selected for further study of silk fibroin (SF) content on the mechanical, morphological, thermal properties of PLA nanocomposite. SF contents were 1, 3, 5 wt.%.

CHAPTER II

LITERATURE REVIEW

2.1 Biocomposites

Due to the concerns about environment and sustainability issues, the development of biocomposites from bio-based polymers and natural fibers has attracted excessive interests among researcher in the worldwide (La Mantia and Morreale, 2011). Biocomposites are defined as biocompatible and/or eco-friendly composites. There are made from natural and bio fibres that become eco-friendly and such composites are termed as green composites (Singh, Afrin, and Karim, 2017). The major attractions about green composites are that they are environmentally friendly, fully degradable and sustainable. These composites can be easily disposed of or composted without harming the environment.

Bio-based polymers are widely used in the medical and packaging engineering fields. Meanwhile aliphatic polyesters contain flexible ester bonds and they can degrade into nontoxic matters in different pH solutions, they might be the most promising bio-based polymers for medical (Cheung, Lau, Tao, and Hui, 2008) and packaging applications (Fang Wang, Liu, Yuan, Yang, Li, and Gao, 2016; H. Wang, Liu, Chu, She, Jiang, Zhai, Jiang, and Li, 2015). With their excellent biocompatibility, polylactic acid (PLA)(Aoki, Kinoshita, Miyazaki, Saito, Fujie, Iwaya, Takeoka, and Saitoh, 2013; Chitrattha and Phaechamud, 2016; Cui, Jiang, Yuan, Cao, Li, Tang, and Qin, 2020; Y. Liu, Liang, Zhang, Lan, and Qin, 2017), polyglycolic acid (PGA)(K.-B. Lee, Yoon, Woo, and Choi, 2003; Samantaray, Little, Haddleton, McNally, Tan, Sun, Huang, Ji, and Wan, 2020), and polycaprolactone (PCL)(Bai, Li, Duo, Hao, Zhang, Shi, Guo, Ren, and Feng, 2017; Lima, Sousa, Arruda, Almeida, and Canedo, 2019; Malikmammadov, Tanir, Kiziltay, Hasirci, and Hasirci, 2017), as well as their copolymers are becoming the most commonly used synthetic biodegradable polymers in the medical field.

2.2 Poly (lactic acid) (PLA)

Poly (lactic acid) or polylactide (PLA) is a renewable aliphatic polyester with the most widely researched and utilized biodegradable. PLA has a recognized capability either to replace conventional petrochemical-based polymers for industrial application and for several medical application (Henton, Gruber, Lunt, and Randall, 2005; Savioli Lopes, Jardini, and Maciel Filho, 2012).

The production of PLA had several advantages compared to other biopolymers, including i) Eco-friendly - PLA made from sustainable and renewable materials (starch, corn, bagasse, rice, etc.) and breaks up into water and carbon dioxide throughout simple hydrolysis into. ii) Biocompatibility - the most fascinating characteristic of PLA, particularly with respect to biomedical applications. iii) Processability - PLA has superior thermal processability compared to other biopolymers such as polycaprolactone (PCL), poly (hydroxy alkanooate) (PHA), and poly (ethylene glycol) (PEG). It can be processed by film extrusion, injection molding, blow molding, fiber spinning, thermoforming, and film forming (Auras, Harte, and Selke, 2004). iv) Energy saving - PLA needs 25-55% lower energy to produce than petroleum-based polymers and approximations display that this can be further condensed to lower than 10% in the upcoming (Rasal, Janorkar, and Hirt, 2010). The chemical structure of PLA is shown in Figure 2.1.

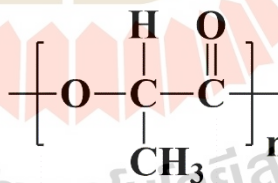


Figure 2.1 Chemical structure of poly (lactic acid) (PLA)

PLA has been viewed as one of the most favorable materials due to its excellent biodegradability, biocompatibility, composability, renewability, good transparency, good barrier properties, low toxicity, high strength, high modulus, and excellent process-ability. It has extra properties such as water vapor transport properties and breathability, and buffering capacity to liquid sweat than that of polyester and cotton (Shanmugam and Sundaramoorthy, 2015). Thus, PLA has been extensively used in a variety of application. The product of PLA degradation are

nontoxic making it an ordinary choice for medical applications (Athanasίου, Niederauer, and Agrawal, 1996). PLA is being used in the applications of biomedical such as implants for orthopedic devices and sustained drug delivery systems because of its hydrophobicity. It has small contact angle which would promote low adherence to the wound site (Y. Wu, Li, and Gao, 2009). Moreover, it is considered nontoxic and has been accepted by the food and drug administration (FDA) to be safe for apply in food packaging.

Nevertheless, PLA has many disadvantages, such as brittleness, slow crystallization rate, low degree of crystalline, poor toughness, poor thermal stability, low degradation rate, hydrophobicity, a poor gas barrier, and lack of reactive side-chain group leading to limit its application (Burg, Holder, Culberson, Beiler, Greene, Loeb sack, Roland, Mooney, and Halberstadt, 1999; Rasal, Janorkar, and Hirt, 2010; Yeh, Huang, Chai, and Chen, 2009). PLA homopolymers have some properties as shown in Table 2.1. They request processing temperatures in excess of 185-190°C (Garlotta, 2001).

Table 2.1 General characteristics of a commercial PLA, 3D Printing Monofilament – General Purpose Grade (Ingeo™ Biopolymer 4043D Technical data sheet, produced by NatureWorks LLC)

Characteristics	Unit	Amount	ASTM method
<i>Physical properties:</i>			
Weight Average Molecular Weight (Mw)	g/mol	233066	GPC
Number Average Molecular Weight (Mn)	g/mol	137244	
Polydispersity index		1.698	
Specific gravity	kg/m ³	1.24	D792
MFR (@210°C, 2.16kg)	g/10min	6	D1238
Glass transition temperature, T _g	°C	55-60	D3418
Melting temperature, T _m	°C	145-160	D3419

Table 2.1 General characteristics of a commercial PLA, 3D Printing Monofilament – General Purpose Grade (Ingeo™ Biopolymer 4043D Technical data sheet, produced by NatureWorks LLC) (continued)

Characteristics	Unit	Amount	ASTM method
<i>Optical properties:</i>			
UV light transmission:			(Auras, Harte, and Selke, 2004)
190 to 220 nm	%	<5	
225 to 250 nm	%	85	
>300 nm	%	95	
Visible light transmission:	%	95	
Clarity		Transparent	
Color			
L*		90.64 ± 0.21	
a*		-0.99 ± 0.01	
b*		-0.50 ± 0.04	
<i>Mechanical properties:</i>			
Tensile Yield Strength	MPa	60	D882
Tensile Strength at Break	MPa	53	D882
Tensile Modulus	MPa	3.6	D882
Tensile Elongation	%	6	D882
Notched Izod Impact	J/m	16	D256
Flexural Strength	MPa	83	D790
Flexural Modulus	MPa	3.8	D790
Heat Distortion Temperature (0.45 MPa)	°C	55	E2092

2.3 The improvement of PLA properties

In recent year, numerous PLA based technologies have immersed with an importance on attaining mechanical properties, chemical properties, degradation, biological properties, and antimicrobial activity equal or superior to conventional polymer. The common requirement for a physical or chemical modification of PLA to complete appropriate properties for its proposed consumer and biomedical applications, has required significant attention in the last decade. The effective application of PLA in biomedical and consumer applications relies not only on mechanical properties being better than or equal to conventional plastics, but also on controlled surface properties (e.g., roughness, hydrophilicity, and reactive functionalities).

Properties of PLA can be improved by using numerous modifications, such as polymer blending, copolymerization, plasticization, and polymer composite. Especially, polymer composites of PLA with selected nanofillers is considered as a topical method that can lead to main enhancements of PLA characteristic features.

Copolymerization had been considered as a powerful means to obtain polymer materials with properties unachievable by homopolymers. Properties of the PLA including tensile and impact performances of a copolymer could be changed in a flexible technique by operating the architecture of the molecule, order of monomers, and composition.

Ghalia and Dahman (2017) evaluated the effect of multi-functional chain extenders of polylactic acid-co-polyethylene glycol (PLA-co-PEG) copolymer on the molecular weight, mechanical, thermal stability, and degradation. PLA-co-PEG were synthesized at 80PLA/20PEG using direct melt polycondensation without solvent. The styrene- glycidyl acrylate copolymer contents were 0.25, 0.50, 0.75, 1.00, 1.25, and 1.50 wt% using as chain extender (CE). Obviously, at the presence of CE enhanced the mechanical properties of copolymers. Compared with 60 MPa for neat PLA, a long chain branch structure has led to a small enhancement of tensile strength to 70 MPa at 1.25%CE. A noteworthy increase of 17% was observed for the elongation at break (EB) of copolymers after adding 1.5% CE. In the ranges of 1-1.25%CE, the impact strength of copolymers increased to 7.9 KJ/m². Additionally, differential scanning

calorimetric (DSC) results of 1.25%CE showed enhancement of glass transition temperature (T_g) at 62°C, melting temperature (T_m) at 161°C, and percent crystallinity (χ_c) 34.9% as a result from the chain extension processes. The CEs have a positive effect on the enhancement of thermal stability. Furthermore, the compatibility and interfacial adhesion between the PLA and PEG chains were enhanced in the existence of the CE contents as shown in SEM imaged. The weight loss of 1.5%CE was only 3% during 30 days of degradation time, while the weight loss of the copolymer was 28%, during the same time interval.

Plasticizers were applied not only to enhance the processability of polymers but also to improve flexibility and ductility of glassy polymers. A favorite plasticizer for PLA should be one, which suggestively lowers T_g of PLA, was biodegradable, nontoxic, nonvolatile, and shows slight leaching or migration during aging.

Yeh, Huang, Chai, and Chen (2009) reported the effects of triacetine (TAc) using as plasticizer on tensile properties, chain mobility, crystallization, and microstructure of the PLA//TAc blends. With increasing TAc contents, T_g and T_m of PLA_xTAc_y blends significantly declined. Nevertheless, α -form of PLA crystals were found during the annealing processes of the series specimens of PLA_xTAc_y blends as demonstrated by WAXD. In fact, β -form of PLA crystals, less perfect crystal, were found as the TAc contents of PLA_xTAc_y blend reach 30 wt.%. Likely, the presence of α and β form of PLA crystals in recrystallized process was ascribed to the predictable rise in the free volume and molecular mobility of the PLA molecules as the increase of TAc contents in PLA_xTAc_y blend. Then PLA molecules could recrystallize at comparatively low temperatures during the heat-scanning processes by the plasticized and relatively mobile. The PLA showed relatively high tensile strength but low elongation at break. With increasing TAc contents from 0 to 25 wt. % in the blend, the tensile strength and elongation at break of PLA_xTAc_y blends reduced from 52.6 to 30 MPa and significantly increased from 2.8 to 267.2%, respectively. Nevertheless, both tensile strength and elongation at break of PLA_xTAc_y blend reduced instantaneously with increasing TAc contents from 25 to 30 wt.%.

Avolio, Castaldo, Avella, Cocca, Gentile, Fiori, and Errico (2018) studied phenomenon of Poly(lactic acid) /plasticizer/calcium carbonate on the time evolution

of properties. PLA/plasticizer/ CaCO_3 have been prepared by a two-step melt mixing process. The esterified oligomers of lactic acid (OLAs) with different chain terminals (hydroxyl and carboxyl) were used as plasticizers for PLA. With adding CaCO_3 up to 9 wt.% into PLA, nanocomposites were successfully added preservative the plasticity of PLA nanocomposites and with beneficial effects on the elastic modulus and yield stress. Mechanical, thermal and transport properties were measured as a function of aging time, up to 20 weeks, to estimate the phase evolution of the plasticized nanocomposites. A fascinating enhancement in the time stability of mechanical and transport properties was emphasized and related to the effect of particles/plasticizer interactions on phase structure.

In addition, the many researches have been achieved on the PLA blend with several flexible biodegradable polymers. Because polymer blending with biodegradable polymer is observed as a valuable and cost-effective technique to produce new materials with an extensive range of properties and maintained fully biodegradability.

Teamsinsungvon, Jarapanyacheep, Ruksakulpiwat, and Jarukumjorn (2017) studied the blend of PLA and poly(butylene adipate-co-terephthalate) (PBAT). Mechanical, morphological, and thermal properties of PLA/PBAT blends were evaluated. PBAT contents were 10, 20, and 30 wt%. The blends were prepared using melt processing. PLA/PBAT blends increased in elongation at break and impact strength but decreased in tensile strength and Young's modulus. In addition, PBAT cold crystallization temperature and degree of crystallinity of the blends decreased while thermal stability of PLA improved.

Especially, polymer composites of PLA with selected nanofillers such as organomodified layered silicates (OMLS) (S.-M. Huang, Hwang, Liu, and Lin, 2010), carbon nanotubes (CNTs) (Tang, Chen, Wang, Xu, Hsiao, Zhong, and Li, 2012), zinc oxide (Murariu, Paint, Murariu, Raquez, Bonnaud, and Dubois, 2015), silica nanofillers (SiO_2) (Hakim et al., 2017; G. Wu, Liu, Jia, and Dai, 2016), titanium dioxide (TiO_2) (Xiu, Qi, Bai, Zhang, and Fu, 2017), is considered as a modern method that can lead to main developments of some properties such as mechanical properties, thermal properties, degradation, biological properties, and antimicrobial activity of PLA.

Gupta, Mishra, Srivastava, Gangwar, Nath, and Maiti (2013) studied the novel poly (lactic acid) (PLA)/TiO₂ hybrid nanofibers. PLA/TiO₂ hybrid nanofibers were prepared through technique of electrospin. For UV protection improving, titanium precursor was hydrolyzed and then electrospayed instantaneously on the continuous electrospun PLA nanofibres surface. After that the hydrolyzed Ti precursor was reformed into TiO₂ particle located onto the nanofibre surface only to attain better light scattering by nano TiO₂ on surface. The structural transition was studied by using XRD, XPS, FTIR, and Raman studies. The major phase was anatase with a small amount of brookite phase after the hydrothermal treatment. The much more absorption of UV light by the hybrids was confirmed and the optical band gap was slowly decreased with increasing time of hydrothermal treatment representing greater UV absorption properties of the hybrids. The antimicrobial activity was tested and found 70% reduction in bacterial growth using 90 min hydrothermally treated hybrids as related to neat PLA nanofibre.

2.4 Improving interfacial adhesion of PLA composites

The dispersibility of particles was the main problems correlated to the nanocomposites based on polymer matrices and nanoparticles within the high molecular organic matrix. The repulsive forces between particle surfaces in polymer matrix are really restricted, leading to strong agglomeration of nanoparticles. As the uniform and high level of distribution of nanoparticles is the important state to achieve respected properties, the important attempt has been made in order to expand the compatibility between the nanofiller and the polymer matrix.

One of the efficient methods used in order to change the elementary properties of PLA is grafting of PLA with reactive monomers. Glycidyl methacrylate (GMA) has been used as a compatibilizing material in composites since GMA is a bifunctional monomer comprising of an epoxy group at one end and an acrylic group in another end. The epoxy group of GMA can react with many other groups such as hydroxyl and carboxyl groups, the acrylic group allows GMA to be grafted onto polymer chain through free-radical grafting. Therefore, PLA-g-GMA has been increasingly used as

a compatibilizer in many studies. The chemical structure of PLA-g-GMA is show in Figure 2.2.

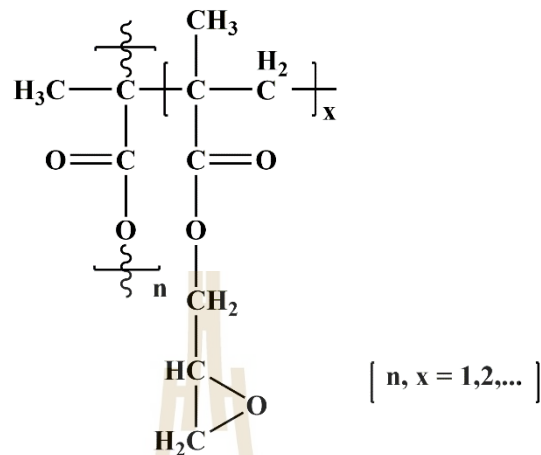


Figure 2.2 Chemical structure of PLA-g-GMA (Vp, Mohanty, and Nayak, 2016)

Liu, Jiang, and Chen (2012) studied the preparation of PLA-g-GMA in a batch mixer using benzoyl peroxide as an initiator, which was used as compatibilizers between PLA and starch. The compatibilizing effect of PLA-g-GMA was determined on the mechanical properties, morphological properties, thermal properties, and medium-resistance of the PLLA/starch blends. They found that the graft content of PLA-g-GMA reach as high as 11.0 wt.% as the GMA concentration is 20 wt.%. PLA-g-GMA copolymer improved interfacial adhesion of PLA/starch blends. The starch granules were clearly observed in PLA/starch blends, however the starch granules were well dispersed and enclosed by PLA due to compatibilizing effect of PLA-g-GMA copolymer. Furthermore, the PLA/starch blends compatibilized presented better mechanical properties and stronger medium-resistance in comparison with the simple PLA/starch blends at 15 % the PLA-g-GMA.

Sajna, Smita, and Sanjay (2015) investigated influence of PLA-g-GMA as a compatibilizer on properties of poly (lactic acid)/banana fiber biocomposites. PLA/silane treated banana fiber (SiB) biocomposites with various GMA content were performed by melt blending followed by injection molding techniques. The influence of GMA content on the mechanical properties, thermal properties, and moisture

resistance properties of the PLA/SiB composite was studied. They found that PLA/SiB biocomposite provided optimum tensile and flexural strength, which is ascribed to the greater compatibility between fiber and PLA matrix when adding 15wt.% GMA content in the composite. Moreover, incorporating with GMA into PLA/SiB biocomposites improved the moisture absorption resistance and thermal stability.

Thanh, Ruksakulpiwat, and Ruksakulpiwat (2017) studied the influences of PLA-g-GMA on the dispersion of cellulose nanofibers (CNFs) from cassava pulp (CP) in PLA matrix and impact strength of CNFs-reinforced PLA biocomposites. The biocomposites were prepared by melt mixing, followed by hot melt pressing. PLA-g-GMA was applied as a compatibilizer in order to expand the compatibility of PLA/CNFs composite. They found that most nanofibers with the diameter in the range of 10-30 nm and infinite length were found from TEM. The dispersion of CNFs in PLA/CNFs composites was improved with adding 20 wt.% of PLA-g-GMA. Furthermore, impact strength of biocomposites was insignificantly improved compared to that of pure PLA by incorporating 1.0 wt.% CNFs into PLA matrix and using PLA-g-GMA as a compatibilizer.

Aleksandra Buzarovska (2013) prepared PLA and functionalized TiO₂ nanoparticles with propanoic acid by solution blending method with 0.5, 2, 5 and 10wt.% of modified TiO₂ nanoparticles. The influence of functionalized TiO₂ nanoparticles on thermal properties, puncture characteristics as well as photodegradability of the PLA/TiO₂ nanocomposite films were investigated. The functionalization of TiO₂ nanoparticles with propanoic acid was investigated by FTIR and UV-Visible spectroscopy. SEM micrographs presented good dispersibility in both composites complete with less than 2 wt.% of TiO₂ with modified and unmodified nanoparticles. Additionally, higher crystallinity and slightly increased T_g of PLA/TiO₂ were recognized at all nanofiller loadings, resulting in increased brittleness of the PLA films. However, the functionalization of TiO₂ nanoparticles with propanoic acid did not have important effect on the photodegradation behavior of the PLA films.

Luo (2014) studied the nanocomposites of modifying nano-TiO₂ with lactic acid (g-TiO₂) and PLA. PLA/g-TiO₂ were prepared using the melt blending in twin-screw extruder. The g-TiO₂ contents were varied between 0 to 8 wt%. The g-TiO₂ was prepared through the solution without catalyst with 7 wt.% of grafting rate. The test

on the thermal property, dynamic mechanical property, and thermal deformation temperature were evaluated. The adding nano TiO₂ helped improve its energy storage modulus and this should be related to a lot of graft polymers on the surface of nanometer TiO₂ particles. The thermal decomposition temperature of PLA increased with adding TiO₂ into PLA and this was very useful for materials processing and production. In addition, thermal deformation temperature of the nanocomposites improved insignificantly compared with pure PLA with increasing nano TiO₂ content.

2.5 Titanium-Silicon oxide

Titanium-silicon oxide (Ti_xSi_y) acts for an innovative class of materials that have fascinated much consideration in current years. Titania-silica materials have been widely used as catalyst and supports for an extensive type of reactions (Gao and Wachs, 1999). Composites made out of silica (SiO₂) and titania (TiO₂), not only take advantage of both TiO₂ (the photocatalytic properties and an active catalytic support) and SiO₂ (high thermal stability and admirable mechanical strength), but also covers their applications and extra properties coming from the generated new active sites because of the chemical interaction of TiO₂ with SiO₂ between two materials (Shivatharsiny Rasalingam, Rui Peng, and Koodali, 2014).

Although TiO₂ has been applied as a photocatalyst for the degradation of pollutants, but low adsorption efficacy, surface area, and porosity restrict its application. To overcome these aforementioned challenges, a usual strategy is to combine TiO₂ into supporting materials such as SiO₂.

The application of Ti_xSi_y oxide as catalysis and supports set about three categories base on their exclusive physico-chemical properties including: (i) photocatalysis that is related to the support effect and the quantum-size effect; (ii) acid catalysis that is associated with the generation of new acid sites; and (iii) outstanding catalytic support materials that keep improved thermal and mechanical stability because fo SiO₂ while conserving the catalytic performance of TiO₂ (Gao and Wachs, 1999). The considerate of the structural properties of Ti_xSi_y oxide and the relationships with the physico-chemical properties and reactivity is also of excessive importance in an inclusive range of applied science.

2.5.1 Titanium dioxide (TiO₂)

Titanium dioxide (TiO₂) called as titania, is an important chemical and environmental material. It is well known as a valued material with applications in textiles, photocatalysis, paints, as filler in paper, etc. Nano-TiO₂ particles possess many good properties such as good chemical resistance, high chemical stability (Zapata, Palza, Cruz, Lieberwirth, Catalina, Corrales, and Rabagliati, 2013), attractive photocatalytic activity, excellent photostability, biocompatibility, antimicrobial biomaterials (Fonseca, Ochoa, Ulloa, Alvarez, Canales, and Zapata, 2015).

Natural titanium dioxide occurs in three crystal alterations, as the well-known naturally occurring minerals anatase (tetragonal, $a = b = 3.782 \text{ \AA}$, $c = 9.502 \text{ \AA}$), rutile (tetragonal, $a = b = 4.854 \text{ \AA}$, $c = 2.953 \text{ \AA}$) and brookite (rhombohedral, $a = 5.436 \text{ \AA}$, $b = 9.166 \text{ \AA}$, $c = 5.135 \text{ \AA}$) (Etacheri, Di Valentin, Schneider, Bahnemann, and Pillai, 2015). rutile is the most common and stable form while both of anatase and brookite can be transformed to rutile when submitting the material at temperatures above 700 °C (in pure state, when no additives have been added). Rutile, anatase and brookite all hold six coordinates titanium.

In all the three TiO₂ forms, the stacking of the octahedral results in threefold coordinated oxygen atoms (Periyat, Pillai, McCormack, Colreavy, and Hinder, 2008). The structures of anatase, rutile, and brookite are revealed in Figure 2.3. Physical and chemical properties of the three TiO₂ structures are exhibited in Table 2.2.

Table 2.2 Physical and chemical properties of rutile, anatase, and brookite (Hamdan, 2012)

Properties	Rutile	Anatase	Brookite
Molecular formular	TiO ₂		
Molar mass, g/mol	79.866		
Crystal System	Tetragonal	Tetragonal	Orthorhombic
Color	White solid	-	-
Density, g/cm ³	4.27	3.90	4.13
Energy gap, eV	3.06	3.29	-
Melting point, °C	1855	Transformed into rutile	Transformed into rutile
Boiling point	2972	-	-
Refractive index	2.609	2.488	2.583
Dielectric constant, ϵ	110-117	48	78
Hardness, Mohs scale	7.0-7.5	5.5-5.6	-

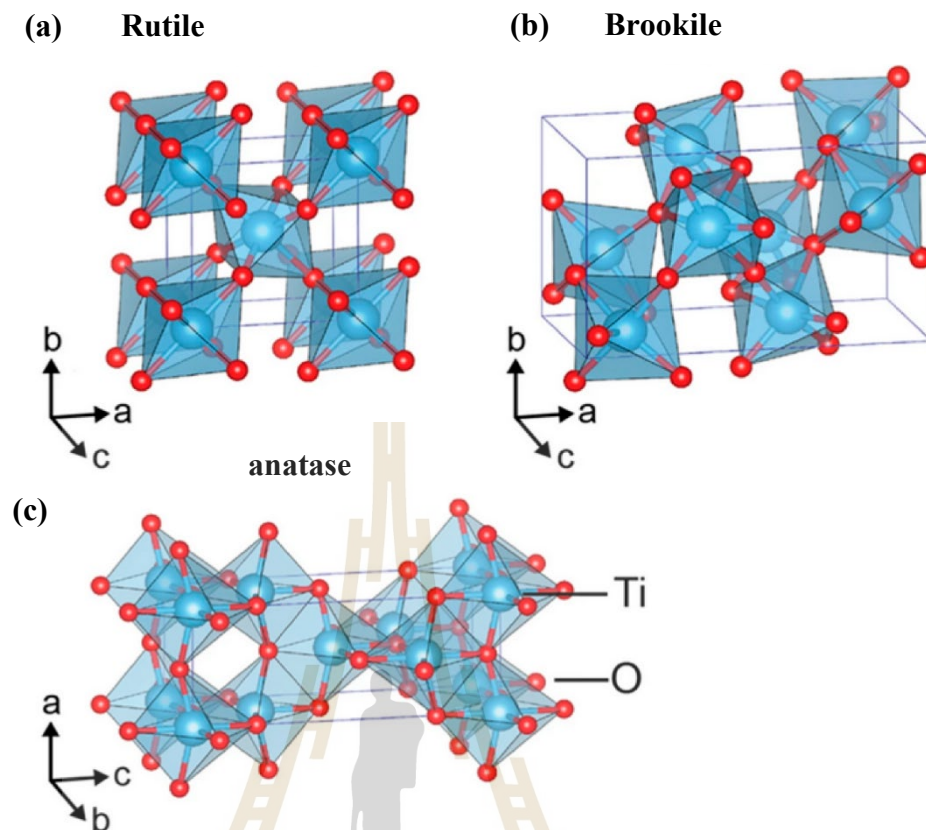


Figure 2.3 Crystal structures of TiO_2 (a) rutile (b) brookite and (c) anatase (Ti (blue); O (red)) (Haggerty et al., 2017).

2.5.2 Silicon dioxide (SiO_2)

Silicon dioxide (SiO_2) called as silica, is a chemical compound that contains oxygen and silicon. The structures of SiO_2 are shown in Figure 2.4. All silica forms are identical in chemical composition while they have dissimilar atom arrangements. Silica can be separated into two groups including crystalline and amorphous silica (or non-crystalline silica). The crystalline silica have structures with repeating patterns of silicon and oxygen (Figure 2.4a). While chemical structures of amorphous silica are more randomly linked when compared to crystalline silica (Figure 2.4b). All of silica forms are odorless solids composed of silicon and oxygen atoms. Silica particles converted suspended in air and form non-explosive dusts. Silica may association with other metallic elements and oxides to form silicates.

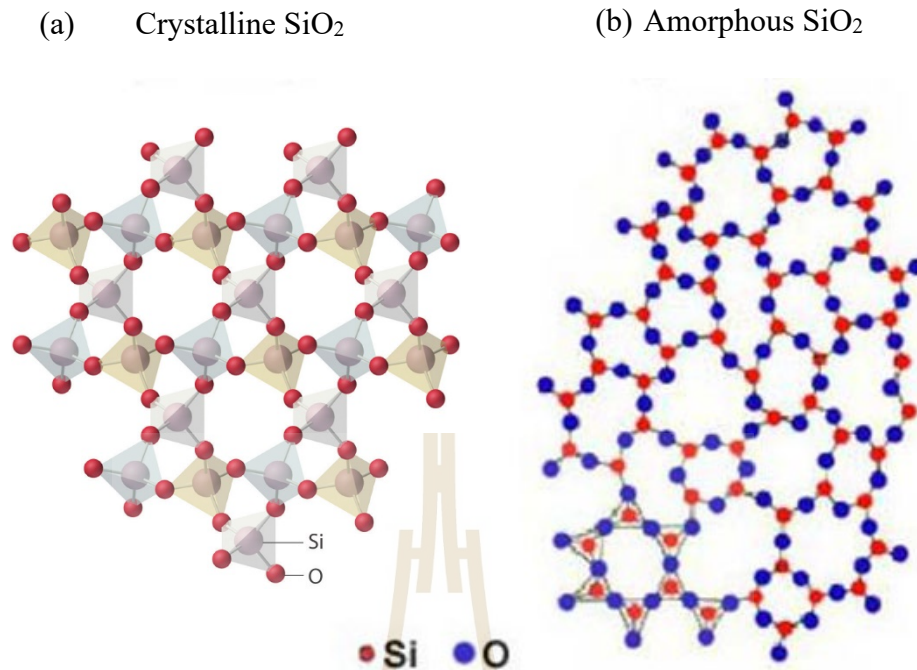


Figure 2.4 Structure of (a) crystalline and (b) amorphous SiO₂
 (<https://chem.libretexts.org/>; <https://mo-sci.com/glass-processing-temperatures/>)

Within inorganic oxide fillers, the silica particles have admitted much concentration because of their well-defined ordered structure, the ease surface modification, high surface area, and cost-effective production (F. Wu, Lan, Ji, Liu, Yang, and Yang, 2013). The addition of SiO₂ into polymer material is acknowledged to improve strength, modulus of elasticity, wear resistance, heat and fire resistances, insulating properties, etc (Serenko and Muzafarov, 2016). In addition, SiO₂ has been widely applied in a food additive, drug delivery, bioimaging, gene delivery, and engineering. Additionally, SiO₂ is classified by the FDA as a “generally regarded as safe” (GRAS) agent, thus making it an ultimate candidate for biomedical applications (Ha, Weitzmann, and Beck Jr, 2013).

Among inorganic oxide fillers, the silica particles have established more consideration because of their high surface area, the ease surface modification, well-defined ordered structure, and cost-effective production (Figure 2.5). In the polymer composition with silica, silica particles can expand their thermal properties and self-

supporting capacity under working environmental conditions. The silica particles, which are performed by many route such as wet (silica gel, precipitated silica) and thermal (pyrogenic silica) routes starting from silica precursors, and by the extraction from plants have lots of hydroxyl groups on the surface, the so-called silanols group (Si-OH). So, they are extensively used and being a perfect candidate to advance the properties of polymers, including PLA. It has been applied in plastic and paint (Wu, Lan, Ji, Liu, Yang, and Yang, 2013), biomedical, and increased thermal degradation in PLA nanocomposites (Khankruea, Pivsa-Art, Hiroyuki, and Suttiruengwong, 2013).

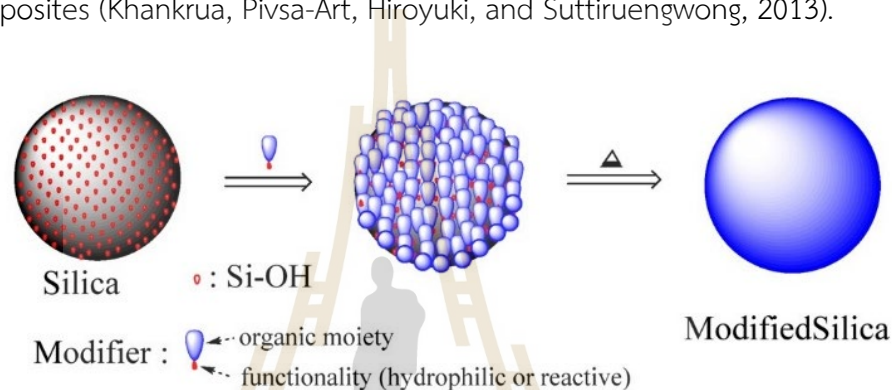


Figure 2.5 Functionalization on the surface of silica particle with modifier (Lee and Yoo, 2016)

2.5.3 Sol-gel process

Sol-gel process is an adaptable method that has established commercial success as chosen properties of a material can be attained through control over the synthesis route (Ullattil and Periyat, 2017). It is a wet chemical route for the synthesis of colloidal dispersions (sols) of inorganic and organic hybrid materials, particularly oxides and oxides-based hybrid at relatively low temperatures. Three methods are applied to make sol-gel monoliths including; (i) gelation of a solution of colloidal powders; (ii) hydrolysis and polycondensation of alkoxide precursors followed by hypercritical drying of gels; (iii) hydrolysis and polycondensation of alkoxide precursors followed by aging and drying under ambient atmospheres (Hench and West, 1990).

Sols are dispersions of colloidal particles in a liquid and colloids are solid particles with diameters of 1-100 nm (Hench and West, 1990). The sols are

transformed into viscous gels (sol-gel transition) by vigorous stirring at low temperatures (Klein, 1985). At the transition, the sol becomes a rigid, porous mass through dislocation, precipitation or supersaturation. The sol becomes a gel when it can support stress elastically. A gel is an organized, rigid network with pores of submicrometer sizes and polymeric chains whose average length is more than a micrometer (Aragón-Santamaría, Santos-Delgado, Maceira-Vidán, and Polo-Diez, 1991). The gels can be dried at room temperature to form glass or they can be ground to make fine powders. In the sol-gel process, it offers inherent advantages such as molecular-scale mixing of reactants to generate highly homogeneous products. However, the grain growth occurs at the same time as agglomeration such that it becomes difficult to separate between primary particles which consist of small grains or crystallites, and secondary particles which are agglomerates of primary particles. The primary particles and agglomerates in secondary particles are shown in Figure 2.6.

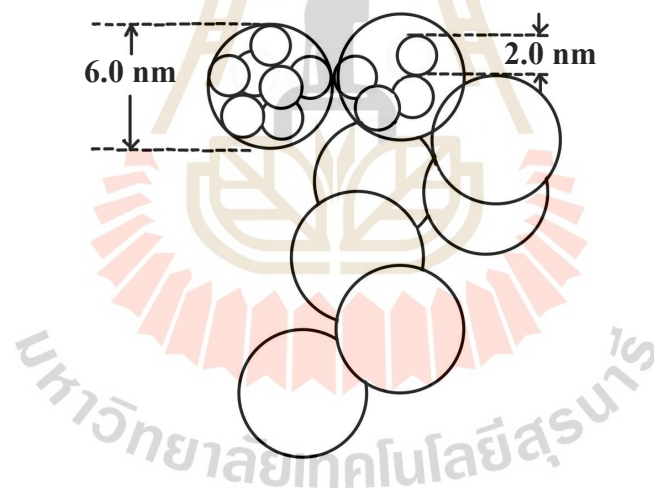


Figure 2.6 Schematic representation of primary and secondary particles in alkoxide gel (Hench and West, 1990).

2.5.4 Synthesis of $\text{TiO}_2\text{-SiO}_2$ via sol-gel method

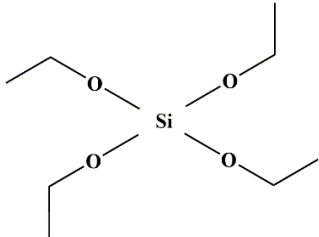
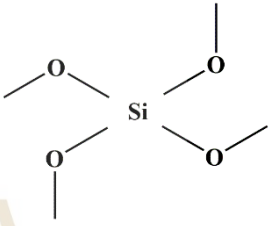
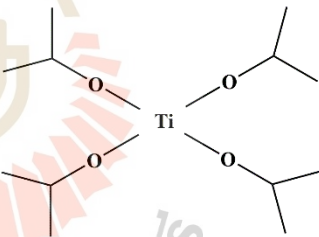
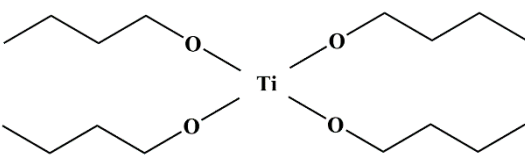
The preparation of titanium-silicon oxides have been widely described in the literature because of their large number of application in catalysis (Dutoit, Schneider, and Baiker, 1995; Pabón, Retuert, and Quijada, 2007). There are many different strategies to synthesize these materials, such as flame hydrolysis,

impregnation, coprecipitation, chemical vapor deposition, sol-gel etc., leading to mixed oxides with different physicochemical properties depending in the composition, the dispersion of the titanium phase, etc. Among them, the sol-gel method is an adaptable method that has established commercial success as chosen properties of a material can be obtained through control over the preparation route. In addition, this method offers intrinsic advantages such as molecular-scale mixing of reactants to generate highly homogeneous products (Liu and Davis, 1994).

Typical sol-gel process are two basic steps involved: (i) partial hydrolysis of metal alkoxide to form reactive monomers; (ii) polycondensation of these monomers to form colloid-like oligomers (sol); and (iii) extra hydrolysis to promote polymerization and cross-linking leading to a 3D matrix (gel). As polymerization and cross-linking progress, the viscosity of the sol slowly increased until the sol-gel transition point, where viscosity suddenly enlarged and gelatin occurs (Vijatović, Bobić, and Stojanović, 2008). The adaptable precursors for the sol-gel synthesis of oxide are metal alkoxides, but organic and inorganic salts are also often used (Whitehouse, Dreyer, Yamashita, and Fenn, 1985; Yamada, Yoshinaga, and Katayama, 1998).

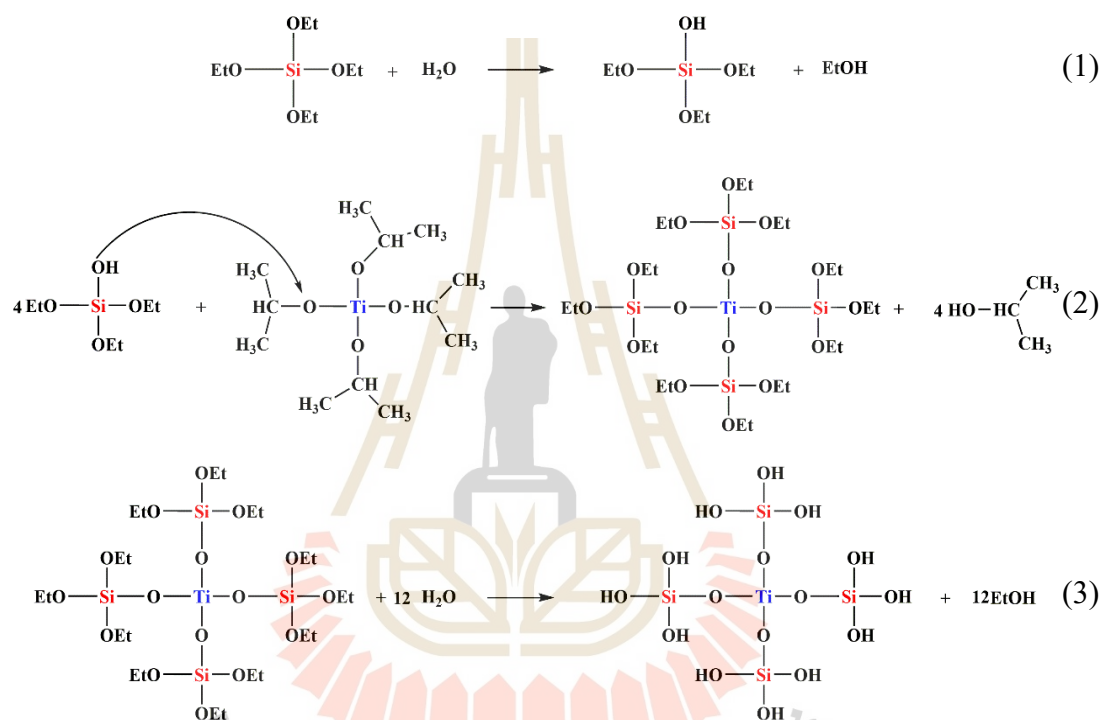
The structural and electrical properties of the final product are powerfully dependent on the nature of the precursor solution, deposition conditions and the substrate. The most common silica and titania precursors and their chemical structures are shown in table 2.3.

Table 2.3 Common silica and titania precursors and their chemical structures.

Precursor	Chemical structure
Tetraethyl orthosilicate (TEOS)	
Tetramethyl orthosilicate (TMOS)	
Titanium (IV) isopropoxide (TTIP)	
Titanium (IV) butoxide (TNBT)	

The greatest ordinary process is found on Yoldas (Yoldas, 1980). The Si alkoxide is pre-hydrolyzed in an alcohol, such as methanol, ethanol, or isopropanol,

solution of concentrated acid (HNO_3 , HCl , or H_2SO_4) and water under magnetic stirring to generate silanol groups (Si-OH). Pre-hydrolysis of the TEOS solution may also be kept up under refluxing at 80°C in HCl or acetic acid. Then the silanol groups of Si alkoxide are reacted with Ti alkoxide added drop by drop to avoid sudden precipitation of the TiO_2 species formed. The predictable reactions occurring in the system are shown below:



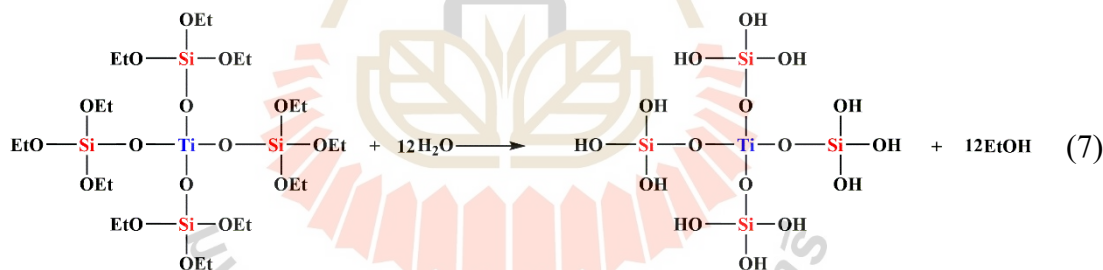
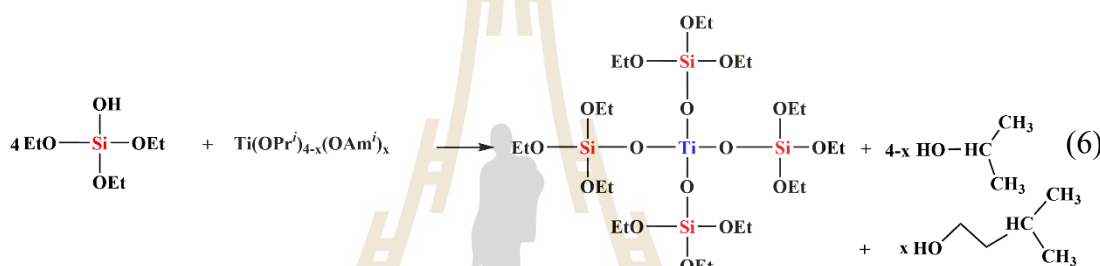
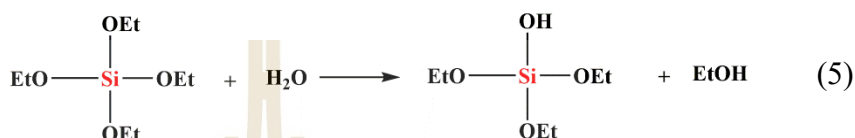
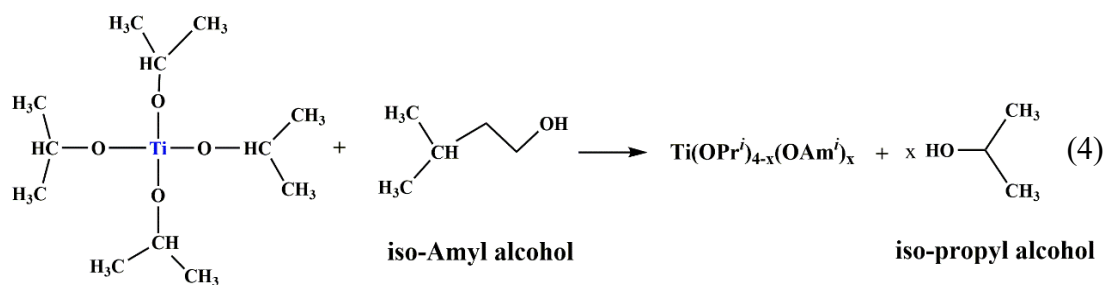
However, the different reaction rates of the alkoxide precursors is an inherent challenge in the synthesis of mixed oxides by hydrolytic sol-gel process. It provides the products weak towards phase separation rather than the formation of homogeneous polymeric gel structures. This occurrence is showed in the hydrolysis reactions that continue through nucleophilic substitution mechanisms and rely on the electronic partial charge, δ_+ of the metal atoms. The Ti atom (Ti^{4+}) has an expressively large positive partial charge ($\delta_+ \sim 0.6$) obtained from its higher electrophilic character that imparts higher reactivity with water than the Si atom (Si^{4+}) in tetra-alkoxysilanes. Consequently, phase homogeneity has been enhanced by: (i) the pre-hydrolysis of the SiO_2 precursor (ii) slowing of the Ti-alkoxide precursor through chemical modification

including the substitution of alkoxide groups with chelating multidentate ligands, and (iii) used of single-source precursors (Torma, Peterlik, Bauer, Rupp, Hüsing, Bernstorff, Steinhart, Goerigk, and Schubert, 2005). Highly reproducible polymeric gel materials have been established by covering these methodologies through the optimization of the sol–gel reaction.

Kim, Choi, and Lee (2000) proposed the fitting pre-edge of the sample with the linear combination of two reference X-ray absorption near edge structure (XANES) spectra to define the Ti-O-Si and Ti-O-Ti connectivity in a quantitative manner in Ti-Si binary oxides. They found that the fraction of Ti-O-Ti in mixed oxides was increased up to 0.55 when Ti/Si was varied from 0.04 to 0.5. The large variation of each fraction occurred around 0.15-0.2 of Ti/Si, which was equivalent with the formation of anatase titania as detected by XRD. The pre-edge fitting results combined with XRD and XPS showed that monolayer coverage was reached around 7-10 wt.% of Ti loading where the amount of Ti in Ti-O-Si was saturated to 0.56 mmol Ti/g of material for titania supported on silica with a surface area of 300 m² g⁻¹.

Fernandez, Jose, Mathew, Pr, and Nv (2007) studied the rapid precipitation by preparation of the TiO₂-SiO₂ mixed oxides under ultra-low hydrolysis conditions without involving any complex stabilizing agents. This may be achieved by adjusting the ratio of H₂O/alkoxide ratio less than 1 to prevent the homo-condensation of the titanium alkoxide by approving an increase in gel time that promotes Ti-O-Si linkage formation. The ethanol (alcohol medium) serves as a solvent and also participates in the esterification reaction producing water as a by-product.

Vives and Meunier (2008) studied the decrease of reactivity of titanium isopropoxide (TIP) by using acetic acid as modify agent to prepared titanium *iso*-amyloxide through the reaction of TIP with *iso*-amyl alcohol that has a highly branched alkyl group, and is expected to reduce the hydrolysis rate of TIP. The alcohol exchange reaction and the predictable reactions are shown below:



IR spectroscopy of the $\text{TiO}_2\text{-SiO}_2$ mixed oxide by modification of TIP precursor with *iso*-amyl alcohol showed the existence of Si-O-Ti and Si-O-Si bonds allowing suppose a composite microstructure of the gels. In addition, it retained the anatase phase at high temperature.

Liu, Liu, Yang, Li, Zu, Zhang, and Jia (2009) prepared titania-silica mixed oxides by a sol-gel method with citric acid (CA). They reported that the $\text{TiO}_2\text{-SiO}_2$ materials hold a mesoporous silicate framework with high specific surface area and thermal stability. The weak hydrogen bonding through the hydroxyl groups of CA lets the hydroxylated compound to act as a ligand as present in Figure 2.7.

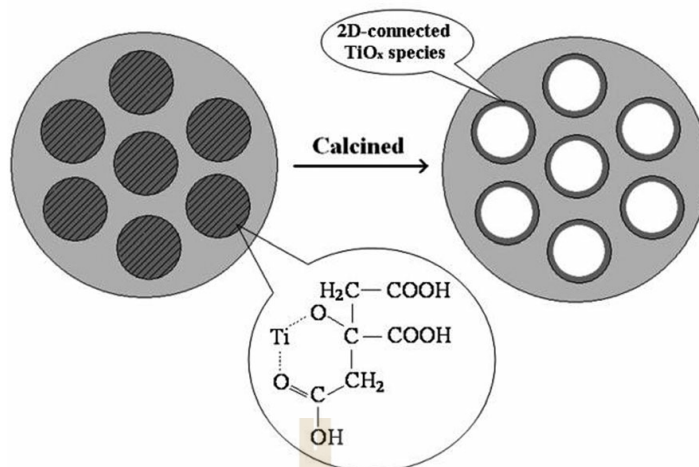
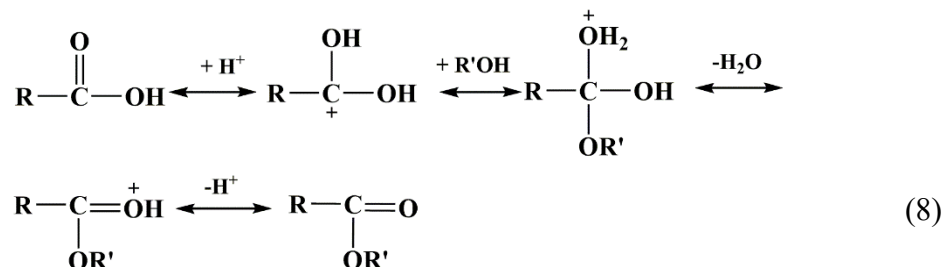


Figure 2.7 Proposed model for the formation process of mesostructured $\text{TiO}_2\text{-SiO}_2$ materials through titanium-citric acid complexes. (Liu, Liu, Yang, Li, Zu, Zhang, and Jia, 2009)

It is also recognized that several metal cations can be solubilized by CA because of its unique coordination ability and in this study, CA coordinates with Ti^{4+} of Titanium (IV) butoxide (TNBT) to form titanium-CA complexes, so falling the reaction rate of hydrolysis, condensation, and polymerization of titanium species. The titanium is chelated by the citrate units through the α -alkoxyl and β -carboxylic acid oxygen atoms. During this procedure, a portion of the non-hydrolyzed TiO_x species can polymerize to form Ti-O-Ti bonds, and the others may react with surface Si-OH of silica to form Ti-O-Si linkages leading to minimizing the formation of bulk titania.

Li, Tsai, Wu, and Wang (2013) prepared $\text{TiO}_2\text{-SiO}_2$ binary oxides with three various Ti/Si atomic ratios (3/1, 1/1, and 1/3) by a coprecipitation method. These catalysts were applied to catalyze the reaction between lactic acid and *n*-butanol/ethanol to produce *n*-butyl lactate and ethyl lactate. Performances of TiO_2 catalyst improved significantly when added Si. Ti/Si atomic ratio of 1/3 presented as the best catalytic activity (per unit catalyst weight) which exhibited 92.3% *n*-butyl lactate yield at 150°C and 91% ethyl lactate yield at 170°C. The catalyst acid content and surface area improved with increasing Si content and reached maximum values at a Ti/Si atomic ratio of 1/3. The reaction between an adsorbed lactic acid molecule and

an alcohol molecule in the liquid phase was proposed by The Eley–Rideal mechanism for the esterification on Ti–Si catalysts. The expected reaction as shown in Eq 8.



where R is CH₃CH(OH), R' is C₄H₉ or C₂H₅, and H⁺ is a proton donated from the Brønsted acid sites.

The optimum Ti/M atomic ratio of Ti–Si mixed oxides was much smaller than those of Ti–Al and Ti–Zr mixed oxides, which might be interrelated to the electronegativity difference between Si, Al, and Zr. Turnover frequency data recommend that strong acid sites on the titania-rich mixed oxides are more effective for catalyzing the esterification than the weak acid sites on the silica-rich mixed oxides.

Huang, Motealleh, Zheng, Janish, Carter, and Cornelius (2017) prepared SiO₂-TiO₂ nanofibers from partially hydrolyzed tetraethyl orthosilicate, and titanium isopropoxide via sol-gel method. In addition, all nanofibers were spun from sols without any additives typically used to facilitate electrospinning with the range of TiO₂ concentration within SiO₂-TiO₂ fibers from 25 to 100 mol%. SiO₂, SiO₂-TiO₂, and TiO₂ nanofiber structures were examined by SEM and TEM. Inorganic fiber spinning was highly dependent on sol reaction temperature, time, and solution composition. They observed twisted and ribbon-like nanofibers with dumbbell-shaped cross-sections at high TiO₂ concentrations. This result was ascribed to jet branching and splitting during electrospinning. Electrospun fibers were amorphous at room temperature, but thermally converted into crystalline anatase, which suffered additional structural changes at higher temperatures into rutile. The transformation of anatase-rutile thermal phase was highly dependent upon TiO₂ concentration.

2.6 Silk fibroin (SF)

For medical and pharmaceutical applications, a wide variation of natural and synthetic biodegradable polymers has been investigated. Natural biodegradable polymers like collagen, gelatin, chitosan and silk fibroin have promising advantages over synthetic polymers because they have promising properties, including excellent biodegradability, biocompatibility, and bioresorbability (Cao and Wang, 2009). Especially, nanometer-sized fibers have the potential for a range of highly useful applications such as conductive polymeric biosensors, filter membranes, biomedical scaffolds, wound-dressing materials, artificial organs, nanoelectronics, nanocomposites and chemical protective clothing. Biomedical textiles and fiber-based implants are used either in an internal or external (inside or outside the body) biological environment as a medical device (including non-implantable materials from wound dressings, implantable materials like vascular grafts, heart valves and sutures to wearable medical implants and polymer sensors) to improve the health and medical condition of the patient (G. Li, Li, Chen, He, Han, Wang, and Kaplan, 2015).

Silk proteins are normally defined as biopolymers, which are present in the glands of arthropods such as silkworms, spiders, scorpions, mites, and bees, and then spun into fibers during their metamorphosis. The composition, structure, and properties of silks collected from different sources show variation. Generally, silk based for preparing biomaterials is silk produced by *Bombyx mori* (B. mori) that is also known as mulberry silk (Kundu, Rajkhowa, Kundu, and Wang, 2013).

The *Bombyx mori* silks are composed of double silk fibroin cores (fibroin microfilament bundles 0.5–2 μm) coating with sericin (glue-like glycoproteins, 20–30 wt.% of the fiber), each of which is made of nanocrystals and/or semicrystalline domains so that the twin filaments stick together to form the composite material or cocoon (Figure 2.8). The sericin needs to be removed using extraction/washing after harvesting the silk cocoons in order to generate purified silk fibroin for medical use. Composition of silk is given in Table 2.4.

Besides the primary organization, secondary structure and the classified organization of silk fibroin determine many of its biomaterial properties. Silk fibroin of silkworms is a commonly available natural biopolymer with several applications in the

human body due to their mechanical strength, elasticity, biocompatibility, and biodegradability.

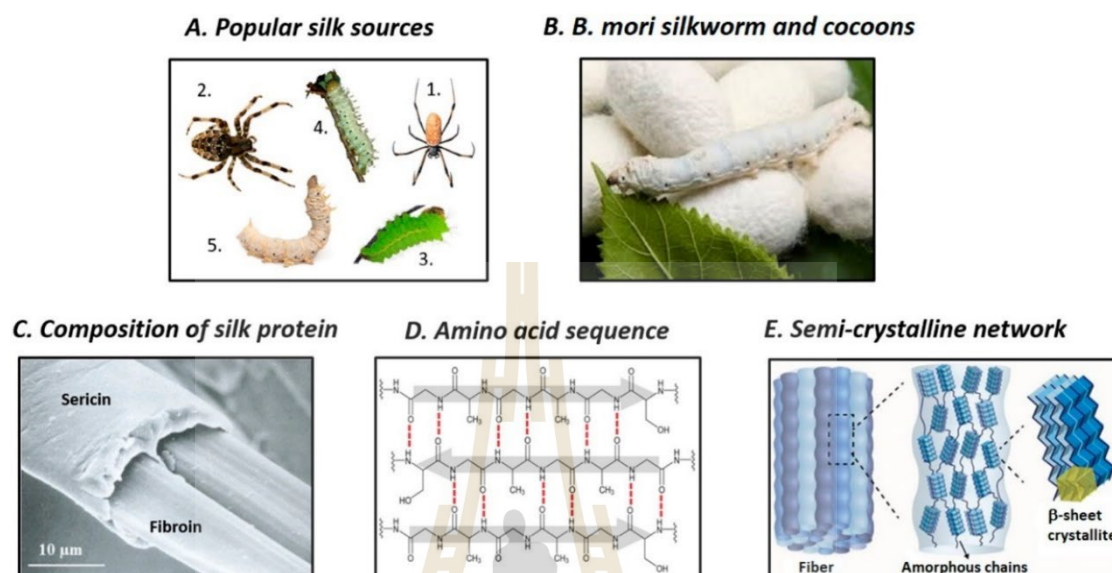


Figure 2.8 Overview of the origin and structures of silk fibroin (Nguyen, Nguyen, Nguyen, Le, Huynh, Vo, Trinh, Kim, and Le, 2019).

The *Bombyx mori* silk protein (i.e., silk fibroin) is composed of a glycoprotein (P25), a heavy (H) (≈ 391 kDa), and a light (L) (≈ 26 kDa) chain that are linked together by a disulfide bond at the C-terminus (Shimura, Kikuchi, Ohtomo, Katagata, and Hyodo, 1976) (Figure 2.9). The C-terminal and N-terminal capping sequences are completely nonrepeating amino acid residues (Holland, Numata, Rnjak-Kovacina, and Seib, 2019). The hydrophobic domains of H-chains composing of the repeated amino acid sequence contain Glycine-X (X being alanine, serine, threonine, and valine) repeats and can form anti-parallel β -sheets. In addition, among these hydrophobic domains have the hydrophilic consisting of bulky and polar side chains and form the amorphous part of the secondary structure (Ayoub, Garb, Tinghitella, Collin, and Hayashi, 2007; Omenetto and Kaplan, 2010; Porter and Vollrath, 2009). The L-chain conformation in amorphous blocks is random coil, which is hydrophilic in nature and relatively elastic to silk (Vollrath and Knight, 2001).

Table 2.4 Composition of silk fiber (Rangi and Jajpura, 2015).

Component	Content, %
Fibroin	70-80
Sericin	20-30
Carbohydrate	1.2-1.6
Inorganic matter	0.7
Wax mater	0.4-0.8
Pigment	0.2

The two main different structures in silk fibroin are Silk I and Silk II. The structure of Silk I contains random-coil and amorphous regions. The Silk II structural form of the silk fibroins has been characterized as an antiparallel β -sheet structure. The Silk I is a water-soluble structure while the Silk II excludes water and is insoluble in several solvents including mild acid and alkaline conditions. Structure of silk fiber is shown in Table 2.5. In regenerated silk fibroins, the silk I structure easily converts to a β -sheet structure by chemical methods such as treatment with methanol (J. Huang, Wong Po Foo, and Kaplan, 2007).

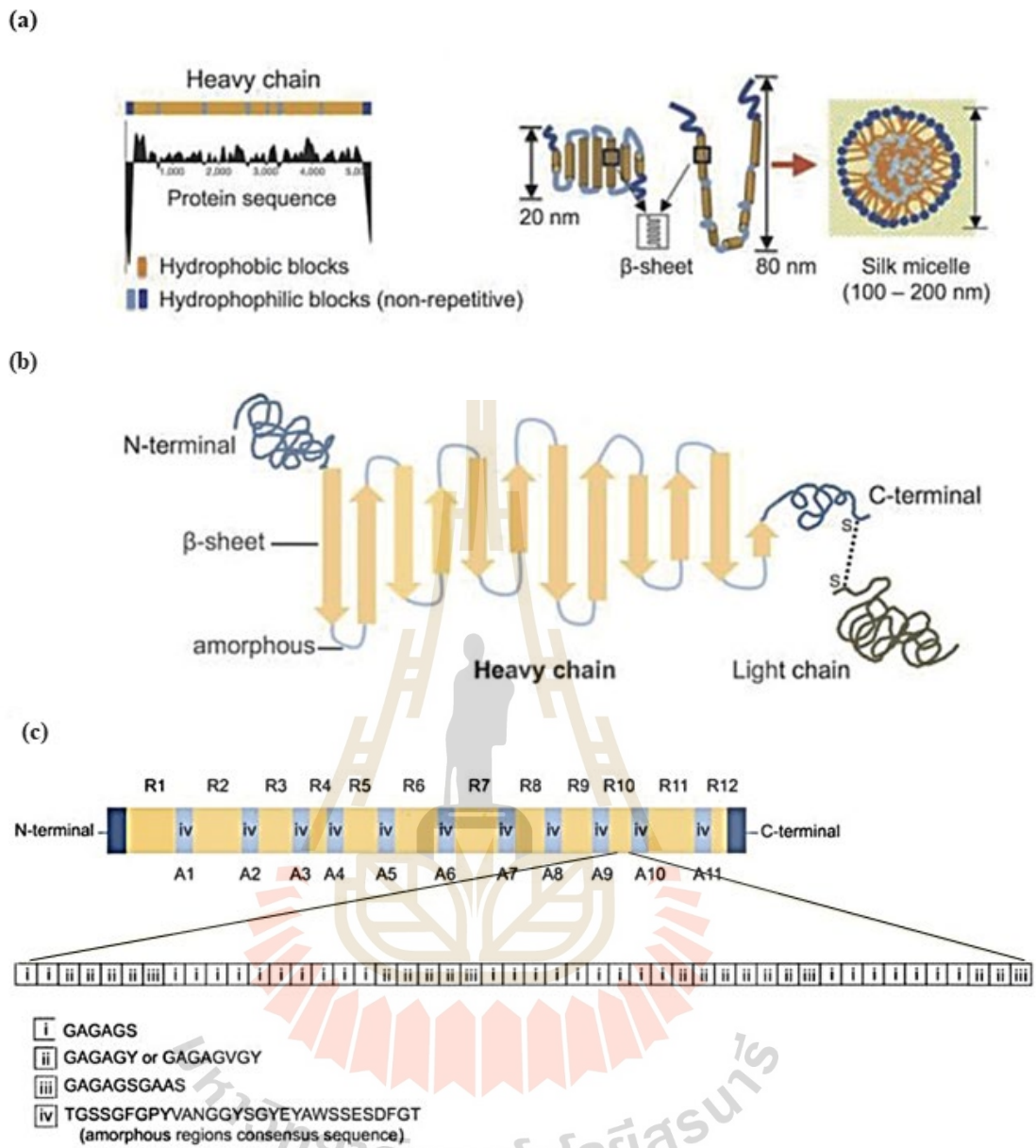


Figure 2.9 Silk structure. (a) Solution conformation of *Bombyx mori* silk, (b) 2D silk fibroin schematic, and (c) Primary structure of the *Bombyx mori* silk heavy chain (Holland, Numata, Rnjak-Kovacina, and Seib, 2019).

Table 2.5 Structure of silk fibers from Bombyx mori silkworm (Cao and Wang, 2009).

Silk fiber	Silk fibroin (72-81%)		Silk sericin (19-58%)	
	H-chain	L-chain	P 25 glycoprotein	a glue-like protein
Molecular Weight	325 kDa	25 kDa	25 kDa	~300 kDa
Polarity	Hydrophobic		Hydrophilic	
Structure	silk I (random-coil or unordered structure) silk II (crystalline structure) silk III (unstable structure)		non-crystalline structure	
Function	the structure protein of fibers filament core protein		binds two fibroins together coating protein	

Silk fiber has a great potential as reinforcing medium in composites. However, the critical factors that determine the mechanical properties of any particular silk are the precise control of size, number, distribution, orientation and spatial arrangement of crystalline and non-crystalline domains at the nanometer scale (Omenetto and Kaplan, 2010).

In addition, the reinforcement by cellulose nano fibers (CNF) instead of micro-sized fibers is recognized as being more effective due to interactions between the nano-sized elements that make up a percolated network connected by hydrogen bonds or entanglements, once a good dispersion in the matrix is achieved. More specifically, CNF delivers enhanced toughness to the composites compared to pulp fibers. Nevertheless, the adequate dispersion of hydrophilic cellulosic fibers in a matrix of mostly hydrophobic polymers is a critical aspect to be addressed, which is especially difficult in the case of nanofibers (Nakagaito, Fujimura, Sakai, Hama, and Yano, 2009).

2.7 PLA composites

During the past decade, a large number of investigations have been performed on the polymer composites with various nanofillers. Because the addition of filler into PLA improves some properties such as mechanical properties, thermal properties, crystallinity, degradability and antimicrobial properties of PLA. Polymer composites with the addition of selected nanofillers into PLA such as organomodified layered silicates (OMLS) (Huang, Hwang, Liu, and Lin, 2010), carbon nanotubes (CNTs) (Cui, Jiang, Yuan, Cao, Li, Tang, and Qin, 2020; Tang, Chen, Wang, Xu, Hsiao, Zhong, and Li, 2012), zinc oxide (Murariu, Paint, Murariu, Raquez, Bonnaud, and Dubois, 2015), modified organo-montmorillonite clay (OM-MMt) (Dintcheva and Al-Malaika, 2020), silica nanofillers (SiO_2) (Hakim et al., 2017; G. Wu, Liu, Jia, and Dai, 2016), titanium dioxide (TiO_2) (Y. Luo, Lin, and Guo, 2019; Xiu, Qi, Bai, Zhang, and Fu, 2017), is considered as a modern approach that can lead to major improvements of PLA characteristic features.

2.7.1 PLA/ TiO_2 composites

Nakayama and Hayashi (2007) studied poly (L-lactic acid)/ TiO_2 on the optical, mechanical, thermal, and photodegradation properties of nanocomposite films. TiO_2 nanoparticles was synthesized and modified the surface of TiO_2 using

propionic acid and *n*-hexylamine. Neat PLA and PLA/TiO₂ nanocomposite films with 1, 5, 10 wt.% of surface modified TiO₂ were prepared by solution casting method. As a result, the nanocomposite films obtained high transparency without depending on the amount of added TiO₂ nanoparticles, similar to pure PLA films. ATEM micrograph of the nanocomposite films suggested that the TiO₂ nanoparticles of 3-6 nm in diameter were uniformly dispersed in PLA matrices. In addition, PLA/TiO₂ nanocomposite films could be efficiently photodegraded by UV irradiation in comparison with pure PLA.

Buzarovska and Grozdanov (2012) investigated the influence of TiO₂ on thermal properties and crystallinity of PLA. PLA/TiO₂ nanocomposites (with various loadings of TiO₂ (0.5, 1, 2, 5, and 10 wt.%) were prepared by solution casting method. The TiO₂ nano filler had no significant influence on the characteristic temperatures (T_g , T_c , and T_m), but had high impact on the crystallinity of these systems. The degree of crystallinity (χ_c) significantly increased for PLA nanocomposites loaded with up to 5 wt.% of TiO₂, while for 10 wt.% of TiO₂ it decreased below χ_c of the pure PLA. The degradation of the PLA/TiO₂ composites was evaluated hydrolytically in 1N NaOH, enzymatically in α -amylase solutions, and under UV irradiation. The catalytic effect of TiO₂ nano particles on the degradation processes under UV light exposure ($\lambda = 365$ nm) and hydrolytic degradation was confirmed with the increase of the filler content.

Gupta, Mishra, Srivastava, Gangwar, Nath, and Maiti (2013) studied the novel poly (lactic acid) (PLA)/TiO₂ hybrid nanofibers. PLA/TiO₂ hybrid nanofibers were prepared via electrospinning technique. Hydrolyzed titanium precursor was electrospayed simultaneously on the continuous electrospun PLA nanofibres surface. After that the hydrolyzed precursor was transformed into titania particle placed onto the nanofibre surface only to achieve better light scattering by nano TiO₂ on surface for improved UV protection. The structural transition was studied by using XRD, FTIR, Raman and XPS studies. The predominant phase was anatase with a small extent of brookite phase after the hydrothermal treatment. The much greater absorption of UV light by the hybrids was demonstrated and the optical band gap (both for direct and indirect) was gradually reduced with increasing time of hydrothermal treatment indicating superior UV absorption properties of the hybrids. The antimicrobial activity

was verified and found 70% reduction in bacterial growth using 90 min hydrothermally treated hybrids as compared to pure PLA nanofibre.

Lee, Lee, Park, Busnaina, and Lee (2013) evaluated the effect of outdoor sunlight exposure accompanied by the presence of TiO₂ (nanoparticles, size: <100 nm) on the degradation of PLA. PLA and PLA-TiO₂ films were manufactured by dripping the sample solution onto a table and allowing the solution to dry overnight at room temperature. After that comparative experiments using PLA films with and without TiO₂ were performed using sunlight exposure for 6 h. The surface of PLA film was observed using SEM images to identify the roughness as a surface property. The presence of TiO₂ nanoparticles improved the degradation efficiency, even though a high concentration of TiO₂ and a long exposure time were required to dramatically increase the degradation speed, which acted as a catalyst.

Luo (2014) studied the nanocomposites of modifying nano-TiO₂ with lactic acid (g-TiO₂) and poly (lactic acid) (PLA). PLA/g-TiO₂ were prepared using the melt blending in twin-screw extruder. The g-TiO₂ contents were varied between 0 to 8 wt%. G-TiO₂ was prepared via the solution without catalyst, and the grafting rate was about 7 wt.%. The test on the dynamic mechanical property, thermal property, and thermal deformation temperature were investigated. The adding nano TiO₂ helped improve its energy storage modulus and this should be related to a lot of graft polymers on the surface of nanometer TiO₂ particles. The thermal decomposition temperature of PLA increased with adding TiO₂ and this was very useful for materials processing and production. In addition, thermal deformation temperature of the nanocomposites increased slightly compared with pure PLA as the content of nano TiO₂ increased.

Fonseca, Ochoa, Ulloa, Alvarez, Canales, Zapata (2015) studied PLA composites with different amounts of TiO₂ (~10 nm) nanoparticles with various TiO₂ loading (1, 3, 5 and 8 wt.%) were prepared by the melting process and their thermal, mechanical, and shear viscosity properties were evaluated. The antimicrobial and antifungal behavior of these nanocomposites against *Escherichia coli* and *Aspergillus fumigatus* were also investigated. Adding 5 wt.% of TiO₂, T_c increased about 12% showing that the nanoparticles acted as nucleating agents. The elastic modulus increased ~54% compared to neat PLA at 5 wt.% of TiO₂. However, PLA/TiO₂

nanocomposites showed lower shear viscosity than neat PLA, possibly reflecting degradation of the polymer due to the particles. In addition, the PLA/TiO₂ composites with 8 wt.% TiO₂ showed a reduction of *Escherichia coli* colonies of ~82% after 2 h of contact (no UVA irradiation) compared to pure PLA. Furthermore, a reduction of bacteria of PLA nanocomposites containing 8wt.% TiO₂ increased to 94% and 99.99% under UVA irradiation for *Escherichia coli* and *Aspergillus fumigatus*, respectively.

Zhang, Huang, Yang, Chen, Zou, Lin, and Qu (2015) prepared polylactide/TiO₂ nanocomposites (~20 nm) with different contents of nanoscale TiO₂ (0.5-15 wt.%) via melt blending with a vane extruder. The vane extruder was beneficial for the dispersion of composites and especially suitable for the processing of thermo-sensitive polymer because of its short thermal-mechanical history and thus resulting in the reduction of degradation. The dispersion of nanoparticles in PLA matrix under elongational flow field and the physical properties of its nanocomposites were investigated. The results showed that PLA/TiO₂ nanoparticles were well dispersed in the polymer matrix via elongational flow and these nanoparticles had an inhibition for cold crystallization process to some extent. Thermal stability of the PLA/TiO₂ composites was improved with the presence of TiO₂. Moreover, the toughness and UV resistance of the composites were also enhanced by adding TiO₂.

Toniatto, Rodrigues, Marsi, Ricci, Marciano, Webster, and Lobo (2017) studied the nanocomposites of poly (lactic acid) (PLA) with high loadings of titanium dioxide nanoparticles (0, 1, 3 and 5 wt% TiO₂) and their bactericidal properties. PLA electrospun fiber-TiO₂ nanocomposites were prepared for further evaluation of their bactericidal activity and cell viability. The bactericidal effect of electrospun PLA/TiO₂ against *Staphylococcus aureus* (*S. aureus*) bacteria. They noticed that only higher concentrations of TiO₂ promoted bacteria death (PLA/TiO₂ 3 and 5%). Meanwhile, after 24 h, this bactericidal effect increased from 30% to 60% when using PLA/TiO₂-5%. It was very illustrative and certainly repeated the bactericidal effect of PLA/TiO₂-5%. This strongly indicates that PLA/TiO₂ is a very promising material for obtaining a bacteria-inert implant coating material. Accordingly, these results showed that this material has important implications for designing surfaces for use in numerous surgical implants.

Luo, Cao, and Guo (2018) studied the photocatalytic degradation of PLA/ modified TiO_2 by grafting lactic acid oligomer (g- TiO_2) under accelerating artificial ultraviolet irradiation conditions for the period up to 100 days. The PLA/g- TiO_2 with 0, 0.5, 1.0, 2.0, 5.0, 8.0, and 15.0 wt.% of g- TiO_2 were prepared by melt blending via a corotating twin-screw extruder. The change of surface color, gloss loss, morphology, weight loss, intrinsic viscosity, chemical structure, and mechanical properties at different irradiation times. The structural change accompanied by the degradation of the irradiated samples clearly showed that the photodegradation of PLA/ TiO_2 nanocomposites process was via a bulk erosion mechanism. The photodegradability of PLA/ TiO_2 samples was higher than that of pure PLA and promoted a lot from a good dispersion of TiO_2 nanoparticles. This study suggested that the photodegradation of PLA could be controlled by loading dispersed g- TiO_2

2.7.2 PLA/ SiO_2 composites

Khankrua, Pivsa-Art, Hiroyuki, and Suttiruengwong (2013) determined thermal and mechanical properties of PLA/silica nanocomposites. The nanocomposites of PLA with hydrophilic fumed silica has been prepared by twin screw extrusion with various silica contents (0.1 to 5.0 wt% for polymer based). From the SEM micrographs, it can be seen that by the addition of silica at low contents between 0.1-0.5 wt%, the dispersion of silica nanoparticles through the polymer matrix was good but above that contents, the silica particles tended to agglomerate and formed larger particles because of the interaction between the polar groups on surface of silica. The presence of silica nanoparticles increased the onset and inflection temperature of thermal degradation in PLA nanocomposites. The heat deflection temperature (HDT) value of PLA nanocomposites at 5 wt% of silica loading was found to be 55.3°C which was lower than that of neat PLA. The glass transition temperature (T_g) of PLA was around 55-60 °C which was comparable to HDT of PLA (55-57°C), so the material becomes softer and defect when the temperature was scan to this range of temperature. The mechanical performances of nanocomposites depended on the content and the dispersion of silica particles in the polymer matrix. At low silica content, the mechanical properties were slightly increased whereas the mechanical

properties were worsened at the higher silica loading because of the agglomerate of silica in the polymer matrix.

Wu, Lan, Ji, Liu, Yang, and Yang (2013) studied the direct grafted poly(lactic acid) (PLA) chains onto a silicon surface by in situ amidation and compounding PLA/PLA-grafted SiO₂ nanocomposites (PLA-g-SiO₂) via a Haake torque rheometer with with 0.3, 0.5, 1.0, 2.0, 3.0, and 5.0 wt.% PLA-g-SiO₂. Thermal and rheological properties of PLA/PLA-g-SiO₂ nanocomposites were evaluated. The cold crystallization rate was accelerated PLA-grafted-SiO₂. And it increased the degree of crystallinity of PLA. Shear rheology testing indicated that PLA/PLA-g-SiO₂ nanocomposites still exhibited the typical homopolymer-like terminal behavior at low frequency range even at a content of PLA-g-SiO₂ of 5 wt %, compared to PLA/SiO₂, it was also found that the nanocomposites showed stronger shear-thinning behaviors in the high frequency region after grafting.

Ge, Zhu, Yin, Zhang, and Wang (2014) determined the crystallization and thermal stability of stereocomplex poly (lactic acid)/SiO₂ (sc-PLA/SiO₂) composites by in-situ polycondensation. The composites were prepared through solution mixing followed by vacuum drying with 0.5, 1, 3, 5 wt.% of SiO₂. They found that good dispersion of SiO₂ particles could be obtained when the loading was less than 3wt%. Crystallization properties of sc -PLA were improved due to the addition of SiO₂. The maximum of both melt crystallization temperature (T_{mc}) and crystallinity (X_c) simultaneously occurred at 1 wt% loading of SiO₂. Additionally, thermal stability of the composites was not affected greatly by agglomeration in a certain range. The initial decomposition temperature increased by 75°C (5wt.% loading of SiO₂) compared with the crude.

Pilić, Radusin, Ristić, Silvestre, Lazić, Baloš, and Duraccio (2016) studied the influence of different silica nanoparticles (SiO₂) content on crystalline behavior, and thermal, mechanical and barrier properties of poly (lactic acid) (PLA) and its nanocomposites. Neat PLA films and PLA films with different percentage of hydrophobic fumed silica nanoparticles (0.2, 0.5, 1, 2, 3 and 5 wt.%) were prepared by solution casting method. From SEM analysis, the nanocomposite preparation and selection of specific hydrophobic spherical nano-filler provided a good dispersion of

the silica nanoparticles in the PLA matrix. The mechanical properties of the nanocomposite improved with the addition of silica nanoparticles, the most significant improvement being observed for the lowest silica content (0.2 wt.%). Barrier properties were improved for all measured gases at all loadings of silica nanoparticles. The degree of crystallinity for PLA was slightly increased by adding 0.2 and 0.5 wt.% of nanofiller.

Wu, Liu, Jia, and Dai (2016) studied PLA/nano-SiO₂ nanocomposite filament on mechanical properties and surface friction properties via melt-spinning. The nano-SiO₂ was modified by the γ -Aminopropyl triethoxysilane coupling agent under trademark KH-550. The KH-550 coupling agent can improve the dispersion of nano-SiO₂ in PLA and increase their compatibility. It has two different groups, in which one group can link with the hydroxyl (-OH) on surface of SiO₂, another can link with PLA. So, the SiO₂ and PLA were connected through KH-550. The results showed that the nano-SiO₂ modified by 5% KH-550 could disperse evenly and loosely in nano-scale, and 1 wt% and 3 wt% nano-SiO₂ dispersed throughout PLA evenly. The breaking tenacity of PLA nanocomposite increased with adding 1 wt.% SiO₂ but declined when 3 wt% SiO₂ was added. The friction coefficient of PLA composite filament rose apparently with increase of nano-SiO₂ contents. In addition, the thermo-decomposing temperature of composite filaments mixed with 1 wt.% or 3 wt.% SiO₂ increased by 8.2 or 13.6 °C, the glass transition temperature (T_g) increased by 7.66 °C or 10.10 °C, and the melting temperature (T_m) increased by just 0.51 or 1.43 °C.

Hakim et al. (2017) studied influence of the SiO₂ modifications on the morphology, crystallization behavior, and mechanical properties of PLA/SiO₂ composites films using reactive extrusion-calendering in pilot plant. The PLA/SiO₂ composites contained 2.5 ± 0.1 wt.% of SiO₂. TEM micrographs showed that the improved chemical affinity of both surface treated SiO₂ toward the PLA extrudate (PLA_{REX}) end groups did not improve particle dispersion. The nucleating effect of untreated SiO₂ showed more efficiently than both surface-modified silica. The activation energy for the isothermal crystallization process, as determined by an Arrhenius method, suggested that addition of untreated SiO₂ enhances the crystallization rate of PLA_{REX}. Nevertheless, the tensile behavior of PLA nanocomposites remained unchanged whether SiO₂ were added or not.

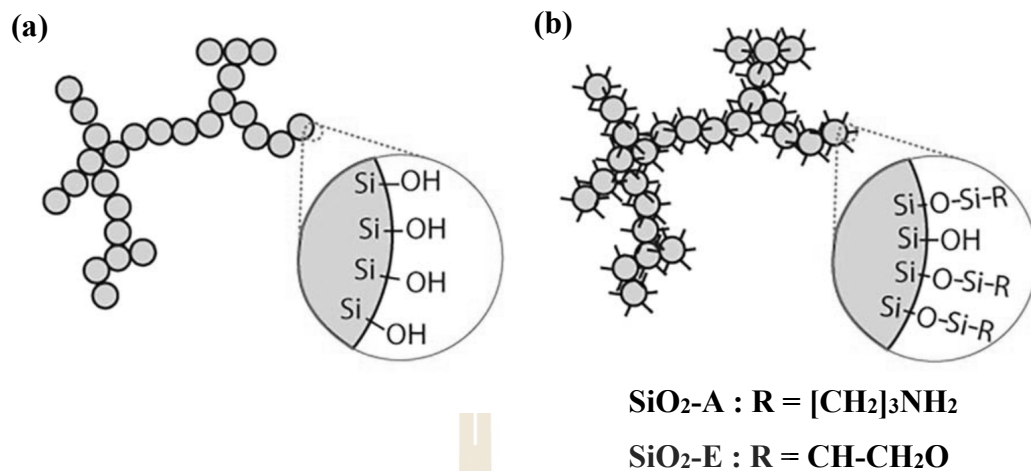


Figure 2.10 Schematic representation of the (a) surface-unmodified SiO₂ and (b) surface-modified SiO₂ aggregate. (Hakim et al., 2017).

2.7.3 PLA/natural fiber composites

Nowadays, there has been a rapid growth in research and innovation in the natural fibre composite (NFC) area. Interest is warranted due to the advantages of these materials compared to others, such as synthetic fibre composites, including low environmental impact and low cost and support their potential across a wide range of applications. Much attempt has gone into increasing their mechanical performance to extend the capabilities and applications of this group of materials. Several investigations on PLA composites prepared from natural and modified fibers have shown that their mechanical properties scale with the mass fraction of added fibers.

Zhu, Feng, Zhang, Guo, Zhang, and Chen (2009) described the preparation and characterization of blend films composed of regenerated silk fibroin (SF) and poly (lactic acid) (PLA). The blending ratios of SF/PLA were 100:0, 98:2, 95:5, 93:7 and 90:10 (wt.%). The blend film was also prepared by solution cast method. The effects of SF/PLA blend ratios on the mechanical and physical properties of the blend films were investigated. Compared to pure SF film, the mechanical and thermal properties of the blend films were improved, and surface hydrophilicity and swelling capacity decreased due to the secondary structural transition of SF to Silk II. Among

the blend films with different ratios, the SF/PLA blend film with 7 wt.% PLA content showed excellent mechanical properties. Meanwhile, the bovine serum albumin (BSA) adsorption amount on the blend film increased with the increase of PLA content. In vitro cell adhesion test showed that the blend film was a good matrix for the growth of L929 mouse fibroblast cells. Consequently, controlling the PLA content in the SF film can improve the mechanical and physical properties of the SF film and provide a promising opportunity to widen potential application of SF in the biomaterials field.

Zhao, Cheung, Lau, Xu, Zhao, and Li (2010) prepared silk/PLA biocomposites by using melting compound methods. The effect of silk fiber on the structural, thermal and dynamic mechanical properties and enzymatic degradation behavior of the PLA matrix was investigated. As silk fiber was incorporated into PLA matrix, the stiffness of the PLA matrix at higher temperature (70-160°C) was remarkably enhanced and the dimension stability also was improved, but its thermal stability became poorer. Moreover, the presence of silk fibers also significantly enhanced the enzymatic degradation ability of the PLA matrix. The higher the silk fiber content, the more the weight loss.

Shanmugam and Sundaramoorthy (2015) developed and characterized an electrospun mat from Eri (*Samia Cynthia ricini*) silk fibroin (ESF) and poly L-lactic acid (PLA) blends for wound dressing application. The polymer solution was prepared by dissolving a mixture of ESF and PLA in different ratios viz., 87.5:12.5 and 100:0 in a solvent containing mixture of chloroform and Tri-fluoro acetic acid (TFA) (30:70). The mats were produced from 100% ESF and blend of ESF-PLA by electro spinning method. Tetracycline hydrochloride (TCH) was added with the polymer of 100% ESF and ESF-PLA and the mats were prepared. Physical, chemical and biological properties of the mats were evaluated for using these mats as a skin contact layer of multilayer wound dressing system. A mean diameter of ESF fibres and ESF-PLA fibres were 320 nm and 502 nm, respectively. The contact angle with water of the ESF mat was 23° and the ESF-PLA mat was 79°. The vapour transmission rate of the ESF-PLA mat was lower than that of the 100% ESF mat. However, they were found to be lower than the level at which dehydration would occur. TCH loaded mats showed an effective zone of inhibition against gram positive and gram-negative bacteria. A cytotoxicity study on

neuroblast cells showed that the ESF mat did not impair the growth of cells. The *in vivo* study on a rat model showed that the wound healing performance of the mats developed from 100% ESF and ESF-PLA were better compared to the conventional open wound and gauze cloth wound dressing systems.

W. Liu, Li, Zheng, Zhang, Liu, Yang, and Han (2016) prepared fibrous silk fibroin (SF)/poly(L-lactic acid) (PLLA) scaffold via electrospinning dissolving completely in 1,1,1,3,3,3-Hexafluoro-2-propanol(HFIP) and trifluoroacetic acid (TFA). The scaffolds investigated the morphological, mechanical, and degradation properties of the scaffolds fabricated using different electrospinning conditions, including collection distance (17 cm, 20 cm, and 23 cm), working voltage (12 kV, 15 kV, and 18 kV), and the SF:PLLA mass ratio (S40P60, S50P50, and S60P40). In addition, *in vitro* cell-scaffold interactions were evaluated in terms of chondrocyte adhesion to the scaffolds as well as the cytotoxicity and cytocompatibility of the scaffolds. The optimum electrospinning conditions for generating a fibrous SF/PLLA scaffold with the best surface morphology (ordered alignment and suitable diameter) and tensile strength (~1.5 MPa) were a collection distance of 20 cm, a working voltage of 15 kV, and a SF:PLLA mass ratio of S50P50. The degradation rate of the SF/PLLA scaffolds was found to be determined by the SF:PLLA mass ratio, and it could be increased by reducing the PLLA proportion. Furthermore, chondrocytes spread well on the fibrous SF/PLLA scaffolds and secreted extracellular matrix, indicating good adhesion to the scaffold. The cytotoxicity of SF/PLLA scaffold extract to chondrocytes over 24 and 48 h in culture was low, indicating that the SF/PLLA scaffolds are biocompatible. Chondrocytes grew well on the SF/PLLA scaffold after 1, 3, 5, and 7 days of direct contact, indicating the good cytocompatibility of the scaffold.

Thanh, Chaiwat, and Yupaporn (2017) investigated biocomposites of poly (lactic acid) and cellulose nanofibers (CNFs) from cassava pulp (CP) (1 wt.%) preparing by melt mixing, following by hot melt pressing. Glycidyl methacrylate (GMA) grafted poly (lactic acid) (PLA-g-GMA) was used as a compatibilizer. The morphology of biocomposites, characterized by scanning electron microscopy (SEM), reveals that without using PLA-g-GMA, the poor dispersion of CNFs in PLA matrix was observed. By using PLA-g-GMA, the dispersion of CNFs in PLA matrix was improved. Moreover, the

impact strength results show that by incorporating 1.0 wt.% CNFs into PLA matrix and using PLA-g-GMA as a compatibilizer, the impact strength of biocomposites was slightly enhanced compared to that of pure PLA.

Taddei, Tozzi, Zuccheri, Martinotti, Ranzato, Chiono, Carmagnola, and Tsukada (2017) studied the composite nanofibrous scaffolds by electrospinning a trifluoroacetic acid (TFA) solution containing *B.mori* silk fibroin (SF) and poly (L-lactic acid) (PLLA) in a 1:1 weight ratio. SF, PLLA and SF/PLLA nanofibres were prepared with average diameter sizes of 360 ± 90 nm, 470 ± 240 nm and 580 ± 220 nm, respectively. They found that the crystallisation of PLLA was hindered by the presence of SF, which crystallized specially and underwent conformational changes that did not significantly change its general β -sheet structure. The two components were thermodynamically compatible and the intermolecular interactions between them were revealed for the first time. Human keratinocytes were cultured on nanofibres and their viability and proliferation were determined. Preliminary in vitro tests showed that the incorporation of SF into the PLLA component enhanced cell adhesion and proliferation with respect to the unfunctionalised material. SF has been successfully used to modify the biomaterial properties and confirmed to be an efficient bioactive protein to mediate cell-biomaterial interaction.

Wang, Wu, Venkataraman, and Hu (2019) investigated the interaction and miscibility of proteins and synthetic biocompatible polymers based on silkworm silk fibroin (SF) and polylactic acid (PLA) in the macro- and micro-meter scales, which can dramatically control the cell responses and enzyme biodegradation on the biomaterial interface. SF/PLA blends films were prepared by solution casting method, which based on a mass ratio of Silk fibroin: PLA=90:10 (SP90), 70:30 (SP70), 50:50 (SP50), 30:70 (SP30), 10:90 (SP10), with pure silk (SP100) and pure PLA (SP0) using as controls. Silk fibroin provides controllable crystal content and biodegradability, while PLLA provides hydrophobicity and thermal stability in the system. The morphology of the blend films was uniform on a macroscopic scale, yet with tunable micro-phase patterns at different mixing ratios (Figure 2.11).

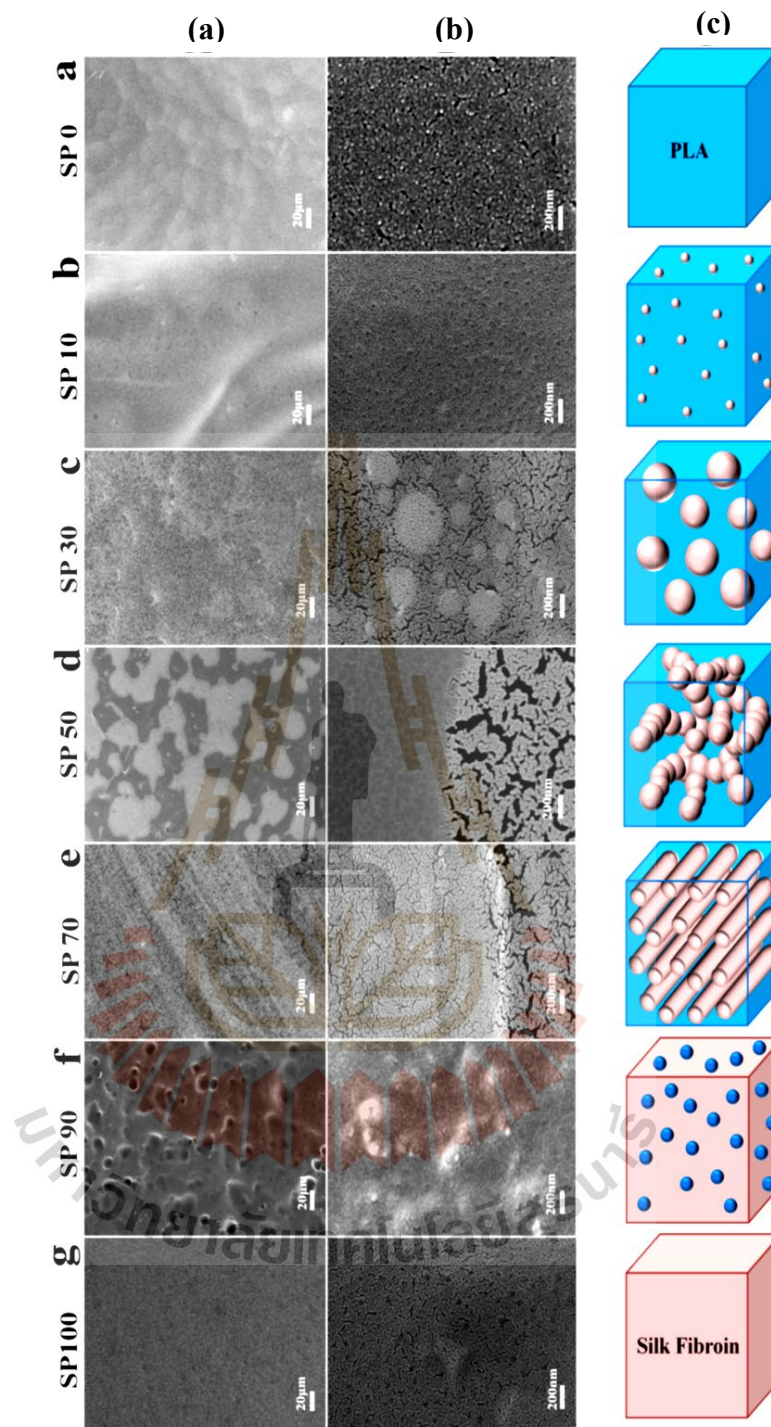


Figure 2.11 SEM images of SF/PLA blend films within (a) 20 μm bar and (b) 200 nm bar. (c) Schematic of the SF-PLA interaction mechanisms based on the SEM images (Fang Wang, Wu, Venkataraman, and Hu, 2019).

FTIR analysis revealed that structures of the blend system, such as beta-sheet crystal content, gradually changed with the mixing ratios. All blended samples have better stability than pure SF and PLA samples as evidenced by thermogravimetric analysis. Protease XIV enzymatic study showed that the biodegradability of the blend samples varied with their blending ratios and microscale morphologies. This study provided a useful platform for understanding the fabrication strategies of protein-synthetic polymer composites that have direct biomedical and green chemistry applications.



CHAPTER III

EXPERIMENTAL

3.1 Materials

Poly (lactic acid) (PLA, grade 4043D) was supplied from Nature Works LLC. Tetraethylorthosilicate (TEOS, 98%, AR grade) and Titanium (IV) isopropoxide (TTIP, 98%, AR grade) were purchased from Acros. Sodium carbonate (Na_2CO_3 , AR grade) was supplied from Sigma-Aldrich. Absolute ethanol ($\text{C}_2\text{H}_5\text{OH}$, AR grade), ammonium hydroxide (NH_4OH , AR grade) and hydrochloric acid (HCl, AR grade) were supplied from Carlo Erba Reagents. And silk cocoons of *Bombyx mori* silkworms was supplied from Queen Sirikit Sericulture Center, Nakhon ratchasima province, Thailand.

3.2 Experimental

3.2.1 Synthesis of titanium-silicon oxide (Ti_xSi_y)

Titanium-silicon oxide (Ti_xSi_y) was synthesized by a modified Stöber method including instantaneous hydrolysis and condensation of TEOS was prepared using sol-gel methods (W. B. Kim, Choi, and Lee, 2000). The experimental procedure used to prepare the Ti_xSi_y oxide particles was showed in Figure 3.1

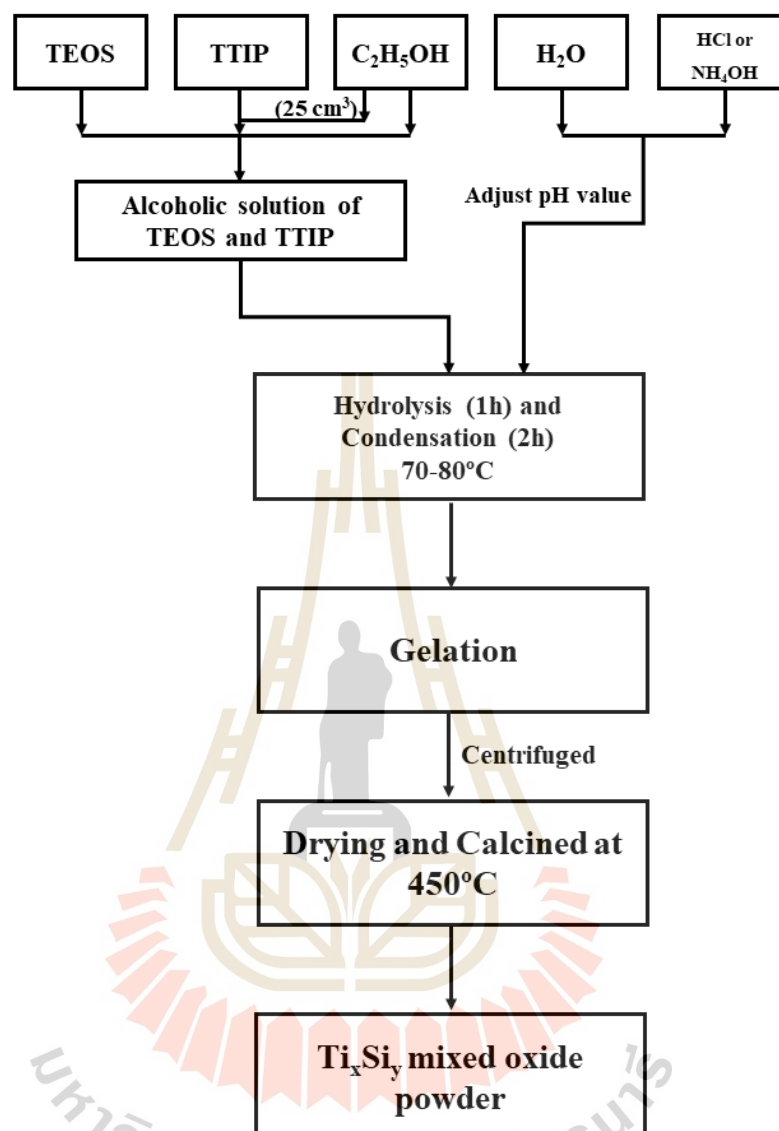


Figure 3.1 Experimental procedures for preparing Ti_xSi_y oxide particles.

TEOS and TTIP were used without purification. Total moles of the Ti-alkoxide and Si-alkoxide were fixed at 0.22 mol. For pre-hydrolysis step, the mixture of two alkoxides was added into five-neck round bottom flask contained 150 cm³ ethanol for 1h. For condensation step, a condenser was involved to avoid the solvent vaporizing out of reaction. The reactor temperature was increased to 75-80°C though stirring. TTIP and 25 ml of ethanol was gradually added drop by drop to reactor for 1h

and then yellowish transparent sol was found after an hour of further mixing. DI water was added in the sol and aged at 80°C for 2h at room temperature. Then, the aged gel was further refined for 6000 rpm for 10 minutes in centrifugal separator. Finally, the attained solid particles was calcined at 450°C for 3h. A reference pure SiO₂ sample was prepared in NH₄OH with the same way described above but without the addition of TTIP (T. G. Kim, An, Han, Hur, Park, and Choi, 2017). In addition, reference pure TiO₂ was prepared in acid condition at the same way with Ti_xSi_y oxide (Karkare, 2014). Composition of sol-gel liquid solution used for the preparation of Ti_xSi_y oxide are shown in Table 3.1 and 3.2.

Table 3.1 Mole of component in the preparation of Ti_xSi_y oxide synthesized at various pH values.

Samples	TTIP (mol)	TEOS (mol)	C ₂ H ₅ OH (mol)	HCl/NH ₄ OH (mol)	H ₂ O (mol)
SiO ₂	-	0.120	1.889	0.060 ^b	0.440
Ti _x Si _y pH 8.0	0.011	0.109	1.889	0.025 ^b	0.440
Ti _x Si _y pH 9.0	0.011	0.109	1.889	0.060 ^b	0.440
Ti _x Si _y pH 10.0	0.011	0.109	1.889	0.075 ^b	0.440
TiO ₂	0.120	-	4.293	0.081 ^a	0.702

^a mole of HCl, ^b mole of NH₄OH

Table 3.2 Mole of component in the preparation of Ti_xSi_y oxide at pH 9.0 at various ratio between Ti and Si.

Samples	TTIP (mol)	TEOS (mol)	C_2H_5OH (mol)	NH_4OH/HCl (mol)	H_2O (mol)
SiO_2	-	0.120	1.889	0.060 ^b	0.440
$Ti_{70}Si_{30}$	0.020	0.100	1.889	0.060 ^b	0.440
$Ti_{50}Si_{50}$	0.011	0.109	1.889	0.060 ^b	0.440
$Ti_{40}Si_{60}$	0.008	0.112	1.889	0.060 ^b	0.440
TiO_2	0.120	-	4.293	0.081 ^a	0.702

^a mole of HCl, ^b mole of NH_4OH

3.2.2 Characterization of titanium-silicon oxide

3.2.2.1. ^{29}Si Solid-state nuclear magnetic resonance spectroscopy (^{29}Si solid-state NMR)

The ^{29}Si solid-state NMR spectra was used to evaluate the structural of the silicate phase in SiO_2 and Ti_xSi_y oxide. ^{29}Si NMR spectra was recorded on a Bruker Avance III HD 500 MHz spectrometer (Germany).

3.2.2.2. Fourier transform infrared spectroscopy (FTIR)

Infrared spectra of Ti_xSi_y oxide, TiO_2 , and SiO_2 were recorded by Fourier transform infrared spectroscopy (FTIR) (Bruker, Tensor 27) using attenuated total reflectance (ATR) equipped with platinum diamond crystal (TYPE A225/QL). The spectra was recorded in the wave number from 400-4000 cm^{-1} with 4 cm^{-1} resolutions through the accumulation of 64 scans. All samples of Ti_xSi_y oxide, TiO_2 , and SiO_2 were dried in oven at 70°C for 4 hours before testing.

3.2.2.3 Field emission scanning electron microscope (FE-SEM)

FE-SEM images of Ti_xSi_y oxide, TiO_2 , and SiO_2 were examined by a field-emission scanning electron microscope (FESEM-EDS, Carl Zeiss Auriga). The film specimens were coated with carbon prior to the investigation. Acceleration voltage of 3 kV was used to collect SEM images of the sample.

3.2.2.4 X-ray diffraction (XRD)

The diffractograms of Ti_xSi_y oxide, TiO_2 , and SiO_2 recorded by powder X-ray diffraction (Bruker, Model D2 phaser, Germany), with $CuK\alpha$ radiations scanning from $10-90^\circ$ at a rate of $0.05^\circ/s$ with current 35 mA and 35 mV.

3.2.2.5 X-ray absorption near-edge structure spectroscopy (XANES) and extended X-ray absorption fine structure spectroscopy (EXAFS)

All TiO_2 and SiO_2 standard compounds and Ti_xSi_y oxide samples were analyzed by XANES and EXAFS spectroscopy at the Ti *K*-edge at beamline 8 of the electron storage ring (using an electron energy of 1.2 GeV, a bending magnet, beam current of 80–150 mA, and 1.1 to 1.7×10^{11} photons per s) at the Synchrotron Light Research Institute (SLRI), Nakhon Ratchasima, Thailand (Klysubun, Tarawarakarn, Thamsanong, Amonpattaratkit, Cholsuk, Lapboonrueng, Chaichuay, and Wongtepa, 2020). Finely ground, homogenized powder of each sample was spread as thin film (area 2.0 cm \times 0.5 cm) and carefully dispersed with a spatula to yield a homogeneous particle distribution and to avoid hole effects on Kapton tape (Lanmar Inc., Northbrook, IL, USA) mounted on a sample holder. For each standard compound and oxide sample, at least five spectra were attained. All XANES and EXAFS spectra were measured in the transmission mode with ionization chamber detectors. For the acquisition of all spectra, a Ge (220) double crystal monochromator with an energy resolution ($\Delta E/E$) of 2×10^{-4} was used. An energy range of 4936–5824 eV with an energy step of 2, 0.2, 0.05k eV was used for Ti *K*-edge spectra. The photon energy was calibrated against the *K*-edge of Ti foil at 4966 ± 0.2 eV. Finally, the normalized XANES and EXAFS data were processed and analyzed after background subtraction in the pre-edge and post-edge regions using software package including (i) ATHENA for XAS data processing, (ii) ARTEMIS for EXAFS data analysis using theoretical standards from FEFF,

and (iii) HEPHAESTUS software for a collection of beamline utilities based on tables of atomic absorption data. This package is based on the IFEFFIT library of numerical and XAS algorithms and is written in the Perl programming language using the Perl/Tk graphics toolkit (N. M. Ravel and Newville, 2005).

3.2.2.6 X-ray fluorescence (XRF)

The chemical compositions of Ti_xSi_y oxide, TiO_2 , and SiO_2 were investigated by energy dispersive XRF (EDS Oxford Instrument ED 2000) with Rh X-ray tube with a vacuum medium.

3.2.2.7 Particle size distribution

Particle size distribution of Ti_xSi_y oxide, TiO_2 , and SiO_2 were evaluated by a diffraction particle size analyzer (DPSA) (Malvern Instruments, model Mastersizer 2000). The Ti_xSi_y oxide, TiO_2 , and SiO_2 were dispersed in absolute ethanol and analyzed by He-Ne laser. The average particle size distribution was investigated from the standard volume percentiles at 10, 50 and 90%. The average volume weighted diameter was used to define the average particle size.

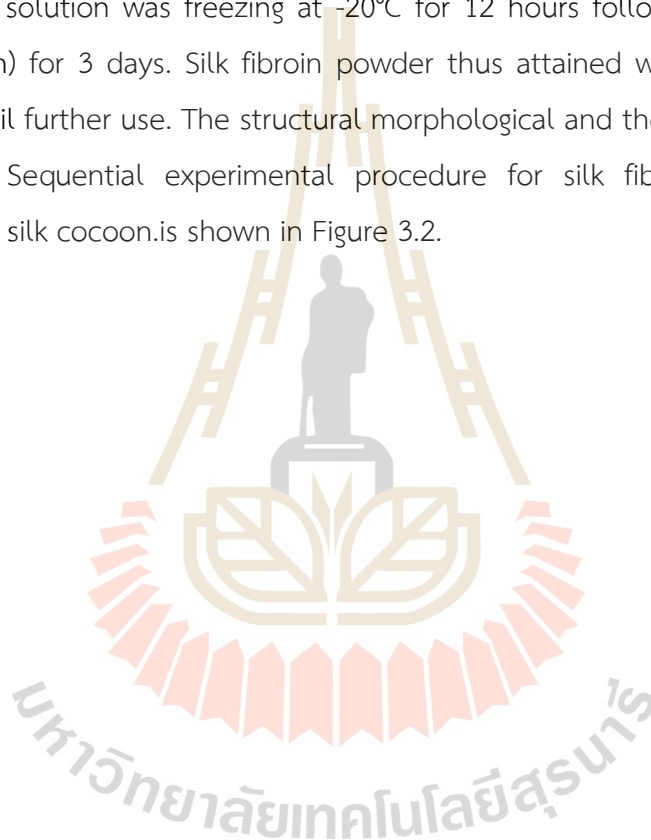
3.2.2.8 Specific surface area

Specific surface area of Ti_xSi_y oxide, TiO_2 , and SiO_2 were investigated by a nitrogen adsorption analyzer (BELSORP MINI II, model Bel-Japan). The sample of Ti_xSi_y oxide, TiO_2 , and SiO_2 were degassed at 300°C for 3 h before measurement. Brunauer, Emmett, Teller (BET) and Barrett, Joyner, Halenda (BJH) method were used to calculate the specific surface area and pore size distribution, respectively.

3.2.3 Preparation of regenerated silk fibroin powder

Regenerated silk fibroin powder was prepared as described by U.-J. Kim, Park, Joo Kim, Wada, and Kaplan (2005) and Vishwanath, Pramanik, and Biswas (2016). Briefly, the silk cocoons were cut into fine pieces and cleaned to remove any remains. Silk fibroin was extracted from the cocoons by degumming process in which the cut cocoon pieces was boiled in an aqueous solution of 2% w/v Na_2CO_3 for 30 mins and then rinse thoroughly with deionized water (DI) to remove sericin protein and dried overnight at 40°C .

After the degumming step, silk fibroin was prepared using two different solvent. In one process, the degummed silk was re-dissolved in CaCl_2 solution at 80-100°C under continuous stirring for 2 h. The second process, degummed silk was dissolved in Ajisawa's solvent system, ternary solvent made of CaCl_2 , H_2O , $\text{C}_2\text{H}_5\text{OH}$ solution at a molar ratio of 1:8:2 (Ajisawa, 1998), at 80-100°C for 2 h, filtered, and dialyzed for 5 days against distilled water with several changes until the conductivity of dialyzed water was the same as that of distilled water in order to remove salt and alcohol. The solution was freezing at -20°C for 12 hours followed by freeze drying (lyophilization) for 3 days. Silk fibroin powder thus attained was kept in an airtight container until further use. The structural morphological and thermal properties were investigated. Sequential experimental procedure for silk fibroin extraction from *Bombyx mori* silk cocoon is shown in Figure 3.2.



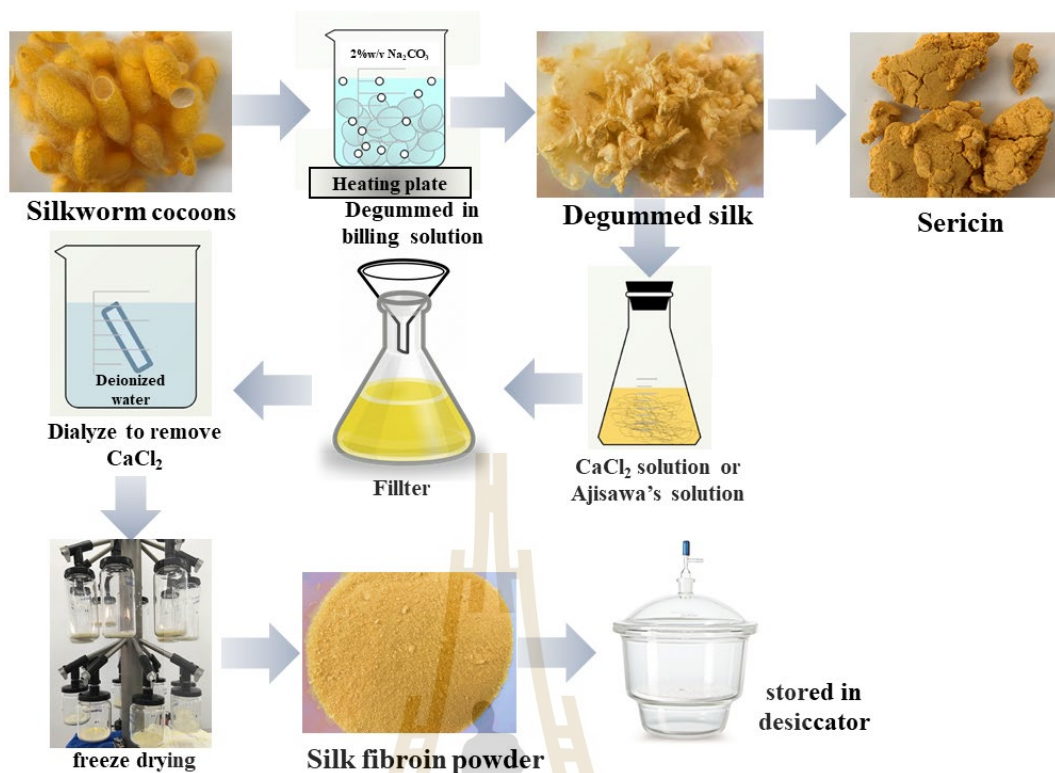


Figure 3.2 Sequential experimental procedure for silk fibroin extraction from Bombyx mori silk cocoon.

3.2.4 Characterization of silk fibroin powder

The determine the functional group of materials existed in cocoons, degummed silk, and silk fibroin were analyzed with Fourier transform infrared spectroscopy (Bruker, Tensor 27) using attenuated total reflectance (ATR) equipped with platinum diamond crystal (TYPE A225/QL). The spectra was recorded in the wave number from $400\text{-}4000\text{ cm}^{-1}$ with 4 cm^{-1} resolutions through the accumulation of 64 scans. The structural characterization of silk fibroin was powder X-ray diffraction (Bruker, Model D2 phaser, Germany), with $\text{CuK}\alpha$ radiations scanning from $10\text{-}90^\circ$ at a rate of $0.05\text{ }^\circ/\text{s}$ with current 35 mV and 35 mA . Surface morphology of cocoons, degummed silk, silk fibroin, and sericin were analyzed with a scanning electron microscope (JEOL, JSM-6010LV) at an accelerating voltage of $5\text{-}10\text{ kV}$ and working distance 15 mm . All samples were sputtered with a thin layer of gold. In addition, thermogravimetric analysis of cocoons, degummed silk, silk fibroin, and sericin were

examined using thermogravimetric analyzer (TGA/DSC1, Mettler Toledo). The temperature was raised from the room temperature to 650°C under nitrogen and then heated to 800°C under air atmosphere with heating rate of 10°C/min. The weight change was recorded as a function of temperature.

3.2.5 Preparation of PLA/TiO₂, PLA/SiO₂ and PLA/Ti_xSi_y oxide composites

PLA, PLA/TiO₂, PLA/SiO₂ and PLA/Ti_xSi_y oxide composites with appropriate percentage of Ti_xSi_y oxide (1, 3, 5 wt.%) was prepared by solvent-casting method. The polymer was dissolved in solvent (10% w/v) by stirring. Firstly, Ti_xSi_y oxide was dispersed in chloroform with ultrasonic treatment for 1 day. After that, PLA was added to the Ti_xSi_y oxide and strictly stirred for 4 days. The dispersions of PLA composites were additionally ultrasonically treated for 1 h using with frequency of 42 kHz for four times per day. The treated dispersions were slightly poured onto Petri dishes, and the solvent was evaporated under room temperature. The films were dried to constant mass dried at room temperature for ~ 24 h. and kept in oven at 40°C for 4 h. Film thickness were measured by using a micrometer in eight replicates for each sample, which an average value was attained.

3.2.6 Preparation of PLA/SF composites

PLA and PLA/SF composites with different loading of SF (1, 3, 5 wt.%) were prepared by solvent-casting method. The polymer was dissolved in solvent (10% w/v) by stirring. Firstly, SF was dissolved in chloroform with ultrasonic treatment for 1 day. PLA was added to the SF solutions and rigorously stirred for 4 days. The dispersions of PLA composites were additionally ultrasonically treated for 1 h using ultrasonic bath with frequency of 42 kHz for four times per day. The treated dispersions were gradually poured onto Petri dishes, and the solvent was allowed to evaporate under constant influence of ultrasound. The films were dried to constant mass dried at room temperature for ~ 24 h. and kept in over at 40°C for 4 h. Film thickness were measured by using a micrometer in eight replicates for each sample, from which an average value was obtained.

3.2.7 Preparation of PLA/Ti_xSi_y/SF composites

PLA and PLA/Ti_xSi_y/SF composites with 3wt.% of Ti_xSi_y oxide and different SF content (1,3,5 wt.%) were prepared by solvent-casting method. The polymer was dissolved in solvent (10% w/v) by stirring. Firstly, Ti_xSi_y oxide and SF was dissolved in chloroform with ultrasonic treatment for 1 day. PLA was added to the Ti_xSi_y oxide and SF mixed solutions and rigorously stirred for 4 days. The dispersions of PLA composites were additionally ultrasonically treated for 1 h using ultrasonic bath with frequency of 42 kHz for four times per day. The treated dispersions were poured onto Petri dishes, and the solvent was allowed to evaporate under constant influence of ultrasound. The films were dried to constant mass dried at room temperature for ~ 24 h. and kept in over at 40°C for 4 h. Film thickness were measured by using a micrometer in eight replicates for each sample, from which an average value was obtained.

3.2.8 Characterization of PLPLA/Ti_xSi_y, PLA/SF, and PLA/Ti_xSi_y/SF composites

3.2.8.1. Mechanical properties

The tensile properties of the films of PLA and PLA composites were obtained using an Instron universal testing machine (UTM, model 5565) with a load cell of 5 kN according to the ASTM standard method D882-18. Specimen samples, 10 cm x 2.54 cm. Crosshead speed was set at 50 cm/min. The values were presented the average of seven measurements.

3.2.8.2. Thermal properties

Thermal properties of PLA and PLA composites films were carried out using a differential scanning calorimeter (DSC204F1, Netzsch) equipped with a liquid nitrogen cooling system. The sample was heated from room temperature to 180°C with a heating rate of 5°C (1st heating scan) and kept for 5 minutes to erase the thermal history. Then it was cooled to room temperature (25°C) with a cooling rate of 5°C/min. Finally, it was heated again to 180°C with heating rate 5°C/min (2nd heating scan). The degree of crystallinity (χ_c) of PLA and PLA nanocomposites was estimated using the follow equation (3.1):

$$\chi_c = \frac{\Delta H_m}{\Delta H_m^0 \left(1 - \frac{\%wt \text{ filler}}{100}\right)} \times 100 \quad (3.1)$$

where ΔH_m are the melting enthalpy in the second heating process and ΔH_m^0 , which is the melting enthalpy of an infinitely large crystal, was taken as 93.6 J/g (Tang, Zhang, Liu, and Zhu, 2012).

Thermogravimetric analysis of PLA and PLA composite films were examined using thermogravimetric analyzer (TGA/DSC1, Mettler Toledo). The temperature was raised from the room temperature to 650°C under nitrogen and then heated to 800°C under air atmosphere with heating rate of 10°C/min. The weight change was recorded as a function of temperature.

3.2.8.3. Morphological property

Morphological properties of PLA and PLA composites film were examined by a scanning electron microscope (JEOL, JSM-6010LV). The cross-sections of the films after tensile test and the freeze-fractured films in liquid nitrogen were sputtered with gold. Acceleration voltage 9-12 kV was used to collect SEM images of sample.

3.2.8.4. Water vapor transmission rate (WVTR)

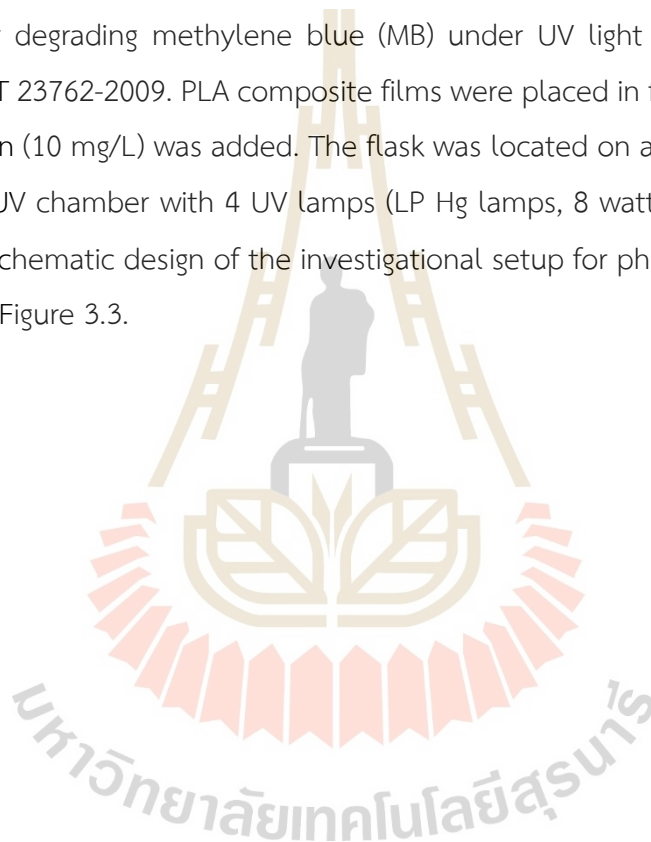
WVTR, a modified ASTM E96/E96M, is a measure of the rate of water passed through the of PLA and PLA composites film at an individual time interval. The composite films were cut into circular discs with 1.5 cm of diameter and were located on the top of the glass vial containing 5 mL water. Constant humidity was maintained by placing it in the desiccators maintained at room temperature and relative vapor pressure (RVP) = 0 by using silica gel. The vial assembly was weighted for every hour at first day, and then the weighting was made every day over a 20-day period. By statistical method, when the straight line effectively fits the weight change vs time plot by linear regression with $r^2 \geq 0.99$, the constant rate of weight change was attained. WVTR was calculated using the equation (3.2) (Elsner, Shefy-Peleg, and Zilberman, 2010; Pei Shan Teo and Chow, 2014). WVTR ($\text{g m}^{-2} \text{ day}^{-1}$) for each type of composites film was investigated with three individually prepared films as the replicated experimental units.

$$WVTR = \frac{G}{t x A} \quad (\mathbf{g \cdot m^{-2} \cdot day^{-1}}) \quad (3.2)$$

where G, weight change of the vial with water and film (from the straight line) (g); t, the duration for the measurement (day); G/t, slope of the straight line, g/day; A, the test area of the film (m²).

3.2.8.5. Photocatalytic degradation of methylene blue (MB)

The photocatalytic activity of PLA composite films was evaluated by degrading methylene blue (MB) under UV light according to Chinese standard GB/T 23762-2009. PLA composite films were placed in flask and then 200 mL of MB solution (10 mg/L) was added. The flask was located on a mechanical shaker at 50 rpm in a UV chamber with 4 UV lamps (LP Hg lamps, 8 watts, main light emission at 245 nm). Schematic design of the investigational setup for photocatalytic process is presented in Figure 3.3.



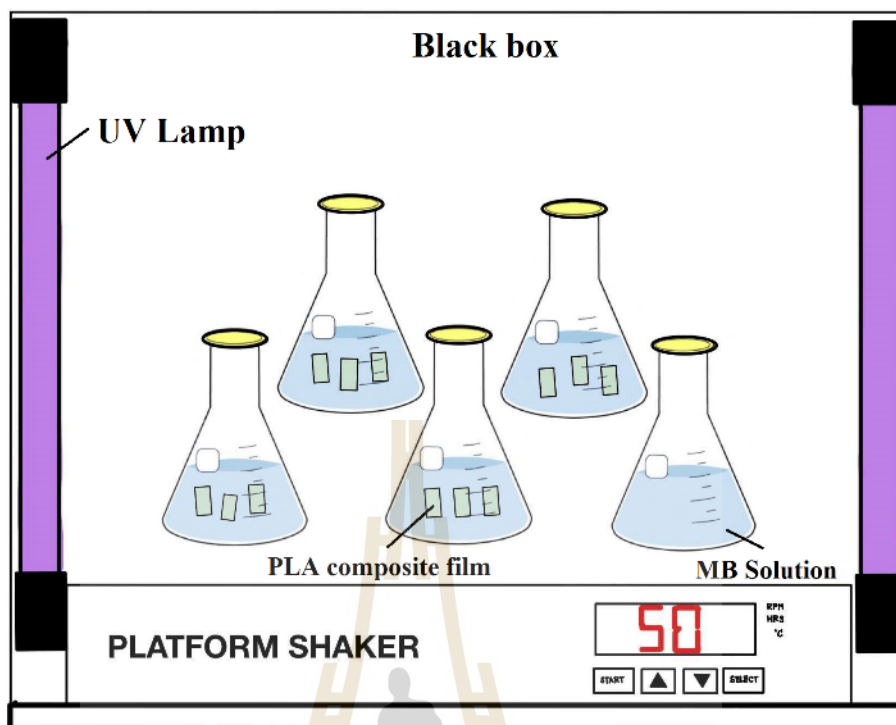


Figure 3.3 Schematic illustration of the experimental setup for photocatalytic process

The 4 mL MB solution was collected every 60 min, and analyzed using UV-vis spectrophotometer (Cary300, Agilent Technology). In order to keep the volume of MB solution in the flask, the sample were placed back after each measurement. The maximum absorbance of MB occurs at 664 nm (Figure 3.4).

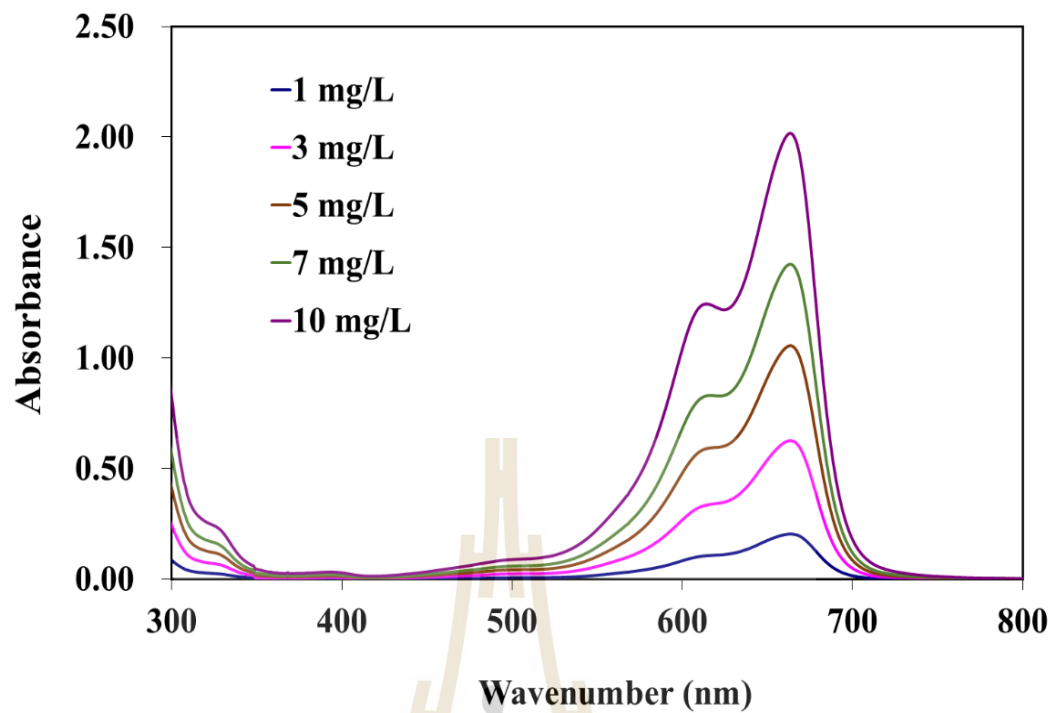


Figure 3.4 Wavelength-absorbance curves of methylene blue (MB) aqueous solutions

The spectrometer was calibrated with solution of MB at 1mg/L, 3mg/L, 5mg/L, 7mg/L, and 10mg/L concentrations respectively. Calibration curve of methylene blue aqueous solutions are shown in Figure 3.5. In order to precise the probable decomposition of MB under UV light, the PLA and composites film and the solution stored in a black box with absence of any photocatalyst. The concentration of MB was also collected every 60 min to estimate the absorption of MB.

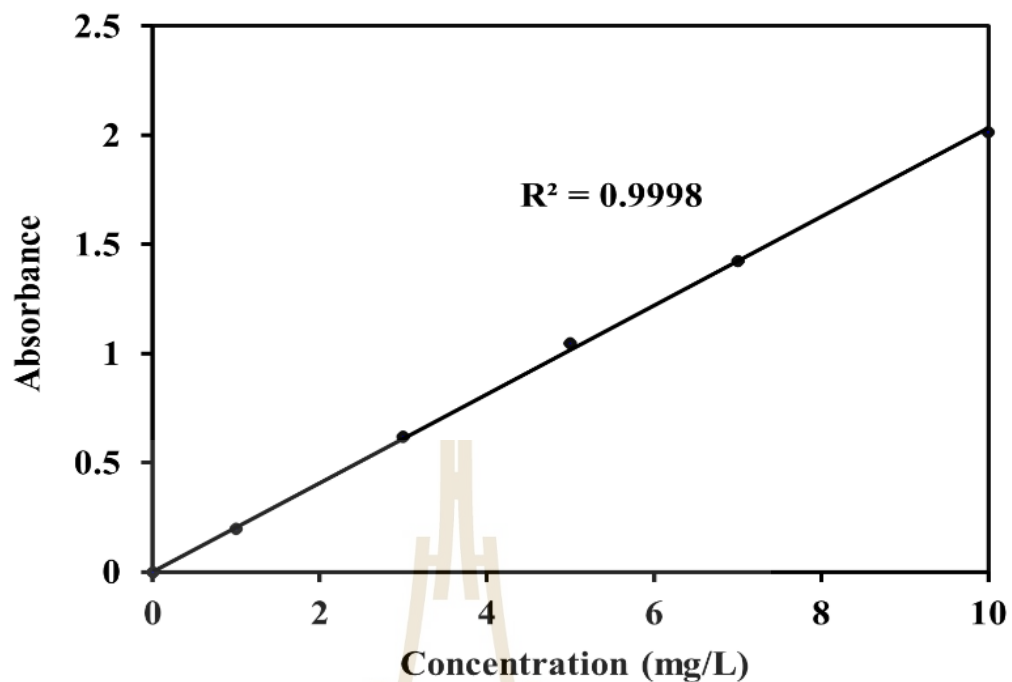


Figure 3.5 Calibration curve of methylene blue aqueous solutions

3.2.8.6. Light transmittance and opacity measurements

The UV-vis transmission spectra of the film specimens were recorded in the range of 200-800 nm using a UV-vis spectrophotometer (Cary300, Agilent Technology). The film specimen was directly placed in a cell, and an empty cell was employed as reference. The opacity of the PLA and PLA composites films with well-controlled thicknesses was used to estimate the opacity (AU.nm/mm) of the films:

$$Opacity = Abs_{600}/X \quad (3.3)$$

where Abs_{600} is the absorbance at 600 nm, and X is the film thickness (mm). This test was evaluated with three specimens for each type of film (Fathi Achachlouei and Zahedi, 2018).

3.2.8.7. Hydrolytic degradation

Hydrolytic degradation of PLA and PLA composite films (10 x 10 mm²) were carried out at 37°C in small bottles containing 1 M NaOH (pH 13). Following the incubation for a given time (0, 60, 120, 180, 240, 300, 360 and 420 minutes), the films were periodically removed, washed with distilled water, dried in oven at 40°C for 48h. The weight loss (W_{loss}) was estimated using following equation (3.4):

$$W_{loss}(\%) = \frac{W_0 - W_t}{W_0} \times 100 \quad (3.4)$$

where W_0 is the initial weight of polymer film and W_t is the weight of degraded sample measured at time t after drying in oven for 48h (Buzarovska and Grozdanov, 2012).

3.2.8.8. In vitro degradation

The degradation study of PLA and PLA composite was done according to the standard BS EN ISO 10993-13:2010 (Felfel et al., 2016) and ASTM F1635-16 (Racksanti, Janhom, Punyanitya, Watanesk, and Watanesk, 2015). Each of the sample of PLA and PLA composite (0.4-0.5 g) was accurately weighed. Then the samples were immersed separately in 0.01M phosphate buffered saline (PBS) (pH = 7.4 ± 0.2) solution and kept at 37°C with different soaking times from 1 to 8 weeks (0, 2, 4, 6, 8). The specimens were washed with deionized water to remove the salts at several time points, then oven dried at 40°C for 48 h. After that, the dry weight of the samples was recorded. The percentage weight loss was evaluated using the following equation (3.5);

$$W_{loss}(\%) = \frac{W_t - W_0}{W_0} \times 100 \quad (3.5)$$

where W_t is the weight of degraded sample measured at time t after drying at 40 °C in oven for 48 h and W_0 is the initial weight of the sample. At each time

point, all samples were weighed and mechanically tested permitting the degradation pathway of each separate samples to be followed with time.

The tensile properties of each specimen were measured by an Instron universal testing machine (UTM, model 5565) with a load cell of 5 kN and crosshead speed of 50 cm/min. The values were presented the average of five measurements.

3.2.8.9. Antimicrobial activity

The antimicrobial activity of the PLA and PLA composites films was investigated using the JIS Z 2801:2006 method. The ability of PLA and PLA composite films to restrain the growth of *Escherichia coli* and *Staphylococcus aureus* were measured. The bacteria were incubated at 37°C for 24 h. A plate containing a test sample was inoculated with 0.2 mL of an overnight culture of *Escherichia coli* and *Staphylococcus aureus*. The bacteria cultures concentration was adjusted to 10⁶ CFU/mL. All petri dishes of PLA and PLA composites were incubated at 37°C for 24 h and colony-forming unit (CFU) were counted.

The percent reduction of the colonies was estimated using the following equations, which relate the number of colonies from the neat PLA with the number of colonies from the PLA nanocomposites were evaluated using the following equation (3.6) and (3.7);

$$\% \text{ Reduction} = \frac{(\text{Log CFU at 0h} - \text{Log CFU at 24h})}{\text{Log CFU at 0h}} \times 100 \quad (3.6)$$

$$\text{Antimicrobial activity}(R) = Ut - At \quad (3.7)$$

Where Ut is an average of CFU per milliliter after inoculation on untreated test pieces after 24 h; At is an average of CFU per milliliter after inoculation on antibacterial test pieces after 24 h.

CHAPTER IV

RESULTS AND DISCUSSION

4.1 The effect of pH on structural and physical properties of titanium-silicon oxide

4.1.1 ^{29}Si Solid-state nuclear magnetic resonance spectroscopy (^{29}Si solid-state NMR)

To study the structural of Ti_xSi_y oxide (especially for 1:1 atomic ratio) and SiO_2 to identify the formation of the framework silicon atoms in these material, ^{29}Si Solid-state NMR spectroscopy have been employed.

The structural analysis ^{29}Si NMR was given in Figure 4.1, which presents the spectra of the silica and the $\text{Ti}_{50}\text{Si}_{50}$ oxide. ^{29}Si NMR spectra of oxides generally exhibit three peaks for different environments for Si: isolated silanol groups $(\text{SiO})_3\text{Si-OH}$, Q^3 ; geminal silanols $(\text{SiO})_2\text{Si}-(\text{OH})_2$, Q^2 ; and silicon in the siloxane binding environment without hydroxyl groups $(\text{SiO})_4\text{Si}$, Q^4 (Q^n represents a SiO_4 unit, with n ; number of bridging in oxygen atoms) (Degirmenci, Erdem, Ergun, Yilmaz, Michel, and Uner, 2008; Schraml-Marth, Walther, Wokaun, Handy, and Baiker, 1992). According to related reference, the three resonance signals of pure SiO_2 (Synthesis by sol-gel method) appearing at -93.9, -103.3, and -110.2 ppm can be attributed to the configurations of Q^2 , Q^3 , and Q^4 , respectively. The spectrum of silica (Figure 4.1a) exhibits a chemical shift of -110 ppm, which is attributed to the Q^4 units, and a minor peak is appeared at -103 ppm that would conform to Q^3 units corresponding siloxane (Si-O-Si) and silanol ($\equiv\text{Si-OH}$) groups of silica. The strength of Q^4 units are major in pure silica representing a three-dimensional network of the silica as shown in the intensity of peaks in Figure 4.1a. Also, dependent on the chemical shift of Q^3 there would be a tiny proportion of Si nuclei directly bonded to hydroxyl groups (Pabón, Retuert, and Quijada, 2007). Additionally, Figure 4.1b shows that for the formation of the $\text{Ti}_{50}\text{Si}_{50}$ oxide, the silica was chemically combined with titanium oxide, and subsequently Ti-

atom disturbed in the three-dimensional silica network and the microstructure around the silicon atoms.

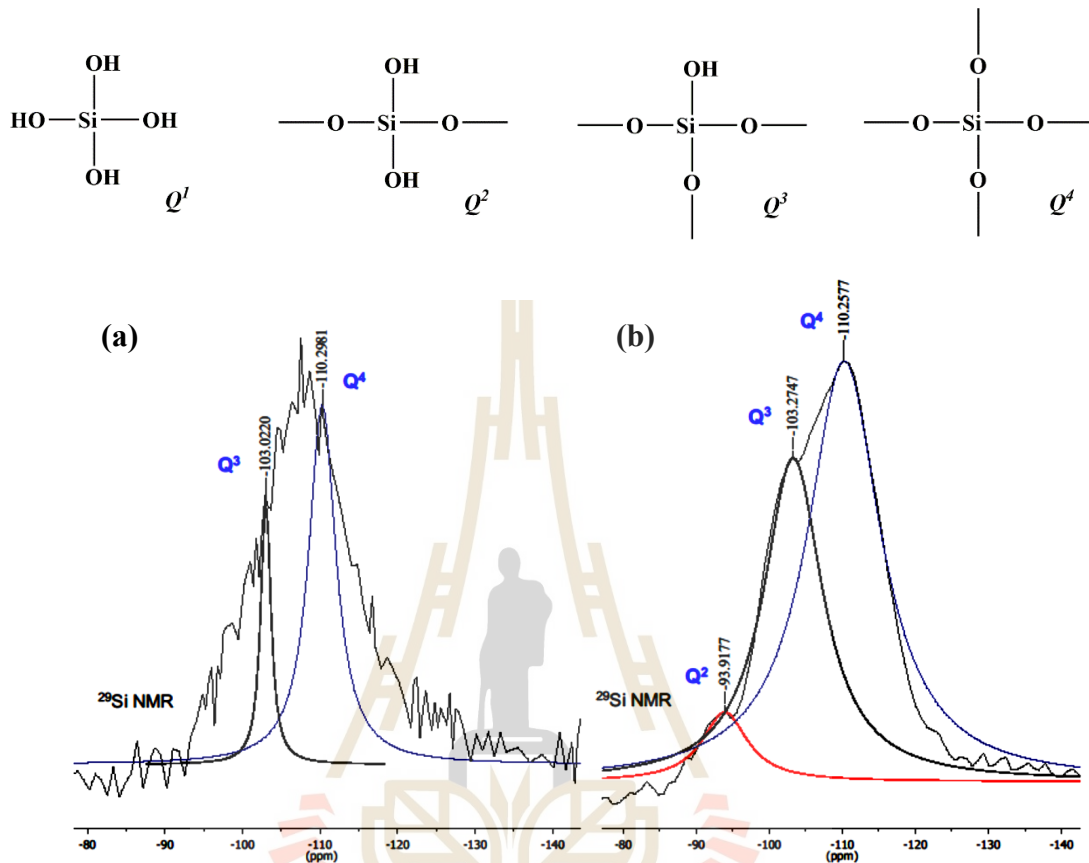


Figure 4.1 ^{29}Si -NMR patterns of (a) SiO_2 and (b) $\text{Ti}_{50}\text{Si}_{50}$ oxide.

A very significant increase in Q^3 units (mono-substitution) is realized comparison this peak with the amount of siloxane and silanol group in pure SiO_2 , where they correspond to the silanol groups or Si-OH bonds. The appearance of Q^2 units was observed, which may be attributed to disubstitute silica in tetrahedra, maybe due to the existence of Ti-O-Si-O-Ti-O groups indicating a considerable existence of Si-O-Ti bonds in this sample suggestive of atomic mixing (Dirken, Smith, and Whitfield, 1995). Similar observation was reported by Pabón, Retuert, and Quijada (2007). Obviously, Ti atoms have been replaced some Si atoms in the SiO_2 network, indicating that as a consequence of the synthesis performed by the sol-gel method defined through this

work a lot of Si-O-Ti bonds was created, in agreement with the results of the FTIR and XRD.

4.1.2 Fourier transform infrared spectroscopy (FTIR)

FTIR spectroscopy (FTIR) was applied to define the functional group of materials presented in all Ti_xSi_y oxide samples. The analysis was recorded using FTIR spectrometer in a range between 4000 and 400 cm^{-1} . FTIR spectra of TiO_2 , SiO_2 , and Ti_xSi_y oxides synthesized at various pH values are shown in Figure 4.2.

The FTIR spectrum of all Ti_xSi_y oxides showed three main peaks with the wavenumbers of 801, 949 and 1052 cm^{-1} . The peak at 440, 801 and 1052 cm^{-1} were corresponding to the rocking, symmetric and asymmetric stretching vibration of Si-O-Si of silica, respectively (Sahu, Hong, Wang, and Huang, 2009). The peak at 949 cm^{-1} was commonly corresponded to Ti-O-Si vibrations indicating the existence of Ti-O-Si linkages (Yamashita et al., 1998), this band can also be corresponded to the Si-OH bond which should be attributed to Si-OH bonding; however, this absorption band disappeared after the SiO_2 particles were calcined at 450°C. On the other hand, the 949 cm^{-1} absorption band was still observed for all Ti_xSi_y oxide samples which have been calcined at a temperature of 450°C. Accordingly, the 949 cm^{-1} peak in FTIR spectra for Ti_xSi_y oxide particles should not be attributed to Si-OH bonds but associated with Si-O-Ti bonding (Vives and Meunier, 2008; Yu and Wang, 2000). This indicated titanium combining into the framework of silica. In addition, the absence of the Ti-O-Ti bond of the oxides samples may be too weak to be detected at 1400 cm^{-1} (Chiahung, Hsunling, Yaoling, Shuling, Shaoli, and Yaohsuan, 2012). Therefore, the influence of pH on the FTIR of the Ti_xSi_y oxide was not observed.

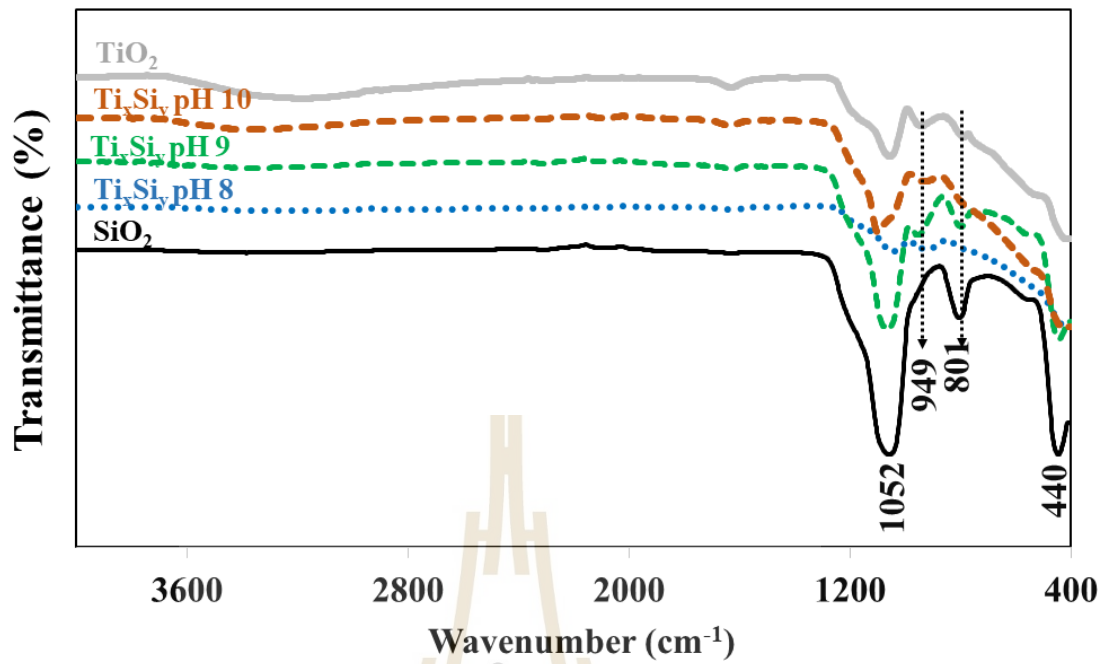


Figure 4.2 FTIR spectra of TiO₂, SiO₂, and Ti_xSi_y oxides synthesized at various pH values.

Based on the evidence from NMR and FTIR, the probable mechanism for Ti_xSi_y oxides synthesized was suggested in Figure 4.3.

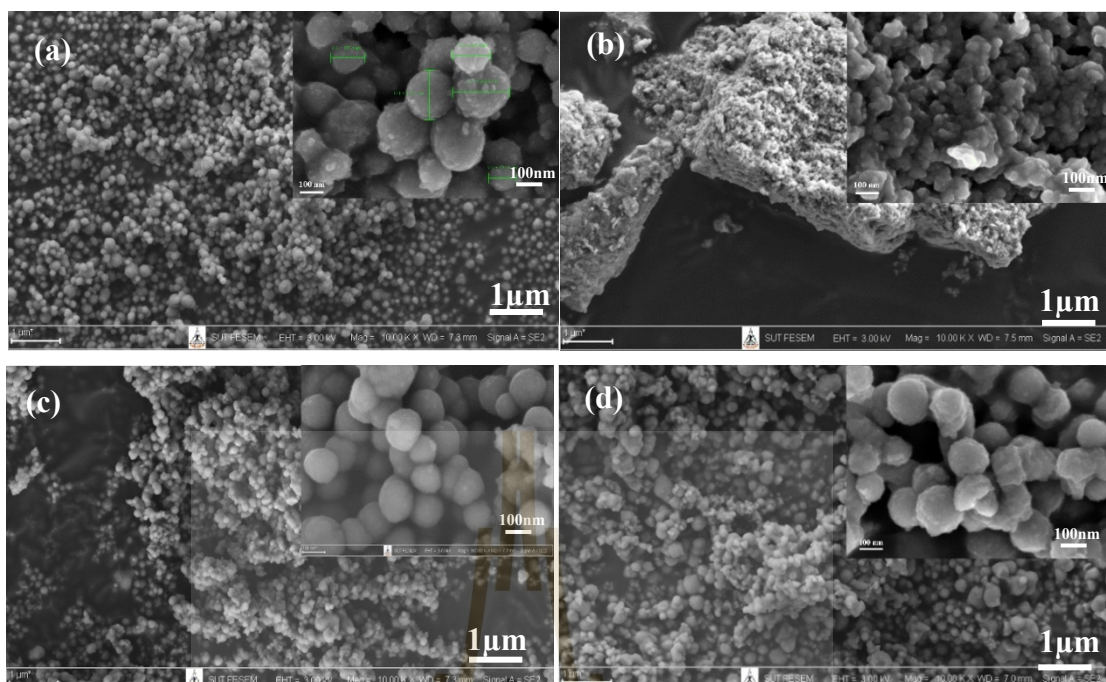


Figure 4.4 SEM images of Ti_xSi_y oxides synthesized at various pH values: (a) SiO_2 , (b) Ti_xSi_y pH 8.0, (c) Ti_xSi_y pH 9.0, (d) Ti_xSi_y pH 10.0.

However, the sizes of the Ti_xSi_y oxides particles at pH 10 were nano-sized with the appearance of agglomeration (Figure 4.4d). Wu, Wu, and Lü, (2006) claimed that the colloidal sol-gel technique can be generated the large particles compose of agglomerated nanoparticles and that either condensed or porous polycrystalline of microparticles. So, the pH 9.0 was selected to synthesis compositionally controlled the Ti_xSi_y oxides particles with spherical in shape.

4.1.4 X-ray diffraction (XRD)

XRD is a nondestructive analytical technique that is usually applied for the structural characterization of Ti_xSi_y oxides materials. XRD patterns of Ti_xSi_y oxides powders synthesized at various pH values of 8.0, 9.0 and 10.0 are shown in Figure 4.5. Silica showed one amorphous peak locating at 2θ angles at 23° . In most of the Ti_xSi_y oxides powders preparing at pH 8 and 9, XRD patterns exhibit the broad amorphous peak because of the existence of silica. Furthermore, this formation of the Ti_xSi_y oxides suggesting that titanium oxide combined to the silica by atomic mixing, and

consequently the distribution of Ti atoms was occurred in the microstructure around the silicon atoms and the three-dimensional silica network. However, The Ti_xSi_y oxides powders prepared at pH 10.0 exhibits intense TiO_2 anatase peak suggesting the forming of higher crystallites of anatase was presented when high pH of sol-gel solution were applied during hydrolysis (Alias, Ismail, and Mohamad, 2010). It can be obviously seen that the crystallinity of the XRD peaks is enhanced by adjusting the pH value of sol.

Furthermore, the XRD peaks for Ti_xSi_y oxides powder with $pH > 9$ present the crystalline nature with 2θ angles at 25° (101) and 48° (200), which correspond to the crystalline phase (anatase) of TiO_2 (Sahu, Hong, Wang, and Huang, 2009; Yamashita et al., 1998) due to sufficient amount of OH^- to form TiO_2 . This may be noticed that pH affects particles size and degree of crystallinity. The crystal structure of TiO_2 was tetragonal; $a = b = 3.782 \text{ \AA}$, $c = 9.502 \text{ \AA}$ (Etacheri, Di Valentin, Schneider, Bahnemann, and Pillai, 2015). However, no rutile phase was detected in any case according to the absence of (110) diffraction peak at 27.4° .

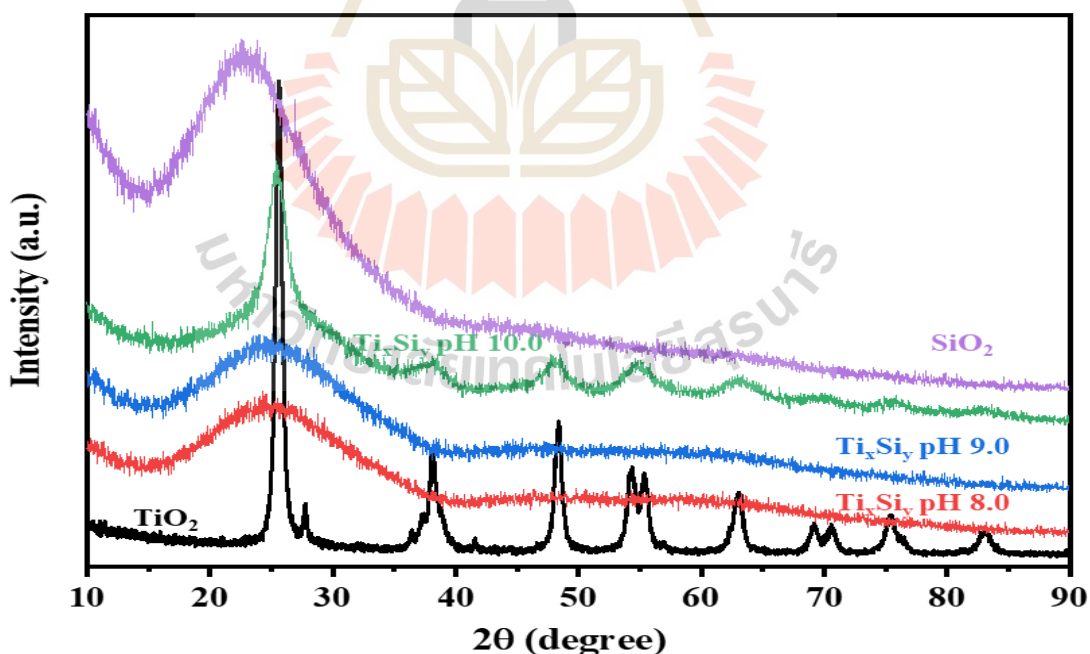


Figure 4.5 XRD patterns of Ti_xSi_y oxide synthesized at various pH values.

4.1.5 X-ray Absorption Near-Edge Structure spectroscopy (XANES)

XANES at Ti *K*-edge contains several well-defined pre-edge peaks that are related to the local structure surrounding Ti atom. To further investigate the structural differences in the Ti_xSi_y oxides materials, Ti *K*-edge XANES spectra of standard TiO_2 anatase, synthesis TiO_2 materials, and Ti_xSi_y oxides synthesized at various pH values were collected and have been presented in Figure 4.6. The spectrum is mostly separated into two regions: (i) pre-edge region (4940 to 4990 eV) and (ii) post-edge region (4990 to 5010 eV). The four- (TiO_2), five- ($(Ti=O)O_4$) and six- (TiO_6) coordinate Ti can be corresponded to the pre-edge peak at 4969, 4970.5 and 4972 eV (attribute to 1s-to-3d transition), respectively (Hsiung, Wang, and Wang, 2006).

In Figure 4.6, both of TiO_2 anatase and synthesis TiO_2 display three minor pre-edge peaks, which are attribute from the 1s level of Ti to $1t_{1g}$, $2t_{2g}$, and $3e_g$ molecular orbitals (in sequence of increasing energy) (Davis and Liu, 1997). The three minor pre-edge peaks for TiO_2 anatase are outstanding fingerprints for the crystalline phase of titanium dioxide materials thus the formation of anatase is specified by the near edge region of TiO_2 . As silicon merged into the Ti_xSi_y oxide, a large single pre-edge feature was to dominate the other weaker feature. The large pre-edge feature in Ti_xSi_y oxides samples designates that the greater number of Ti occupies sites of tetrahedral symmetry, as anticipated for samples in which Ti substitutes directly for Si in the oxide sample. In addition, the pre-edge region of all Ti_xSi_y oxides did not change with various synthesized pH values. Furthermore, the larger in intensity of pre-edge peaks in the XANES spectra of the Ti_xSi_y oxides than for TiO_2 anatase indicate that Ti no longer resides totally in sites of octahedral when mixed with Si. So, the results from XANES spectra of mixed oxide sample are in a reasonable agreement with XRD results.

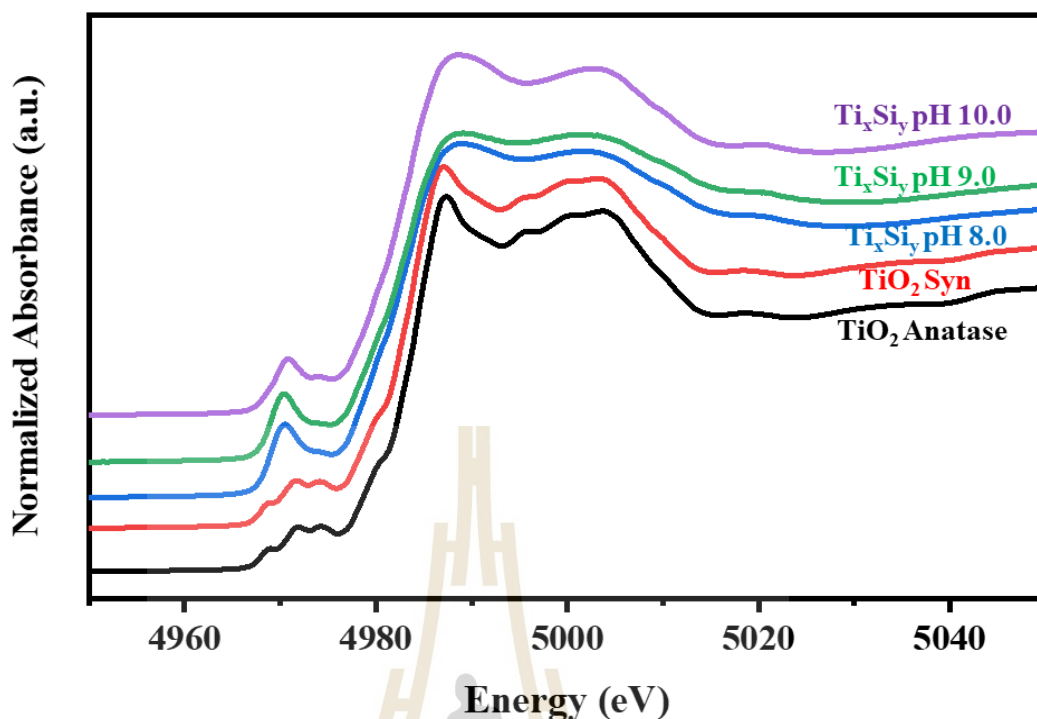


Figure 4.6 Ti *K*-edge XANES spectra of Ti_xSi_y oxides synthesized at various pH values.

4.1.6 Extended X-ray absorption fine structure spectroscopy (EXAFS)

The local atomic research may be helpful to probe the changed phase, bond distance between the atom, and coordination number by using EXAFS analysis.

The investigation of coordination number of Ti atom and bond distances between Ti-O and Ti-Si atom were performed by the EXAFS analysis at the Ti *K*-edge. The program package of *Athena-Artemis* was used to perform the background noise correction and the normalization of the raw data (N. M. Ravel and Newville, 2005). To define the local atom structure and relative bond length with consider to the absorbing atom, the EXAFS data were FT to the *R*-space. The ATOM and FEFF codes were used to simulate the FT data (in *R*-space) by creating systematic theoretical structure of SiO_2 (Sharma, Varshney, Park, Ha, Chae, and Shin, 2015). The range of data reserved for the transformation was $3-9 \text{ \AA}^{-1}$ in *k*-space. Structural parameters were attained, without the phase corrections, by fitting the data in *R*-space, within the intermission of $1.1-3 \text{ \AA}$ (Figure 4.7). The shell parameter such as Ti-O and Ti-Si bond distances(*R*), coordination

number (CN), Debye-Waller factor (σ^2), and R-factor are present in Table 4.1. Note that the amplitude reduction factor (S_0^2) was preliminarily determined to be 0.52 by fitting the EXAFS spectrum of SiO_2 .

The first and second shells in the FTs arise from the single scattering paths of cation-oxygen and cation-cation, respectively (Khemthong, Photai, and Grisdanurak, 2013). In this study, we first focus on the Ti-O and Ti-Si shells of all Ti_xSi_y oxides samples. TiO_2 anatase has an average Ti-O bond distance of 1.95 Å. The results from curve fitting of the EXAFS provide and interatomic distance of 1.99, 1.82, and 1.94 Å for Ti atom dilute silica of Ti_xSi_y oxides synthesized at various pH 8.0, 9.0 and 10.0, respectively. This result compared favorably with bond distance of Ti-O in titanium silicalite molecular sieve of 1.80 Å corresponding with the cation existing in a tetrahedral environment (Pei, Zajac, Kaduk, Faber, Boyanov, Duck, Fazzini, Morrison, and Yang, 1993). Neurock and Manzer (1996) calculated a Ti-O bond distance using density functional methods of 1.81 Å suggesting Ti in a tetrahedral cluster. Obviously, the value of 1.83 Å described for the Ti-O bond distance in Ti_xSi_y oxides synthesized at pH 9.0 is agreeable with an absolute of the Ti atoms occupy in a tetrahedral environment, which supports the comparable assumption from XANES.

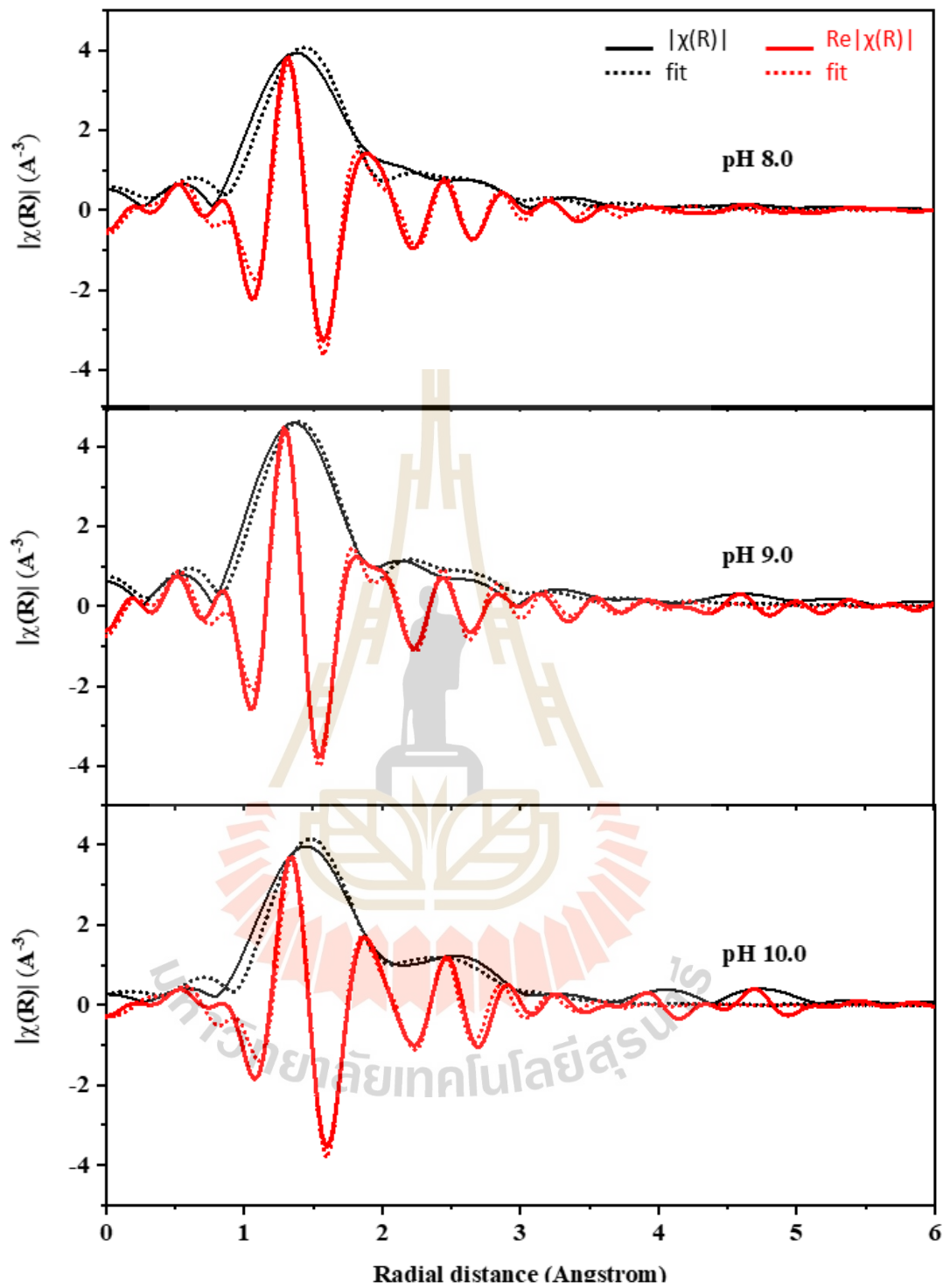


Figure 4.7 The experimental EXAFS data of Ti_xSi_y oxide synthesized at various pH values in R -space within the intermission of 1.1-3 \AA .

Table 4.1 Structure parameter (obtained from fittings of Ti K-edge EXAFS data) of first two coordination shells around Ti atom of Ti_xSi_y oxide synthesized at various pH values.

Sample	Shell	Bond	ΔE (eV)	CN	R(\AA)	σ^2	R-factor
Ti_xSi_y pH 8.0	1	Ti-O	4.11 \pm 3.34	4.14 \pm 0.18	1.99 \pm 0.02	0.0053 \pm 0.0013	0.0176
	2	Ti-Si		1.27 \pm 0.44	2.79 \pm 0.03	0.0018 \pm 0.0019	
Ti_xSi_y pH 9.0	1	Ti-O	2.72 \pm 2.03	4.07 \pm 0.12	1.83 \pm 0.01	0.0042 \pm 0.0008	0.0082
	2	Ti-Si		1.00 \pm 0.13	2.77 \pm 0.02	0.0020 \pm 0.0020	
Ti_xSi_y pH 10.0	1	Ti-O	6.70 \pm 3.29	4.08 \pm 0.19	1.94 \pm 0.02	0.0049 \pm 0.0024	0.0158
	2	Ti-Si		1.52 \pm 0.22	2.81 \pm 0.03	0.0013 \pm 0.0031	

Furthermore, all of the Ti_xSi_y oxide presented a small value for the Debye-Waller factor corresponding to the structural disturbance in the materials (Sharma, Varshney, Park, Ha, Chae, and Shin, 2015). The Debye-Waller factor was used to describe influences of static and thermal disorder on the EXAFS spectrum. A big value for the σ^2 can be caused by a variance in the ligand distances (static disorder) whereas the small Debye-Waller factors artificially increase a ligand contribution (Scherk, Ostermann, Achterhold, Iakovleva, Nazikkol, Krebs, Knapp, Meyer-Klaucke, and Parak, 2001; Wellenreuther, Parthasarathy, and Meyer-Klaucke, 2010).

4.1.7 X-ray fluorescence (XRF)

The chemical composition of TiO_2 , SiO_2 , and Ti_xSi_y oxide synthesized at various pH values synthesized at various pH values by XRF are shown in Table 4.2. The XRF analysis showed that Ti_xSi_y oxide synthesized at pH 8.0 showed higher %atomic of Si (54.39%) than pH 9.0 (47.87%) and pH 10 (9.82%) because TTIP can be faster hydrolyzed than TEOS in solution at high pH. In contrast, atomic content of Ti in Ti_xSi_y oxide synthesized at various pH values increased with increasing pH values of sol (43.72%).

Table 4.2 Percentage of atomic and atomic ratio of Ti and Si in TiO_2 , SiO_2 , and Ti_xSi_y oxide synthesized at various pH values.

Sample	Atomic (%)		Atomic ratio of Ti/Si
	Si	Ti	
SiO_2	100	0	-
Ti_xSi_y pH 8.0	54.39	45.61	0.84
Ti_xSi_y pH 9.0	47.87	52.13	1.09
Ti_xSi_y pH 10.0	9.82	93.18	9.49
TiO_2	0	100	-

4.1.8 Particle size distribution

The particle sized TiO_2 , SiO_2 , and Ti_xSi_y oxide synthesized at various pH values determining by the Zetasizer Nano ZS and SEM micrographs are shown in Table 4.3 and Figure 4.8. The mean particle size distribution of TiO_2 , SiO_2 , were 40.3 and 147.8 nm, while Ti_xSi_y oxide synthesized at pH 9.0 presented the mean particle size distribution at 136.2 nm. However, the mean particle size distribution of Ti_xSi_y oxide synthesized at pH 8.0 and 10.0 were cover rage of 350-650 nm due to the tendency of agglomeration.



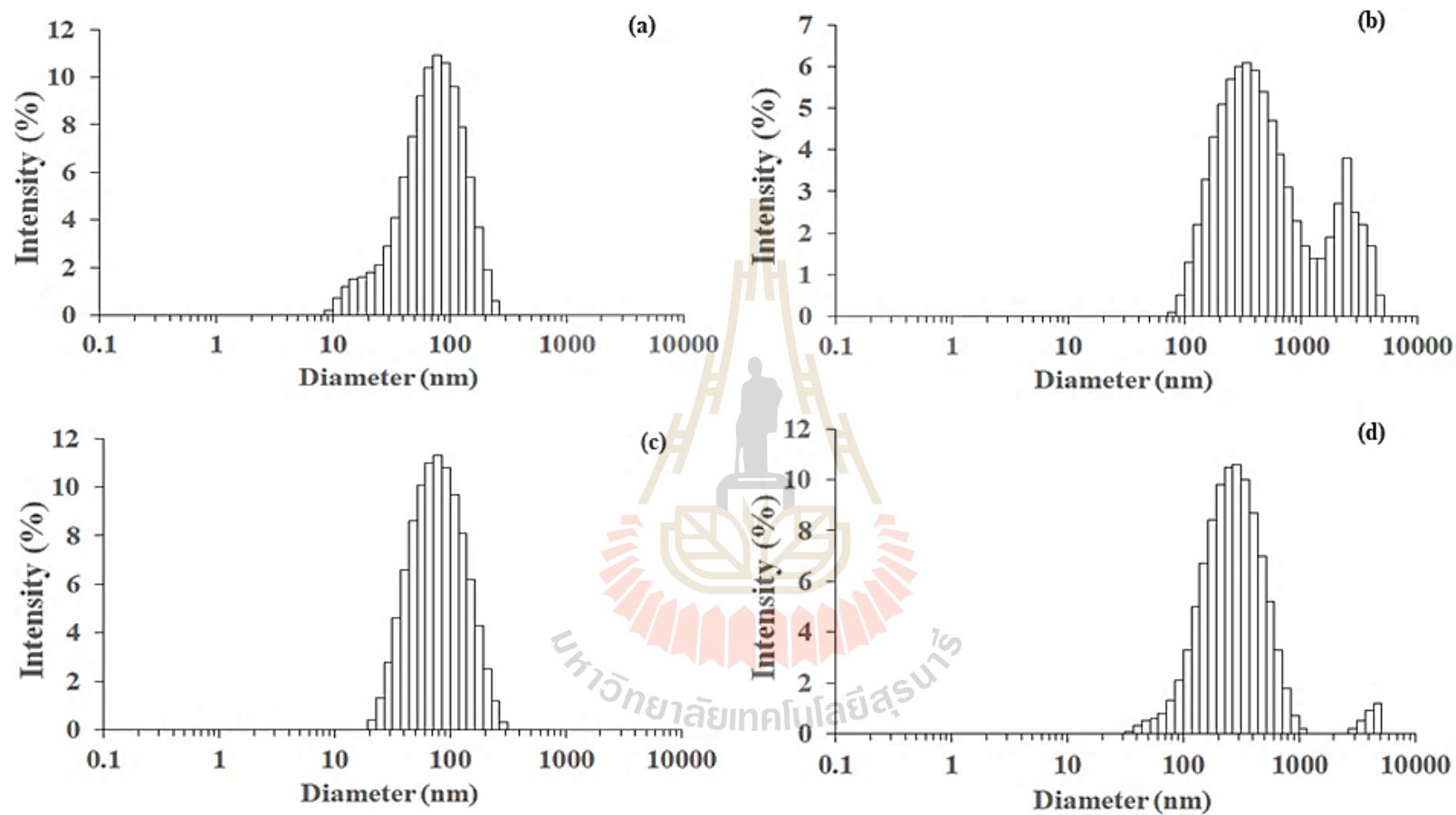


Figure 4.8 Particle size distributions measured on a Zetasizer Nano ZS of SiO_2 and Ti_xSi_y oxide synthesized at various pH values; (a) SiO_2 , (b) Ti_xSi_y pH 8.0, (c) Ti_xSi_y pH 9.0, (d) Ti_xSi_y pH 10.0.

Table 4.3 The particle sized of TiO₂, SiO₂, and Ti_xSi_y oxide synthesized at various pH values.

Sample	Particle size, (nm)	PDI	Number averaged diameter, d _n (nm)
SiO ₂	147.8	0.248	144.2±11.3
Ti _x Si _y pH 8.0	639.3	0.627	41.5±16.7
Ti _x Si _y pH 9.0	136.2	0.239	135.4±12.3
Ti _x Si _y pH 10.0	397.0	0.322	114.2±24.2
TiO ₂	40.3	0.490	27.8±6.3

To determine the correct diameter of TiO₂, SiO₂, and Ti_xSi_y oxide, SEM micrographs (Figure 4.3) was used to measuring the correct diameter by image J. The number averaged diameter, d_n was calculated from a minimum of 200 particles according to the following equations (Wu, Zhang, Yuan, Zhang, and Zhou, 2010):

$$d_n = \frac{\sum_i n_i d_i}{\sum_i n_i} \quad (4.1)$$

$$SD = \sqrt{\frac{\sum_i n_i (d_i - d_n)^2}{N}} \quad (4.2)$$

Where d_i is the diameter of particle

n_i is the total number of particles having diameter, d_i

It can be observed that the number averaged diameter increased with increasing pH value of synthesis.

4.1.9 Nitrogen adsorption-desorption isotherms

The textural properties of the SiO_2 , TiO_2 , and Ti_xSi_y oxide synthesized at various pH values are shown in Table 4.4. It can be observed that the surface areas (S_{BET}) of the $\text{Ti}_{50}\text{Si}_{50}$ oxide were 177.02, 225.68, and 62.75 m^2g^{-1} for Ti_xSi_y pH 8.0, 9.0 and 10.0, respectively. In addition, mean pore diameter of the Ti_xSi_y oxide were 2.56, 5.85, and 27.31 nm. While S_{BET} of SiO_2 and TiO_2 was 116.90 and 74.07 m^2g^{-1} with average pore size 37.08 and 12.75 nm.

Table 4.4 Specific surface area, pore volume and mean pore size of TiO_2 , SiO_2 , and Ti_xSi_y oxide synthesized at various pH values.

Sample	Specific Surface Area, S_{BET} (m^2g^{-1})	Pore Volume, V_p (cm^3g^{-1})	Mean pore diameter, d_p (nm)
SiO_2	116.90	1.06	51.08
Ti_xSi_y pH 8.0	177.02	0.11	2.56
Ti_xSi_y pH 9.0	225.68	0.33	5.85
Ti_xSi_y pH 10.0	62.75	0.42	27.31
TiO_2	74.07	0.23	12.75

A typical nitrogen adsorption-desorption isotherm of the SiO_2 , TiO_2 , and Ti_xSi_y oxide synthesized at various pH values is present in Figure 4.9. The isotherm of SiO_2 is type II curve according to the IUPAC isotherm classifications, indicating that the obtained SiO_2 particles contained macropores. Inflection point occurs near the completion of the first adsorbed monolayer, which is typical for non-porous or macroporous materials with pore >50 nm. In addition, all Ti_xSi_y oxide exhibited type II isotherms with pore diameter 2.56, 5.85, and 27.31 nm. However, the isotherm of TiO_2 is type IV curve of the IUPAC isotherm classifications. An abrupt hysteric loop is detected from this curve, which is typical for mesoporous materials with pore in range

of 2 to 50 nm that show capillary condensation and evaporation (Gregg and Sing, 1982; Zhang, Zhang, and Chan, 2005).

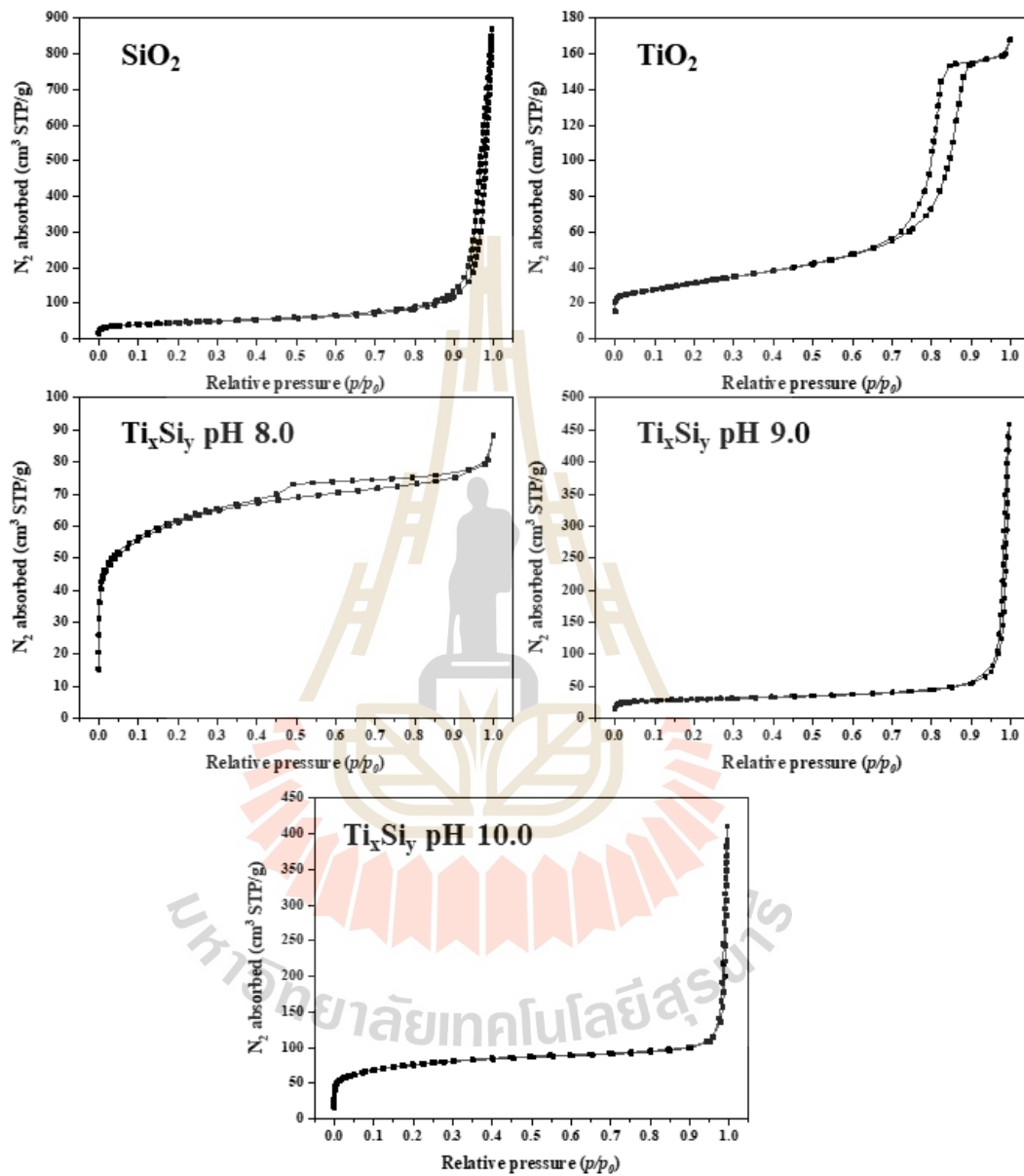


Figure 4.9 Nitrogen adsorption-desorption isotherms of SiO₂, TiO₂, and Ti_xSi_y oxide synthesized at various pH values.

Therefore, the uniform spherical shape of particles of titanium silicon oxide with equivalent atomic compositions of Ti and Si and a specific surface area

above 200 m²/g prepared by controlling the pH at about 9 was used to prepared mixed oxide in next studied.

4.2 The effect of atomic ratio of Ti/Si ratio on structural and physical properties of titanium-silicon oxide

4.2.1 Fourier transform infrared spectroscopy (FTIR)

FTIR spectroscopy is widely applied to define the functional group of materials presented in all Ti_xSi_y oxide samples. The analysis was recorded using FTIR spectrometer in a range between 4000 and 400 cm^{-1} . FTIR spectra of TiO_2 , SiO_2 , and Ti_xSi_y oxides samples with different Ti/Si atomic ratios are shown in Figure 4.10.

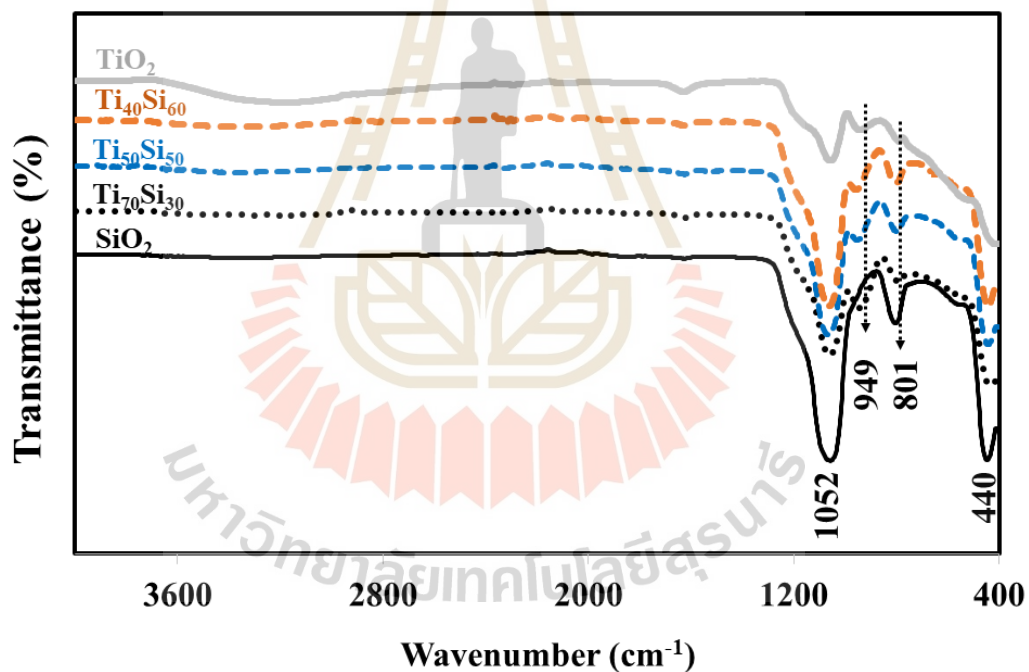


Figure 4.10 FTIR spectra of TiO_2 , SiO_2 , and Ti_xSi_y oxides synthesized with different atomic ratio of Ti/Si ratio

From the FTIR spectra of all Ti_xSi_y oxides, the peak at 949 cm^{-1} was commonly corresponded to Ti-O-Si vibrations indicating the existence of Ti-O-Si linkages (Yamashita et al., 1998). Nevertheless, one should be careful in distributing

this peak to Ti-O-Si since this vibration can also be ascribed to the existence of Si-OH, and Ti-OH group (Fernandez, Jose, Mathew, Pr, and Ny, 2007; Vives and Meunier, 2008). However, this absorption band disappeared after the SiO₂ particles were calcined at 450°C. On the other hand, the 949 cm⁻¹ absorption band was still observed for all Ti_xSi_y oxide samples which have been calcined at a temperature of 450°C. Accordingly, the 949 cm⁻¹ peak in FTIR spectra for Ti_xSi_y oxide particles should not be attributed to Si-OH bonds but associated with Si-O-Ti bonding (Vives and Meunier, 2008; Yu and Wang, 2000). This may be indicated titanium combining into the framework of silica. Except this peak, three additional peaks at 460, 800, and 1050 cm⁻¹ are because of the rocking, bending, and stretching of Si-O-Si bonds, respectively.

4.2.2 Field emission scanning electron microscope (FE-SEM)

FE-SEM images of TiO₂ and Ti_xSi_y oxides powder nanoparticles synthesized at various pH values are shown in Figure 4.11

FE-SEM image of TiO₂ exhibits large majority particles with high agglomeration as shown in Figure 4.11a. Ti₇₀Si₃₀ and Ti₅₀Si₅₀ oxides show that the particles are homogeneous with a good nanostructure and mostly spherical in shape when Ti/Si more than 1 (Figure 4.11b and 4.11c). However, the size of Ti₄₀Si₆₀ oxides particles gradually aggregated with increasing mole of Si (Figure 4.11d).

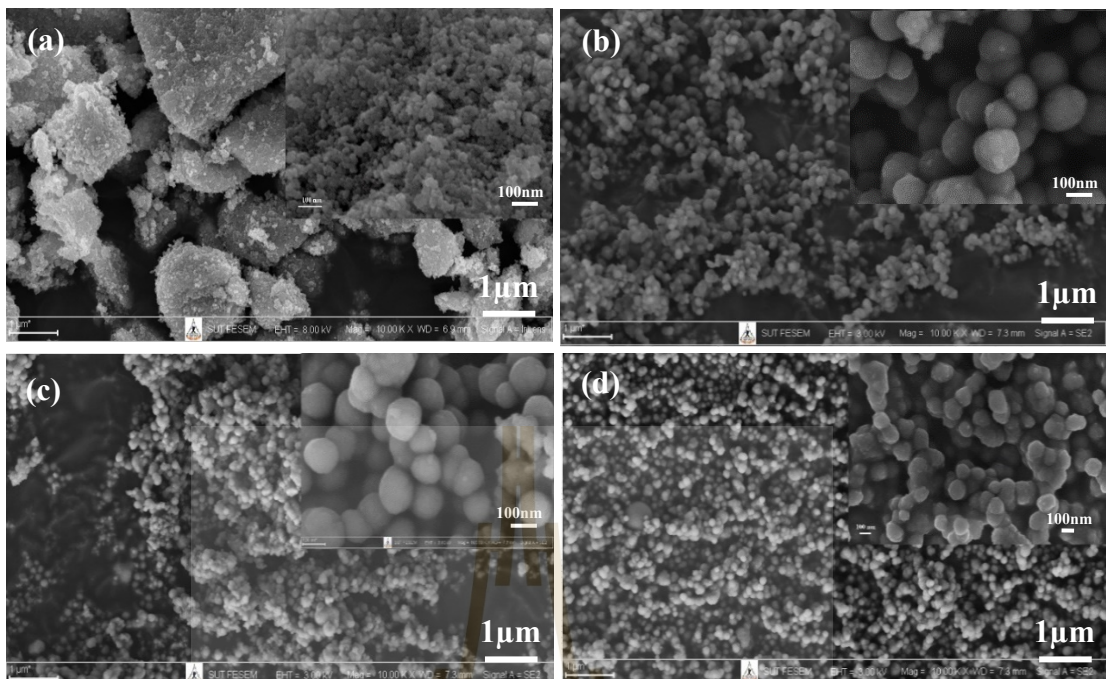


Figure 4.11 SEM images of TiO_2 and Ti_xSi_y oxides synthesized with different atomic ratio of Ti/Si ratio; (a) TiO_2 , (b) $\text{Ti}_{70}\text{Si}_{30}$, (c) $\text{Ti}_{50}\text{Si}_{50}$, (d) $\text{Ti}_{40}\text{Si}_{60}$.

4.2.3 X-ray diffraction (XRD)

Figure 4.12 illustrates the XRD patterns of the Ti_xSi_y oxide powders synthesized with different Ti/Si atomic ratio. All the materials, $\text{Ti}_{70}\text{Si}_{30}$, $\text{Ti}_{50}\text{Si}_{50}$, and $\text{Ti}_{40}\text{Si}_{60}$ do not show any diffraction signal. In addition, their Ti_xSi_y oxide exhibit only broad signals corresponding to homogeneous distributing of titanium atom onto SiO_2 network. However, the nonappearance of XRD diffraction signals indicated that anatase crystallization remains restricted by the segregation of the titania aggregates from the silica network (van Grieken, Aguado, López-Muñoz, and Marugán, 2010).

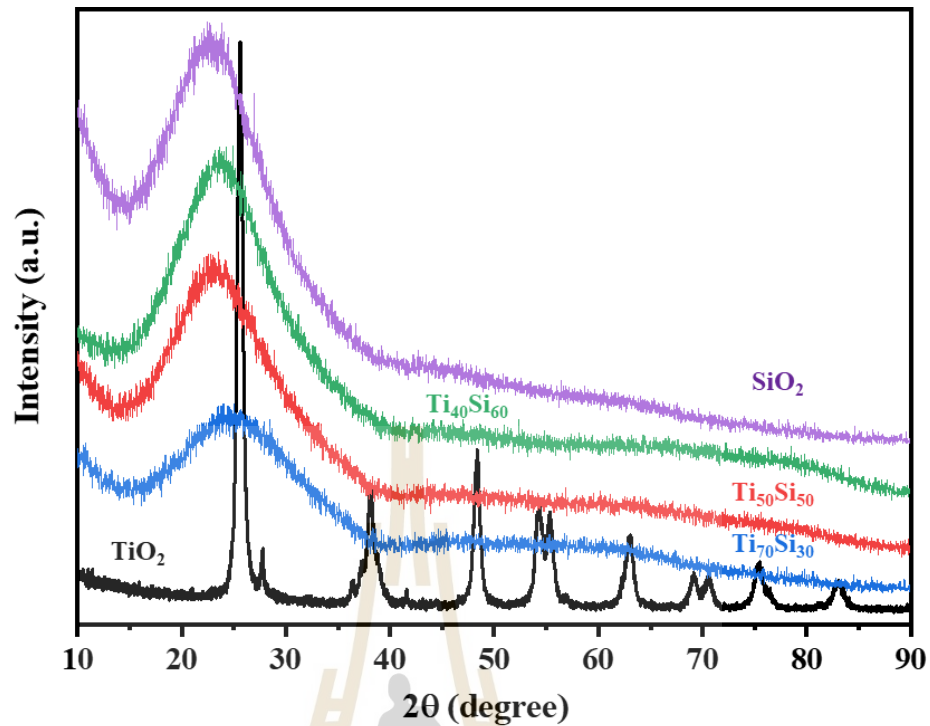


Figure 4.12 XRD patterns of Ti_xSi_y oxide with different Ti/Si atomic ratio.

4.2.4 X-ray Absorption Near-Edge Structure spectroscopy (XANES)

XANES at Ti K -edge comprises numerous well-defined pre-edge peaks that are associated with the local structure surrounding Ti atom. To extra investigate the structural changes in the Ti_xSi_y oxides materials, Ti K -edge XANES spectra of standard TiO_2 anatase, synthesis TiO_2 materials, and Ti_xSi_y oxides synthesized with different Ti/Si ratio were collected and have been presented in Figure 4.13.

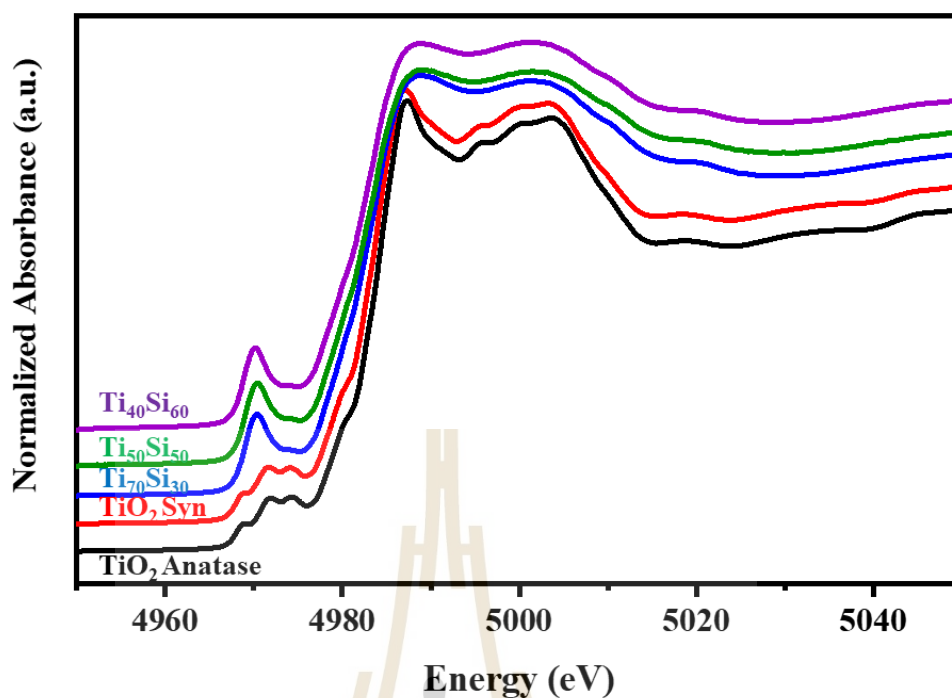


Figure 4.13 Ti K-edge XANES spectra of Ti_xSi_y oxide with different atomic ratio of Ti/Si ratio.

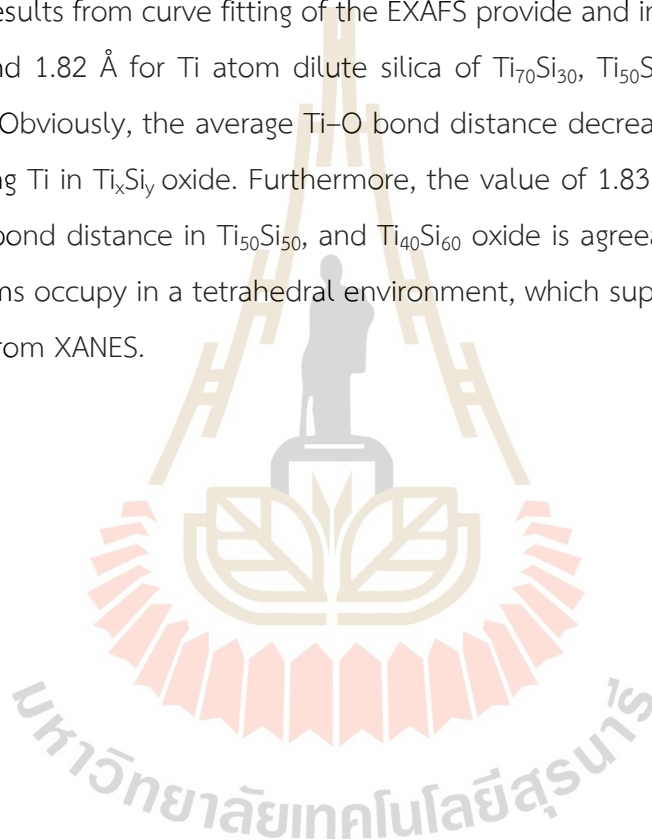
Both of TiO_2 anatase and synthesis TiO_2 show three small pre-edge peaks, while $Ti_{70}Si_{30}$, $Ti_{50}Si_{50}$, and $Ti_{40}Si_{60}$ oxide presented a large single pre-edge peak indicating that Ti^{4+} is in a tetrahedral symmetry. Normally, three weak pre-edge peaks, which are attribute to transitions from the $1s$ level of Ti to $1t_{1g}$, $2t_{2g}$, and $3e_g$ molecular orbitals (in sequence of increasing energy) (Davis and Liu, 1997; Kim, Choi, and Lee, 2000). TiO_2 with anatase structure present three small pre-edge peaks attributed to an octahedral symmetry of Ti cation surrounded by six O anions. At low Ti contents in $Ti_{40}Si_{60}$, Ti is anticipated to additional directly for Si in the tetrahedral SiO_2 framework. However, the pre-edge peaks for the Ti_xSi_y oxides are not as strong as that projected for Ti in a totally tetrahedral environment.

4.2.5 Extended X-ray absorption fine structure spectroscopy (EXAFS)

The investigation of coordination number of Ti atom and bond distances between Ti-O and Ti-Si atom were performed by the EXAFS analysis at the Ti K-edge. The program package of *Athena-Artemis* was used to perform the background noise

correction and the normalization of the raw data (N. M. Ravel and Newville, 2005). Structural parameters were obtained by fitting the data in *R-space*, within the interval of 1.1-3 Å (Figure 4.14). The shell parameter such as Ti-O and Ti-Si bond distances (R), coordination number (CN), Debye-Waller factor (σ^2), and R-factor of Ti_xSi_y oxide with different Ti/Si ratio are present in Table 4.5.

In this study, we first attention on the Ti-O and Ti-Si shells of $Ti_{70}Si_{30}$, $Ti_{50}Si_{50}$, and $Ti_{40}Si_{60}$ oxide samples. TiO_2 anatase has an average Ti-O bond distance of 1.95 Å. The results from curve fitting of the EXAFS provide and interatomic distance of 1.90, 1.83, and 1.82 Å for Ti atom dilute silica of $Ti_{70}Si_{30}$, $Ti_{50}Si_{50}$, and $Ti_{40}Si_{60}$ oxide, respectively. Obviously, the average Ti-O bond distance decreased from 1.90 to 1.82 with increasing Ti in Ti_xSi_y oxide. Furthermore, the value of 1.83 and 1.82 Å described for the Ti-O bond distance in $Ti_{50}Si_{50}$, and $Ti_{40}Si_{60}$ oxide is agreeable with an absolute of the Ti atoms occupy in a tetrahedral environment, which supports the comparable assumption from XANES.



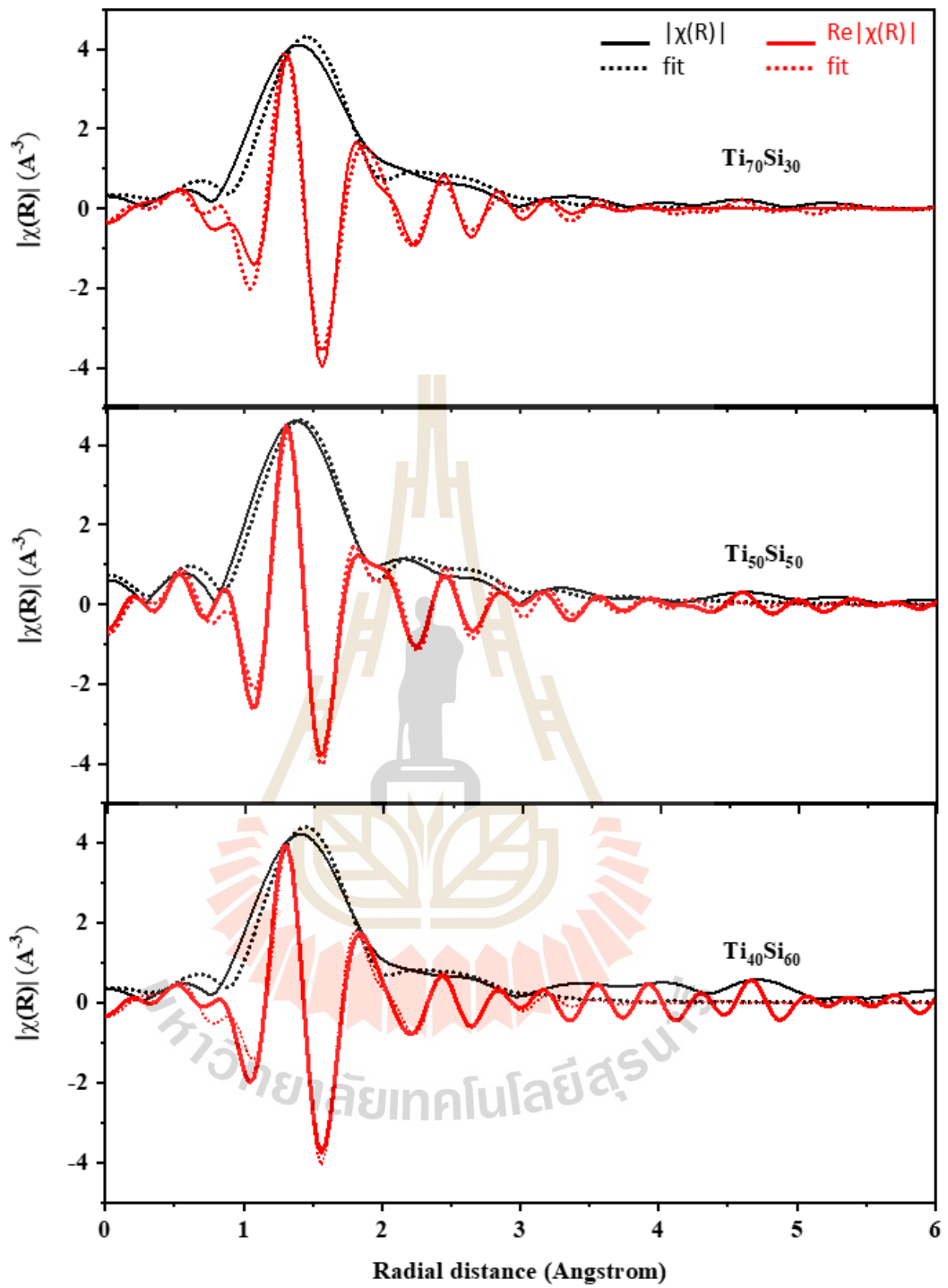


Figure 4.14 The experimental EXAFS data of Ti_xSi_y oxide with different Ti/Si ratio in R -space within the intermission of 1.1-3 \AA .

Table 4.5 Structure parameter (obtained from fittings of Ti *K-edge* EXAFS data) of first two coordination shells around Ti atom of Ti_xSi_y oxide with different Ti/Si ratio.

Sample	Shell	Bond	ΔE (eV)	CN	R(Å)	σ^2	R-factor
$Ti_{70}Si_{30}$	1	Ti-O	6.68±3.23	4.15±0.19	1.90±0.02	0.0051±0.0014	0.0198
	2	Ti-Si		0.97±0.21	2.800±0.04	0.0006±0.0050	
$Ti_{50}Si_{50}$	1	Ti-O	2.72±2.03	4.07±0.12	1.83±0.01	0.0042±0.0008	0.0082
	2	Ti-Si		1.00±0.13	2.77±0.02	0.0020±0.0020	
$Ti_{40}Si_{60}$	1	Ti-O	6.54±2.27	4.09 ±0.13	1.82±0.01	0.0048±0.0010	0.0103
	2	Ti-Si		1.19±0.03	2.79±0.03	0.0023±0.0017	

4.2.6 X-ray fluorescence (XRF)

The chemical composition of TiO_2 , SiO_2 , and Ti_xSi_y oxide with different atomic ratio of Ti/Si ratio by XRF are shown in Table 4.6. Percentage of Si-atom in $\text{Ti}_{70}\text{Si}_{30}$, $\text{Ti}_{50}\text{Si}_{50}$, and $\text{Ti}_{40}\text{Si}_{60}$ oxide by XRF analysis were 29.79, 47.87, and 60.19%, respectively. While, percentage of Ti in $\text{Ti}_{70}\text{Si}_{30}$, $\text{Ti}_{50}\text{Si}_{50}$, and $\text{Ti}_{40}\text{Si}_{60}$ oxide were 70.21, 52.13, and 39.81%, respectively.

Table 4.6 Percentage of atomic and atomic ratio of Ti and Si in Ti_xSi_y oxide with different Ti/Si ratio, TiO_2 , and SiO_2

Sample	Atomic (%)		Atomic ratio of Ti/Si
	Si	Ti	
SiO_2	100	0	-
$\text{Ti}_{70}\text{Si}_{30}$	29.79	70.21	2.36
$\text{Ti}_{50}\text{Si}_{50}$	47.87	52.13	1.09
$\text{Ti}_{40}\text{Si}_{60}$	60.19	39.81	0.66
TiO_2	0	100	-

4.2.7 Particle size distribution

The particle sized TiO_2 , SiO_2 , and Ti_xSi_y oxide synthesized with different atomic ratio of Ti/Si ratio determining by the Zetasizer Nano ZS and SEM micrographs are shown in Table 4.7 and Figure 4.15. The mean particle size distribution of $\text{Ti}_{70}\text{Si}_{30}$, $\text{Ti}_{50}\text{Si}_{50}$, and $\text{Ti}_{40}\text{Si}_{60}$ oxide presented the mean particle size distribution at 573.1, 136.1, and 825.5 nm, respectively due to the tendency of agglomeration. In addition, the correct diameter of $\text{Ti}_{70}\text{Si}_{30}$, $\text{Ti}_{50}\text{Si}_{50}$, and $\text{Ti}_{40}\text{Si}_{60}$ oxide were determined by SEM micrographs (Figure 4.11) was used to measuring the correct diameter by image J. The number averaged diameter of $\text{Ti}_{70}\text{Si}_{30}$, $\text{Ti}_{50}\text{Si}_{50}$, and $\text{Ti}_{40}\text{Si}_{60}$ oxide were 149.3, 135.4, and 131.8 nm, respectively. It can be observed that the number averaged diameter decreased with increasing Ti incorporation into the silica network.

Table 4.7 The particle sized of TiO_2 , SiO_2 , and Ti_xSi_y oxide with different atomic ratio of Ti/Si ratio.

Sample	Particle size, d (nm)	PDI	Number averaged diameter, d_n (nm)
SiO_2	147.8	0.248	144.2 ± 11.3
$\text{Ti}_{70}\text{Si}_{30}$	573.1	0.630	149.3 ± 15.5
$\text{Ti}_{50}\text{Si}_{50}$	136.2	0.239	135.4 ± 12.3
$\text{Ti}_{40}\text{Si}_{60}$	825.5	0.907	131.8 ± 13.3
TiO_2	40.3	0.490	27.8 ± 6.3



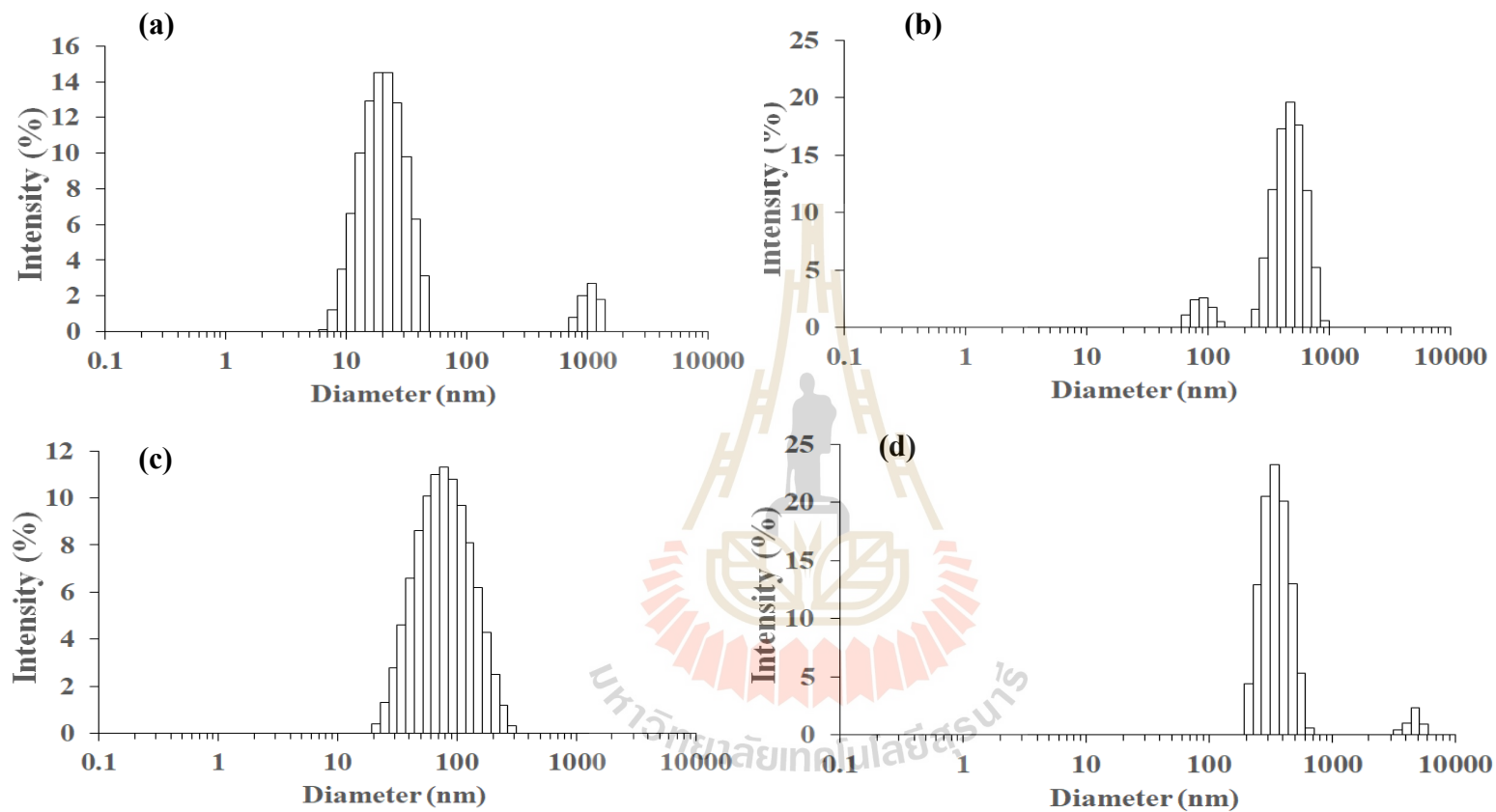


Figure 4.15 Particle size distributions measured on a Zetasizer Nano ZS of TiO_2 and $\text{TiO}_2\text{-SiO}_2$ oxide with different atomic ratio of Ti/Si ratio; (a) TiO_2 , (b) $\text{Ti}_{70}\text{Si}_{30}$, (c) $\text{Ti}_{50}\text{Si}_{50}$, (d) $\text{Ti}_{40}\text{Si}_{60}$.

4.2.8 Nitrogen adsorption-desorption isotherms

The textural properties of the SiO_2 , TiO_2 , and Ti_xSi_y oxide with different Ti/Si ratio are present in Table 4.8. It can be observed that the surface areas (S_{BET}) of the $\text{Ti}_{70}\text{Si}_{30}$, $\text{Ti}_{50}\text{Si}_{50}$, and $\text{Ti}_{40}\text{Si}_{60}$ oxide were 569.07, 225.68, and 68.34 m^2g^{-1} , respectively. The S_{BET} show an increasing trend with the Ti content increased. According to a previous study, the S_{BET} of the Ti_xSi_y oxide increased with increasing Ti content into the silica network (Kosuge, 1999).

Table 4.8 Specific surface area, pore volume and average pore size of SiO_2 , TiO_2 , and Ti_xSi_y oxide with different Ti/Si ratio.

Sample	Specific Surface Area, S_{BET} (m^2g^{-1})	Pore Volume, V_p (cm^3g^{-1})	Average pore diameter, d_p (nm)
SiO_2	116.90	1.06	51.08
$\text{Ti}_{70}\text{Si}_{30}$	569.07	1.42	10.96
$\text{Ti}_{50}\text{Si}_{50}$	225.68	0.33	5.85
$\text{Ti}_{40}\text{Si}_{60}$	68.34	0.36	21.97
TiO_2	74.07	0.23	12.75

A typical nitrogen adsorption-desorption isotherm of the SiO_2 , TiO_2 , and Ti_xSi_y oxide with different Ti/Si ratio are present in Figure 4.16. The isotherm of SiO_2 is type II curve according to the IUPAC isotherm classifications. $\text{Ti}_{70}\text{Si}_{30}$, $\text{Ti}_{50}\text{Si}_{50}$, and $\text{Ti}_{40}\text{Si}_{60}$ oxide exhibited type II isotherms with pore diameter 10.96, 5.85, and 21.97 nm corresponding to mesoporous materials with pore in range of 2 to 50 nm. Whereas the isotherm of TiO_2 is type IV curve of the IUPAC isotherm classifications.

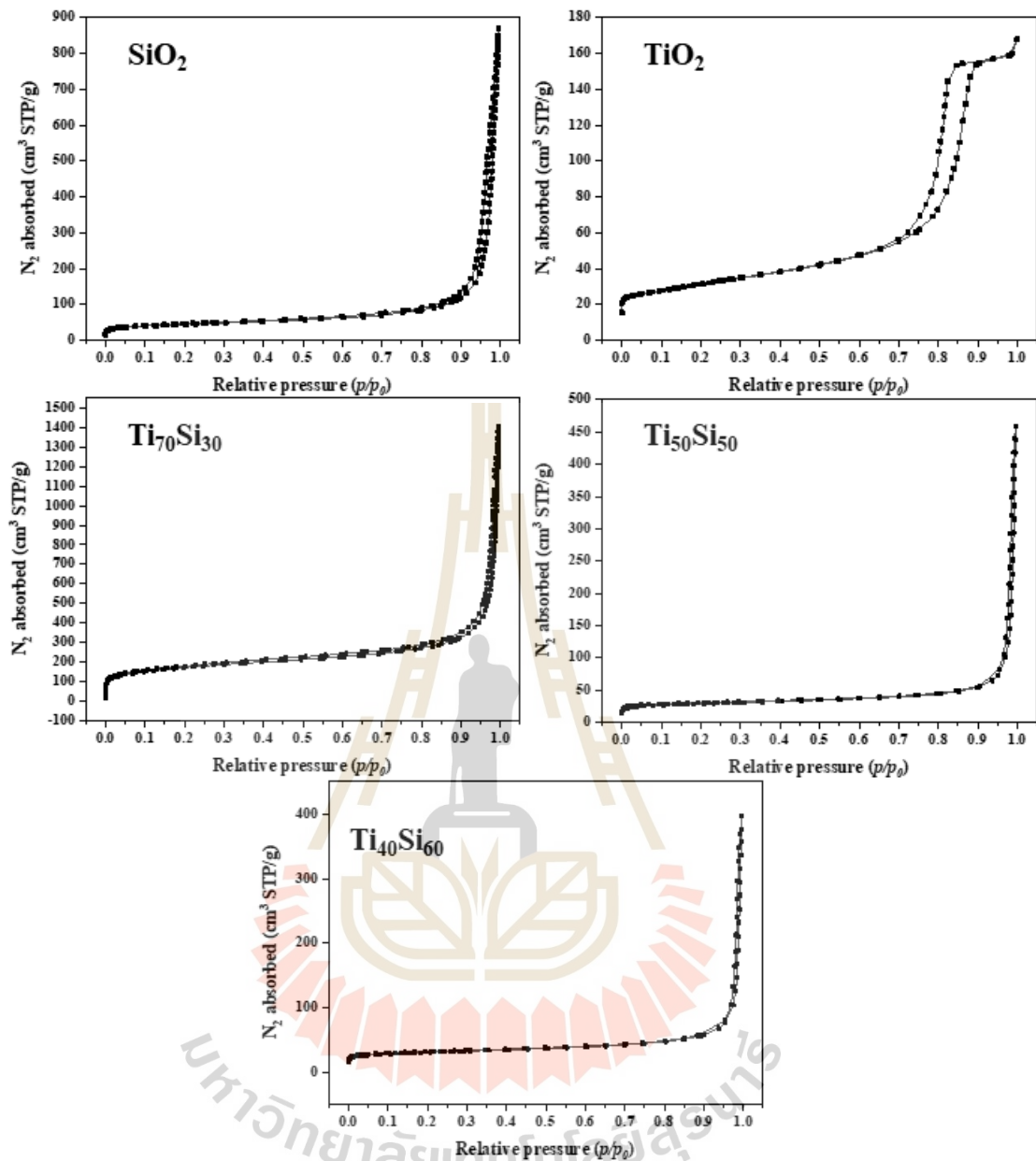


Figure 4.16 Nitrogen adsorption-desorption isotherms of SiO₂, TiO₂, and Ti_xSi_y oxide with different Ti/Si ratio

4.3 The effect of Ti_xSi_y oxide on properties of PLA/Ti_xSi_y composites

4.3.1 Mechanical properties

Tensile properties of PLA, PLA/TiO₂, PLA/SiO₂, PLA/Ti_xSi_y, and PLA/TiO₂SiO₂ composites at various filler contents are list in Table 4.9.

During tensile testing, it was observed that fracture behavior of the film changed of PLA, PLA/TiO₂, PLA/SiO₂, PLA/Ti_xSi_y, and PLA/TiO₂SiO₂ composites. This was demonstrated in the tensile stress-strain curves as shown in Figure 4.17. The composite shows the elastic behavior with adding filler into PLA matrix consequently increasing toughness of PLA. Moreover, the addition of Ti₇₀Si₃₀ oxide slightly increased tensile strength but decreased elongation at break of PLA due to the adding of nanoparticle to polymer matrix was also found to results in a decreased in ductile properties. However, the addition of TiO₂SiO₂ and Ti₄₀Si₆₀ oxide increased elongation at break of PLA. This may be due to the particles of TiO₂SiO₂ in the formulation are homogenously distributed in the polymer matrix contributing to the occurrence of plastic deformations in the whole sample, allowing so higher elongation than that of the pure PLA.

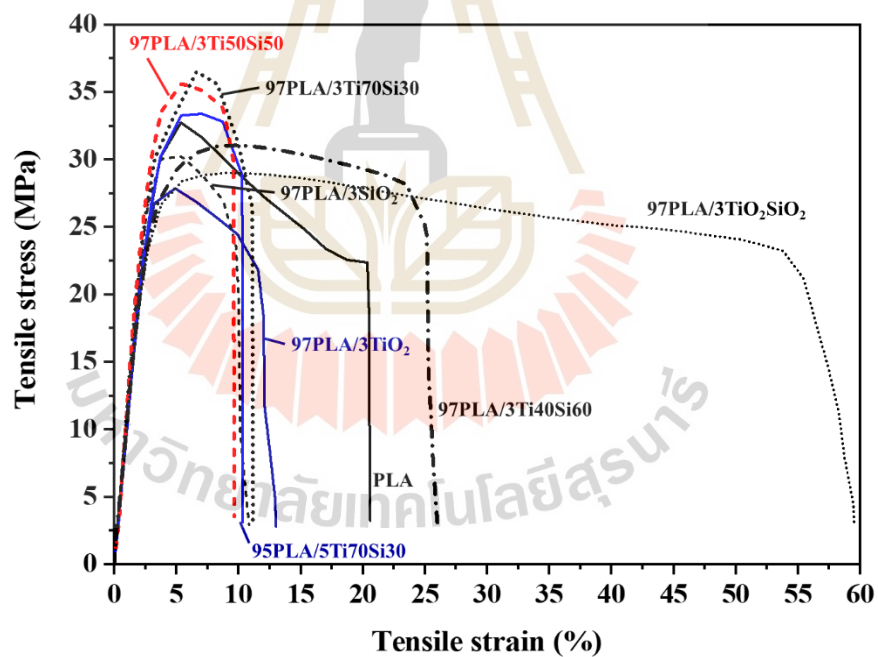


Figure 4.17 Stress-strain curves of PLA, PLA/TiO₂, PLA/SiO₂, PLA/Ti_xSi_y, and PLA/TiO₂SiO₂ composites at various filler contents.

Table 4.9 Tensile properties of PLA, PLA/TiO₂, PLA/SiO₂, PLA/Ti_xSi_y, and PLA/TiO₂SiO₂ composites at various filler contents.

Sample	Tensile strength (MPa)	Elongation at break (%)	Young's Modulus (GPa)
PLA	33.94±1.38	19.62±8.64	0.98±0.23
99PLA/1TiO ₂	27.73±1.54	29.94±7.82	1.03±0.11
97PLA/3TiO ₂	28.22±1.47	18.10±4.24	1.01±0.04
95PLA/5TiO ₂	32.82±2.45	13.60±4.68	1.20±0.08
99PLA/1SiO ₂	29.15±1.54	24.95±8.01	1.05±0.03
97PLA/3SiO ₂	29.75±1.38	11.80±4.96	1.07±0.10
95PLA/5SiO ₂	29.71±1.80	9.70±2.80	1.01±0.08
99PLA/1Ti ₇₀ Si ₃₀	30.57±2.39	21.98±3.36	1.03±0.04
97PLA/3Ti ₇₀ Si ₃₀	35.64±3.21	11.12±1.81	1.18±0.06
95PLA/5Ti ₇₀ Si ₃₀	32.06±2.29	9.88±2.81	1.01±0.10
99PLA/1Ti ₅₀ Si ₅₀	29.16±1.78	9.08±2.75	1.13±0.10
97PLA/3Ti ₅₀ Si ₅₀	35.31±2.01	9.61±2.57	1.29±0.12
95PLA/5Ti ₅₀ Si ₅₀	34.25±0.61	7.44±2.19	1.21±0.10
99PLA/1Ti ₄₀ Si ₆₀	29.22±1.24	32.70±5.35	0.97±0.09
97PLA/3Ti ₄₀ Si ₆₀	30.67±1.74	22.30±2.53	1.02±0.05
95PLA/5Ti ₄₀ Si ₆₀	33.71±2.61	6.86±1.94	1.22±0.08
99PLA/1TiO ₂ SiO ₂	26.43±0.72	29.81±6.17	0.92±0.05
97PLA/3TiO ₂ SiO ₂	29.00±1.42	58.37±5.00	0.96±0.07
95PLA/5TiO ₂ SiO ₂	32.47±1.86	23.85±6.08	1.08±0.14

The addition of 3wt% of Ti₇₀Si₃₀ and Ti₅₀Si₅₀ slightly increased tensile strength and Young's modulus and decreased %elongation at break of PLA composites films compared to neat PLA (Figure 4.18, 4.19, and 4.20). The addition of nanoparticles to polymer matrix was also found to result in a decrease in ductile properties (Chu, Zhao, Li, Fan, and Qin, 2017). With increasing mixed oxide content from 1 to 3 wt.%

resulted in increasing tensile strength of PLA. This is maybe because of a better interfacial adhesion between oxide filler and the PLA matrix by the Van der Waals force or induction interactions and decreased thereafter when adding mixed oxide content up to 5 wt.% but slightly higher than pure PLA. This discontinuity could be attributed to increased filler quantity leading to weaker filler-matrix interface and agglomeration of filler particles, which consequently decreases the tensile strength. However, tensile strength of PLA/TiO₂, PLA/SiO₂, PLA/Ti₄₀Si₆₀, and PLA/TiO₂SiO₂ composites improved with increasing filler content. These results were corresponding to SEM observation. The agglomeration of nanofiller caused high stress concentration leading to great voids during tensile process. Moreover, this great void could progress into cracks resulting in significant reduction in tensile strength of the PLA nanocomposites (Jiang, Liu, and Zhang, 2009). Young's modulus of the PLA composites insignificantly changed with incorporating with Ti_xSi_y oxide (Figure 4.20). However, elongation increased with adding 1wt% of Ti_xSi_y oxide and decreased with increasing mixed oxide contents from 3 to 5 wt.% (Figure 4.19) due to the particles act more as defects inside the polymer matrix, causing the rupture of the sample during the cold drawing and so inhibiting further elongation. So, this resulted in the stiffening and hardening of the composite films were removed shape ductile. Nevertheless, the addition of TiO₂SiO₂ and Ti₄₀Si₆₀ in PLA matrix increased elongation at break of PLA.

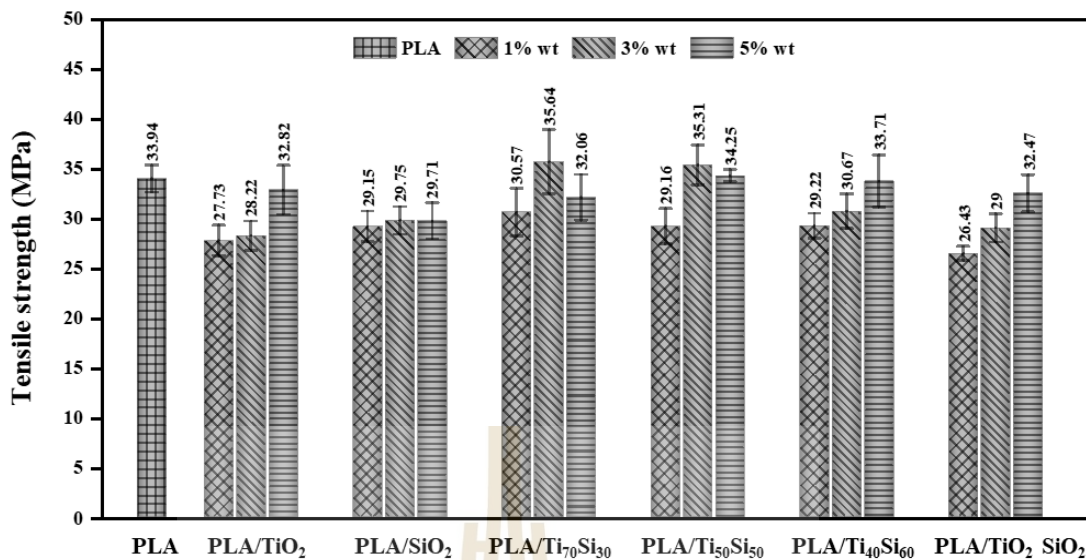


Figure 4.18 Tensile strength of PLA, PLA/TiO₂, PLA/SiO₂, PLA/Ti_xSi_y, and PLA/TiO₂SiO₂ composites at various filler contents.

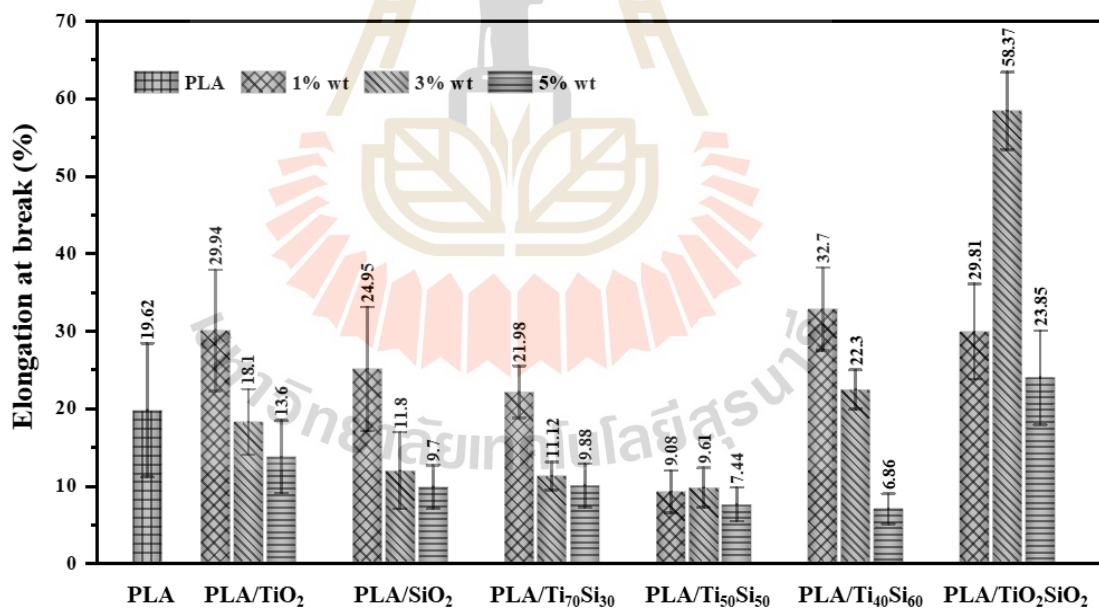


Figure 4.19 Elongation at break of PLA, PLA/TiO₂, PLA/SiO₂, PLA/Ti_xSi_y, and PLA/TiO₂SiO₂ composites at various filler contents.

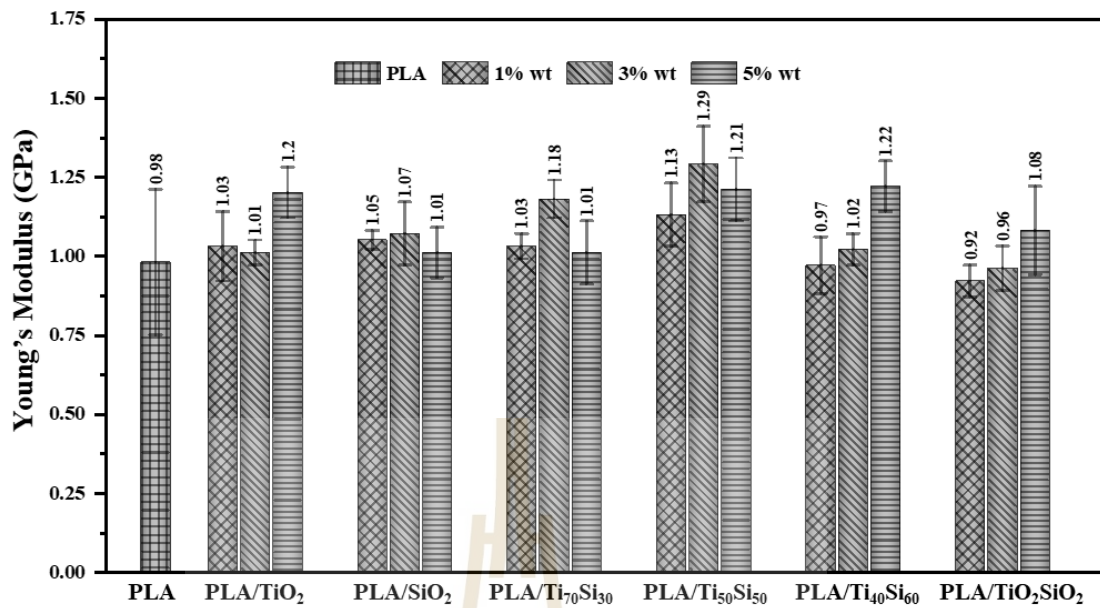


Figure 4.20 Young's modulus of PLA, PLA/TiO₂, PLA/SiO₂, PLA/Ti_xSi_y, and PLA/TiO₂SiO₂ composites at various filler contents.

4.3.2 Thermal properties

The thermal behavior of pure PLA and PLA composites with TiO₂, SiO₂, Ti₇₀Si₃₀, Ti₅₀Si₅₀, Ti₄₀Si₆₀ and TiO₂SiO₂ were detected by differential scanning calorimetry (DSC). The DSC first heating scans (1st heating scans), cooling scans and second heating scans (2nd heating scans) of PLA and PLA composites were performed. DSC thermograms of PLA, PLA/TiO₂, PLA/SiO₂, PLA/Ti_xSi_y, and PLA/TiO₂SiO₂ composites are shown in Figure 4.21, 4.22, and 4.23. Thermal properties of all samples are listed in Table 4.10. Glass transition temperature (T_g), cold crystallization temperature (T_{cc}), and melting temperature (T_m) of the composites were observed.

Table 4.10 Thermal characteristics of PLA and PLA/Ti_xSi_y composites (the second heating, heating rate 5°C/min).

Samples	T _g (°C)	T _{cc} (°C)	ΔH _c (J/g)	T _{m1} (°C)	T _{m2} (°C)	ΔH _m (J/g)	χ _c (%)
PLA	58.87	108.47	36.15	145.84	153.35	31.73	33.86
99PLA/1TiO ₂	59.03	109.10	29.75	146.30	153.39	31.11	33.54
97PLA/3TiO ₂	56.86	107.36	33.61	144.89	152.72	33.17	36.50
95PLA/5TiO ₂	56.93	113.28	31.20	146.29	153.63	29.24	32.85
99PLA/1SiO ₂	58.31	109.64	31.55	146.14	145.90	30.78	33.18
97PLA/3SiO ₂	56.64	109.22	33.06	145.39	145.33	33.31	36.65
95PLA/5SiO ₂	52.31	104.62	33.07	142.88	142.23	32.18	36.15
99PLA/1Ti ₇₀ Si ₃₀	58.61	109.61	30.50	146.22	153.40	31.33	33.77
97PLA/3Ti ₇₀ Si ₃₀	54.81	109.3	34.41	145.07	152.75	32.71	35.99
95PLA/5Ti ₇₀ Si ₃₀	51.84	103.09	26.80	141.29	150.22	32.18	36.15

Table 4.10 Thermal characteristics of PLA and PLA/Ti_xSi_y composites (the second heating, heating rate 5°C/min) (Continued).

Samples	T _g (°C)	T _{cc} (°C)	ΔH _c (J/g)	T _{m1} (°C)	T _{m2} (°C)	ΔH _m (J/g)	χ _c (%)
99PLA/1Ti ₅₀ Si ₅₀	59.07	108.56	33.89	146.50	154.34	30.16	32.51
97PLA/3Ti ₅₀ Si ₅₀	55.96	108.14	33.06	144.41	152.50	34.44	37.89
95PLA/5Ti ₅₀ Si ₅₀	54.03	108.05	33.65	143.82	151.75	32.52	36.53
99PLA/1Ti ₄₀ Si ₆₀	58.23	108.14	33.63	145.91	153.34	33.78	36.42
97PLA/3Ti ₄₀ Si ₆₀	57.40	108.72	34.16	145.33	153.01	33.38	36.73
95PLA/5Ti ₄₀ Si ₆₀	49.01	100.43	25.80	139.31	149.16	32.60	36.62
99PLA/1TiO ₂ SiO ₂	46.7	102.9	31.06	146.14	147.0	28.61	30.84
97PLA/3TiO ₂ SiO ₂	46.6	102.9	32.60	145.39	147.3	32.07	35.28
95PLA/5TiO ₂ SiO ₂	46.6	100.5	37.85	142.88	144.2	40.02	44.96

The neat PLA has T_g at 58.87°C, T_{cc} at 109.47°C, and double T_m at 145.84 and 152.35°C, respectively. The double melting endotherms of neat PLA was explained by the melting and recrystallization. The peak at low temperature was attributed to the melting of the crystals formed during the nonisothermal melt crystallization, while the peak at high temperature was corresponded to re-melting of newly formed crystallite during melting and recrystallization during DSC heating scans (Sarasua, Prud'homme, Wisniewski, Le Borgne, and Spassky, 1998). The T_c of the neat PLA did not appear in the cooling cycle. The addition of TiO_2 , SiO_2 , $Ti_{70}Si_{30}$, $Ti_{50}Si_{50}$, $Ti_{40}Si_{60}$ and TiO_2SiO_2 in PLA matrix show insignificant effect on glass transition temp (T_g), cold crystallization temp (T_{cc}) and melting temp (T_m) of PLA. From cooling scan (Figure 4.22), No the crystallization temperature (T_c) was found of all composites in the cooling cycle. However, with addition 5wt.% of $Ti_{70}Si_{30}$ oxide into PLA only present crystallization temperature peak (T_c) of PLA in the cooling cycle while 1 and 3 wt.% of $Ti_{70}Si_{30}$ oxide did not appear in cooling cycle. Cold crystallization is the re-crystallization phenomena during the heating process of polymer (P. Chen, Zhou, Liu, Zhang, Du, and Wang, 2015). In addition, the cold crystallization behavior (Figure 4.23) of the PLA film containing 3wt.% TiO_2 , SiO_2 , $Ti_{70}Si_{30}$, $Ti_{50}Si_{50}$, $Ti_{40}Si_{60}$ and TiO_2SiO_2 nanoparticles and 5wt.% $Ti_{70}Si_{30}$ was also observed. For neat PLA, there is slightly cold crystallization peak around 109.47°C. While adding 5wt.% of $Ti_{70}Si_{30}$ into PLA, the cold crystallization peak of PLA nanocomposites shifted to lower temperature approximately 5°C, showing that the addition of 5 wt.% of $Ti_{70}Si_{30}$, promoted PLA crystallization. That might be attributed to the increase of the chain mobility of PLA and the Ti_xSi_y oxide could act as efficiency cold crystal nuclei site, consequently increasing crystallinity of PLA. These results suggest that $Ti_{70}Si_{30}$ oxide had a positive effect on the promotion of the crystallization of PLA and could act as nucleating agent. Similar to other results, Chen *et al* (P. Chen, Zhou, Liu, Zhang, Du, and Wang, 2015) found that with incorporating of composite nucleating agent (CNA) to PLA the polymer showed an decrease in the T_{cc} . This indicated that crystallization ability of nanocomposite was enhanced.

The T_m of PLA composites was decreased with addition of 5wt.% $Ti_{70}Si_{30}$. This may due to the heterogeneous nucleation effect of $Ti_{70}Si_{30}$ nanoparticles on PLA

during the crystallization process. The lamella formation of PLA was hindered by $\text{Ti}_{70}\text{Si}_{30}$ nanoparticles and led to less perfect crystals of PLA (R.-y. Chen, Zou, Wu, Jia, Huang, Zhang, Yang, and Qu, 2014). While 3wt.% TiO_2 , SiO_2 , $\text{Ti}_{70}\text{Si}_{30}$, $\text{Ti}_{50}\text{Si}_{50}$, $\text{Ti}_{40}\text{Si}_{60}$ and TiO_2SiO_2 nanocomposites did not significant effect on T_m . The degree of crystallinity (χ_c) of neat PLA significant increases with incorporating TiO_2 , SiO_2 , $\text{Ti}_{70}\text{Si}_{30}$, $\text{Ti}_{50}\text{Si}_{50}$, $\text{Ti}_{40}\text{Si}_{60}$ and TiO_2SiO_2 . This implies that TiO_2 , SiO_2 , $\text{Ti}_{70}\text{Si}_{30}$, $\text{Ti}_{50}\text{Si}_{50}$, $\text{Ti}_{40}\text{Si}_{60}$ and TiO_2SiO_2 nanoparticles can act as a nucleating agent for PLA.

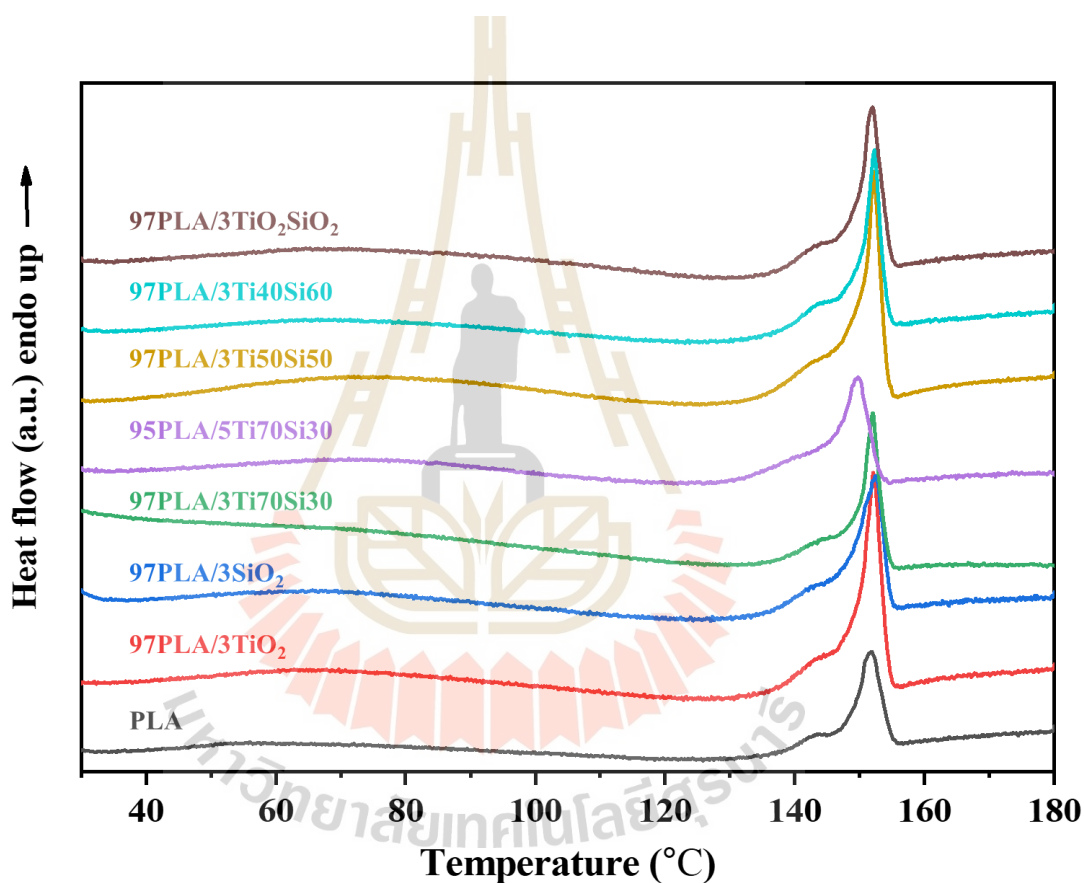


Figure 4.21 DSC thermogram of PLA, PLA/TiO_2 , PLA/SiO_2 , $\text{PLA}/\text{Ti}_x\text{Si}_y$, and $\text{PLA}/\text{TiO}_2\text{SiO}_2$ composites (first heating, heating rate $5^\circ\text{C}/\text{min}$)

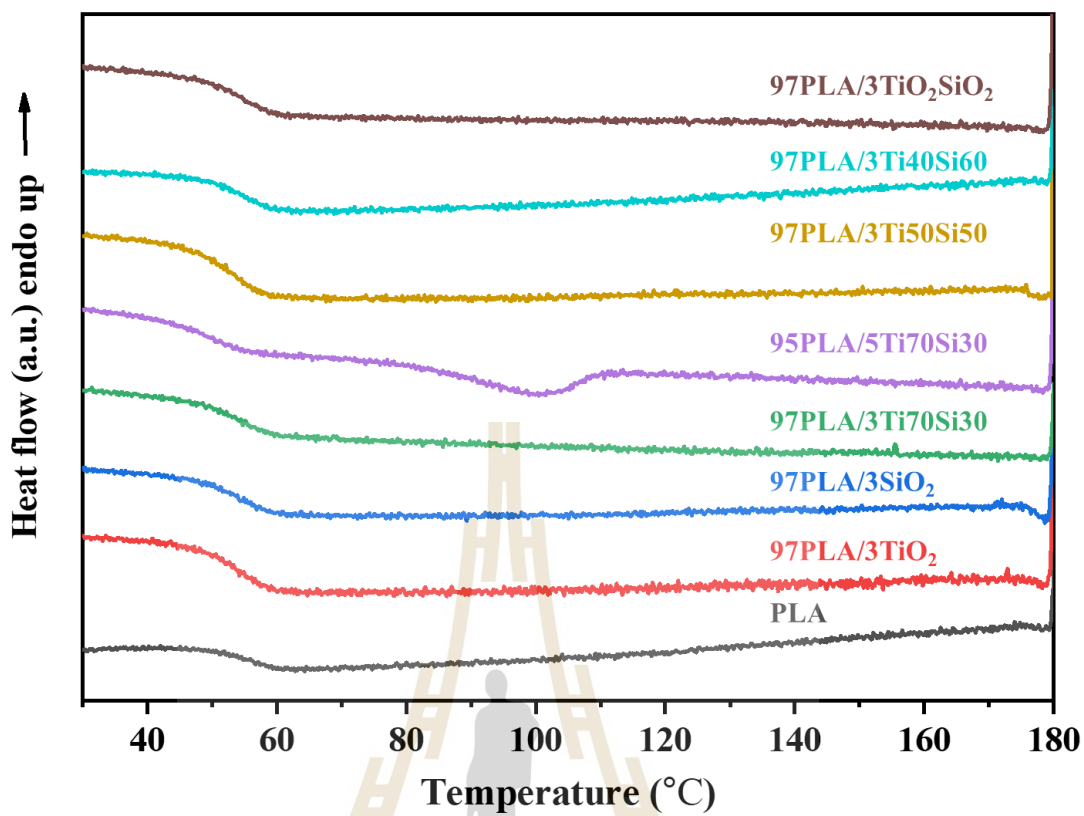


Figure 4.22 DSC thermogram of PLA, PLA/TiO₂, PLA/SiO₂, PLA/Ti_xSi_y, and PLA/TiO₂SiO₂ composites (cooling, cooling rate 5°C/min)

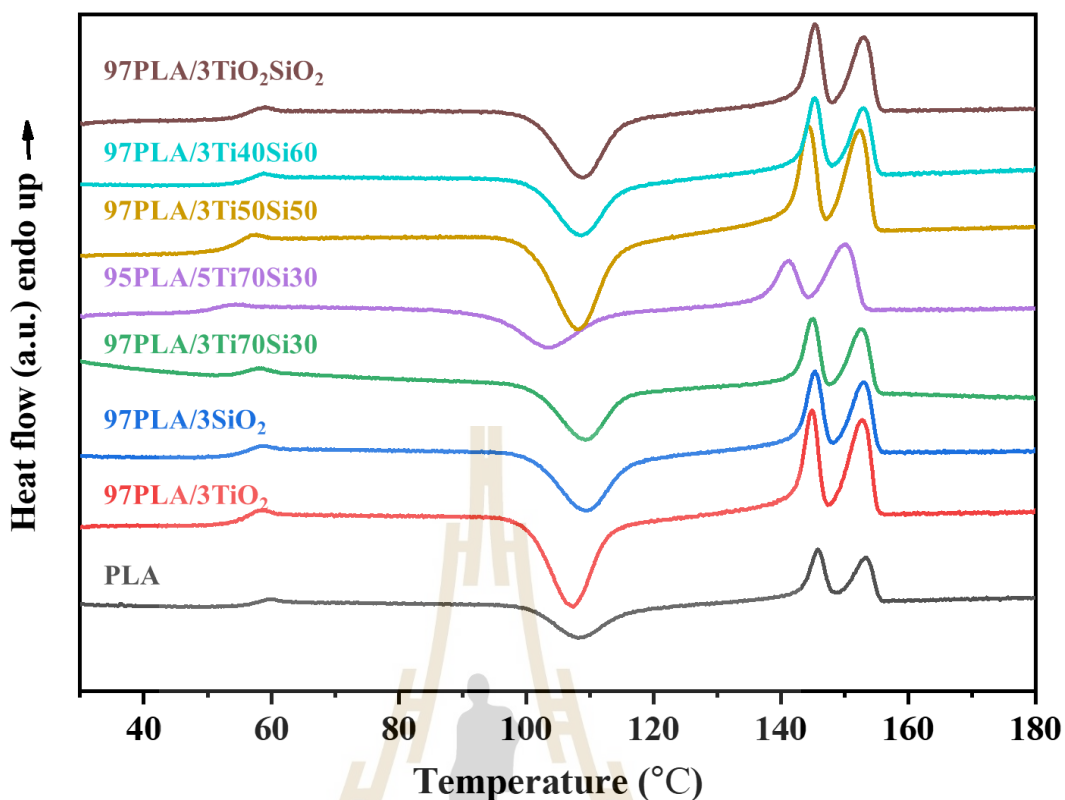


Figure 4.23 DSC thermogram of PLA, PLA/TiO₂, PLA/SiO₂, PLA/Ti_xSi_y, and PLA/TiO₂SiO₂ composites (second heating, heating rate 5°C/min)

TGA and DTG curves of PLA and PLA composites at heating rate 10°C/min are shown in Figure 4.24 and 4.25, respectively. The presence of TiO₂, SiO₂, Ti₇₀Si₃₀, Ti₅₀Si₅₀, Ti₄₀Si₆₀ and TiO₂SiO₂ did not change the thermal decomposition behavior of PLA. The mass loss between 250–365°C was observed, which corresponded to the decomposition of PLA. Then from 365 to 600°C thermal analysis curves slow down to complete the decomposition of PLA matrix until a constant mass was reached. The constant mass remaining at the end of each TGA experiment corresponded to amounts of nanoparticles in PLA nanocomposites. Thermal degradation at 5% weight loss ($T_{0.05}$), 50% weight loss ($T_{0.5}$), decomposition temperature (T_d), final degradation (T_f) and the char formation at 800°C of PLA and PLA composites are presented in Table 4.11. In this work, the onset degradation temperature (T_{onset}) was defined by the temperature at 5% weight loss ($T_{0.05}$) to determine the effect of

TiO₂, SiO₂ and Ti_xSi_y oxide on the thermal stability of PLA composites. It was clear that the T_{onset} of PLA composite shifted to a higher temperature with the presence of 3wt.% of TiO₂, SiO₂, Ti₅₀Si₅₀, Ti₄₀Si₆₀ and TiO₂SiO₂. Consequently, the thermal stability of PLA composites was improved. One of the possible reasons for this behavior is that TiO₂, SiO₂, Ti₅₀Si₅₀, Ti₄₀Si₆₀ and TiO₂SiO₂ particles may acted as heat barrier in the early staged of thermal decomposition (A. Buzarovska and Grozdanov, 2012). Similar data has been reported by Zhang et al., who studied the nanocomposite obtained by adding TiO₂ to poly (lactic acid) (Zhang, Huang, Yang, Chen, Zou, Lin, and Qu, 2015). However, PLA adding 3wt.% of Ti₇₀Si₃₀ oxide present a lower onset temperature than those of pure PLA resulting in a decreased of thermal stability of PLA. In addition, the onset degradation temperature of nanocomposites shifted to a lower temperature with increasing Ti₇₀Si₃₀ oxide nanoparticles loading from 1 to 5 %wt. This suggest that there was maybe a degradation due to water absorption of filler that would be associated with the cleavage of the chain of PLA at ester group (–C–O–) by water molecules due to hydrolysis leading to decreased thermal stability of PLA.

Moreover, the peak in DTG curves represented the temperature maximum degradation rate. PLA/3TiO₂ exhibit the fastest degradation rate at highest temperature compared to neat PLA and other composites. However, the degradation temperature of PLA/Ti₇₀Si₃₀ composite shifted to lower temperature. This suggested that thermal stability of PLA was decreased with the incorporating of Ti₇₀Si₃₀ loading. In addition, when 3 wt.% TiO₂, SiO₂, Ti₇₀Si₃₀, Ti₅₀Si₅₀, Ti₄₀Si₆₀, TiO₂SiO₂, and 5 wt.% Ti₇₀Si₃₀ oxides were added into PLA, the composites left the char residual of nanoparticle at 4.07, 4.14, 3.91, 4.22, 3.53, 4.50 and 5.46%, respectively for PLA nanocomposites. The char residual generally depends on the amount of added nanoparticles (Aleksandra Buzarovska, 2013).

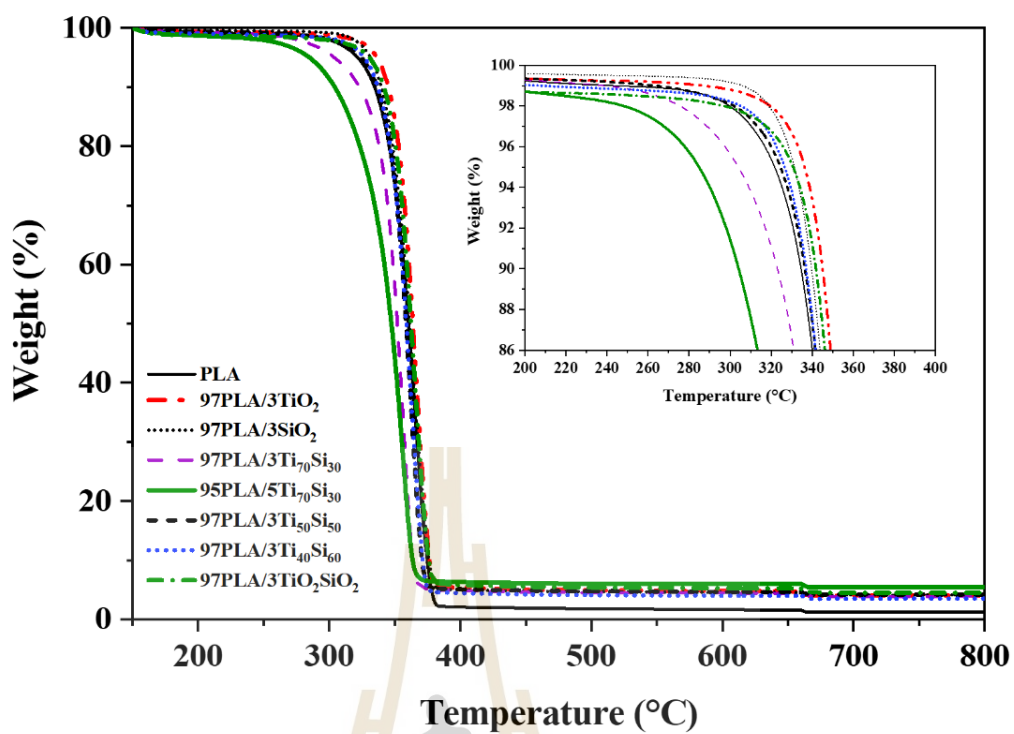


Figure 4.24 TGA thermogram of DSC thermogram of PLA, PLA/TiO₂, PLA/SiO₂, PLA/Ti_xSi_y, and PLA/TiO₂SiO₂ composites.



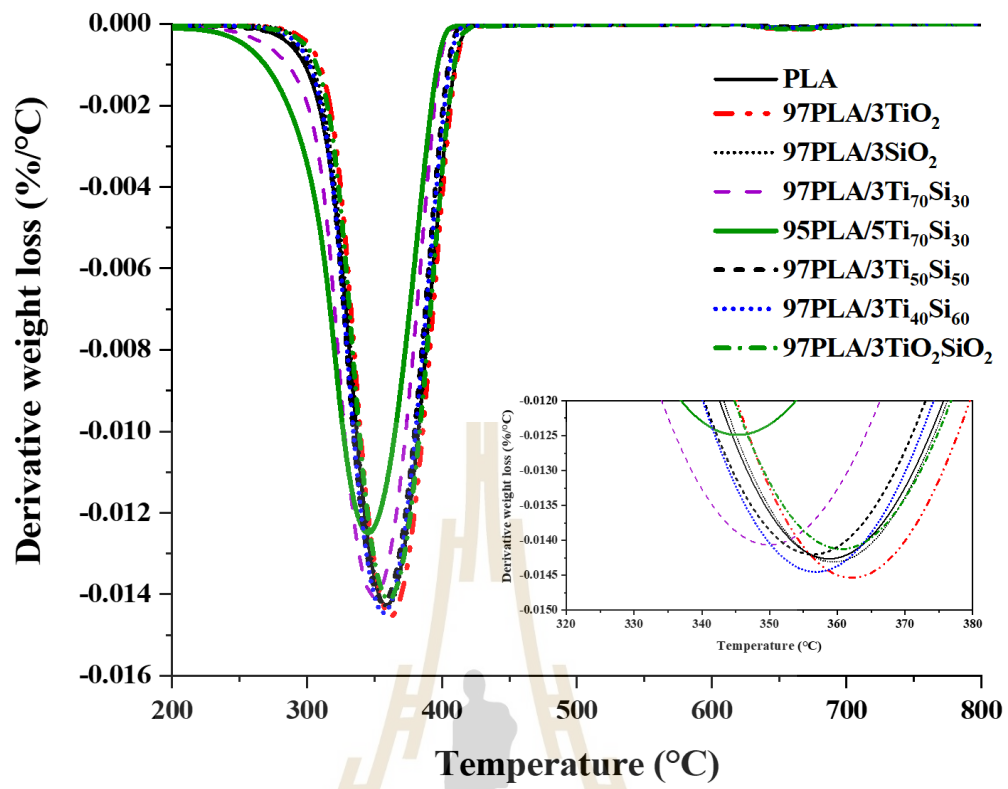


Figure 4.25 DTG Thermogram of PLA, PLA/TiO₂, PLA/SiO₂, PLA/Ti_xSi_y, and PLA/TiO₂SiO₂ composites.

Table 4.11 Thermal degradation temperature of PLA, PLA/TiO₂, PLA/SiO₂, PLA/Ti_xSi_y, and PLA/TiO₂SiO₂ composites

Samples	T _{0.05} (°C)	T _{0.5} (°C)	T _d (°C)	T _f (°C)	Char residual (%)
PLA	321.67	360.33	358.83	424.64	1.20
97PLA/3TiO ₂	336.17	363.67	363.17	429.22	4.07
97PLA/3SiO ₂	331.17	361.17	359.33	427.27	4.14
97PLA/3Ti ₇₀ Si ₃₀	304.00	351.83	350.17	408.68	3.91
95PLA/5Ti ₇₀ Si ₃₀	284.50	347.33	346.33	407.16	5.46
97PLA/3Ti ₅₀ Si ₅₀	324.50	358.36	356.50	425.49	4.22
97PLA/3Ti ₄₀ Si ₆₀	326.50	358.67	356.83	416.83	3.53
97PLA/3TiO ₂ SiO ₂	330.67	362.33	361.33	418.69	4.50

4.3.3 Morphological property

In order to investigate the dispersion and distribution of TiO_2 , SiO_2 , $\text{Ti}_{70}\text{Si}_{30}$, $\text{Ti}_{50}\text{Si}_{50}$, $\text{Ti}_{40}\text{Si}_{60}$ and TiO_2SiO_2 in the PLA composites films, SEM analysis was performed. SEM micrographs of the fracture surface of PLA and PLA adding 3wt.% TiO_2 , SiO_2 , $\text{Ti}_{70}\text{Si}_{30}$, $\text{Ti}_{50}\text{Si}_{50}$, $\text{Ti}_{40}\text{Si}_{60}$ and TiO_2SiO_2 and 5wt.% $\text{Ti}_{70}\text{Si}_{30}$ are shown in Figure 4.26 and the surface of PLA and PLA composites films after tensile test are shown in Figure 4.26.

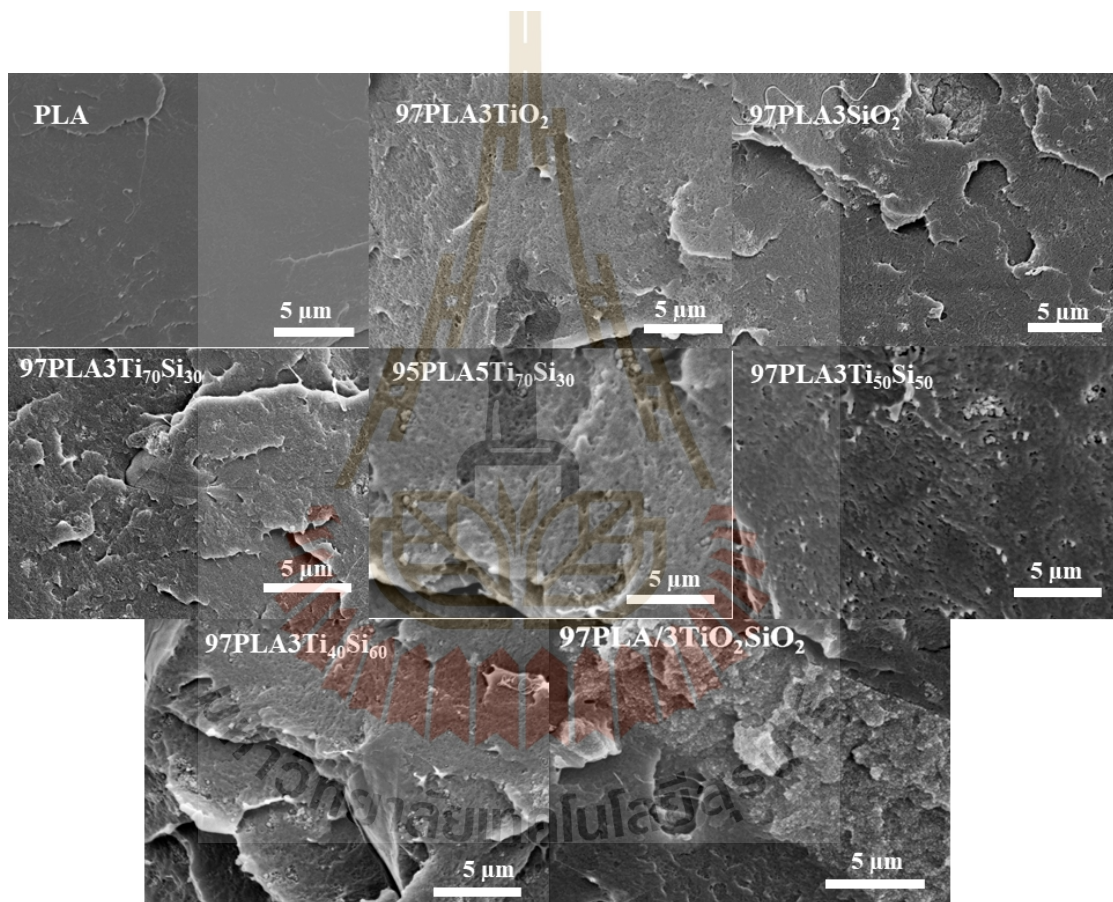
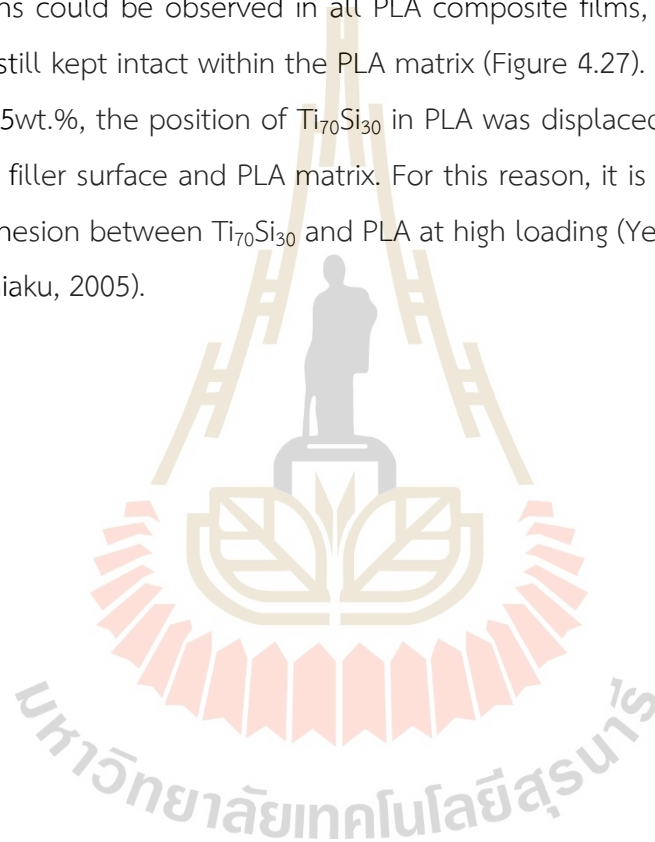


Figure 4.26 SEM micrographs of the fracture surface of PLA, PLA/ TiO_2 , PLA/ SiO_2 , PLA/ Ti_xSi_y , and PLA/ TiO_2SiO_2 composites.

The SEM results showed that relatively brittle and comparatively flat without hole and air bubble surface was found on the fracture surface of pure PLA films. While SEM images of all PLA composites exhibited roughness causing by adding

3wt.% of TiO_2 , SiO_2 , $\text{Ti}_{70}\text{Si}_{30}$, $\text{Ti}_{50}\text{Si}_{50}$, $\text{Ti}_{40}\text{Si}_{60}$ and TiO_2SiO_2 nanoparticles particularly at 3wt.% of TiO_2SiO_2 (Figure 4.26). The enhancement of mechanical properties depend on absence voids, undamaged position of fillers, interfacial bonding between fillers and matrix, and absence of agglomerate of fillers (Garlotta, Doane, Shogren, Lawton, and Willett, 2003). However, the white spots in PLA composites micrographs illustrated the agglomerated of TiO_2 , SiO_2 , $\text{Ti}_{70}\text{Si}_{30}$, $\text{Ti}_{50}\text{Si}_{50}$, $\text{Ti}_{40}\text{Si}_{60}$ and TiO_2SiO_2 in PLA matrix leading to made it poor mechanical properties. In this work, although some agglomerations could be observed in all PLA composite films, 3wt.% of $\text{Ti}_{70}\text{Si}_{30}$, and $\text{Ti}_{50}\text{Si}_{50}$ were still kept intact within the PLA matrix (Figure 4.27). As $\text{Ti}_{70}\text{Si}_{30}$ loading was increased to 5wt.%, the position of $\text{Ti}_{70}\text{Si}_{30}$ in PLA was displaced leading formation of gap between filler surface and PLA matrix. For this reason, it is an indication for poor interfacial adhesion between $\text{Ti}_{70}\text{Si}_{30}$ and PLA at high loading (Yew, Mohd Yusof, Mohd Ishak, and Ishiaku, 2005).



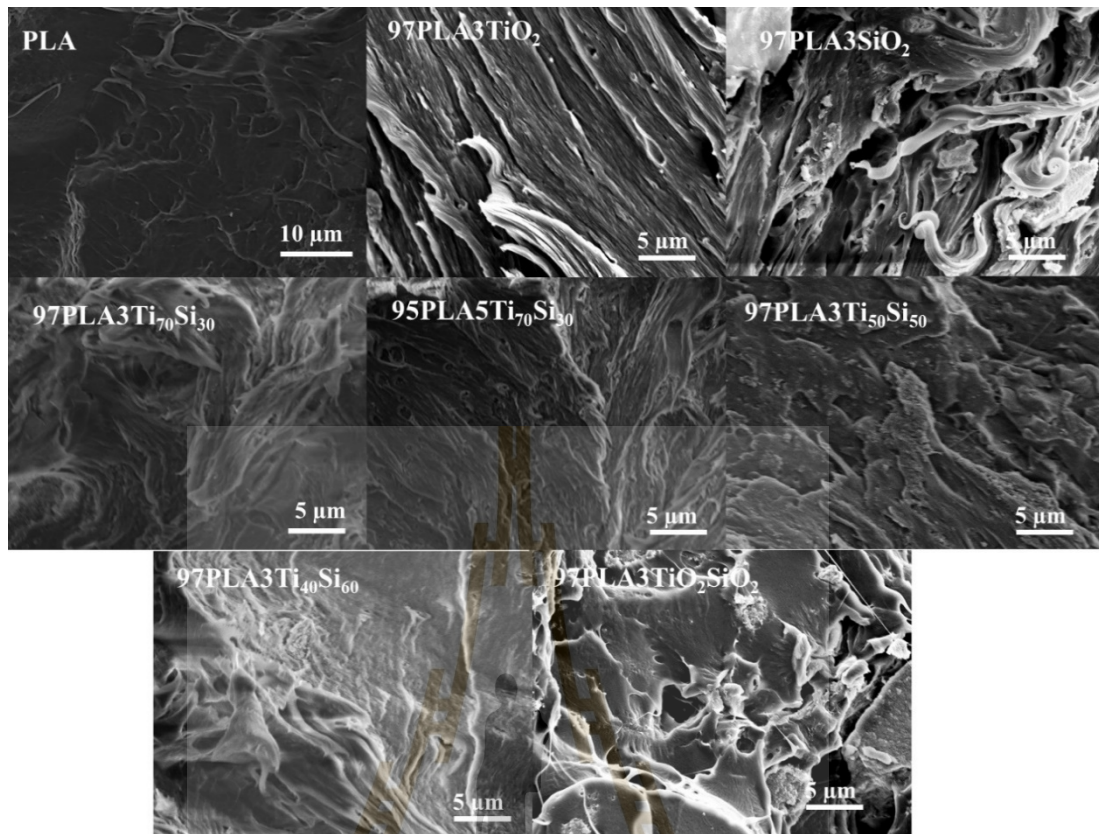


Figure 4.27 SEM micrographs after tensile testing of PLA, PLA/TiO₂, PLA/SiO₂, PLA/Ti_xSi_y, and PLA/TiO₂SiO₂ composites.

4.3.4 Water vapor transmission rate (WVTR)

One of the most important properties of bio-based composites films is to evaluate moisture transfer from the environment to product. The WVTR of the PLA and PLA nanocomposite films is shown in Figure 4.28. The WVTR of PLA films was $0.316 \text{ g m}^{-2} \text{ day}^{-1}$ and it was lower than PLA films incorporating with 3wt.% SiO₂, and Ti₇₀Si₃₀, and Ti₅₀Si₅₀ which are 1.000, 1.023 and $0.523 \text{ g m}^{-2} \text{ day}^{-1}$. In addition, the WVTR of the PLA/Ti₇₀Si₃₀ composite film increased with increasing Ti₇₀Si₃₀ content to 5wt.%. It is common that for a solid polymer, the water vapor transmission follows a simple mechanism including adsorbing at the entering face, dissolving and rapidly creating equilibrium, diffusing through the film, and desorbing at the exit face (Hu, Topolkaev, Hiltner, and Baer, 2001). The low particle diameter of nanoparticles would lead to more indirect pathway reducing the diffusion coefficient (Choudalakis and Gotsis, 2009;

Tantekin-Ersolmaz, Atalay-Oral, Tatlier, Erdem-Şenatalar, Schoeman, and Sterte, 2000). Consequently, hydrophilicity of PLA nanocomposite incorporating with SiO_2 , and $\text{Ti}_{70}\text{Si}_{30}$, and $\text{Ti}_{50}\text{Si}_{50}$ was improved.

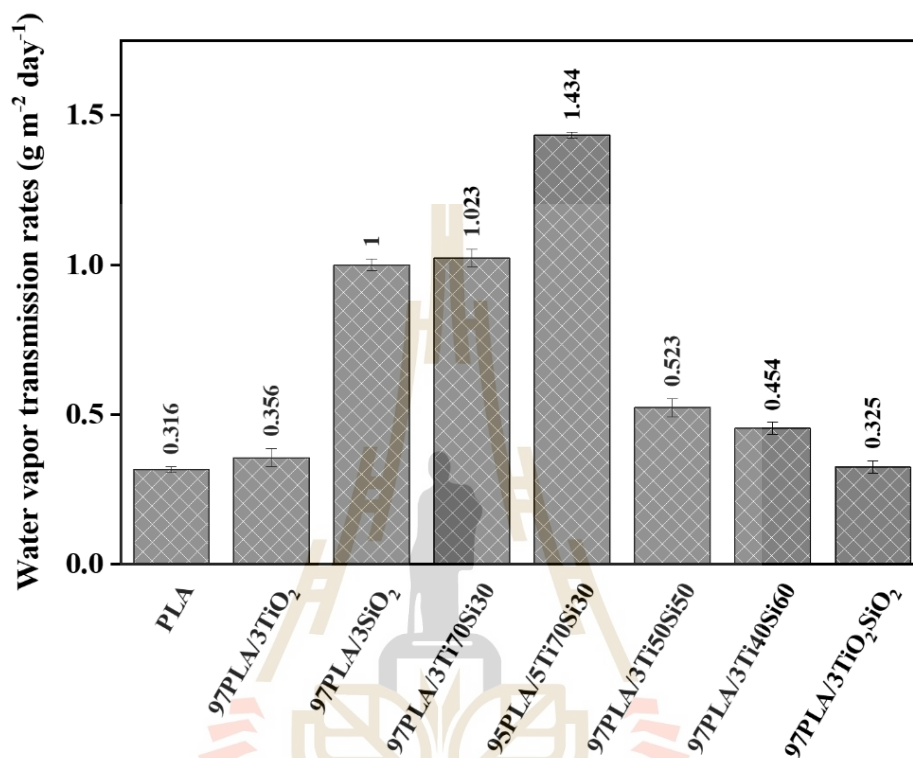


Figure 4.28 Water vapor transmission rate (WVTR) of PLA, PLA/TiO₂, PLA/SiO₂, PLA/Ti_xSi_y, and PLA/TiO₂SiO₂ composites.

4.3.5 Photocatalytic degradation of methylene blue (MB)

Photocatalytic activity of PLA, PLA/TiO₂, PLA/SiO₂, PLA/Ti_xSi_y, and PLA/TiO₂SiO₂ composites films was investigated by degrading methylene blue (MB) in this work. Due to UV irradiation may also lead to decomposition of MB without presence of any photocatalyst.

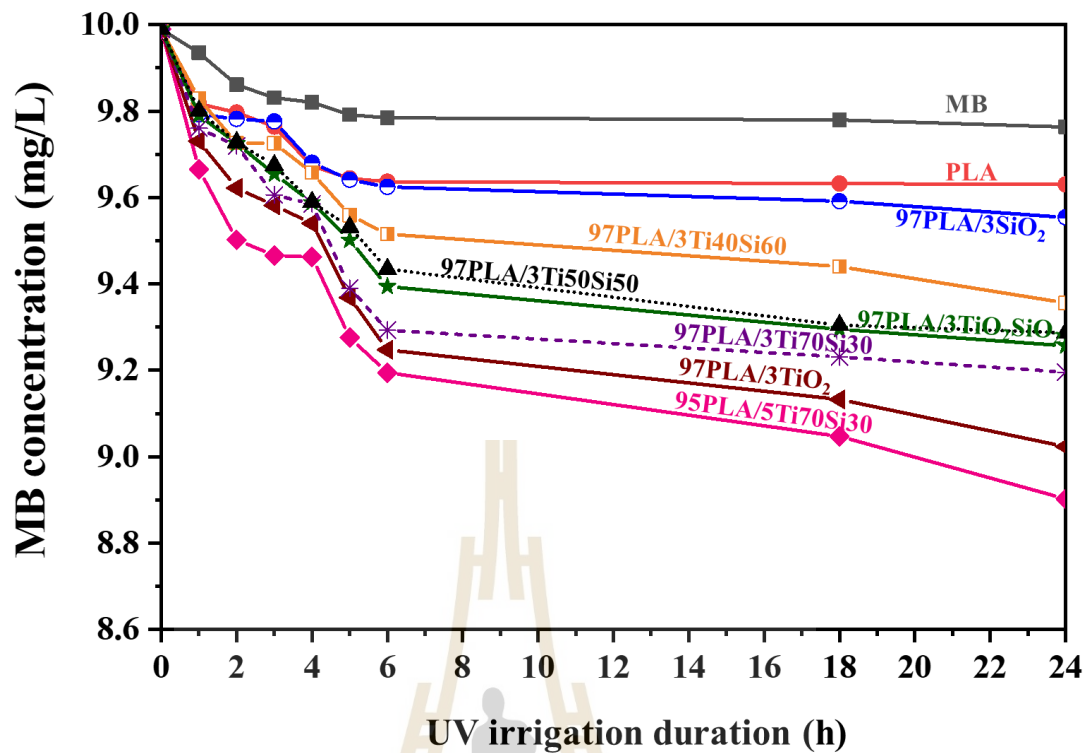
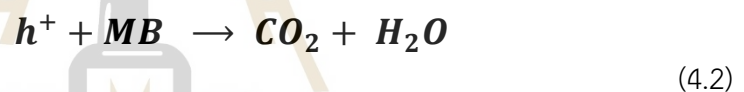
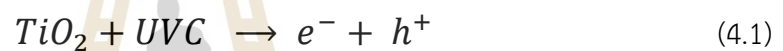


Figure 4.29 Concentration of methylene blue (MB) due to absorption of PLA, PLA/TiO₂, PLA/SiO₂, PLA/Ti_xSi_y, and PLA/TiO₂SiO₂ composites films under UV irradiation.

Figure 4.29 shows the change in concentration of MB in aqueous solution under UV irradiation led it a decomposition of MB. Presence of 3wt.% TiO₂, SiO₂, Ti₇₀Si₃₀, Ti₅₀Si₅₀, Ti₄₀Si₆₀ and TiO₂SiO₂ in PLA film matrix exhibited more efficiency to degrade MB than using only photocatalysis. Efficiency to degrade MB is TiO₂ > Ti₇₀Si₃₀ > TiO₂SiO₂ > Ti₅₀Si₅₀ > Ti₄₀Si₆₀ > SiO₂, respectively. Also, increase of Ti₇₀Si₃₀ loading to 5wt.% improved efficiency of photocatalytic activity of PLA. The photo-activity of mixed oxide was evidently increased because the high content of mixed oxide increasing surface area of filler effectively concentrated MB around the nanoparticle and produced high concentrations of organic compounds for the photocatalysis, consequently, improved photocatalytic activity of PLA. It is well known that photocatalytic activity occurs at the surface photocatalyst. Therefore, surface area of PLA composites film, which in turn depends on size of nanoparticles, film morphology

and thickness, has an effect on photocatalytic reactivity (L. Chen, Zheng, and Liu, 2017). The PLA composite film contained TiO_2 have more efficiency to degrade MB than using only photocatalysis because of the two mechanisms of degradation including the first, MB can be degraded directly by UVC and the second, TiO_2 received light energy more than band-gap energy and then electron in valence band (VB) is excited to conduction band (CB) resulting in generated hole (h^+) (Eq. 4.1). This hole can oxidize MB (Eq. 4.2) or oxidized H_2O to produce OH (Eq. 4.3). the e^- in CB can reduced O_2 at surface of TiO_2 to generate O_2^- (Eq. 4.4). The appearance of radical (OH, O_2^-) and h^+ reacted with MB to generating peroxide derivative and hydroxylate or degrading complete to CO_2 and H_2O (L. Chen, Zheng, and Liu, 2017). The photodegradation mechanism can be summarized by eq 4.1-4.4.



The presence of filler in PLA film matrix show more efficiency to degrade MB than using only photocatalysis. This was due to the photocatalytic activity is influenced by crystal structure, particle size, specific surface area, and porosity of nanoparticle. So, ultrafine powders of mixed oxide show a good catalytic activity. However, agglomeration often takes place, resulting in reduction or even complete loss of photocatalytic activity.

Because of its photocatalytic activity, $\text{Ti}_{70}\text{Si}_{30}$ nanoparticle with high specific surface area ($569 \text{ m}^2\text{g}^{-1}$) can degrade MB, making it a suitable material for photocatalytic application.

4.3.6 Light transmittance and opacity measurements

UV light can create free radicals in products by photochemical reaction leading to negative effect for food. Some of unfriendly effects include deterioration of antioxidants, destruction to vitamins and proteins and changed in color. UV radiation is classified into UV-A (wavelength 320–400 nm), UVB (280–320 nm), and UV-C (200–280 nm) (Asmatulu, Mahmud, Hille, and Misak, 2011; Oleyaei, Zahedi, Ghanbarzadeh, and Moayedi, 2016). Addition of TiO_2 , SiO_2 , $\text{Ti}_{70}\text{Si}_{30}$, $\text{Ti}_{50}\text{Si}_{50}$, $\text{Ti}_{40}\text{Si}_{60}$ and TiO_2SiO_2 into PLA matrix caused a significantly decrease of transmittance in all UV regions (Table 4.12). The results show that the addition of filler into PLA matrix caused a significantly decrease of transmittance of all UV regions. Presence of 3wt.% $\text{Ti}_{70}\text{Si}_{30}$ in PLA film matrix succeed to block more than 99.6% of 240, 300, and 360 nm wavelengths as a representative of UV-C, UV-B, and UV-A radiation, respectively with low opacity of composite film. Moreover, with increasing $\text{Ti}_{70}\text{Si}_{30}$ oxide loading up to 5wt.% into PLA improved UV blocking efficiency.

The PLA films were transparent and colorless, and SiO_2 addition remained a transparent of PLA, while other PLA composite films showed higher opacity than pure PLA film. However, the transparency changed related to increasing $\text{Ti}_{70}\text{Si}_{30}$ oxide contents from 3 up to 5wt.% provided totally opaque films by more than 2 orders of magnitudes in opacity films but still lower than composite film of PLA adding TiO_2 . Similarly, increase of TiO_2 and $\text{Ti}_{70}\text{Si}_{30}$ loading made the PLA composites color appear whiter because of the characteristic whiteness of TiO_2 and $\text{Ti}_{70}\text{Si}_{30}$ nanoparticle. Photographs of PLA, PLA/ TiO_2 , PLA/ SiO_2 , PLA/ Ti_xSi_y , and PLA/ TiO_2SiO_2 composites films are shown in Figure 4.30. These results suggest that the PLA composite produced with $\text{Ti}_{70}\text{Si}_{30}$ oxide was suitable applied to transparency packaging applying with good UV-blocking efficiency.



Figure 4.30 Photographs of films prepared from PLA, PLA/TiO₂, PLA/SiO₂, PLA/Ti_xSi_y, and PLA/TiO₂SiO₂ composites (250-300 μm thickness).



Table 4.12 Transmittance (%) and opacity values of PLA, PLA/TiO₂, PLA/SiO₂, PLA/Ti_xSi_y, and PLA/TiO₂SiO₂ composites films in the visible, UV-A, UV-B, and UV-C regions.

Sample	Transmittance (%)				Opacity (AU.nm.mm)
	UVC (240nm)	UVB (300nm)	UVA (360nm)	Visible (600nm)	
PLA	1.24	24.47	34.77	51.39	1.16
97PLA/3TiO ₂	0.00	0.12	0.41	1.98	6.81
97 PLA /3SiO ₂	0.04	9.48	18.03	38.37	2.31
97 PLA /3Ti ₇₀ Si ₃₀	0.00	0.28	0.75	14.00	3.42
95 PLA /5Ti ₇₀ Si ₃₀	0.00	0.00	0.36	4.06	6.33
97 PLA /3Ti ₅₀ Si ₅₀	0.00	0.32	2.37	15.65	4.74
97 PLA /3Ti ₄₀ Si ₆₀	0.00	0.03	0.81	10.48	3.92
97 PLA /3TiO ₂ SiO ₂	0.00	0.19	1.43	7.30	4.74

4.3.7 Hydrolytic degradation

Figure 4.31 shows the percent weight loss of PLA, PLA/TiO₂, PLA/SiO₂ and PLA/Ti_xSi_y composite films as a function of degradation time in hydrolytic test. The degradation of PLA film was complete about 1200 min, while all of PLA nanocomposite films were hydrolyzed faster than neat PLA. Interestingly, PLA incorporating with 3wt.% TiO₂, SiO₂, Ti₇₀Si₃₀, Ti₅₀Si₅₀, Ti₄₀Si₆₀ and TiO₂SiO₂ exhibited much higher weight loss as a function of time than neat PLA. The presence of filler induced much more apparent change of weight loss of hydrolytic degradation, indicating the enhancement of hydrolytic degradation ability of PLA matrix. This was due to adding nanoparticles help to accelerate the hydrolytic degradation of PLA matrix. 97PLA/3TiO₂, 97PLA/3SiO₂, 97PLA/3Ti₇₀Si₃₀, 97PLA/3Ti₅₀Si₅₀, 97PLA/3Ti₄₀Si₆₀ and 97PLA/3TiO₂SiO₂ were fully degraded at 840, 300, 420, 420, and 560 min, respectively. Moreover, it can be observed that PLA composite containing 5wt.% of Ti₇₀Si₃₀ degraded faster than all the PLA composites and it is fully degraded already about 240 min. Consequently, it could be concluded that the rate of hydrolytic degradation of PLA composites films can be controlled by filler content. This result is in agreement with Buzarovka and Grozdanov (2012) (A. Buzarovska and Grozdanov, 2012).



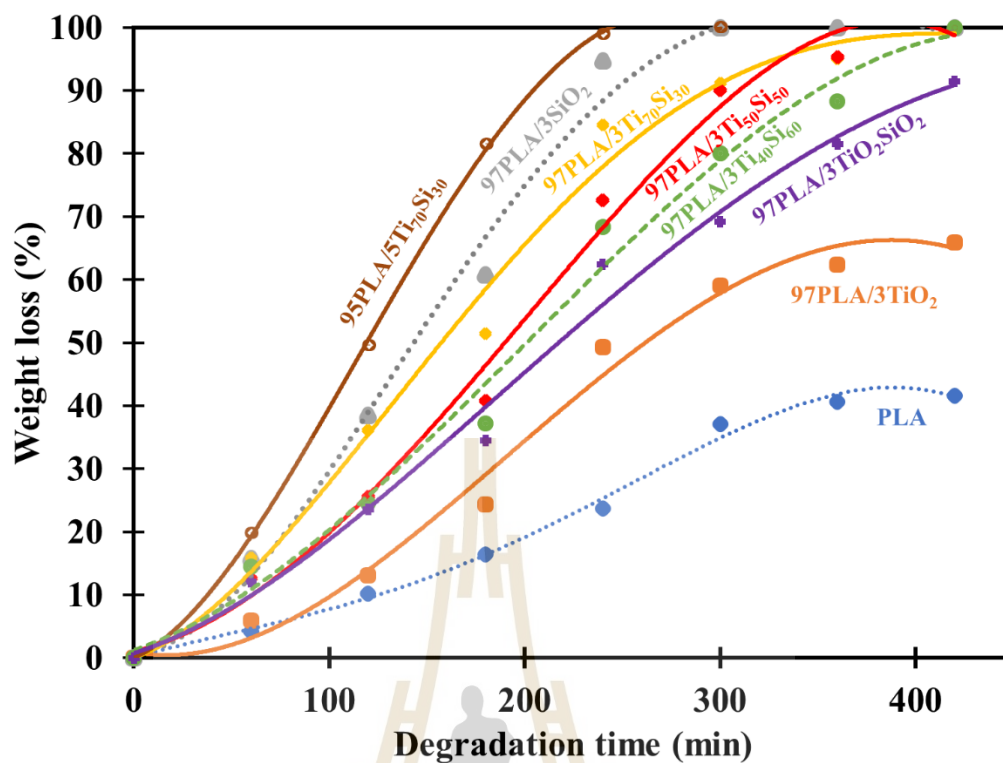


Figure 4.31 Weight loss of hydrolytic degradation of PLA, PLA/TiO₂, PLA/SiO₂ and PLA/Ti_xSi_y composite films as functions of degradation time.

4.3.8 *In vitro* degradation

The degradation of PLA in PLA composites includes several main processes such as water uptake, ester cleavage and formation of oligomer fragments, dissolution of oligomer fragment, etc (Sinha Ray, Yamada, Okamoto, and Ueda, 2002). Then, the factors that affect the hydrolysis tendency of PLA would control the degradation of PLA. The long-term hydrolytic degradation of PLA and PLA nanocomposite films in a phosphate buffered saline (PBS) (pH = 7.4 ± 0.2) solution at 37°C was evaluated by mass loss in 56 days.

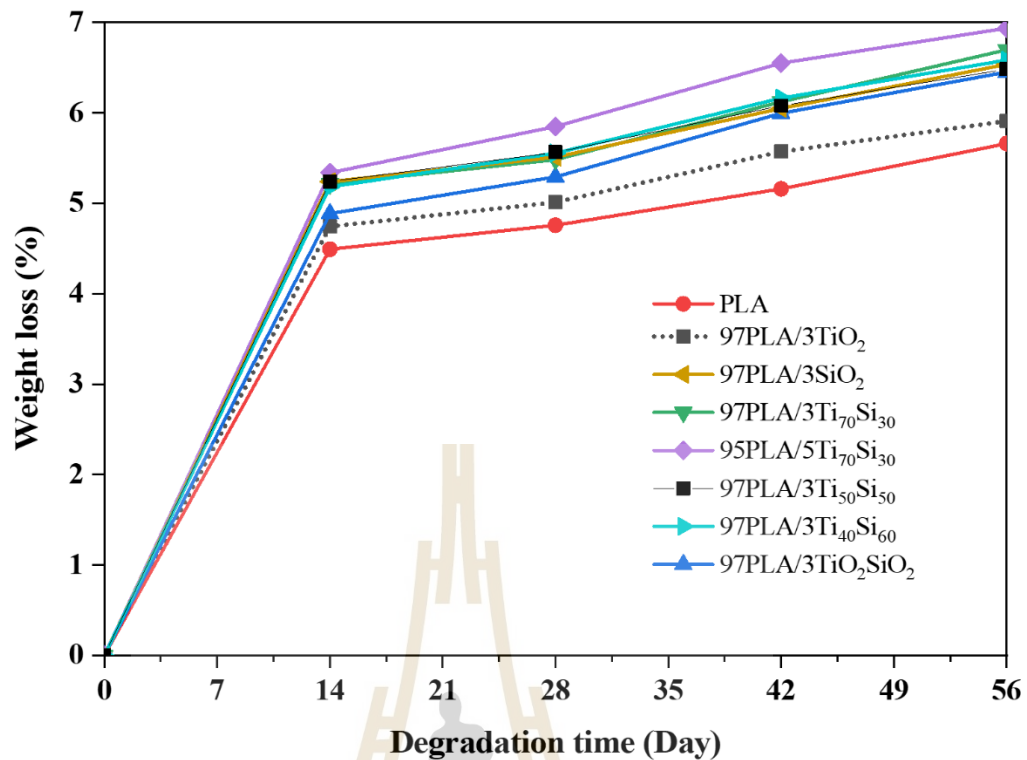


Figure 4.32 Weight loss of PLA, PLA/TiO₂, PLA/SiO₂ and PLA/Ti_xSi_y composite films after different periods of *in vitro* degradation.

Figure 4.32 shows the mass loss of PLA, PLA/TiO₂, PLA/SiO₂ and PLA/Ti_xSi_y composite films with the time of degradation. From 0 to 14 days, all of samples exhibited a dramatic increase in mass loss with increasing immersion time. After this period, the mass loss of all samples accelerated gradually. PLA incorporating with 3wt.% TiO₂, SiO₂, Ti₇₀Si₃₀, Ti₅₀Si₅₀, Ti₄₀Si₆₀, and TiO₂SiO₂ exhibited higher weight loss as a function of immersion time than neat PLA. In this case, TiO₂, SiO₂, Ti₇₀Si₃₀, Ti₅₀Si₅₀, Ti₄₀Si₆₀, and TiO₂SiO₂ dispersed in the PLA matrix, the water molecules penetrated more easily with in the samples to generate the degradation process. The water might be absorbed in the gap between the conglomeration of nanoparticles due to the agglomeration of nanofiller. Consequently, they would employ much time on diffusing into PLA matrix. Therefore, the degradation rate increased in the first period and reached maximum (Luo, Wang, and Wang, 2012). In addition, the mass loss of PLA composite was also found to increase with increasing Ti₇₀Si₃₀ to 5wt.%. Consequently,

it could be concluded that the rate of long-term degradation of PLA composites films dependent upon the content of mixed oxide loading. This result was connected to the hydrophilicity of TiO_2 , SiO_2 , $\text{Ti}_{70}\text{Si}_{30}$, $\text{Ti}_{50}\text{Si}_{50}$, $\text{Ti}_{40}\text{Si}_{60}$, and TiO_2SiO_2 as well as the high-water absorption of nanocomposites (Kaseem, Hamad, and Ur Rehman, 2019).

The changes in the tensile strength, elongation at break and Young's modulus of PLA, PLA/ TiO_2 , PLA/ SiO_2 and PLA/ Ti_xSi_y composite films are shown in Figure 4.33, 4.34, and 4.35. These figures showed that the tensile strength and elongation at break of PLA and all of PLA composite films decreased significantly after 28 days of *in vitro* degradation. This result suggested that the PLA and PLA composite films were mechanically stable during 28 days of *in vitro* degradation. The tensile strengths of the PLA and PLA composites decreased after 28 days of degradation with microcracks appearing on part of their surfaces. It was supposed that the PLA composite would lose their mechanical strengths quickly after the microcracks developed over the whole area of the fibers (Yuan, Mak, and Yao, 2002).

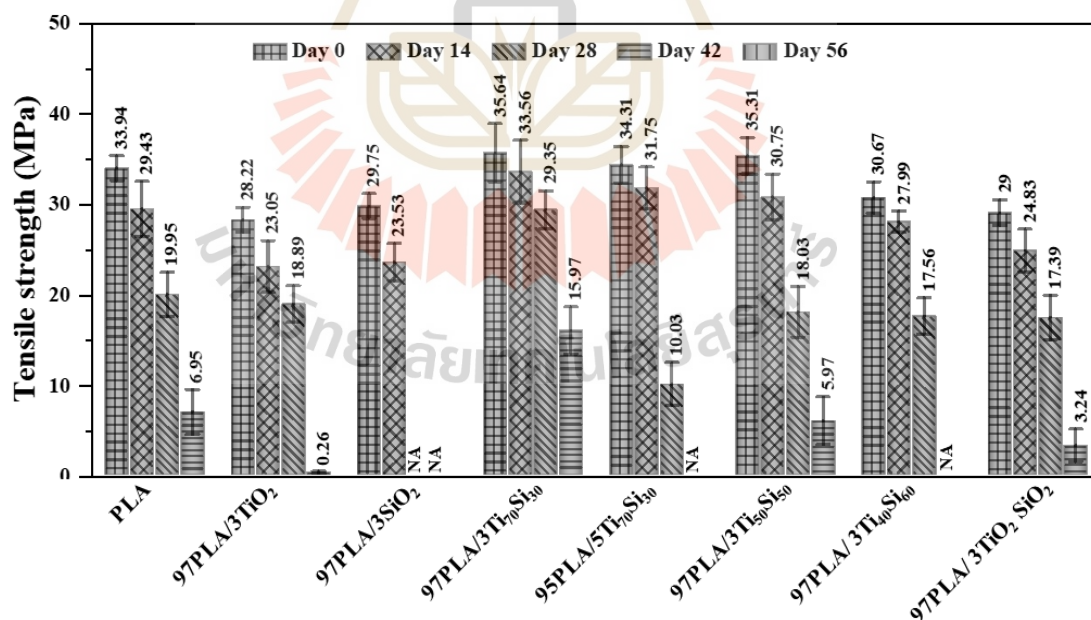


Figure 4.33 Tensile strength of PLA, PLA/ TiO_2 , PLA/ SiO_2 and PLA/ Ti_xSi_y composite films after different period of *in vitro* degradation.

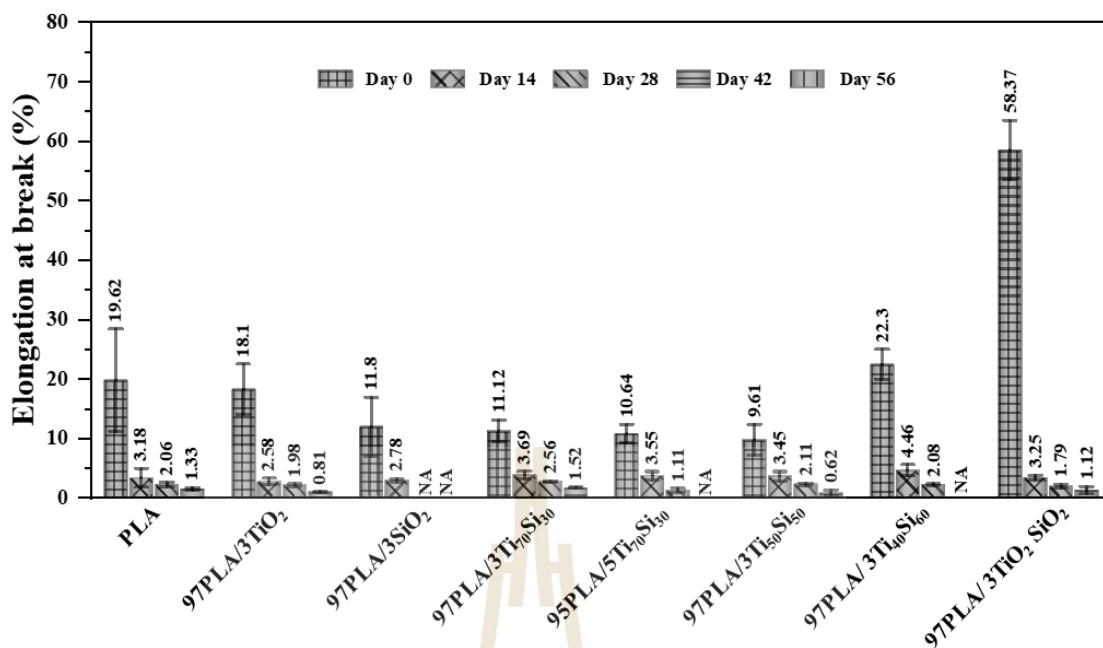


Figure 4.34 Elongation at break of PLA, PLA/TiO₂, PLA/SiO₂ and PLA/Ti_xSi_y composite films after different period of *in vitro* degradation.

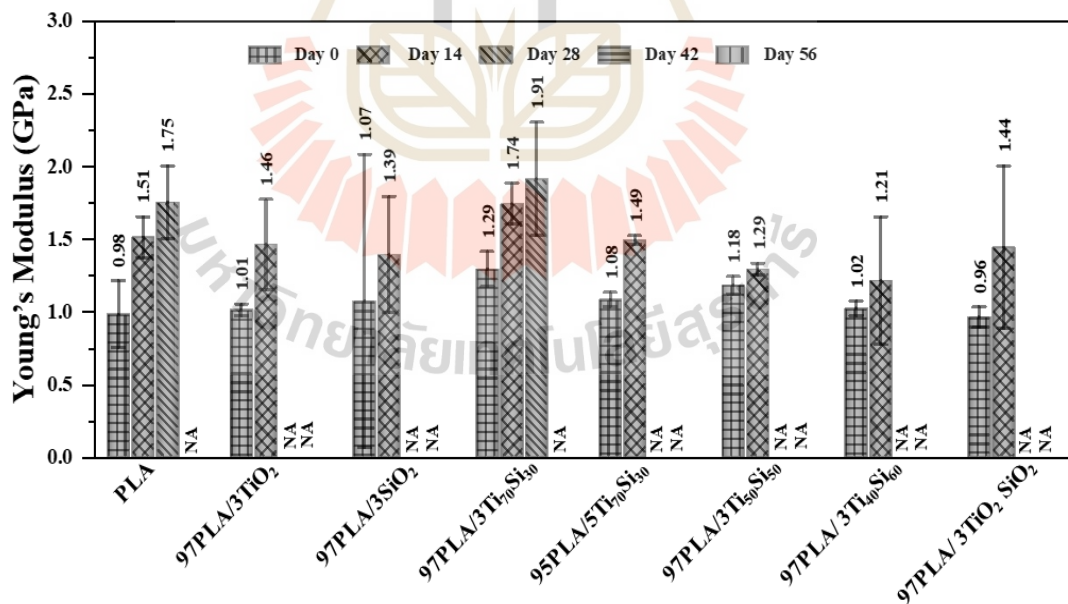


Figure 4.35 Young's modulus of PLA, PLA/TiO₂, PLA/SiO₂ and PLA/Ti_xSi_y composite films after different period of *in vitro* degradation.

4.3.9 Antimicrobial activity

Metal oxide hold greater antibacterial efficiency. So, their reinforcement in polymer composites expressively expands antimicrobial properties of the film, which is desired in biomedical and food packaging applications. Bacteria are generally characterized by cell membrane and its composed mostly of a homogeneous peptidoglycan layer (which consisting of amino acids and sugar). Gram-positive bacteria such as *Staphylococcus aureus* have one cytoplasm membrane with multilayer of peptidoglycan polymer and a thicker cell wall (20-80nm) (Fu, Vary, and Lin, 2005). Whereas gram-negative bacteria such as *Escherichia coli*, bacteria wall is composed of two cell membranes, and outer membrane and a plasma membrane with a thin layer of peptidoglycan with a thickness of 7-8 nm (Fu, Vary, and Lin, 2005). Comparison of bacterial cell wall structure of gram-negative bacteria and gram-positive bacteria are shown in Figure 4.36.

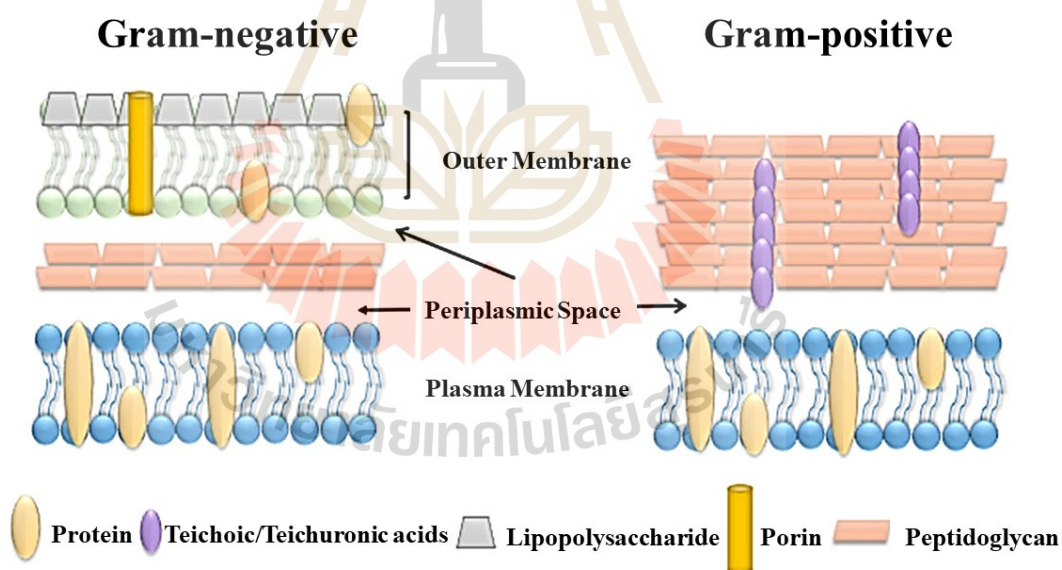


Figure 4.36 Comparison of bacterial cell wall structure of gram-negative bacteria and gram-positive bacteria (Slavin, Asnis, Häfeli, and Bach, 2017).

TiO₂ nanoparticles is known for their antibacterial activity and many recent studies confirm its efficiency as antibacterial agents (Fu, Vary, and Lin, 2005; Joost, Juganson, Visnapuu, Mortimer, Kahru, Nõmmiste, Joost, Kisand, and Ivask, 2015).

So, antibacterial activity of PLA incorporating with 3wt.% of $Ti_{70}Si_{30}$, $Ti_{50}Si_{50}$, TiO_2SiO_2 and 5wt.% of $Ti_{70}Si_{30}$ composites was compared to antibacterial activity of PLA adding 3wt.% of TiO_2 . The results of the antimicrobial activity of gram-negative bacteria (*Escherichia coli* or *E. coli*) and gram-positive bacteria (*Staphylococcus aureus* or *S. aureus*) of PLA, PLA/ TiO_2 , and PLA/ Ti_xSi_y composite films are shown in Table 4.13 and 4.14, respectively. The number of bacteria *Escherichia coli* and bacteria *Staphylococcus aureus* on PLA and PLA composite films at time 0 h (at dilution 10^{-3}) and 24 h (at dilution 10^0) are shown in Figure 4.37.

Antimicrobial activity (R) values of Neat PLA film against *E. coli* and *S. aureus* were 0.09 and 0, respectively. This result indicating that PLA has no antibacterial effect on *E. coli* and *S. aureus*. While 97PLA/3TiO₂ composite film exhibited highest antimicrobial activity (R=5.96 against *E. coli* and R=4.35 against *S. aureus*). From Table 4.13, All of PLA composites exhibited antimicrobial activity agent against *E. coli* (if $R \geq 2$ antimicrobial effectiveness). Moreover, PLA incorporating with 3wt.% of $Ti_{70}Si_{30}$ has enough antimicrobial effectiveness. While PLA adding 3wt.% of TiO_2 and $Ti_{70}Si_{30}$ exhibited antibacterial effect on *S. aureus*. In addition, the increasement of $Ti_{70}Si_{30}$ loading to 5wt.% improved antimicrobial effectiveness of PLA nanocomposites.



Table 4.13 Antimicrobial activity of gram-negative bacteria (*Escherichia coli*) of PLA, PLA/TiO₂, and PLA/Ti_xSi_y composite films.

Samples	Blank (Ut) (t = 24h)	Sample (At) (t = 24h)	Antimicrobial activity ^a (R)
	Log CFU/ml	Log CFU/ml	
PLA	5.96±0.01	5.87±0.02	0.09
97PLA/3TiO ₂	5.96±0.01	0.00±0.00	5.96
97PLA/3Ti ₇₀ Si ₃₀	5.96±0.01	0.00±0.00	5.96
95PLA/5Ti ₇₀ Si ₃₀	5.96±0.01	0.00±0.00	5.96
97PLA/3Ti ₅₀ Si ₅₀	5.96±0.01	3.21±0.04	2.75
97PLA/3TiO ₂ SiO ₂	5.96±0.01	2.53±0.04	3.43

^a Antibacterial activity (R) ≥ 2 = antimicrobial effectiveness

Table 4.14 Antimicrobial activity of gram-positive bacteria (*Staphylococcus aureus*) of PLA, PLA/TiO₂, and PLA/Ti_xSi_y composite films.

Samples	Blank (Ut) (t = 24h)	Sample (At) (t = 24h)	Antimicrobial activity ^a (R)
	Log CFU/ml	Log CFU/ml	
PLA	4.35±0.04	4.35±0.04	0
PLA/3TiO ₂	4.35±0.04	0.00±0.00	4.35
PLA/3Ti ₇₀ Si ₃₀	4.35±0.04	2.96±0.01	2.04
PLA/5Ti ₇₀ Si ₃₀	4.35±0.04	0.00±0.00	4.35
PLA/3Ti ₅₀ Si ₅₀	4.35±0.04	3.17±0.08	1.83
PLA/3TiO ₂ SiO ₂	4.35±0.04	3.21±0.01	1.79

^a Antibacterial activity (R) ≥ 2 = antimicrobial effectiveness

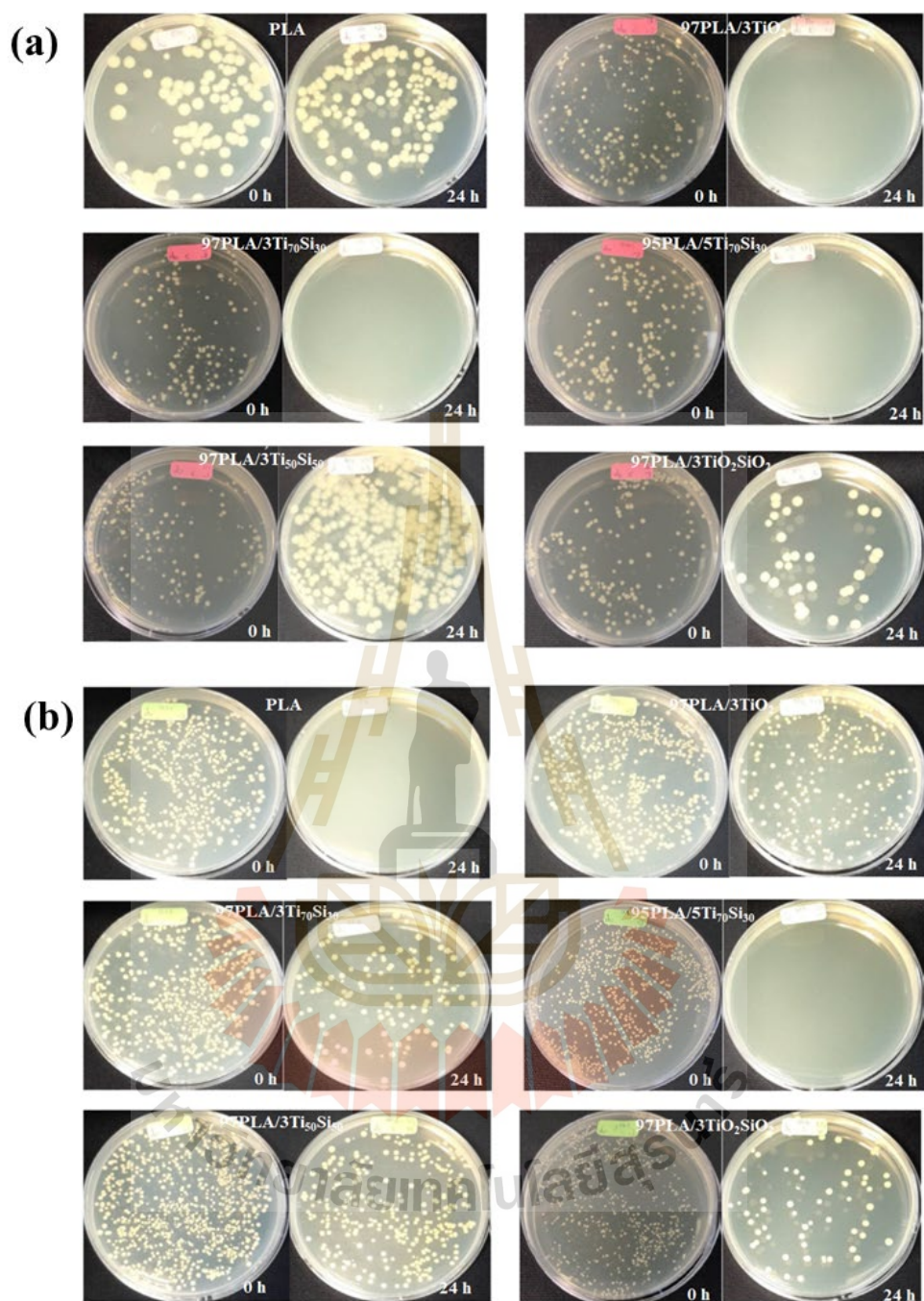


Figure 4.36 The number of (a) bacteria *Escherichia coli* (b) bacteria *Staphylococcus aureus* on of PLA, PLA/TiO₂, and PLA/Ti_xSi_y composite films at time 0 h (at dilution 10⁻³) and 24 h (at dilution 10⁰)

4.4 The effect of silk fibroin on properties of PLA/SF and PLA/Ti_xSi_y/SF composites

4.4.1 Characterization of silk fibroin (SF) powder

Silk fibroin (SF) powder can be prepared either by a solution route desolvation method (a solution route) or by a mechanical method. In this work, we focus on a desolvation method. With the desolvation method, silk fibroin was prepared from *Bombyx mori* cocoons in which cocoons was firstly dissolved in Na₂CO₃, followed by washing several times with distilled water to remove impurities and sericin. After the degumming step, silk fibroin nanoparticles were prepared using two different solvents. In one process, the degummed silk was re-dissolved in CaCl₂ solution at 80-100°C under continuous stirring for 2 h. The second process, degummed silk was dissolved in Ajisawa's solvent system, ternary solvent made of CaCl₂, H₂O, C₂H₅OH solution at a molar ratio of 1:8:2 (Ajisawa, 1998), at 80-100°C for 2 h, filtered, and dialyzed for 5 days against distilled water with several changes until the conductivity of dialyzed water is the same as that of distilled water in order to remove salt and alcohol. The solution was frozen at -20°C for 12 hours followed by freeze drying (lyophilization) for 3 days. The structural morphological and thermal properties were investigated. Products of silk extraction from *Bombyx mori* silkworm in this work are shown in Figure 4.38.

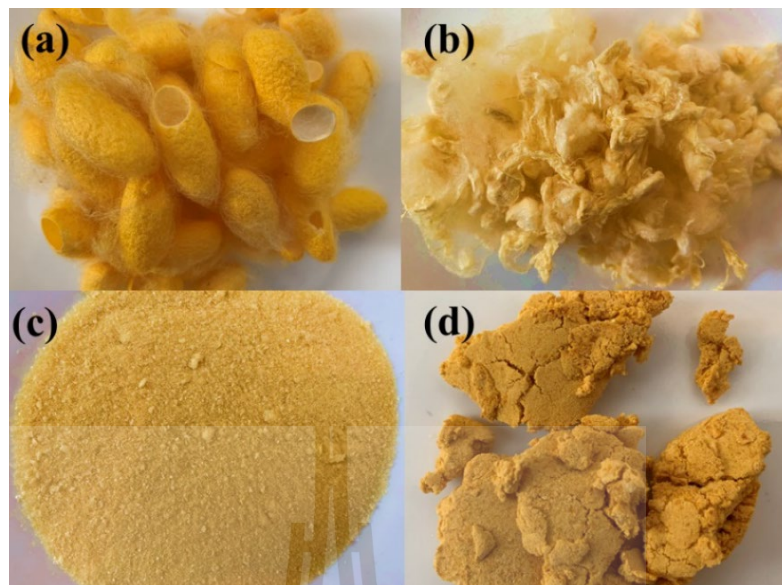


Figure 4.38 Products of silk extraction from *Bombyx mori* silkworm cocoons; (a) cocoons, (b) degummed silk, (c) silk fibroin, and (d) sericin.

4.4.1.1. Determination of %yield of SF

The influence of solvent with various temperature of solution on %yield of silk fibroin is listed in Table 4.15. It was demonstrated that the yield of silk fibroin powder treat with CaCl_2 solution were higher than using Ajisawa's solution. The highest yield of silk fibroin powder was found using CaCl_2 solution at 100°C .

Table 4.15 %yield of silk fibroin extracted from *Bombyx mori* silkworm cocoons using Ajisawa's solution and CaCl₂ solution with various temperature.

Samples	Cocoon (g)	Degummed silk (g)	Fibroin (g)	Yield ^a (%)
80°C Ajisawa's solution	30.00	19.38	2.88	9.60
90°C Ajisawa's solution			2.78	9.27
100°C Ajisawa's solution			2.54	8.47
80°C CaCl ₂ solution			3.19	10.63
90°C CaCl ₂ solution			4.88	16.26
100°C CaCl ₂ solution			6.69	22.30

$$^a \%yield = \frac{g \text{ of silk fibroin}}{g \text{ of cocoon}} \times 100$$

4.4.1.2. Identification of SF

FT-IR spectroscopy is commonly used to investigate the secondary structure of SF because the IR spectrum includes the common absorption bands that are sensitive to the molecular conformation of SF. Absorption band of FTIR spectra and FTIR transmittance spectra of cocoons, degummed silk, silk fibroin and sericin are shown in Table 4.16 and Figure 4.39, respectively. The absorption bands of cocoon, degummed silk, and silk fibroin observed between $1,610\text{-}1,630\text{ cm}^{-1}$ and $1,510\text{-}1,520\text{ cm}^{-1}$ were characteristic of the amide I and amide II functional groups in the secondary structure of silk II (Zhu, Feng, Zhang, Guo, Zhang, and Chen, 2009).

Moreover, all of silk fibroin both treat with Ajisawa's solution and CaCl_2 showed the transmittance peak of the peptide backbone of amide I (C = O stretching), amide II (N-H bending), and amide III (C-N stretching) in the infrared spectra region of $1,700\text{-}1,600\text{ cm}^{-1}$, $1,600\text{-}1,500\text{ cm}^{-1}$, and $1350\text{-}1250\text{ cm}^{-1}$, respectively (Figure 4.40 and 4.41). All these characteristic transmittance peaks indicate the existence of a hydrogen-bonded NH group. Because of the conformational differences between silk I and silk II, the amide I and amide II peaks are at different wavelengths (DeBari and Abbott, 2019). When treat with CaCl_2 solution, the β -sheet structure of silk fiber would mainly change to random coil due to the highly hydration of the concentrated CaCl_2 solution, and the ability of calcium and chloride ions in binding with tyrosine residues in fibroin resulting in interruption of the van der Waals force and hydrogen bonds in fibroin molecules. For this reason, it would cause fibroin to swell and then dissolve (Wang Zhang *et al.*, 2001).

Table 4.16 Typical absorption band of FTIR spectra of silk fibroin.

Samples	Wavenumber (cm ⁻¹)					
	Amide I		Amide II		Amide III	
	α -helix ,Random coil	β -sheet	β -sheet	Random coil	β -sheet	Random coil
Silk Fibroin	1650	1630	1540	1520	1270	1230
Cocoons	NA	1619	NA	1513	NA	1228
Degummed silk	NA	1618	NA	1508	NA	1224
Silk Fibroin	NA	1616	NA	1506	NA	1223
Sericin	1653	NA	1558	NA	NA	NA

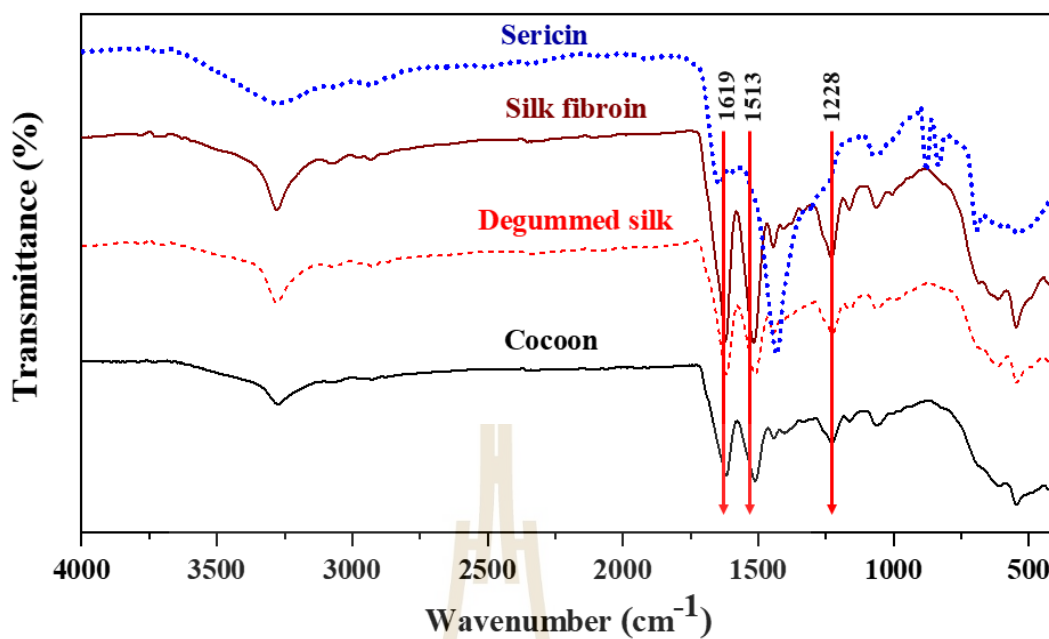


Figure 4.39 FTIR Transmittance spectra of cocoon, degummed silk, silk fibroin and sericin.

However, the presence of α -helices structures in sericin indicates that freeze-drying process induce important changes in sericin structure. These results can be corroborated with those obtained by Tsukada (1983), who presented that sericin extracted from liquid silk for 45 min, in hot water, contains a small fraction of α -helice (10%).

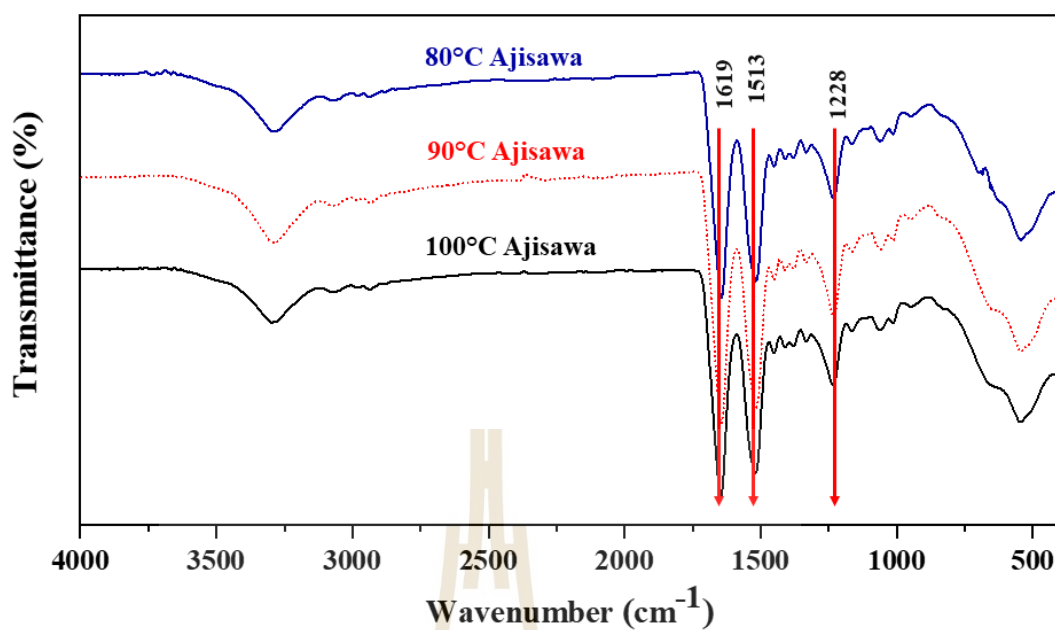


Figure 4.40 FTIR Transmittance spectra of silk produced by Ajisawa's solution.

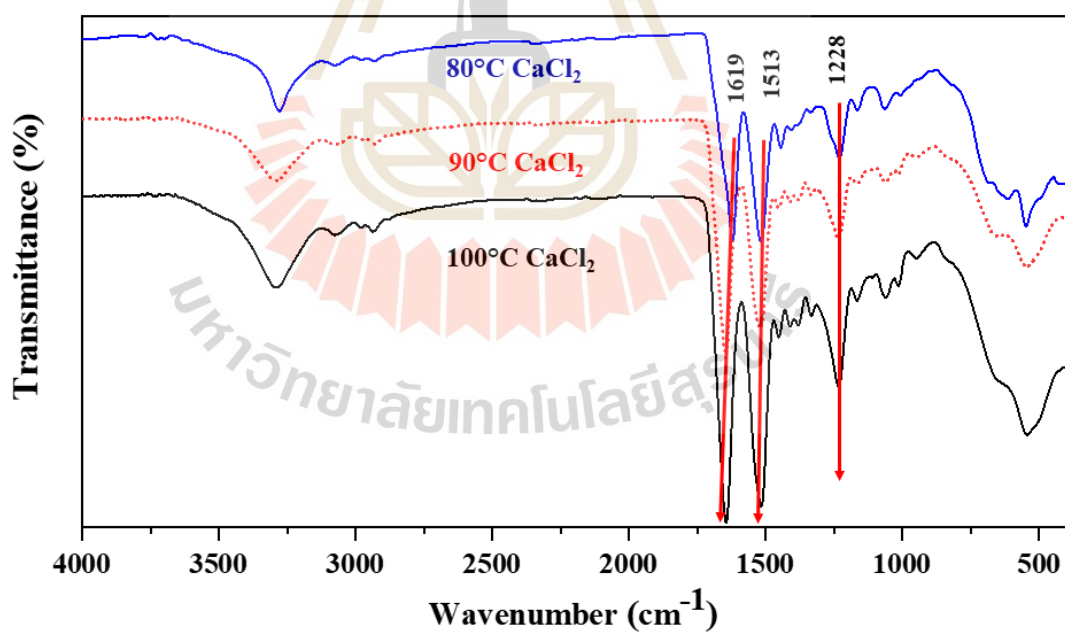


Figure 4.41 FTIR Transmittance spectra of silk produced by CaCl_2 solution.

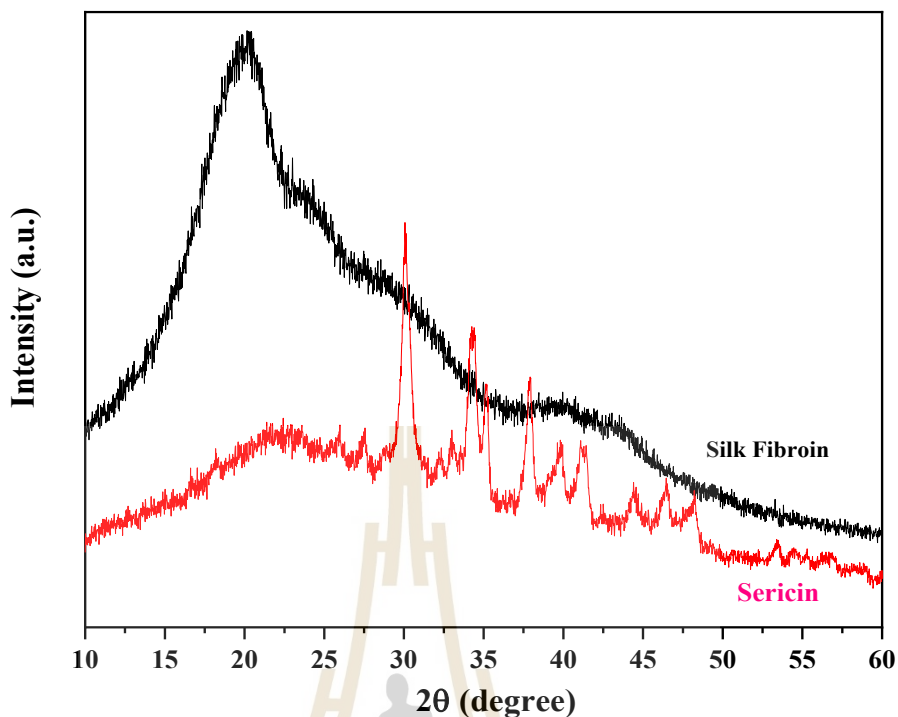


Figure 4.42 X-ray diffraction pattern of silk fibroin (SF) and sericin.

From figure 4.42 shows the XRD pattern of SF and sericin. The SF showed 2θ diffraction peak with 18.4° which corresponded to silk II crystalline spacing. Furthermore, the SF produced with CaCl_2 -solution without alcohol were composed of more silk II. Therefore, it is possible that this CaCl_2 solution has ability to protect the integrity of the fibroin, maintaining more silk II.

In addition, a high tendency of chain aggregation of sericin is produced when water is removed from sericin protein during the lyophilization process. Due to this aggregation, constituents of protein come into proximity, and the β -sheet structure is formed (Martínez, Londoño Zuluaga, Restrepo Osorio, and Álvarez, 2017).

However, sericin was amorphous protein but presented some peak in XRD patterns due to effect of remaining NaCO_3 in degumming step. This result was confirmed by the element maps from EDS. Figure 4.43 showed the spatial distribution of the Na and O elements in a sericin sample suggesting the contaminated of Na_2CO_3 in sericin.

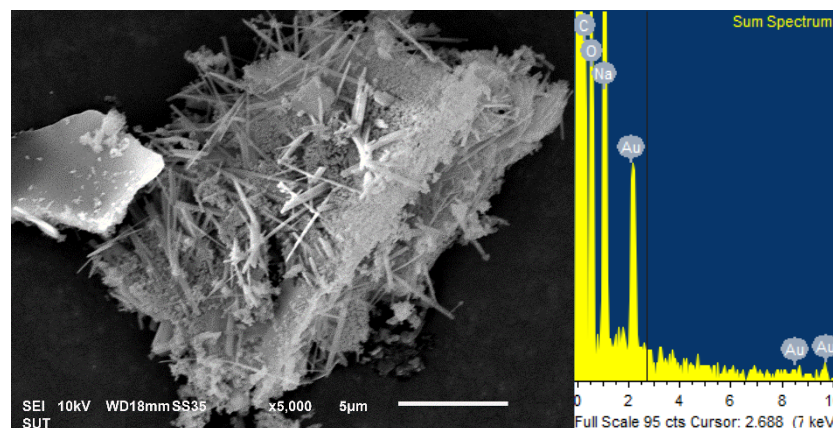


Figure 4.43 SEM images (x5000, 10 kV) and EDS spectra of sericin.

However, different characterization methods can be used to differentiate between the two silk structures. X-ray diffraction (XRD) identifies silk I versus silk II and random-coils of fibroin, while nuclear magnetic resonance is unable to distinguish random coil fibroin from silk I (Asakura, Kuzuhara, Tabeta, and Saito, 1985)

The surface morphology of degummed silk and SF were observed with SEM (Figure 4.44, 4.45, and 4.46). The size and shape of degummed silk were normal, with diameter 7-10 µm. In contrast, silk fibroin of both treats with Ajisawa's solution and CaCl₂ solution were spherical or irregular in shapes. This shape may have result from the fusion of smaller micelles that occurred in the aqueous solution. It is well-known that addition of alcohols such as methanol and ethanol to regenerated liquid silk fibroin could slowly induce it gelling, so that its configuration simultaneously changed. When drying and pulverizing, the powdered silk with a broad size range of micrometer particles (1– 100µm) could be obtained (Y.-Q. Zhang, Shen, Xiang, Zhuge, Gao, and Wang, 2007).

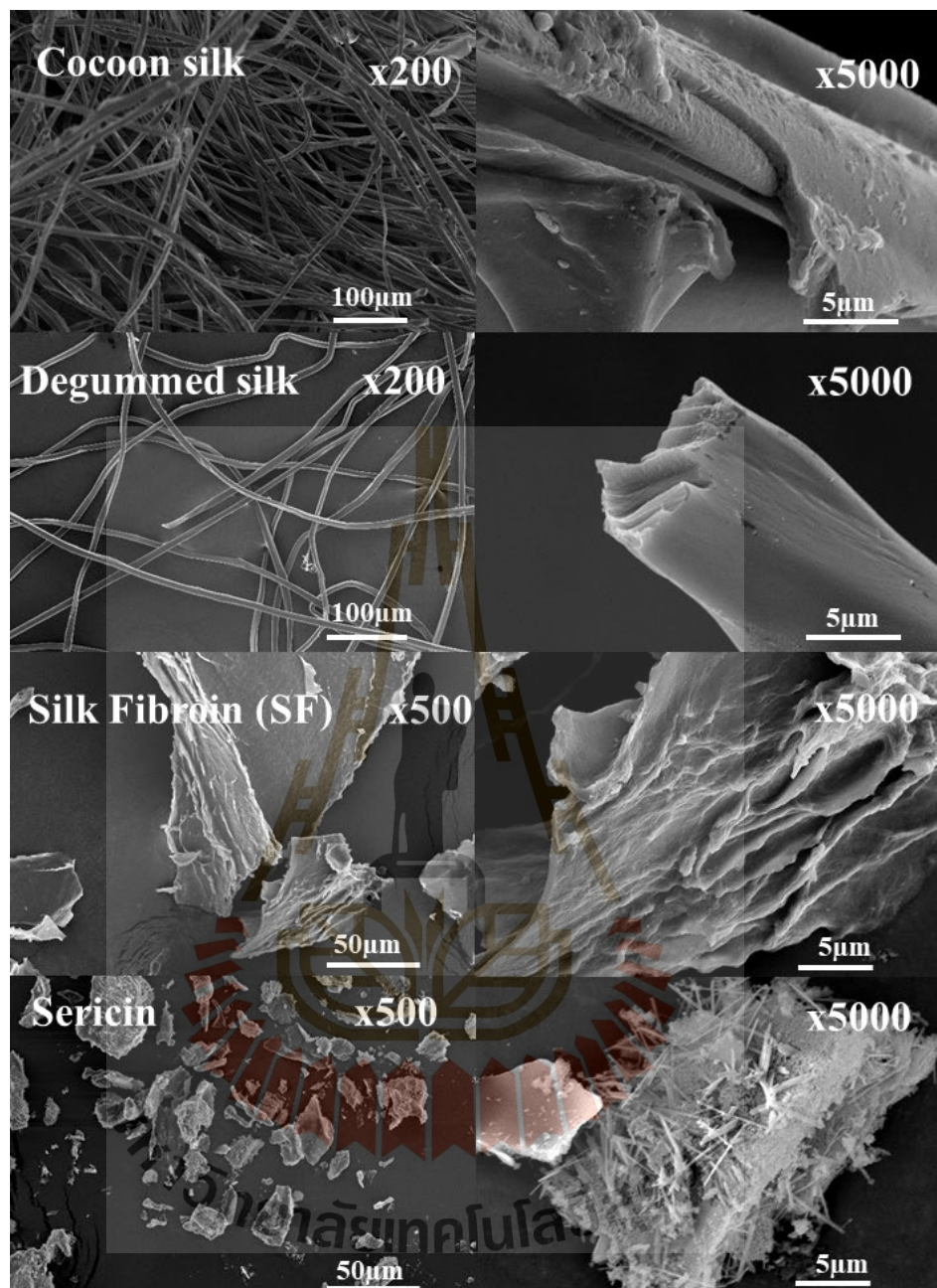


Figure 4.44 SEM images of cocoon, degummed silk, silk fibroin and sericin.

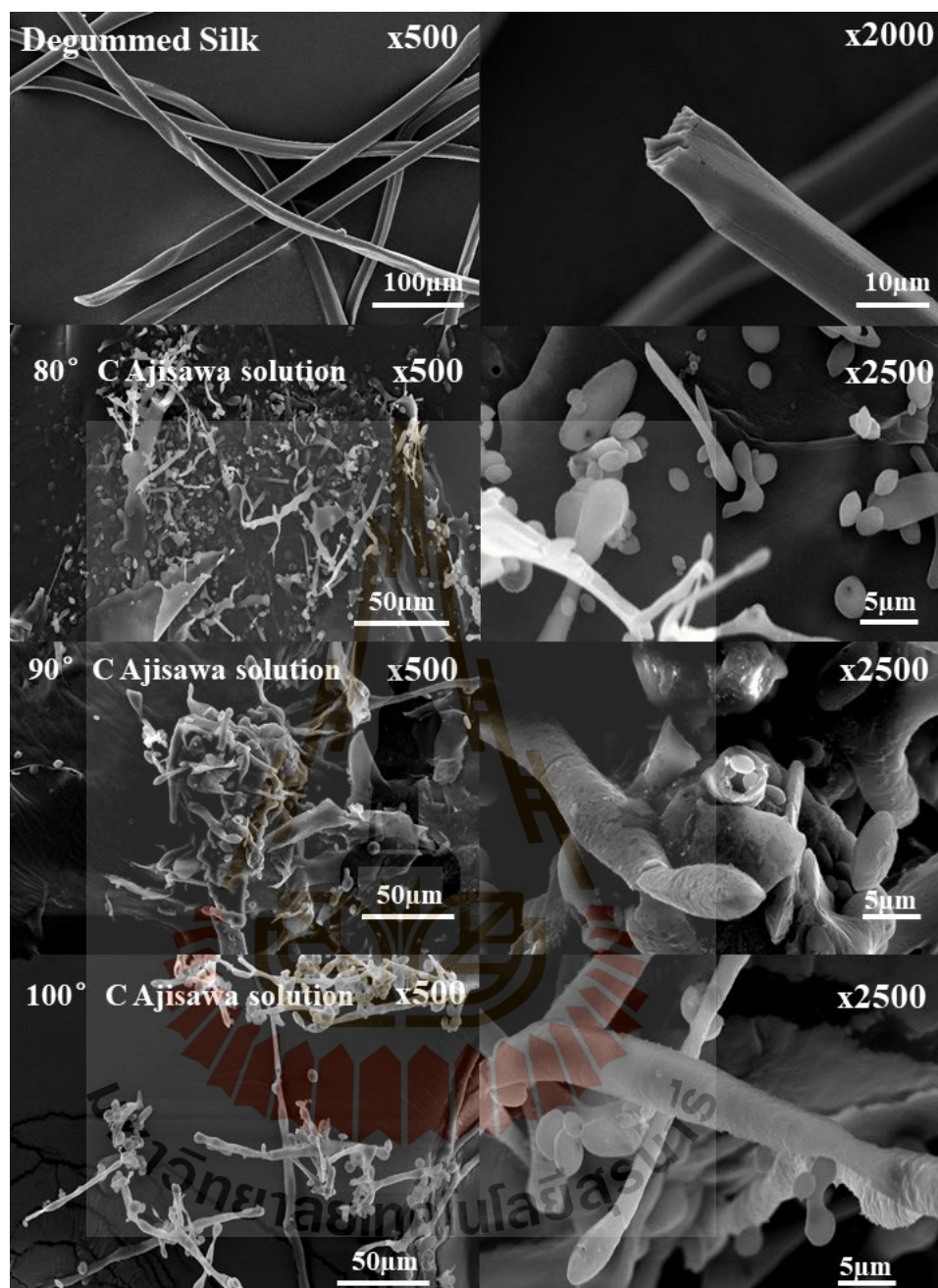


Figure 4.45 SEM images of degummed silk and silk fibroin prepared from Ajisawa's solution.

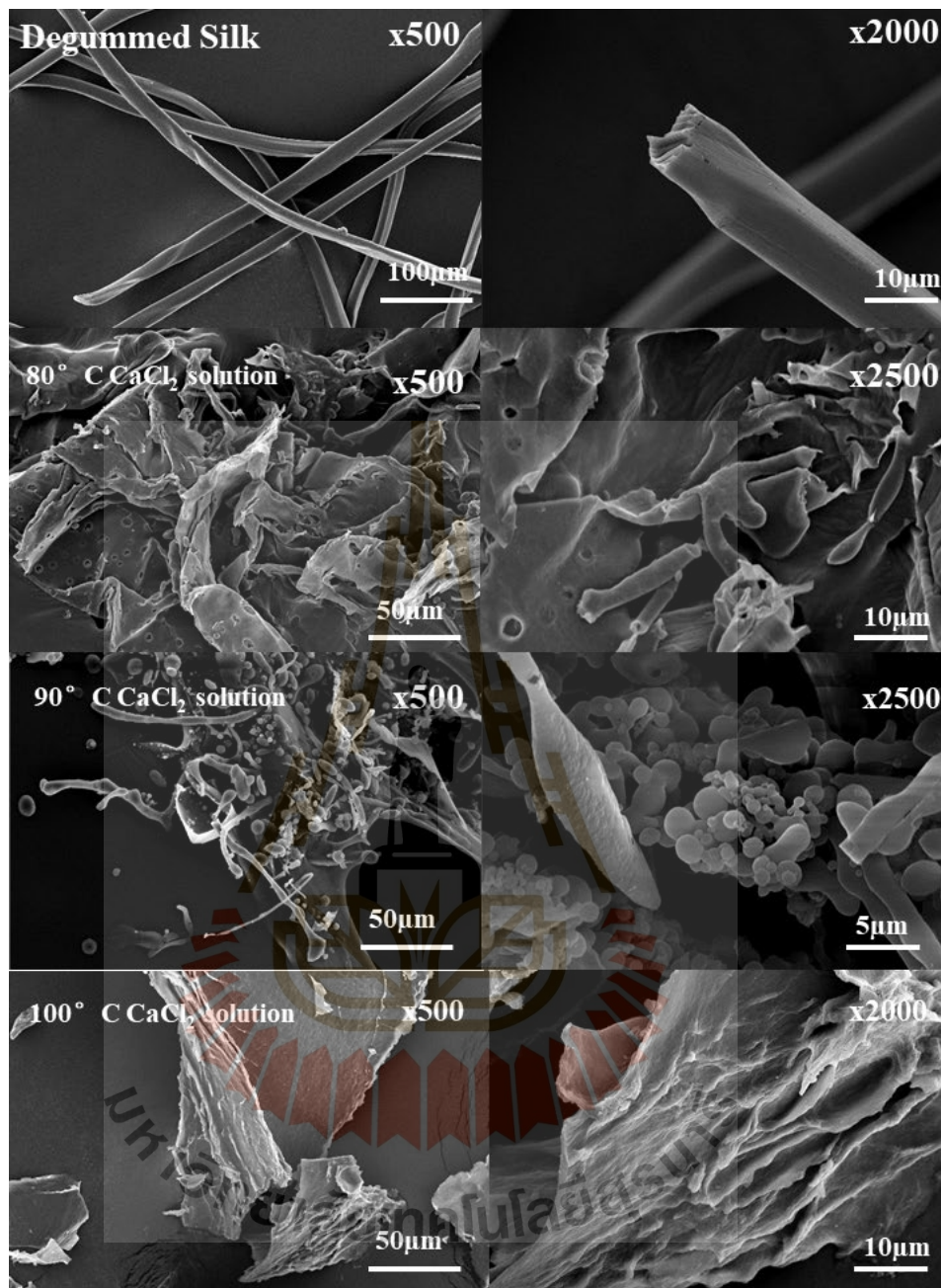


Figure 4.46 SEM images of degummed silk and silk fibroin prepared from CaCl₂ solution.

TGA and DTG curves are shown in Figure. 4.47, and 4.48. TGA curves of all samples shows a weight loss below 100 °C that is attributed to water evaporation. No changes from 100 °C to 210 °C are detected and after that, a fast decrease in weight is observed until 400 °C, which is associated to the thermal degradation of samples (S. Yaowalak, S. Wilaiwan, and Prasong, 2009). However, the thermal degradation of the amorphous part of the silk sericin occur at 210 °C (Martínez, Londoño Zuluaga, Restrepo Osorio, and Álvarez, 2017). The residue of both samples is around 40 % at 400 °C approximately. Similar results were observed by Tsukada (1978). According to Tsukada (1978), sericin goes through a scission and molecular flowing at 250 °C, followed by a decomposition reaction.

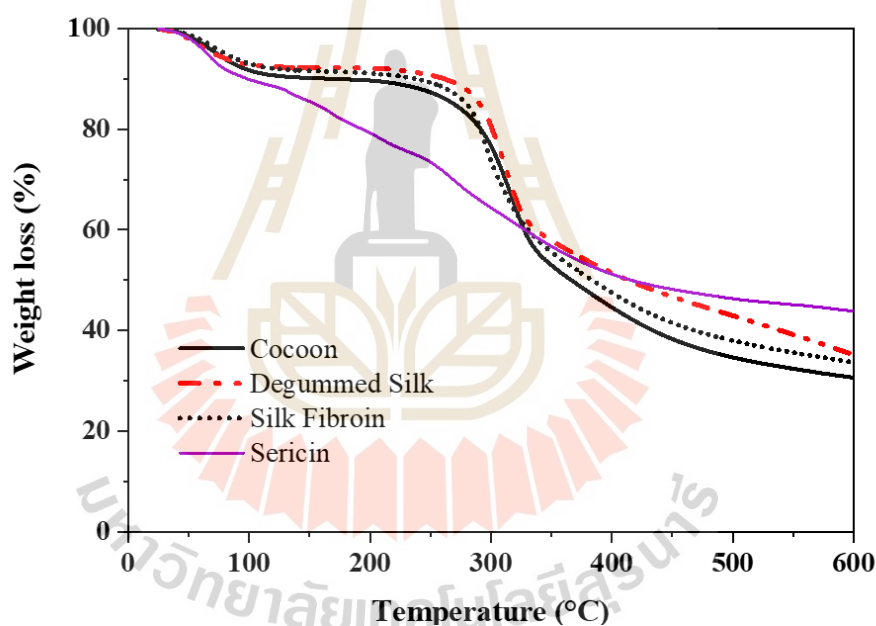


Figure 4.47 TGA curves of cocoon, degummed silk, silk fibroin, and sericin of *Bombyx mori* silk.

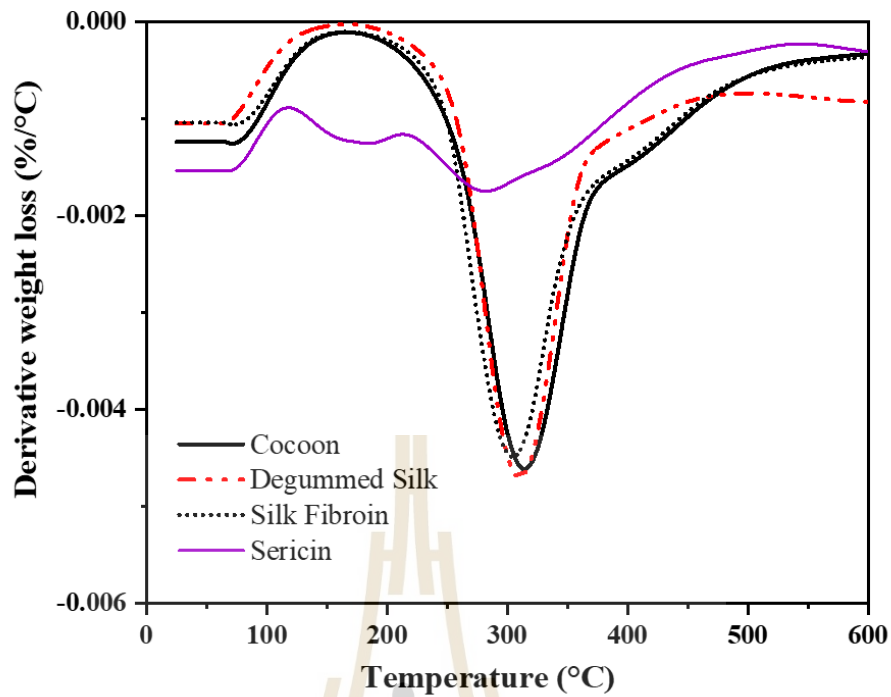


Figure 4.48 DTG curves of cocoon, degummed silk, silk fibroin, and sericin of *Bombyx mori* silk.

Based on yield content of silk fibroin, the highest yield content of silk fibroin obtained from CaCl_2 solution at 100°C was 22.30%. Therefore, this method was used to prepare silk fibroin in this study.

4.4.2 Mechanical properties of PLA/SF and PLA/ Ti_xSi_y /SF composites

To evaluate the effect of SF in the PLA matrix, the mechanical properties of PLA, PLA/SF, PLA/ $\text{Ti}_{70}\text{Si}_{30}$, PLA/ $\text{Ti}_{70}\text{Si}_{30}$ /SF composites were investigated. Tensile properties of PLA, PLA/SF, PLA/ $\text{Ti}_{70}\text{Si}_{30}$, PLA/ $\text{Ti}_{70}\text{Si}_{30}$ /SF composite at various SF contents are presented in Table 4.17, Figure 4.50, 4.51, and 4.52.

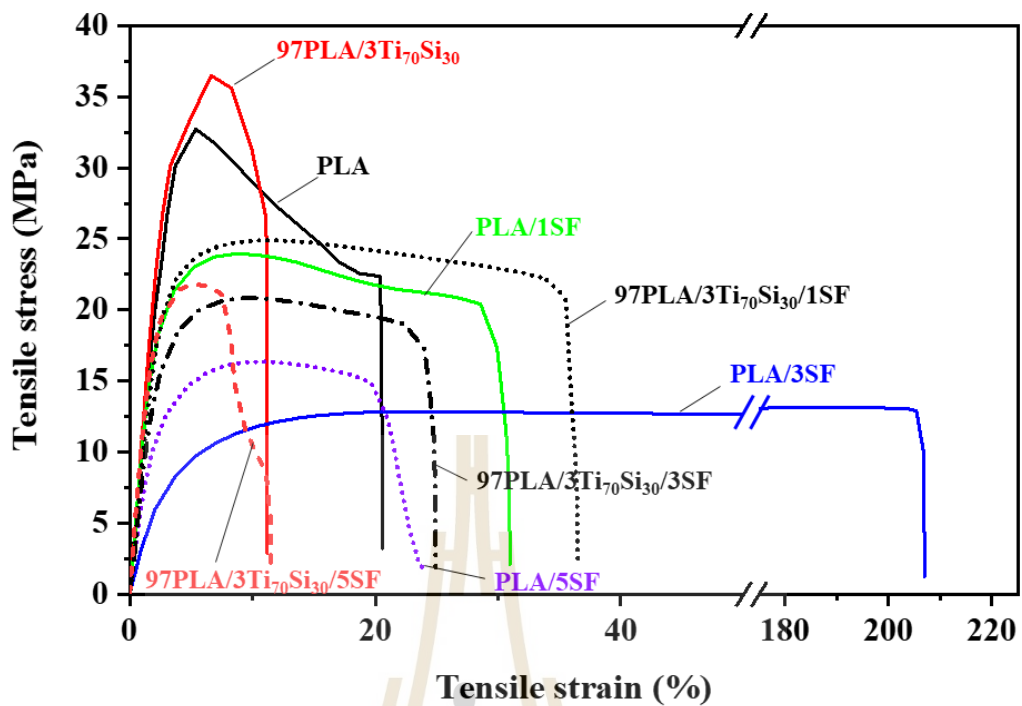


Figure 4.49 Stress-strain curves of PLA, PLA/SF, PLA/Ti₇₀Si₃₀, PLA/Ti₇₀Si₃₀/SF composites at various SF contents.

The stress-strain curves of the PLA, PLA/SF, and PLA/Ti₇₀Si₃₀/SF composites with different SF content are shown in Figure 4.49. For all samples, the curves were linear at low strain, followed by plastic deformation in the region of 5% strain. At higher strains, the composites yielded up to a breaking strain of 20% for the PLA, 206% for 97PLA/3SF, and 36.3% for 97PLA/3Ti₇₀Si₃₀/1SF composites (Figure 4.51). As SF content increased, tensile strength and Young's modulus of PLA/SF and PLA/Ti₇₀Si₃₀/SF composites decreased with increasing SF content up to 3 and 1 wt.% of PLA/SF and PLA/Ti₇₀Si₃₀/SF, respectively due to secondary structural transition of SF from Silk I to Silk II form, resulting in the increase of modulus and toughness (Zhu, Feng, Zhang, Guo, Zhang, and Chen, 2009).

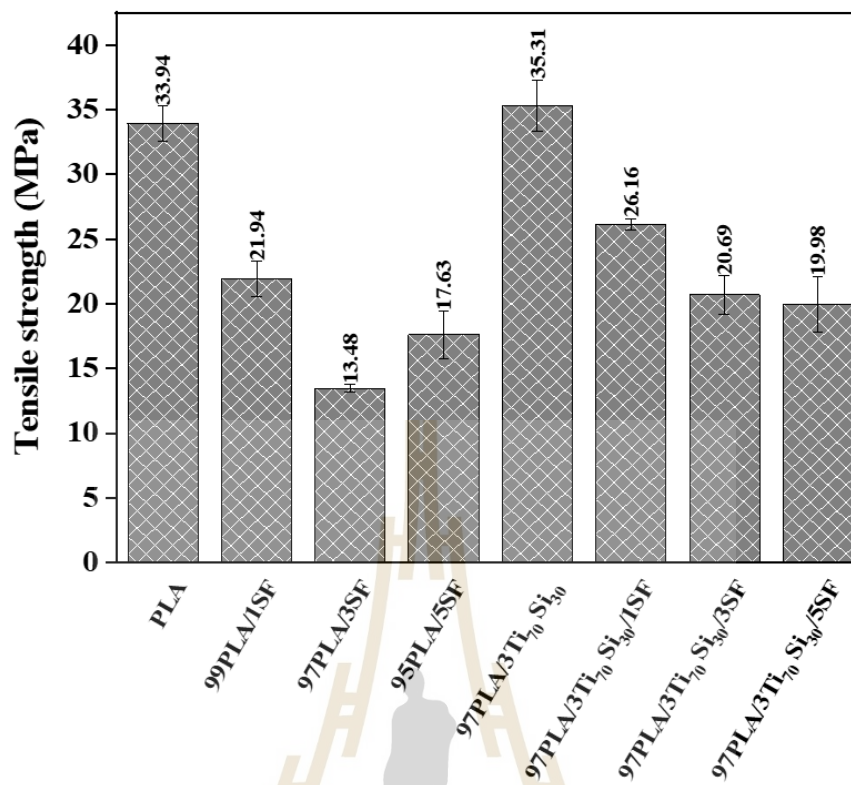


Figure 4.50 Tensile strength of PLA, PLA/SF, PLA/Ti₇₀Si₃₀, PLA/Ti₇₀Si₃₀/SF composite at various SF contents.

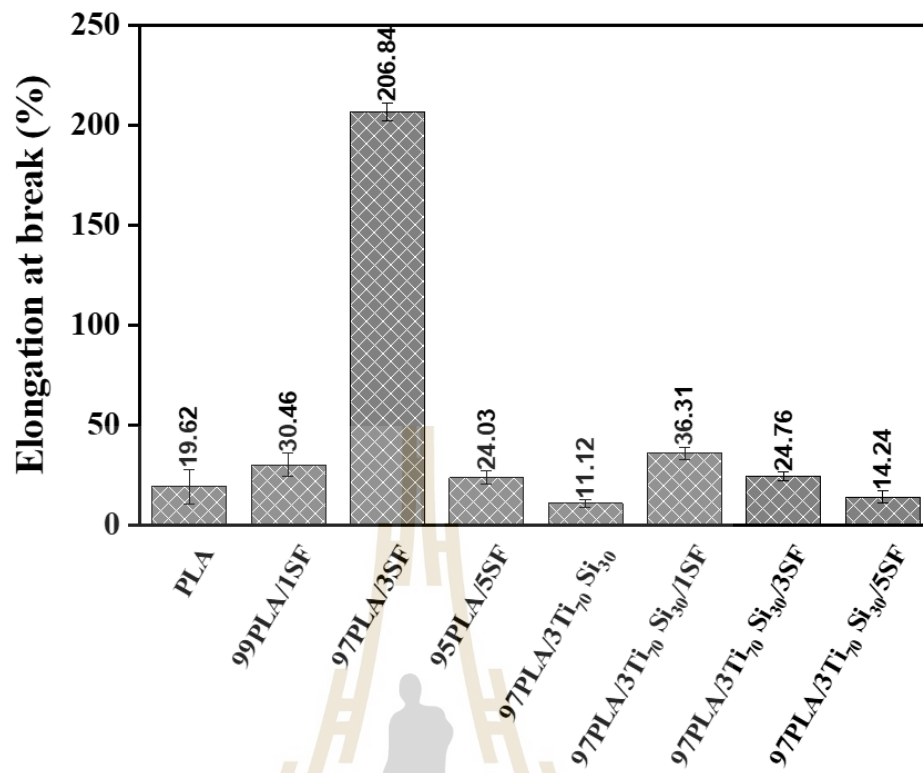


Figure 4.51 Elongation at break of PLA, PLA/SF, PLA/Ti₇₀Si₃₀, PLA/Ti₇₀Si₃₀/SF composite at various SF contents.

However, it was noteworthy that elongation at break of PLA/Ti₇₀Si₃₀/SF showed opposite trend as the content of SF increased to 5 wt.%. This effect was probably due to the lack of interaction between PLA and filler.

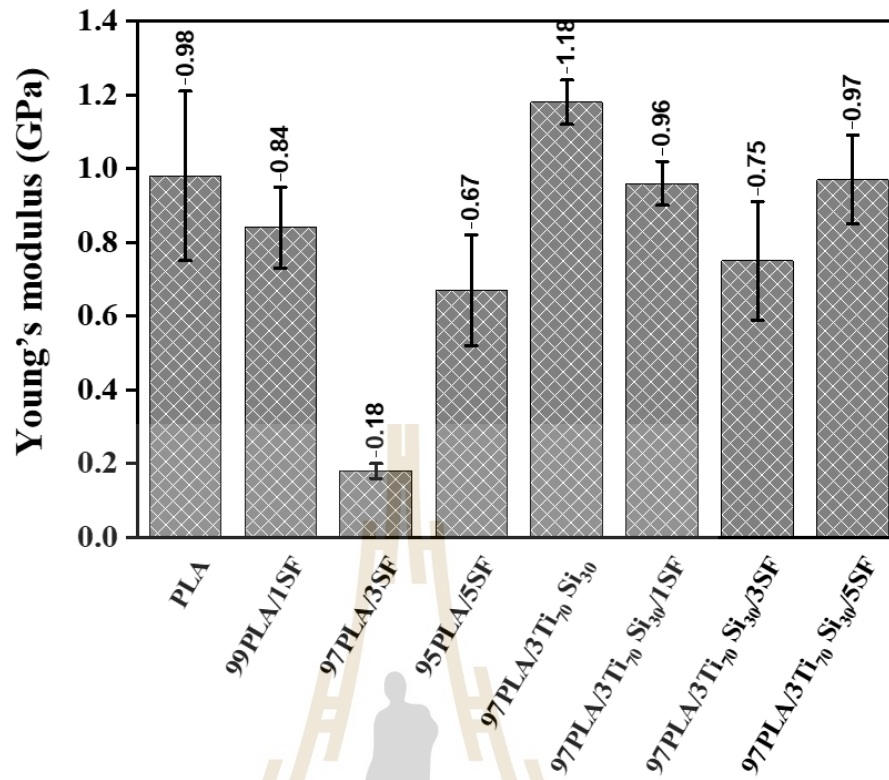


Figure 4.52 Young's modulus of PLA, PLA/SF, PLA/Ti₇₀Si₃₀, PLA/Ti₇₀Si₃₀/SF composite at various SF contents.

Table 4.17 Tensile properties of PLA, PLA/SF, PLA/Ti₇₀Si₃₀, PLA/Ti₇₀Si₃₀/SF composite at various SF contents.

Sample	Tensile strength (MPa)	Elongation at break (%)	Young's Modulus (GPa)
PLA	33.94±1.38	19.62±8.64	0.98±0.23
99PLA/1SF	21.94±1.35	30.46±5.83	0.840±0.11
97PLA/3SF	13.48±0.29	206.84±4.43	0.183±0.002
95PLA/5SF	17.63±1.83	24.03±3.31	0.667±0.15
PLA/Ti ₇₀ Si ₃₀	35.64±3.21	11.12±1.81	1.29±0.12
PLA/Ti ₇₀ Si ₃₀ /1SF	26.16±0.42	36.31±3.03	0.956±0.06
97PLA/Ti ₇₀ Si ₃₀ /3SF	20.69±1.49	24.76±2.10	0.753±0.16
97PLA/Ti ₇₀ Si ₃₀ /5SF	19.98±2.14	14.24±3.04	0.974±0.12

4.4.3 Thermal properties of PLA/SF and PLA/Ti_xSi_y/SF composites

The thermal behaviors of pure PLA, PLA, PLA/SF, and PLA/Ti_xSi_y/SF composites were investigated by the differential scanning calorimetry (DSC). The determined data are listed in Table 4.18. DSC thermograms of neat PLA, PLA/SF and PLA/Ti_xSi_y/SF composites films are shown in Figure 4.53 and 4.54, respectively. All of samples can be seen that the glass transition temperature (T_g), cold crystallization temperature (T_{cc}) and melt temperature (T_m) of PLA and PLA composites were typical of semicrystalline polymer. In the heating scan, the composites showed the same trend as neat PLA but the T_{cc} of composites shifted to higher temperature and the crystallization enthalpy becomes smaller than that of neat PLA. This evidence suggested that T_{cc} of the PLA component becomes more difficult (H.-m. Chen, Wang, Liu, Wang, Yang, Wang, Zhang, and Zhou, 2014).

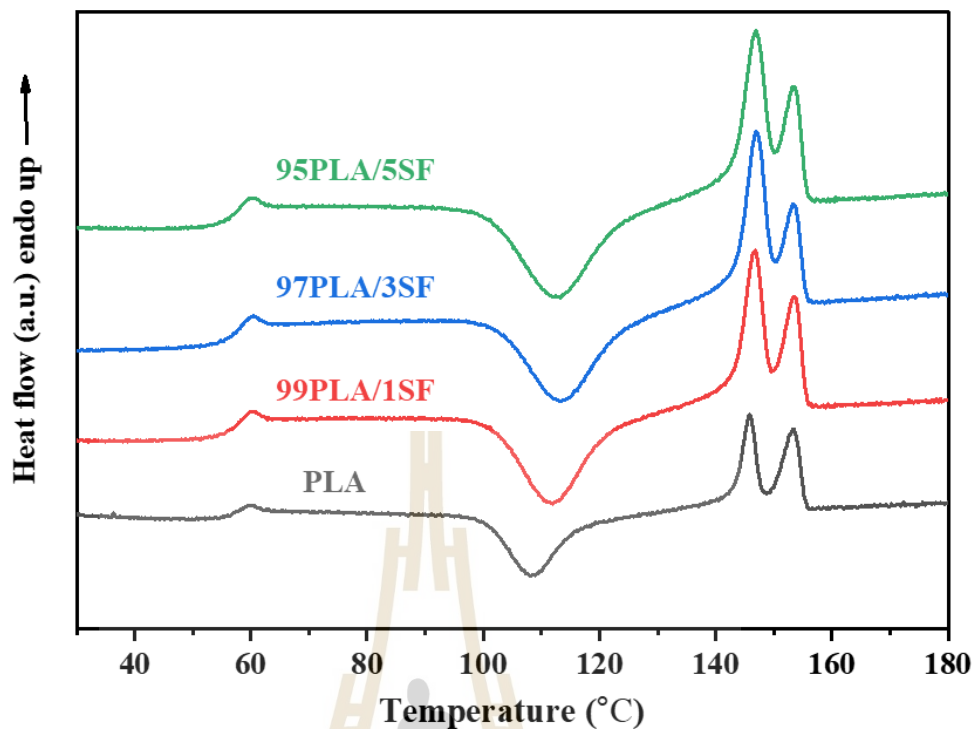


Figure 4.53 DSC thermograms of PLA and PLA/SF composite at various SF contents. (The second heating, heating rate 5°C/min).

With an increasing of the SF content up to 5 wt.%, the heat of crystallization (ΔH_c), heat of fusion (ΔH_m), and degree of crystallinity (χ_c) of the PLA slightly decreased. This may be due an influence on the number of crystallization nuclei of SF in the PLA/SF composites, which causes the collision of spherulites to occur earlier and this affects the final size of the spherulite crystals (Vestena, Grossa, Müllerc, and Piresa, 2016). Similar behavior was observed in PLA/cellulose nanocrystals (CNC) composites (Vestena, Grossa, Müllerc, and Piresa, 2016). Thus, a reduction in the degree of crystallinity of PLA/SF composite with increasing SF content can be observed.

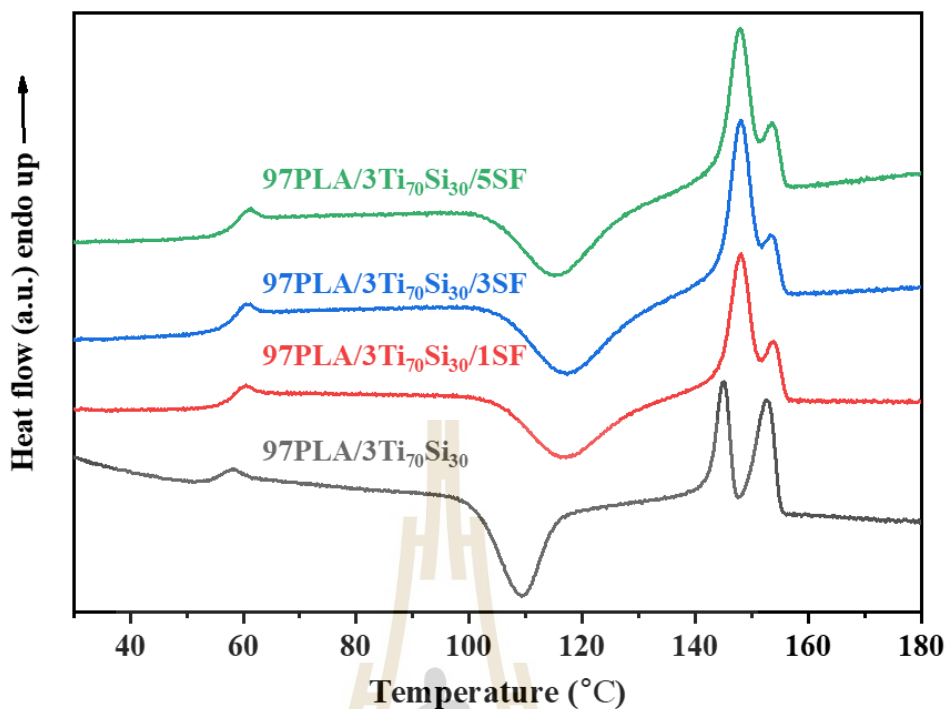


Figure 4.54 DSC thermograms of PLA/Ti₇₀Si₃₀ and PLA/Ti₇₀Si₃₀/SF composite at various SF contents. (The second heating, heating rate 5°C/min).

The T_{cc} of PLA/Ti_xSi_y/SF composites films shifted to higher temperature with increasing SF content is shown in Figure 4.54. It is interesting to note that the cold crystallization temperature (T_{cc}) seems to depend on SF content. Obviously, with the increase SF content (up to 5 wt.%), of the PLLA component becomes more difficult (H.-m. Chen, Wang, Liu, Wang, Yang, Wang, Zhang, and Zhou, 2014).

Table 4.18 Thermal characteristics of PLA, PLA/SF_y, PLA/3Ti₇₀Si₃₀ and PLA/3Ti₇₀Si₃₀/SF composites film (the second heating, heating rate 5°C/min)

Samples	T _g (°C)	T _{cc} (°C)	ΔH _c (J/g)	T _{m1} (°C)	T _{m2} (°C)	ΔH _m (J/g)	χ _c (%)
PLA	58.87	108.47	36.15	145.84	153.35	31.73	33.86
99PLA/1SF	59.18	111.93	30.93	146.78	153.61	30.36	32.73
97PLA/3SF	58.69	113.36	26.58	146.95	153.71	28.76	31.64
95PLA/5SF	58.07	113.32	27.66	146.91	153.59	27.65	31.06
97PLA/3Ti ₇₀ Si ₃₀	54.81	109.3	34.41	145.07	152.75	32.71	35.99
97PLA/3Ti ₇₀ Si ₃₀ /1SF	58.23	116.08	25.17	148.08	154.18	25.87	27.89
97PLA/3Ti ₇₀ Si ₃₀ /3SF	57.40	117.34	26.11	148.00	153.92	24.20	26.63
97PLA/3Ti ₇₀ Si ₃₀ /5SF	59.54	114.97	23.62	148.05	153.64	26.50	29.77

PLA is a decomposable polyester and it is degraded by heat, moisture and UV radiation. Figure 4.55 showed the thermogravimetric (TGA) curves of PLA, PLA/SF, PLA/Ti₇₀Si₃₀, PLA/Ti₇₀Si₃₀/SF composite at various SF contents at a heating rate of 10°C min⁻¹ under N₂ atmosphere and switched to air atmosphere. Derivative thermograms (DTG) curves of PLA, PLA/SF, PLA/Ti₇₀Si₃₀, PLA/Ti₇₀Si₃₀/SF composites are presented in Figure. 4.56. For PLA, PLA/SF, PLA/Ti₇₀Si₃₀, PLA/Ti₇₀Si₃₀/SF composites, the decomposition temperature at 5% (T_{0.05}) and 50% (T_{0.5}) weight loss, decomposition temperature (T_d) and char residual at 800°C are listed in Table 4.19.

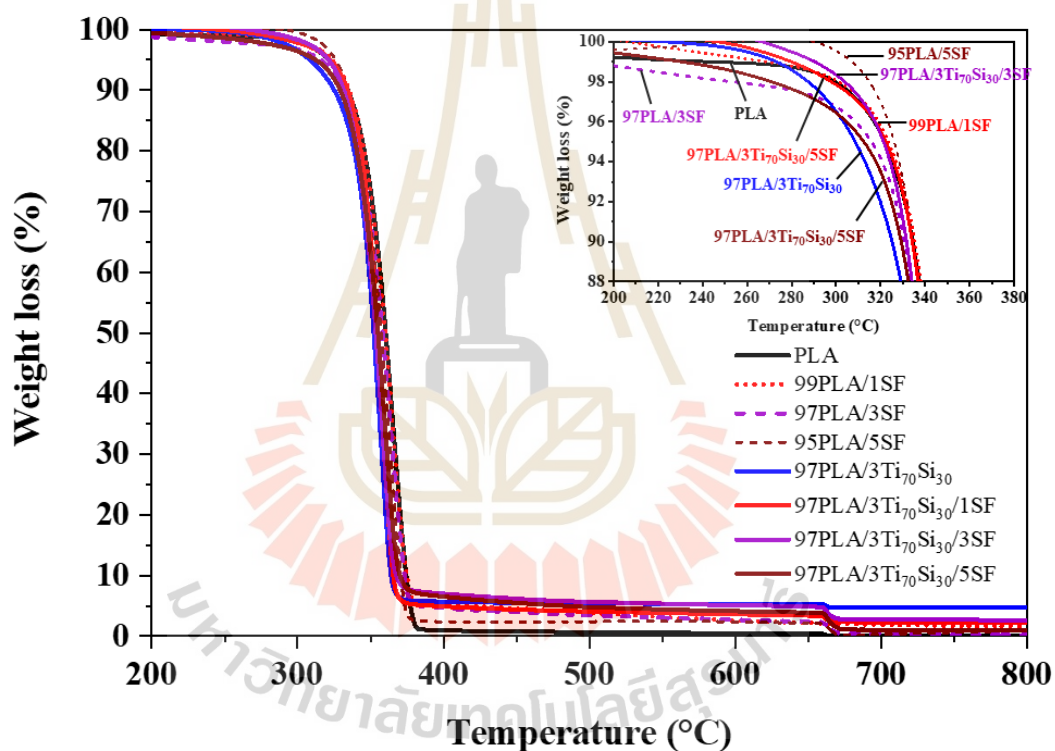


Figure 4.55 TGA thermogram of PLA, PLA/SF, PLA/Ti₇₀Si₃₀, PLA/Ti₇₀Si₃₀/SF composite at various SF contents.

In this work, the onset degradation temperature (T_{onset}) was defined by T_{0.05} to estimate the effect of SF on the thermal stability. It was clear that the T_{onset} of PLA composites shifted to a lower temperature with loading SF. In addition, T_d of of

PLA, PLA/SF, PLA/Ti₇₀Si₃₀, PLA/Ti₇₀Si₃₀/SF composite were lower than that of pure PLA. This suggest that the thermal stability of the composites decreased with adding SF.

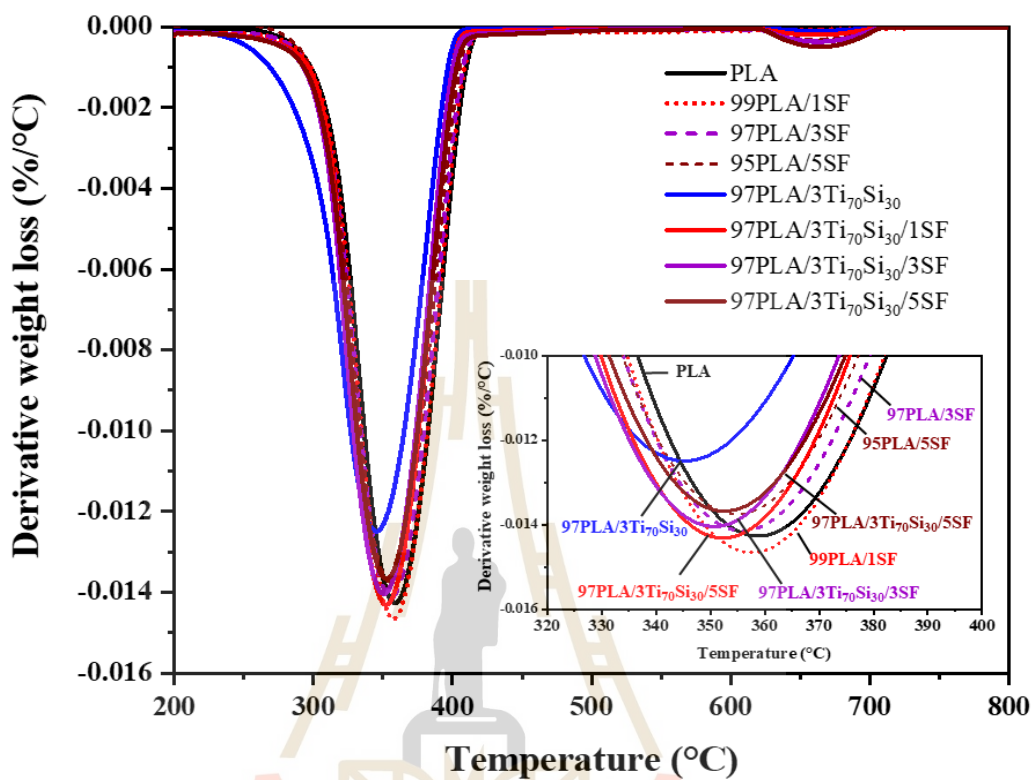


Figure 4.56 DTG Thermogram of PLA, PLA/SF, PLA/Ti₇₀Si₃₀, PLA/Ti₇₀Si₃₀/SF composite at various SF contents.

Table 4.19 Thermal degradation temperature of PLA, PLA/SF, PLA/Ti₇₀Si₃₀, PLA/Ti₇₀Si₃₀/SF composite at various SF contents.

Samples	T _{0.05} , °C	T _{0.5} , °C	T _d , °C	T _f , °C	Residual, %
PLA	321.67	360.33	358.83	424.64	1.20
99PLA/1SF	315.67	359.5	357.67	422.13	0.96
97PLA/3SF	314.00	358.00	356.02	418.65	0.54
95PLA/5SF	325.04	357.17	353.84	419.49	0.02
97PLA/3Ti ₇₀ Si ₃₀	304.00	351.83	349.83	408.68	3.91
97PLA/3Ti ₇₀ Si ₃₀ /1SF	308.17	354.00	351.34	407.23	1.97
97PLA/3Ti ₇₀ Si ₃₀ /3SF	307.33	352.83	350.02	408.58	1.24
97PLA/3Ti ₇₀ Si ₃₀ /5SF	305	354.67	349.82	409.83	1.09

4.4.4 Morphological properties of PLA/SF and PLA/Ti_xSi_y/SF composites

The fracture surface morphologies PLA/SF and PLA/Ti_xSi_y/SF composites with different SF content were observed by scanning electron microscopy (SEM) as shown in Figure 4.57 and 4.58. PLA/SF composite showed that some agglomerates can be observed when adding SF which made the micro surface of the mixed membrane rough, as (Zhu, Feng, Zhang, Guo, Zhang, and Chen, 2009) reported.

The fracture surfaces of PLA/SF and PLA/Ti_xSi_y/SF composites with different SF content after tensile testing were shown in Figure 4.59 and 4.60. SEM revealed the forming of the gap between SF and PLA matrix in the fracture surfaces for the same PLA drawn under similar conditions. In addition, more plastic deformation is visible on the fracture surfaces of the PLA composites. Occasionally, fiber-like particles were visible on the fracture surfaces of the PLA/SF and PLA/Ti_xSi_y/SF composites with Ti_xSi_y and SF filler, as shown in Figure 4.60. However, PLA/Ti_xSi_y/SF composites after tensile testing can observed some agglomerated of SF were directly pulled out from PLA matrix when the composites were broken, and these phenomena indicating the poor interfacial adhesion (Yew, Mohd Yusof, Mohd Ishak, and Ishiaku, 2005).

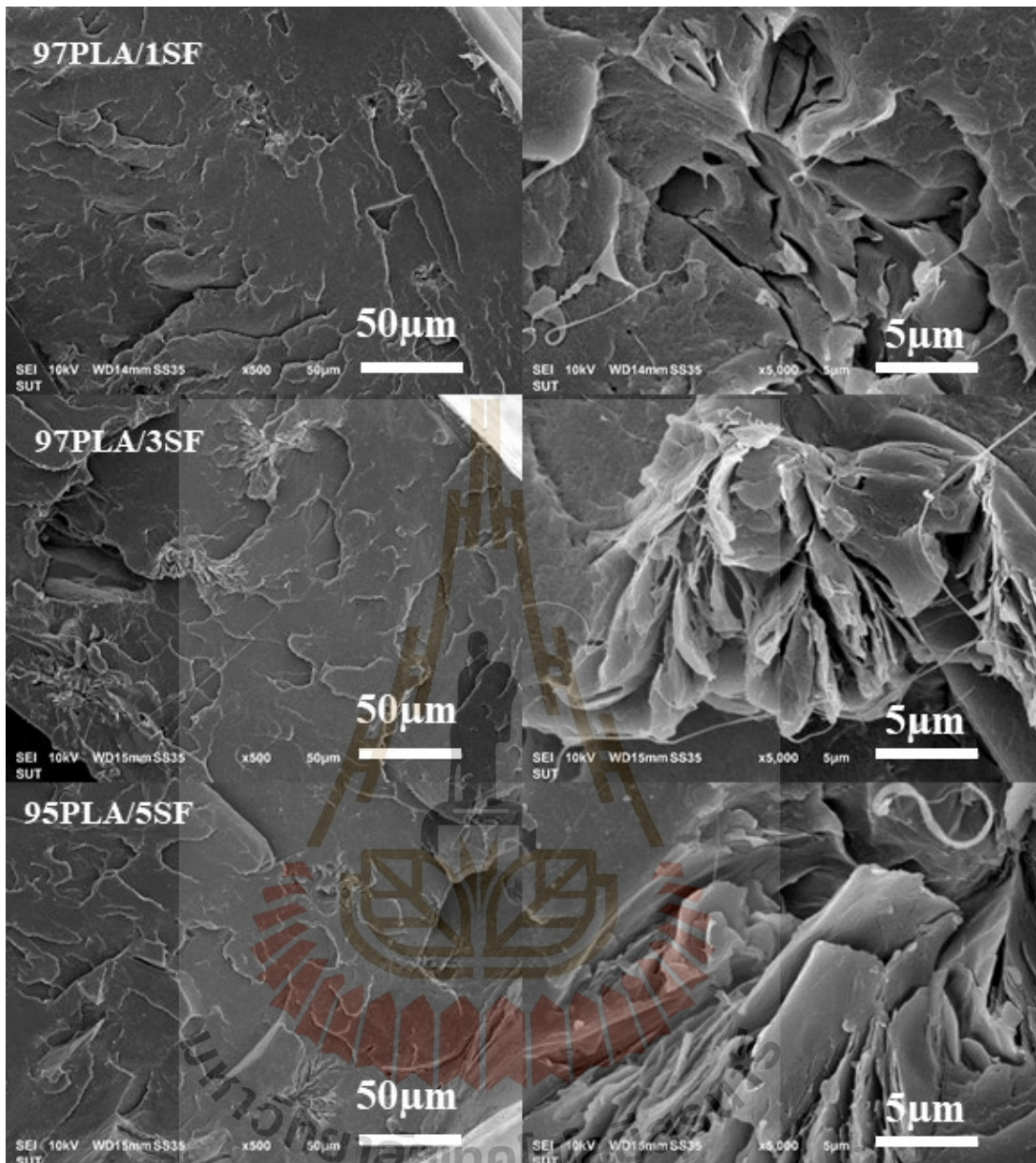


Figure 4.57 SEM micrographs of PLA/SF composite at various SF contents (Fracture surface).

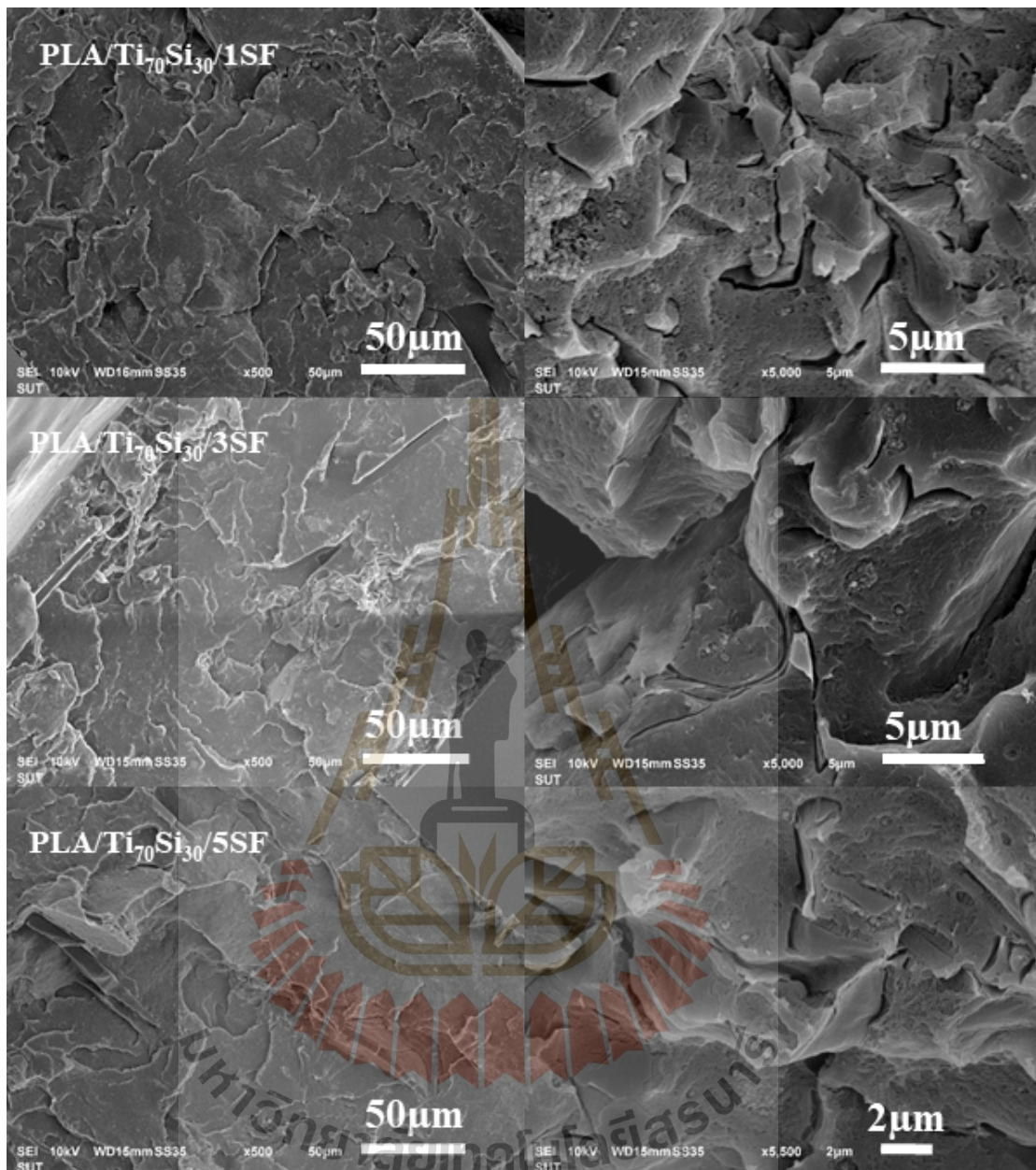


Figure 4.58 SEM micrographs of PLA/Ti₇₀Si₃₀/SF composite at various SF contents (Fracture surface).

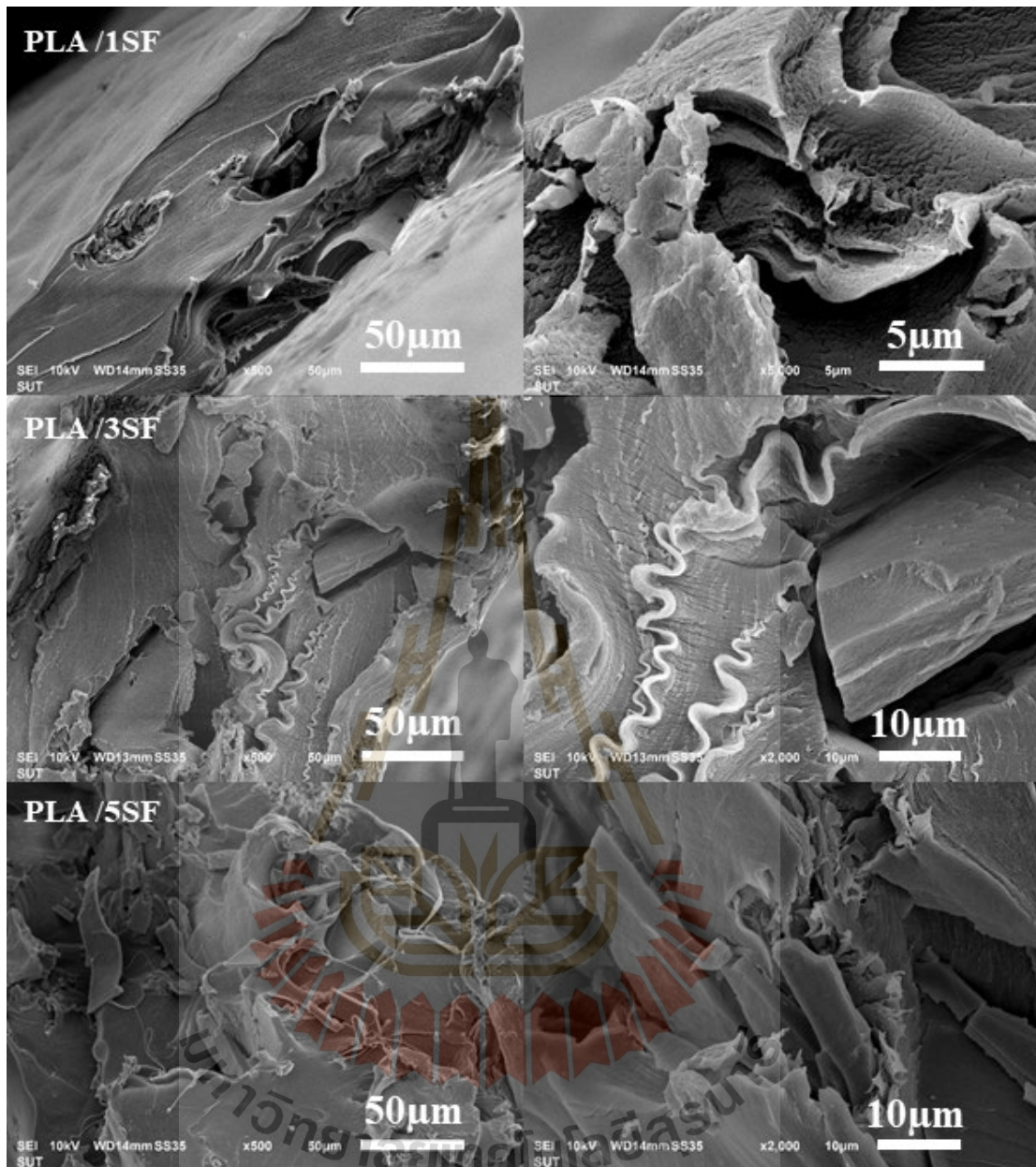


Figure 4.59 SEM micrographs of PLA/SF composite at various SF contents (after tensile test).

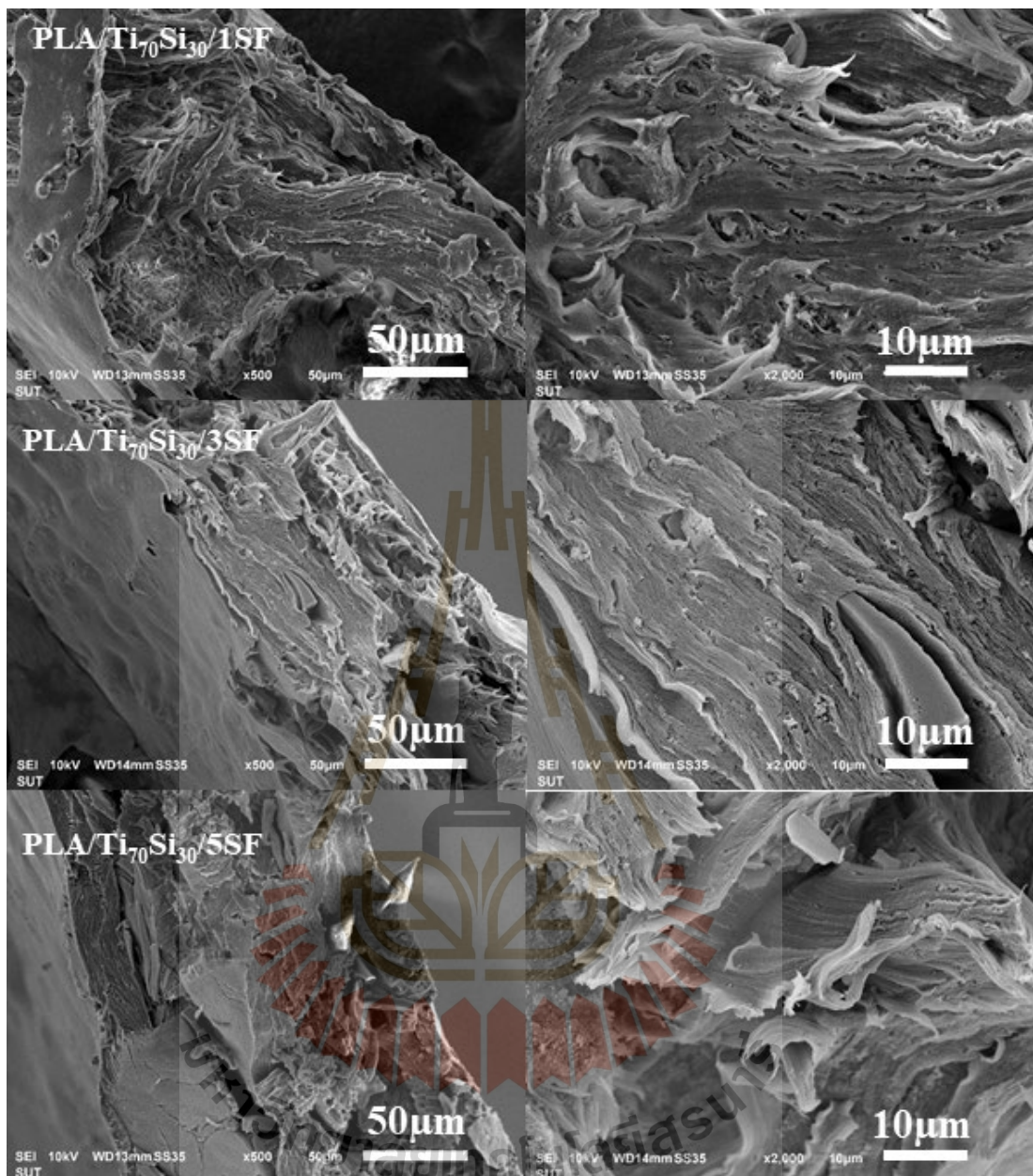


Figure 4.60 SEM micrographs of PLA/Ti₇₀Si₃₀/SF composite at various SF contents (after tensile test).

4.4.5 Water vapor transmission rate (WVTR) of PLA/SF and PLA/Ti_xSi_y/SF composites

The WVTR of PLA, PLA/SF, PLA/Ti₇₀Si₃₀, and PLA/Ti₇₀Si₃₀/SF composite films. is shown in Figure 4.61. The WVTR of PLA films was 0.316 g m⁻² day⁻¹ and it was

lower than PLA/SF composite films. PLA/SF composite film incorporating with 1, 3, and 5 wt.% of which are 1.343, 0.642 and 0.874 $\text{g m}^{-2} \text{day}^{-1}$. In addition, the WVTR of the PLA/Ti₇₀Si₃₀/SF composite film decrease with increasing SF content to 3wt.%. It is common that for a solid polymer, the water vapor transmission follows a simple mechanism including adsorbing at the entering face, dissolving and rapidly creating equilibrium, diffusing through the film, and desorbing at the exit face (Hu, Topolkaev, Hiltner, and Baer, 2001). The crystallinity in SF would lead to more indirect pathway reducing the diffusion coefficient (Choudalakis and Gotsis, 2009; Tantekin-Ersolmaz, Atalay-Oral, Tatlier, Erdem-Şenatalar, Schoeman, and Sterte, 2000).

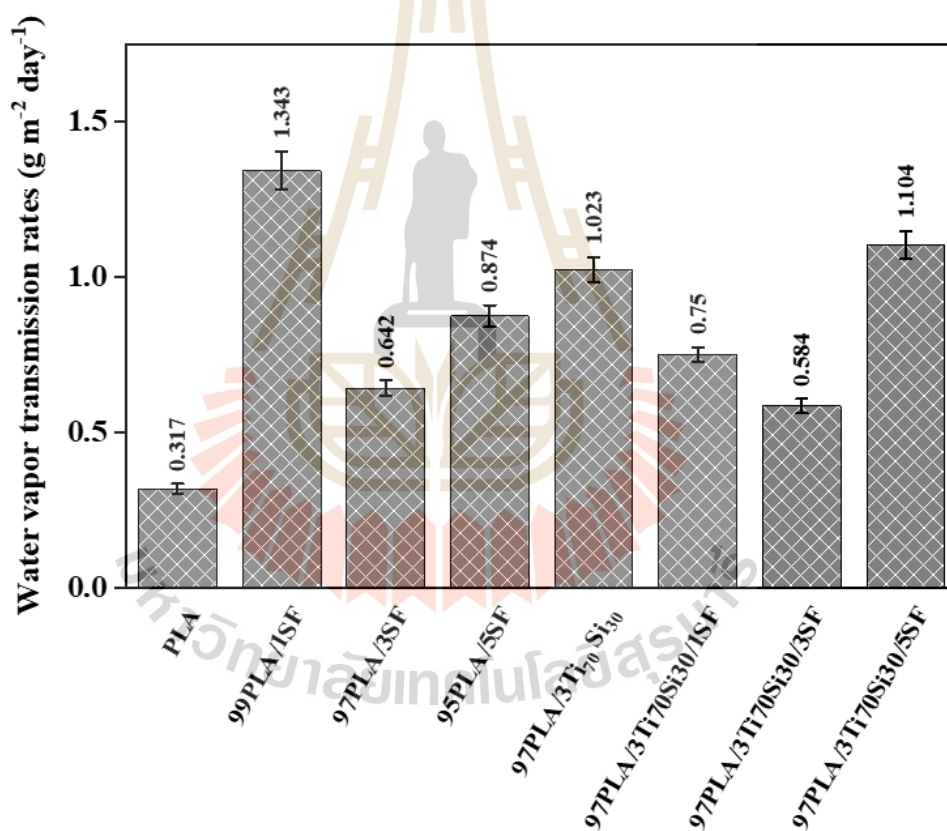


Figure 4.61 Water vapor transmission rate (WVTR) of PLA, PLA/SF, PLA/Ti₇₀Si₃₀, and PLA/Ti₇₀Si₃₀/SF composite films.

4.4.6 Light Transmittance and Opacity Measurements of PLA/SF and PLA/TixSiy/SF composites

UV light can create free radicals in products by photochemical reaction leading to unfriendly effects include deterioration of antioxidants, destruction to vitamins and proteins and changed in color. UV radiation is classified into UV-A (wavelength 320–400 nm), UVB (280–320 nm), and UV-C (200–280 nm) (Asmatulu, Mahmud, Hille, and Misak, 2011; Oleyaei, Zahedi, Ghanbarzadeh, and Moayedi, 2016).



Table 4.20 Transmittance (%) and opacity values of PLA, PLA/SF, PLA/3Ti₇₀Si₃₀ and PLA/3Ti₇₀Si₃₀/SF composites films in the visible, UV-A, UV-B, and UV-C regions.

Sample	Transmittance, %				Opacity (AU.nm.mm)
	UVC (240nm)	UVB (300nm)	UVA (360nm)	Visible (600nm)	
PLA	1.24	24.47	34.77	51.39	1.16
99PLA/1SF	0.05	4.01	8.10	19.91	2.42
97PLA/3SF	0.04	2.62	5.60	13.89	3.43
95PLA/5SF	0.03	2.53	5.25	12.02	3.41
97PLA/3Ti ₇₀ Si ₃₀	0.00	0.28	0.75	14.00	3.42
97PLA/3Ti ₇₀ Si ₃₀ /1SF	0.00	0.00	0.26	1.77	5.84
97PLA/3Ti ₇₀ Si ₃₀ /3SF	0.00	0.00	0.31	2.46	5.55
97PLA/3Ti ₇₀ Si ₃₀ /5SF	0.00	0.00	0.30	2.38	6.50

Addition of SF and $Ti_{70}Si_{30}$ oxide into PLA matrix caused a significantly decrease of transmittance in the all UV regions (Table 4.20). Particularly presence both of SF and $Ti_{70}Si_{30}$ oxide in PLA film matrix succeed to block more than 97-99% of 240, 300, 360, and 600 nm wavelengths as a representative of UV-C, UV-B, UV-A and visible radiation, respectively. The PLA films were transparent and colorless. While transparency change related to increasing from 3% up to 5wt.% SF and $Ti_{70}Si_{30}$ provided totally opaque films by more than 2 and 5 orders of magnitudes in opacity for PLA/SF and PLA/ $Ti_{70}Si_{30}$ /SF composites, respectively. Photographs of the films prepared from PLA, PLA/SF, and PLA/ $Ti_{70}Si_{30}$, and PLA/ $Ti_{70}Si_{30}$ /SF composite are shown in Figure 4.62. These results suggest that the all PLA/SF and PLA/ $Ti_{70}Si_{30}$ /SF composites supplied acceptable optical property and a good prevention against UV-visible induced destructions.

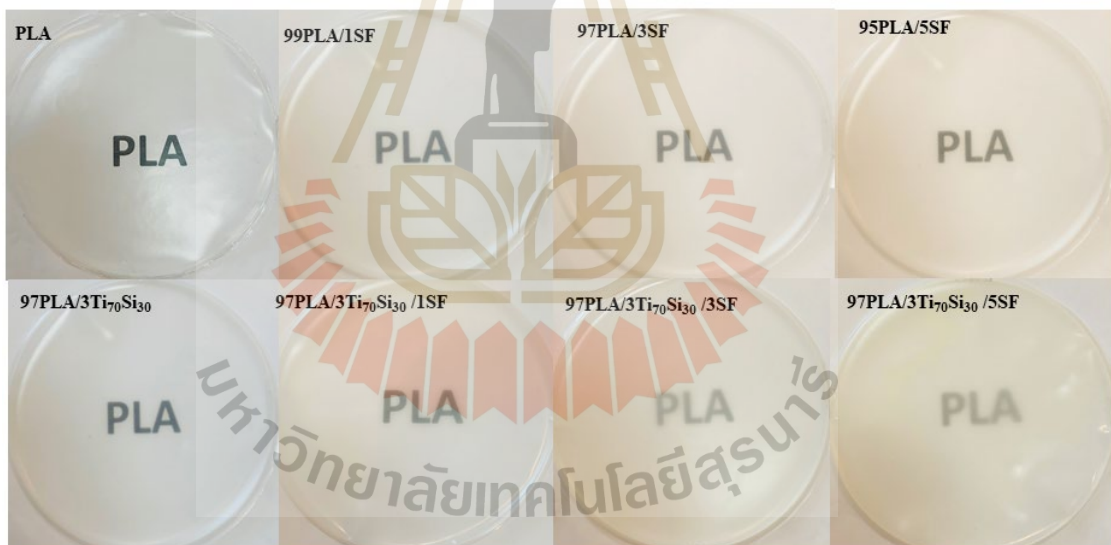


Figure 4.62 Photographs of films prepared from PLA, PLA/SF, and PLA/ $Ti_{70}Si_{30}$, and PLA/ $Ti_{70}Si_{30}$ /SF composite (250-300 μm thickness).

4.4.7 Hydrolytic degradation of PLA/SF and PLA/ $Ti_{70}Si_{30}$ /SF composites

Figure 4.63 shows the percent weight loss of PLA, PLA/SF, PLA/ $Ti_{70}Si_{30}$ and PLA/ $Ti_{70}Si_{30}$ /SF composite films as functions of degradation time in hydrolytic test.

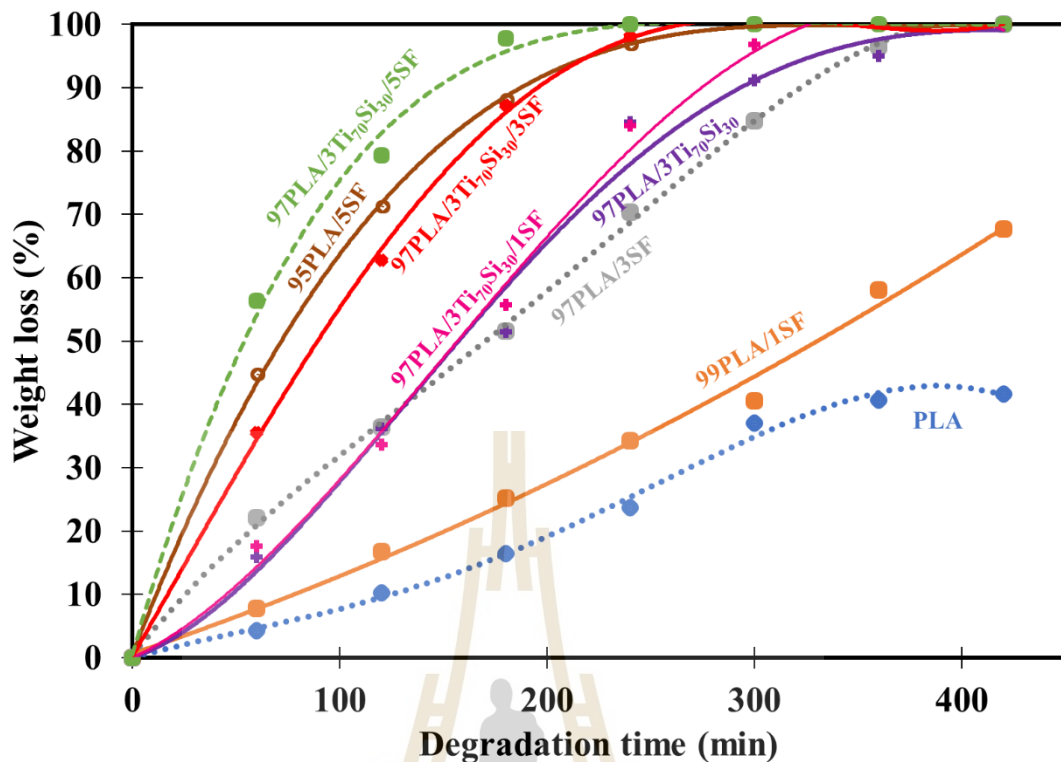


Figure 4.63 Weight loss of hydrolytic degradation of PLA, PLA/SF, PLA/Ti₇₀Si₃₀ and PLA/Ti₇₀Si₃₀/SF composite films as functions of degradation time.

The degradation of PLA film was complete about 1200 min, while all of PLA/SF, PLA/Ti₇₀Si₃₀ and PLA/Ti₇₀Si₃₀/SF composite films were hydrolyzed faster than neat PLA. Interestingly, PLA incorporating with 3 wt.% and 5 wt.%SF exhibited much higher weight loss as a function of time than neat PLA. 99PLA/1SF, 97PLA/3SF, 95PLA/5SF, 97PLA/3Ti₇₀Si₃₀/1SF, 97PLA/3Ti₇₀Si₃₀/3SF and 97PLA/3Ti₇₀Si₃₀/5SF were fully degraded at 720, 420, 300, 360, 300, and 340 min, respectively. Consequently, it could be concluded that the rate of hydrolytic degradation of PLA composites films can be controlled by type of filler and filler content. (A. Buzarovska and Grozdanov, 2012).

4.4.8 In vitro degradation of PLA/SF and PLA/Ti_xSi_y/SF composites

The long-term hydrolytic degradation of PLA and PLA composite films in a phosphate buffered saline (PBS) (pH = 7.4 ± 0.2) solution at 37°C was evaluated by mass loss in 56 days. Figure 4.64 shows the mass loss of PLA, PLA/SF, PLA/Ti₇₀Si₃₀ and

PLA/Ti₇₀Si₃₀/SF composite films with the time of degradation. From 0 to 14 days, all of samples exhibited a dramatic increase in mass loss with increasing immersion time. After this period, the mass loss of all samples accelerated gradually. 97PLA/3Ti₇₀Si₃₀/5SF exhibited higher weight loss as a function of immersion time than neat PLA.

In this case, SF and Ti₇₀Si₃₀ nanoparticle dispersed in the PLA matrix, the water molecules penetrated more easily with in the samples to generate the degradation process. The water might be absorbed in the gap between the conglomeration of nanoparticles due to the agglomeration of nanofiller. Consequently, they would employ much time on diffusing into PLA matrix. Therefore, the degradation rate increased in the first period and reached maximum (Luo, Wang, and Wang, 2012).

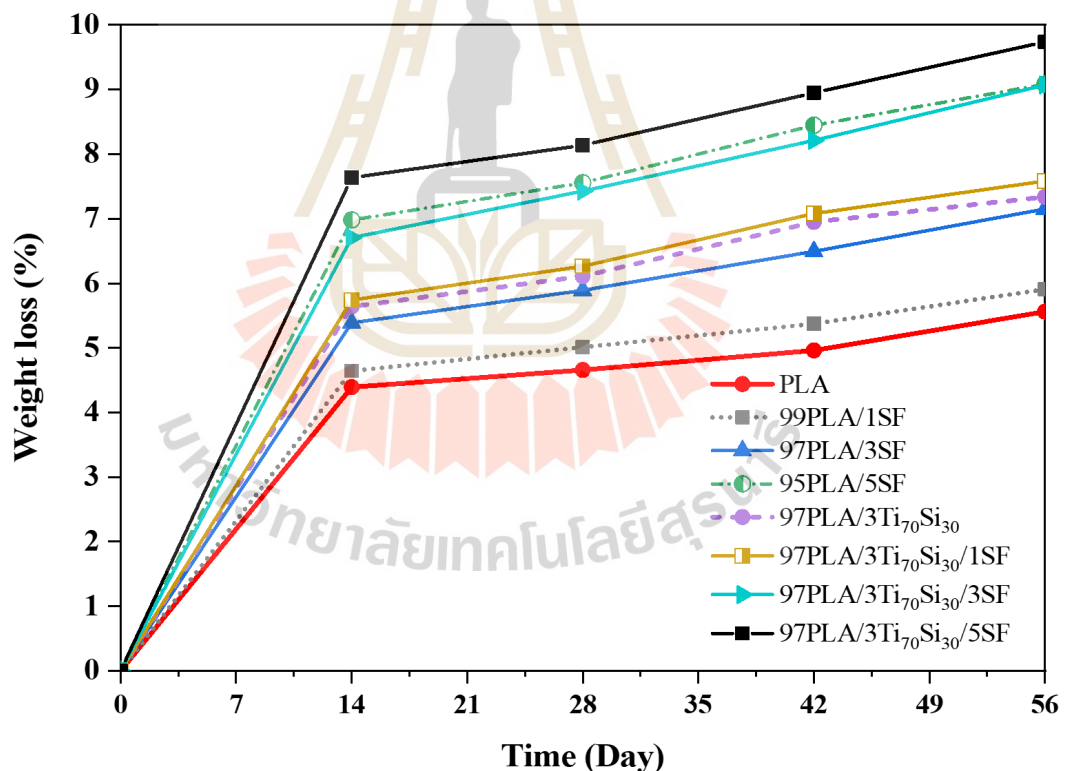


Figure 4.64 Weight loss of PLA, PLA/SF, PLA/Ti₇₀Si₃₀ and PLA/Ti₇₀Si₃₀/SF composite films after different periods of in vitro degradation.

CHAPTER V

CONCLUSIONS

In this research, the effects of pH and Ti/Si atomic ratio of Ti_xSi_y oxide by sol-gel method (Stöber method) on structural and physical properties were studied. ^{29}Si Solid-state nuclear magnetic resonance spectroscopy (^{29}Si solid-state NMR) was used to identify the formation of the framework silicon atom in Ti_xSi_y oxide. The ^{29}Si -NMR spectra showed of Q^2 groups, which may correspond to tetrahedra of disubstituted silica, probably due also to the presence of Ti-O-Si-O-Ti-O groups suggesting an important presence of Si-O-Ti bonds in this sample indicative of atomic mixing. Ti-O-Si vibration of Ti_xSi_y oxide was confirmed by FTIR at 949 cm^{-1} indicating the forming of chemical bond between TiO_2 and SiO_2 . The synthesized $Ti_{70}Si_{30}$ oxides nanoparticles at pH 9.0 were homogeneous with a respectable nanostructure with spherical form. XRD results of Ti_xSi_y oxides presented a broad diffraction peak within the 2θ range 10–40 corresponding to characteristic of amorphous silica. This indicated that the titanium was highly dispersed in the silica matrix. The large pre-edge feature of XANES spectra of all Ti_xSi_y oxide samples confirms that the greater number of Ti occupies sites of tetrahedral symmetry in the Ti_xSi_y oxide. The Ti-O and Ti-Si distances were about 1.9 and 2.8 Å, respectively. In addition, the averaged diameter of Ti_xSi_y oxide was in range of 131-150 nm. Specific surface area, S_{BET} of $569.70\text{ m}^2\text{g}^{-1}$ and pore volume of $1.42\text{ cm}^3\text{g}^{-1}$ have been obtained for $Ti_{70}Si_{30}$ oxide.

The addition of 3 wt.% of $Ti_{70}Si_{30}$ oxide into PLA film improved the tensile strength and Young's modulus of PLA. The incorporation of 5wt.% of $Ti_{70}Si_{30}$ decreased the cold crystallization temperature and increased degree of crystallinity of PLA. Thermal stability of PLA was enhanced with the incorporation of TiO_2 and SiO_2 . Water vapor transmission rate (wvtr) of PLA was significantly increased by incorporation of SiO_2 , $Ti_{70}Si_{30}$, and $Ti_{50}Si_{50}$ nanoparticle. This due to the hydrophilicity of nanoparticles. In this work, the efficiency to degrade MB of nanoparticles was $TiO_2 > Ti_{70}Si_{30} > TiO_2SiO_2 > Ti_{50}Si_{50} > Ti_{40}Si_{60} > SiO_2$, respectively. Moreover, 97PLA/5 $Ti_{70}Si_{30}$ improved

efficiency of photocatalytic activity of PLA. Ti_xSi_y nanoparticles were able to remove UV light, particularly $Ti_{70}Si_{30}$ enhanced a stronger higher UV-shielding potential. Hydrolytic degradation and *in vitro* degradation of PLA are important property of variety of application such as biomedical application and food packaging. PLA incorporating with 3 wt.% SiO_2 , $Ti_{70}Si_{30}$, $Ti_{50}Si_{50}$, $Ti_{40}Si_{60}$ and TiO_2SiO_2 exhibited much higher weight loss as a function of time than neat PLA. The weight loss of PLA nanocomposite was also found to increase with increasing $Ti_{70}Si_{30}$ to 5%wt. Furthermore, PLA adding TiO_2 and $Ti_{70}Si_{30}$ exhibited excellent antibacterial effect on gram-negative bacteria (*E. coli*) and gram-positive bacteria (*S. aureus*) indicating the improved antimicrobial effectiveness of PLA nanocomposites.

To prepare PLA/SF and PLA/ Ti_xSi_y /SF composite, silk fibroin (SF) powder can be prepared in-house by re-dissolving in $CaCl_2$ solution at $100^\circ C$. The structural morphological and thermal properties were investigated by FTIR, SEM, and TGA analysis.

All of PLA/SF and composite showed the higher elongation at break than neat PLA, especially at 3wt.% of SF while the tensile strength and Young's modulus were lower than PLA. Incorporation with SF and $Ti_{70}Si_{30}$, increased tensile strength and Young's modulus of PLA. Elongation at break of all PLA/ $Ti_{70}Si_{30}$ /SF composite was higher than neat PLA. SF revealed insignificant effect on T_g , and T_m of the composite but reduce ΔH_m and ΔH_c . Furthermore, T_{cc} of PLA increased. It may be concluded that SF cannot act as a nucleating agent for PLA. T_{onset} of PLA was enhanced with the incorporation of 5wt.% of SF content but decreased with adding $Ti_{70}Si_{30}$ oxide. Water vapor transmission rate (wvtr) of PLA was significantly increased by incorporation of SF due to the hydrophilicity of SF. Moreover, opacity of PLA/SF, and PLA/ Ti_xSi_y composites increased with increasing SF content and exhibited good preventing against UV-Visible light. All of PLA composites incorporating with SF and $Ti_{70}Si_{30}$ exhibited much higher weight loss as a function of time than neat PLA. The weight loss of PLA/SF nanocomposite was also found to increase with increasing SF content.

REFERENCES

- Ajisawa, A. (1998). Dissolution of silk fibroin with calcium chloride/ethanol aqueous solution; studies on the dissolution of silk fibroin. *J. Sericult. Sci. Jpn.* 67(2): 91-94.
- Alias, S. S., Ismail, A. B., and Mohamad, A. A. (2010). Effect of pH on ZnO nanoparticle properties synthesized by sol-gel centrifugation. *J. Alloys Compd.* 499(2): 231-237.
- Aoki, S., Kinoshita, M., Miyazaki, H., Saito, A., Fujie, T., Iwaya, K., Takeoka, S., and Saitoh, D. (2013). Application of poly-L-lactic acid nanosheet as a material for wound dressing. *Plast. Reconstr. Surg.* 131(2): 236-240.
- Aragón-Santamaría, P., Santos-Delgado, M. J., Maceira-Vidán, A., and Polo-Díez, L. M. (1991). Electron microscopic study of the morphology of lead sulphide and silver sulphide crystals obtained by the silica gel crystal growth technique. *J. Mater. Chem.* 1(3): 409-413.
- Archana, D., Singh, B. K., Dutta, J., and Dutta, P. K. (2013). In vivo evaluation of chitosan-PVP-titanium dioxide nanocomposite as wound dressing material. *Carbohydr. Polym.* 95(1): 530-539.
- Asakura, T., Kuzuhara, A., Tabeta, R., and Saito, H. (1985). Conformational characterization of Bombyx mori silk fibroin in the solid state by high-frequency carbon-13 cross polarization-magic angle spinning NMR, x-ray diffraction, and infrared spectroscopy. *Macromolecules.* 18(10): 1841-1845.
- Asmatulu, R., Mahmud, G. A., Hille, C., and Misak, H. E. (2011). Effects of UV degradation on surface hydrophobicity, crack, and thickness of MWCNT-based nanocomposite coatings. *Prog. Org. Coat.* 72(3): 553-561.
- Athanasiou, K. A., Niederauer, G. G., and Agrawal, C. M. (1996). Sterilization, toxicity, biocompatibility and clinical applications of polylactic acid/ polyglycolic acid copolymers. *Biomaterials.* 17(2): 93-102.

- Auras, R., Harte, B., and Selke, S. (2004). An overview of polylactides as packaging materials. *Macromol. Biosci.* 4(9): 835-864.
- Avolio, R., Castaldo, R., Avella, M., Cocca, M., Gentile, G., Fiori, S., and Errico, M. E. (2018). PLA-based plasticized nanocomposites: Effect of polymer/plasticizer/filler interactions on the time evolution of properties. *Compos. B. Eng.* 152: 267-274.
- Ayoub, N., Garb, J., Tinghitella, R., Collin, M., and Hayashi, C. (2007). Blueprint for a high-performance biomaterial: full-length spider dragline silk genes. *PloS one.* 2(6): 1-13.
- Bai, L., Li, Q., Duo, X., Hao, X., Zhang, W., Shi, C., Guo, J., Ren, X., and Feng, Y. (2017). Electrospun PCL-PIBMD/SF blend scaffolds with plasmid complexes for endothelial cell proliferation. *RSC Adv.* 7(63): 39452-39464.
- Battegazzore, D., Bocchini, S., and Frache, A. (2011). Crystallization kinetics of poly (lactic acid)-talc composites. *eXPRESS Polym. Lett.* 5(10): 849-858.
- Burg, K. J. L., Holder, W. D., Culberson, C. R., Beiler, R. J., Greene, K. G., Loeb sack, A. B., Roland, W. D., Mooney, D. J., and Halberstadt, C. R. (1999). Parameters affecting cellular adhesion to polylactide films. *J Biomater Sci Polym Ed.* 10(2): 147-161.
- Buzarovska, A. (2013). PLA nanocomposites with functionalized TiO₂ nanoparticles. *Polym Plast Technol Eng.* 52(3): 280-286.
- Buzarovska, A., and Grozdanov, A. (2012). Biodegradable poly (L -lactic acid)/TiO₂ nanocomposites: Thermal properties and degradation. *J. Appl. Polym. Sci.* 123(4): 2187-2193.
- Chen, H.-M., Wang, X.-F., Liu, D., Wang, Y.-P., Yang, J.-H., Wang, Y., Zhang, C.L., and Zhou, Z.-W. (2014). Tuning the interaction of an immiscible poly(l-lactide)/poly (vinylidene fluoride) blend by adding poly (methyl methacrylate) via a competition mechanism and the resultant mechanical properties. *RSC Adv.* 4(76); 40569-40579.
- Cai, Y.-H., and Zhao, L.-S. (2016). Thermal behavior of modified poly (L-lactic acid): effect of aromatic multiamide derivative based on 1H-benzotriazole. *E-Polymers.* 16: 303.

- Cai, Y., Yan, S., Fan, Y., Yu, Z., Chen, X., and Yin, J. (2012). The nucleation effect of N, N'-bis(benzoyl) alkyl diacid dihydrazides on crystallization of biodegradable poly (l-lactic acid). *Iran. Polym. J.* 21(7): 435-444.
- Cao, Y., and Wang, B. (2009). Biodegradation of silk biomaterials. *Int. J. Mol. Sci.* 10(4): 1514-1524.
- Chen, H.-M., Wang, X.-F., Liu, D., Wang, Y.-P., Yang, J.-H., Wang, Y., Zhang, C.-L., and Zhou, Z.-W. (2014). Tuning the interaction of an immiscible poly(l-lactide)/poly (vinylidene fluoride) blend by adding poly (methyl methacrylate) via a competition mechanism and the resultant mechanical properties. *RSC Adv.* 4(76): 40569-40579.
- Chen, L., Zheng, K., and Liu, Y. (2017). Geopolymer-supported photocatalytic TiO₂ film: Preparation and characterization. *Constr. Build. Mater.* 151: 63-70.
- Chen, P., Zhou, H., Liu, W., Zhang, M., Du, Z., and Wang, X. (2015). The synergistic effect of zinc oxide and phenylphosphonic acid zinc salt on the crystallization behavior of poly (lactic acid). *Polym. Degrad. Stab.* 122: 25-35.
- Chen, R-Y., Zou, W., Wu, C-R., Jia, S-K., Huang, Z., Zhang, G-Z., Yang, Z-T., and Qu, J-P. (2014). Poly (lactic acid)/poly (butylene succinate)/calcium sulfate whiskers biodegradable blends prepared by vane extruder: Analysis of mechanical properties, morphology, and crystallization behavior. *Polym. Test.* 34: 1-9.
- Cheung, H. Y., Lau, K. T., Tao, X. M., and Hui, D. (2008). A potential material for tissue engineering: Silkworm silk/PLA biocomposite. *Compos. B. Eng.* 39(6): 1026-1033.
- Chiahung, H., Hsunling, B., Yaoling, H., Shuling, L., Shaoi, Y., and Yaohsuan, T. (2012). Synthesis of neutral SiO₂/TiO₂ hydrosol and its application as antireflective self-cleaning thin film. *Int. J. Photoenergy.* 2012.
- Chitrattha, S., and Phaechamud, T. (2016). Porous poly (DL-lactic acid) matrix film with antimicrobial activities for wound dressing application. *Mater. Sci. Eng. C.* 58(Supplement C): 1122-1130.
- Choudalakis, G., and Gotsis, A. D. (2009). Permeability of polymer/clay nanocomposites: A review. *Eur. Polym. J.* 45(4): 967-984.

- Chu, Z., Zhao, T., Li, L., Fan, J., and Qin, Y. (2017). Characterization of antimicrobial poly (lactic acid)/nano-composite films with silver and zinc oxide nanoparticles. *Materials*. 10(6): 659.
- Cui, R., Jiang, K., Yuan, M., Cao, J., Li, L., Tang, Z., and Qin, Y. (2020). Antimicrobial film based on polylactic acid and carbon nanotube for controlled cinnamaldehyde release. *J. Mater. Res. Technol.* 9(5): 10130-10138.
- Davis, R. J., and Liu, Z. (1997). Titania-Silica: A model binary oxide catalyst system. *Chem. Mater.* 9(11): 2311-2324.
- DeBari, M. K., and Abbott, R. D. (2019). Microscopic considerations for optimizing silk biomaterials. *WIREs Nanomed. Nanobiotechnol.* 11(2): e1534.
- Degirmenci, V., Erdem, Ö. F., Ergun, O., Yilmaz, A., Michel, D., and Uner, D. (2008). Synthesis and NMR characterization of titanium and zirconium oxides incorporated in SBA-15. *Top Catal.* 49(3): 204-208.
- Dintcheva, N. T., and Al-Malaika, S. (2020). Photo-stabilization of biopolymers-based nanocomposites with UV-modified layered silicates. *Polym. Degrad. Stab.* 179: 109252.
- Dirken, P. J., Smith, M. E., and Whitfield, H. J. (1995). ^{17}O and ^{29}Si solid state NMR study of atomic scale structure in sol-gel-prepared $\text{TiO}_2\text{-SiO}_2$ materials. *J. Phys. Chem.* 99(1): 395-401.
- Dutoit, D. C. M., Schneider, M., and Baiker, A. (1995). Titania-silica mixed oxides: I. Influence of sol-gel and drying conditions on structural properties. *J. Catal.* 153(1): 165-176.
- Elsner, J. J., Shefy-Peleg, A., and Zilberman, M. (2010). Novel biodegradable composite wound dressings with controlled release of antibiotics: microstructure, mechanical and physical properties. *J Biomed Mater Res B Appl Biomater.* 93(2): 425-435.
- Etacheri, V., Di Valentin, C., Schneider, J., Bahnemann, D., and Pillai, S. C. (2015). Visible-light activation of TiO_2 photocatalysts: Advances in theory and experiments. *J. Photochem. Photobiol., C.* 25(Supplement C); 1-29.

- Fathi Achachlouei, B., and Zahedi, Y. (2018). Fabrication and characterization of CMC-based nanocomposites reinforced with sodium montmorillonite and TiO₂ nanomaterials. *Carbohydr. Polym.* 199: 415-425.
- Felfel, R. M., Leander, P., Miquel, G.-F., Tobias, M., Gerhard, H., Ifty, A., Colin, S., Virginie, S., David, M. G., and Klaus, L. (2016). In vitro degradation and mechanical properties of PLA-PCL copolymer unit cell scaffolds generated by two-photon polymerization. *Biomed. Mater.* 11(1); 015011.
- Fernandez, T., Jose, G., Mathew, S., Pr, R., and Nv, U. (2007). An ultra-low hydrolysis sol-gel route for titanosilicate xerogels and their characterization. *J. Sol-Gel Sci. Technol.* 41(2): 163-168.
- Fonseca, C., Ochoa, A., Ulloa, M. T., Alvarez, E., Canales, D., and Zapata, P. A. (2015). Poly (lactic acid)/TiO₂ nanocomposites as alternative biocidal and antifungal materials. *Mater. Sci. Eng. C.* 57: 314-320.
- Fu, G., Vary, P. S., and Lin, C.-T. (2005). Anatase TiO₂ nanocomposites for antimicrobial coatings. *J. Phys. Chem. B.* 109(18): 8889-8898.
- Gao, X., and Wachs, I. E. (1999). Titania-silica as catalysts: molecular structural characteristics and physico-chemical properties. *Catalysis Today.* 51(2): 233-254.
- Garlotta, D., Doane, W., Shogren, R., Lawton, J., and Willett, J. L. (2003). Mechanical and thermal properties of starch-filled poly (D, L-lactic acid)/poly (hydroxy ester ether) biodegradable blends. *J. Appl. Polym. Sci.* 88(7): 1775-1786.
- Ge, H., Zhu, Z., Yin, H., Zhang, X., and Wang, R. (2014). Fabrication and properties of *sc*-PLA/SiO₂ composites. Paper presented at the IOP Conference Series: Mater. Sci. Eng.
- Ghalia, M. A., and Dahman, Y. (2017). Investigating the effect of multi-functional chain extenders on PLA/PEG copolymer properties. *Int. J. Biol. Macromol.* 95: 494-504.
- Gregg S. J., and Sing, K. S. W. (1982). Adsorption, surface area and porosity Auflage (2 ed. Vol. 86). Academic Press, London: John Wiley & Sons, Ltd.
- Grieken, R., Aguado, J., López-Muñoz, M. J., and Marugán, J. (2010). Sol-gel titania and titania-silica mixed oxides photocatalysts. *Solid State Phenom.* 162: 221-238.

- Gupta, K. K., Mishra, P. K., Srivastava, P., Gangwar, M., Nath, G., and Maiti, P. (2013). Hydrothermal in situ preparation of TiO₂ particles onto poly (lactic acid) electrospun nanofibres. *Appl. Surf. Sci.* 264: 375-382.
- Ha, S.-W., Weitzmann, M. N., and Beck Jr, G. R. (2013). Chapter 4 - Dental and Skeletal Applications of Silica-Based Nanomaterials A2 - Subramani, Karthikeyan. In W. Ahmed & J. K. Hartsfield (Eds.), *Nanobiomaterials in Clinical Dentistry* (pp. 69-91): William Andrew Publishing.
- Haggerty, J. E. S., Schelhas, L. T., Kitchaev, D. A., Mangum, J. S., Garten, L. M., Sun, W., Stone, K. H., Perkins, J. D., Toney, M. F., Ceder, G., Ginley, D. S., Gorman, B. P., and Tate, J. (2017). High-fraction brookite films from amorphous precursors. *Sci. Rep.* 7(1); 15232.
- Hakim, R. H., Cailloux, J., Santana, O. O., Bou, J., Sánchez-Soto, M., Odent, J., Raquez, J. M., Dubois, P., Carrasco, F., and MasPOCH, M. L. (2017). PLA/SiO₂ composites: Influence of the filler modifications on the morphology, crystallization behavior, and mechanical properties. *J. Appl. Polym. Sci.* 134(40); 45367.
- Hamdan, H. H. (2012). Fabrication of TiO₂ nanotubes using electrochemical anodization. (Master of Science in Physics). University of Baghdad. *Baghdad Sci. J.*
- Haraguchi, K. (2021). Biocomposites. In S. Kobayashi & K. Müllen (Eds.), *Encyclopedia of polymeric nanomaterials* (pp. 1-8). Berlin, Heidelberg: Springer Berlin Heidelberg.
- Hench, L. L., and West, J. K. (1990). The sol-gel process. *Chem. Rev.* 90(1): 33-72.
- Henton, D. E., Gruber, P., Lunt, J., and Randall, J. (2005). Polylactic acid technology. In M. M. L. T. D. Amar K. Mohanty, ed (Ed.), *Natural Fiber, biopolymer, and Biocomposites* (pp. 527-578): CRC Press Tylor & Francis Group.
- Holland, C., Numata, K., Rnjak-Kovacina, J., and Seib, F. P. (2019). The biomedical use of silk: past, present, future. *Adv. Healthcare Mater.* 8(1): 1800465.
- Hu, Y., Topolkaev, V., Hiltner, A., and Baer, E. (2001). Measurement of water vapor transmission rate in highly permeable films. *J. Appl. Polym. Sci.* 81(7): 1624-1633.

- Huang, F., Motealleh, B., Zheng, W., Janish, M. T., Carter, C. B., and Cornelius, C. J. (2017). Electrospinning amorphous $\text{SiO}_2\text{-TiO}_2$ and TiO_2 nanofibers using sol-gel chemistry and its thermal conversion into anatase and rutile. *Ceram. Int.*
- Huang, J., Wong Po Foo, C., and Kaplan, D. L. (2007). Biosynthesis and applications of silk-like and collagen-like proteins. *Polym. Rev.* 47(1): 29-62.
- Huang, S.-M., Hwang, J.-J., Liu, H.-J., and Lin, L.-H. (2010). Crystallization behavior of poly (L-lactic acid)/montmorillonite nanocomposites. *J. Appl. Polym. Sci.* 117(1): 434-442.
- Jiang, L., Liu, B., and Zhang, J. (2009). Properties of poly (lactic acid)/poly (butylene adipate-co-terephthalate)/nanoparticle ternary composites. *Ind. Eng. Chem. Res.* 48(16): 7594-7602.
- Joost, U., Juganson, K., Visnapuu, M., Mortimer, M., Kahru, A., Nõmmiste, E., Joost, U., Kisand, V., and Ivask, A. (2015). Photocatalytic antibacterial activity of nano- TiO_2 (anatase)-based thin films: Effects on *Escherichia coli* cells and fatty acids. *J. Photochem. Photobiol., B.* 142: 178-185.
- Karkare, M. M. (2014). Choice of precursor not affecting the size of anatase TiO_2 nanoparticles but affecting morphology under broader view. *Int. Nano Lett.* 4(3): 111.
- Kaseem, M., Hamad, K., and Ur Rehman, Z. (2019). Review of Recent Advances in Polylactic Acid/ TiO_2 Composites. *Materials (Basel, Switzerland)*. 12(22): 3659.
- Khankrua, R., Pivsa-Art, S., Hiroyuki, H., and Suttiruengwong, S. (2013). Thermal and mechanical properties of biodegradable polyester/silica nanocomposites. *Energy Procedia*. 34(Supplement C): 705-713.
- Khemthong, P., Photai, P., and Grisdanurak, N. (2013). Structural properties of CuO/TiO_2 nanorod in relation to their catalytic activity for simultaneous hydrogen production under solar light. *Int. J. Hydrogen Energy*. 38(36): 15992-16001.
- Kim, T. G., An, G. S., Han, J. S., Hur, J. U., Park, B. G., and Choi, S.-C. (2017). Synthesis of size controlled spherical silica nanoparticles via sol-gel process within hydrophilic solvent. *J. Korean Ceram. Soc.* 54(1): 49-54.

- Kim, U.-J., Park, J., Joo Kim, H., Wada, M., and Kaplan, D. L. (2005). Three-dimensional aqueous-derived biomaterial scaffolds from silk fibroin. *Biomaterials*. 26(15): 2775-2785.
- Kim, W. B., Choi, S. H., and Lee, J. S. (2000). Quantitative analysis of Ti–O–Si and Ti–O–Ti bonds in Ti–Si binary oxides by the linear combination of XANES. *J. Phys. Chem. B*. 104(36): 8670-8678.
- Klein, L. C. (1985). Sol-Gel processing of silicates. *Annu. Rev. Mater. Sci* 15(1): 227-248.
- Klysubun, W., Tarawarakarn, P., Thamsanong, N., Amonpattaratkit, P., Cholsuk, C., Lapboonrueng, S., Chaichuay, S., and Wongtepa, W. (2020). Upgrade of SLRI BL8 beamline for XAFS spectroscopy in a photon energy range of 1–13 keV. *Int. J. Radiat. Phys. Chem*. 175: 108145.
- Kosuge, K. (1999). Titanium-containing porous silica prepared by a modified sol–gel method. *J. Phys. Chem. B*. 103(18): 3563-3569.
- Kundu, B., Rajkhowa, R., Kundu, S. C., and Wang, X. (2013). Silk fibroin biomaterials for tissue regenerations. *Adv. Drug Delivery Rev*. 65(4): 457-470.
- La Mantia, F. P., and Morreale, M. (2011). Green composites: A brief review. *Compos. Part A Appl. Sci. Manuf*. 42(6): 579-588.
- Lee, D. W., and Yoo, B. R. (2016). Advanced silica/polymer composites: Materials and applications. *J. Ind. Eng. Chem*. 38(Supplement C): 1-12.
- Lee, J., Lee, J. K., Park, B. H., Busnaina, A., and Lee, H. Y. (2013). Acceleration of poly(L-Lactide) degradation by TiO₂ nanoparticles in sunlight. *J. Nanosci. Nanotechnol*. 13(10): 6983-6987.
- Lee, K.-B., Yoon, K. R., Woo, S. I., and Choi, I. S. (2003). Surface modification of poly (glycolic acid) (PGA) for biomedical applications. *J. Pharm. Sci*. 92(5): 933-937.
- Li, G., Li, Y., Chen, G., He, J., Han, Y., Wang, X., and Kaplan, D. L. (2015). Silk-based biomaterials in biomedical textiles and fiber-based implants. *Adv. Healthcare Mater*. 4(8): 1134-1151.
- Li, H., and Huneault, M. A. (2007). Effect of nucleation and plasticization on the crystallization of poly (lactic acid). *Polymer*. 48(23): 6855-6866.
- Li Hsiung, T., Paul Wang, H., and Wang, H. C. (2006). XANES studies of photocatalytic active species in nano TiO₂–SiO₂. *Radiat. Phys. Chem*. 75(11): 2042-2045.

- Li, K.-T., Tsai, L.-D., Wu, C.-H., and Wang, I. (2013). Lactic acid esterification on titania-silica binary oxides. *Ind. Eng. Chem. Res.* 52(13): 4734-4739.
- Liao, R., Yang, B., Yu, W., and Zhou, C. (2007). Isothermal cold crystallization kinetics of polylactide/nucleating agents. *J. Appl. Polym. Sci.* 104(1): 310-317.
- Lima, J. C., Sousa, J. C., Arruda, S. A., Almeida, Y. M. B., and Canedo, E. L. (2019). Polycaprolactone matrix composites reinforced with brown coir: Rheological, crystallization, and mechanical behavior. *Polym. Compos.* 40(S1): E678-E686.
- Liu, G., Liu, Y., Yang, G., Li, S., Zu, Y., Zhang, W., and Jia, M. (2009). Preparation of titania-silica mixed oxides by a sol-gel route in the presence of citric acid. *J. Phys. Chem. C.* 113(21): 9345-9351.
- Liu, J., Jiang, H., and Chen, L. (2012). Grafting of glycidyl methacrylate onto poly(lactide) and properties of PLA/Starch blends compatibilized by the grafted copolymer. *J. Polym. Environ.* 20(3): 810-816.
- Liu, W., Li, Z., Zheng, L., Zhang, X., Liu, P., Yang, T., and Han, B. (2016). Electrospun fibrous silk fibroin/poly (L-lactic acid) scaffold for cartilage tissue engineering. *J. Tissue Eng. Regen. Med.* 13(5): 516-526.
- Liu, Y., Liang, X., Zhang, R., Lan, W., and Qin, W. (2017). Fabrication of electrospun polylactic acid/cinnamaldehyde/ β -cyclodextrin fibers as an antimicrobial wound dressing. *Polymers.* 9(10): 464.
- Liu, Z., and Davis, R. J. (1994). Investigation of the structure of microporous Ti-Si mixed oxides by X-ray, UV Reflectance, FT-Raman, and FT-IR spectroscopies. *J. Phys. Chem.* 98(4): 1253-1261.
- Luo, Y., Cao, Y., and Guo, G. (2018). Effects of TiO₂ nanoparticles on the photodegradation of poly (lactic acid). *J. Appl. Polym. Sci.* 135(30): 46509.
- Luo, Y., Lin, Z., and Guo, G. (2019). biodegradation assessment of poly (lactic acid) filled with functionalized titania nanoparticles (PLA/TiO₂) under compost conditions. *Nanoscale Res. Lett.* 14(1): 56.
- Luo, Y. B. (2014) A further research on the properties of PLA/TiO₂ nanocomposites. *Appl. Mech. Mater.* 608-609:996-1000.
- Luo, Y. B., Wang, X. L., and Wang, Y. Z. (2012). Effect of TiO₂ nanoparticles on the long-term hydrolytic degradation behavior of PLA. *Polym. Degrad. Stab.* 97.

- Malikmammadov, E., Tanir, T. E., Kiziltay, A., Hasirci, V., and Hasirci, N. (2017). PCL and PCL-based materials in biomedical applications. *J. Biomater. Sci., Polym. Ed., Polymer Edition*; 1-55.
- Martínez, D., Londoño Zuluaga, C., Restrepo Osorio, A., and Álvarez, C. (2017). Characterization of sericin obtained from cocoons and silk yarns. *Procedia Eng.* 200: 377-383.
- Murariu, M., Paint, Y., Murariu, O., Raquez, J.-M., Bonnaud, L., and Dubois, P. (2015). Current progress in the production of PLA–ZnO nanocomposites: Beneficial effects of chain extender addition on key properties. *J. Appl. Polym. Sci.* 132(48): n/a-n/a.
- Nagalakshmaiah, M., Afrin, S., Malladi, R. P., Elkoun, S., Robert, M., Ansari, M. A., Svedberg, A., and Karim, Z. (2019). Chapter 9 - Biocomposites: Present trends and challenges for the future. In G. Koronis & A. Silva (Eds.), *Green Composites for Automotive Applications* (pp. 197-215): Woodhead Publishing.
- Nakagaito, A. N., Fujimura, A., Sakai, T., Hama, Y., and Yano, H. (2009). Production of microfibrillated cellulose (MFC)-reinforced polylactic acid (PLA) nanocomposites from sheets obtained by a papermaking-like process. *Compos. Sci. Technol.* 69(7-8): 1293-1297.
- Nakayama, N., and Hayashi, T. (2007). Preparation and characterization of poly (l-lactic acid)/TiO₂ nanoparticle nanocomposite films with high transparency and efficient photodegradability. *Polym. Degrad. Stab.* 92(7): 1255-1264.
- Neurock, M., and Manzer, L. E. (1996). Theoretical insights on the mechanism of alkene epoxidation by H₂O₂ with titanium silicalite. *Chem. Commun.* (10): 1133-1134.
- Nguyen, T. P., Nguyen, Q. V., Nguyen, V.-H., Le, T.-H., Huynh, V. Q., Vo, D.-V. N., Trinh, Q. T., Kim, S. Y., and Le, Q. V. (2019). silk fibroin-based biomaterials for biomedical applications: A Review. *Polymers.* 11(12).
- Oleyaei, S. A., Zahedi, Y., Ghanbarzadeh, B., and Moayedi, A. A. (2016). Modification of physicochemical and thermal properties of starch films by incorporation of TiO₂ nanoparticles. *Int. J. Biol. Macromol.* 89: 256-264.
- Omenetto, F. G., and Kaplan, D. L. (2010). New opportunities for an ancient material. *Science.* 329(5991): 528-531.

- Pabón, E., Retuert, J., and Quijada, R. (2007). Synthesis of mixed silica–titania by the sol–gel method using polyethylenimine: porosity and catalytic properties. *J. Porous Mater.* 14(2): 151-158.
- Pei, S., Zajac, G. W., Kaduk, J. A., Faber, J., Boyanov, B. I., Duck, D., Fazzini, D., Morrison, T. I., and Yang, D. S. (1993). Re-investigation of titanium silicalite by X-ray absorption spectroscopy: Are the novel titanium sites real. *Catal. Lett.* 21(3): 333-344.
- Pei Shan Teo, and Chow, W. S. (2014). Water vapour permeability of poly (lactic acid)/chitosan binary and ternary blends. *Applied Science and Engineering Progress.* 7(1): 23-27.
- Periyat, P., Pillai, S. C., McCormack, D. E., Colreavy, J., and Hinder, S. J. (2008). Improved high-temperature stability and sun-light-driven photocatalytic activity of sulfur-doped anatase TiO₂. *J. Phys. Chem. C.* 112(20): 7644-7652.
- Pilić, B. M., Radusin, T. I., Ristić, I. S., Silvestre, C., Lazić, V. L., Baloš, S. S., and Duraccio, D. (2016). Hydrophobic silica nanoparticles as reinforcing filler for poly (lactic acid) polymer matrix. *Hemijaska Industrija.* 70(1): 73-80.
- Porter, D., and Vollrath, F. (2009). Silk as a biomimetic ideal for structural polymers. *Adv. Mater.* 21(4): 487-492.
- Qi, Z., Yang, Y., Xiong, Z., Deng, J., Zhang, R., and Zhu, J. (2015). Effect of aliphatic diacyl adipic dihydrazides on the crystallization of poly (lactic acid). *J. Appl. Polym. Sci.* 132(23): n/a-n/a.
- Racksanti, A., Janhom, S., Punyanitya, S., Watanesk, R., and Watanesk, S. (2015). An approach for preparing an absorbable porous film of silk fibroin–rice starch modified with trisodium trimetaphosphate. *J. Appl. Polym. Sci.* 132(8): n/a-n/a.
- Ravel, B. and M. Newville (2005). Data analysis for X-ray absorption spectroscopy using IFEFFIT. *J. Synchrotron Radiat.* 12: 537-541.
- Rangi, A., and Jajpura, L. (2015). The biopolymer sericin: extraction and applications. *J. Text. Eng.* 5(1): 1-5.
- Rani, S., Suri, P., Shishodia, P. K., and Mehra, R. M. (2008). Synthesis of nanocrystalline ZnO powder via sol–gel route for dye-sensitized solar cells. *Sol. Energy Mater. Sol. Cells.* 92(12): 1639-1645.

- Rasal, R. M., Janorkar, A. V., and Hirt, D. E. (2010). Poly (lactic acid) modifications. *Prog. Polym. Sci.* 35(3): 338-356.
- Sahu, D. R., Hong, L. Y., Wang, S.-C., and Huang, J.-L. (2009). Synthesis, analysis and characterization of ordered mesoporous TiO₂/SBA-15 matrix: Effect of calcination temperature. *Microporous Mesoporous Mater.* 117(3): 640-649.
- Samantaray, P. K., Little, A., Haddleton, D. M., McNally, T., Tan, B., Sun, Z., Huang, W., Ji, Y., and Wan, C. (2020). Poly (glycolic acid) (PGA): a versatile building block expanding high performance and sustainable bioplastic applications. *Green Chem.* 22(13): 4055-4081.
- Sarasua, J.-R., Prud'homme, R. E., Wisniewski, M., Le Borgne, A., and Spassky, N. (1998). Crystallization and melting behavior of polylactides. *Macromolecules.* 31(12): 3895-3905.
- Savioli Lopes, M., Jardini, A. L., and Maciel Filho, R. (2012). Poly (lactic acid) production for tissue engineering applications. Paper presented at the *Procedia Eng.*
- Scherk, C. G., Ostermann, A., Achterhold, K., Iakovleva, O., Nazikkol, C., Krebs, B., Knapp, E. W., Meyer-Klaucke, W., and Parak, F. G. (2001). The X-ray absorption spectroscopy Debye-Waller factors of an iron compound and of met-myoglobin as a function of temperature. *Eur Biophys J.* 30(6): 393-403.
- Schraml-Marth, M., Walther, K. L., Wokaun, A., Handy, B. E., and Baiker, A. (1992). Porous silica gels and TiO₂/SiO₂ mixed oxides prepared via the sol-gel process: characterization by spectroscopic techniques. *J. Non-Cryst. Solids.* 143: 93-111.
- Serenko, O. A., and Muzafarov, A. M. (2016). Polym. Compos with surface modified SiO₂ nanoparticles: Structures, properties, and promising applications. *Polym. Sci. Ser. C.* 58(1): 93-101.
- Shanmugam, K., and Sundaramoorthy, S. (2015). Development and characterization of an electrospun mat from Eri silk fibroin and PLA blends for wound dressing application. *RSC Adv.* 5(40): 31352-31364.
- Sharma, A., Varshney, M., Park, J., Ha, T.-K., Chae, K.-H., and Shin, H.-J. (2015). XANES, EXAFS and photocatalytic investigations on copper oxide nanoparticles and nanocomposites. *RSC Adv.* 5(28): 21762-21771.

- Shi, N., and Dou, Q. (2014). Crystallization behavior, morphology, and mechanical properties of poly (lactic acid)/tributyl citrate/treated calcium carbonate composites. *Polym. Compos.* 35(8): 1570-1582.
- Shi, X., Zhang, G., Siligardi, C., Ori, G., and Lazzeri, A. (2015). Comparison of precipitated calcium carbonate/polylactic acid and halloysite/polylactic acid nanocomposites. *J. Nanomater.* 2015: 11.
- Shimura, K., Kikuchi, A., Ohtomo, K., Katagata, Y., and Hyodo, A. (1976). Studies on silk fibroin of *Bombyx mori*. I. Fractionation of fibroin prepared from the posterior silk gland. *J Biochem.* 80(4): 693-702.
- Shivatharsiny Rasalingam, Rui Peng, and Koodali, R. T. (2014). Review Article: Removal of hazardous pollutants from wastewaters: applications of TiO₂-SiO₂ mixed oxide materials. *J. Nanomater.*
- Singh, A. A., Afrin, S., and Karim, Z. (2017). Green Composites: Versatile material for future. In S. M. Jawaid M., Alothman O. (eds) (Ed.), *Green Biocomposites. Green Energy and Technology* (pp. 29-44): Springer, Cham.
- Sinha Ray, S., Yamada, K., Okamoto, M., and Ueda, K. (2002). Polylactide-layered silicate nanocomposite: A novel biodegradable material. *Nano Letters.* 2(10): 1093-1096.
- Slavin, Y. N., Asnis, J., Häfeli, U. O., and Bach, H. (2017). Metal nanoparticles: understanding the mechanisms behind antibacterial activity. *J. Nanobiotechnology.* 15(1): 65.
- Souza, D. H. S., Andrade, C. T. o., and Dias, M. L. (2014). Effect of synthetic mica on the thermal properties of poly (lactic acid). *Polímeros.* 24: 20-24.
- Taddei, P., Tozzi, S., Zuccheri, G., Martinotti, S., Ranzato, E., Chiono, V., Carmagnola, I., and Tsukada, M. (2017). Intermolecular interactions between *B. mori* silk fibroin and poly (L-lactic acid) in electrospun composite nanofibrous scaffolds. *Mater. Sci. Eng., C.* 70: 777-787.
- Tang, H., Chen, J.-B., Wang, Y., Xu, J.-Z., Hsiao, B. S., Zhong, G.-J., and Li, Z.-M. (2012). Shear flow and carbon nanotubes synergistically induced nonisothermal crystallization of poly (lactic acid) and its application in injection molding. *Biomacromolecules.* 13(11): 3858-3867.

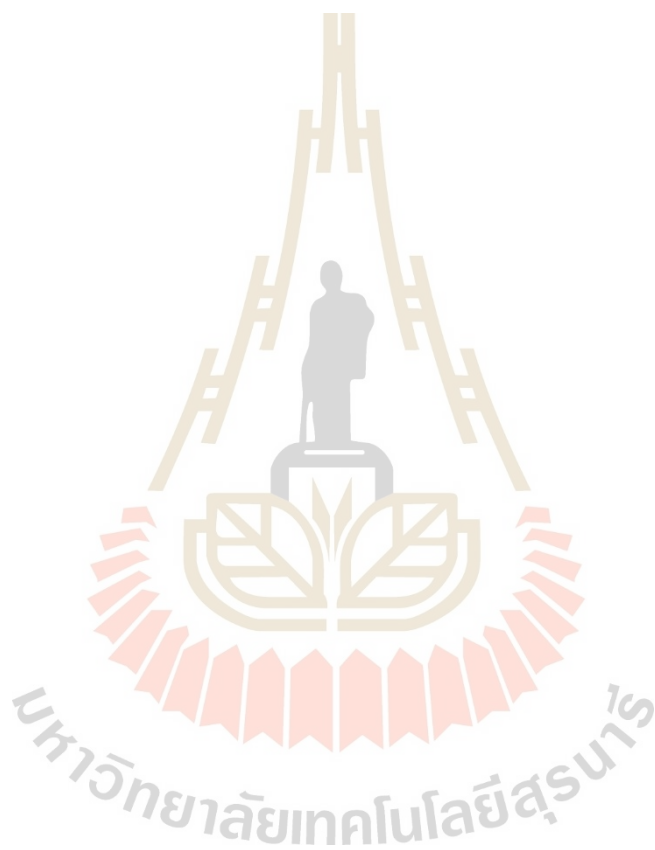
- Tang, Z., Zhang, C., Liu, X., and Zhu, J. (2012). The crystallization behavior and mechanical properties of polylactic acid in the presence of a crystal nucleating agent. *J. Appl. Polym. Sci.* 125(2): 1108-1115.
- Tantekin-Ersolmaz, Ş. B., Atalay-Oral, Ç., Tatlier, M., Erdem-Şenatalar, A., Schoeman, B., and Sterte, J. (2000). Effect of zeolite particle size on the performance of polymer-zeolite mixed matrix membranes. *J. Membr. Sci.* 175(2): 285-288.
- Teamsinsungvon, A., Jarapanyacheep, R., Ruksakulpiwat, Y., and Jarukumjorn, K. (2017). Melt processing of maleic anhydride grafted poly (lactic acid) and its compatibilizing effect on poly (lactic acid)/poly (butylene adipate-co-terephthalate) blend and their composite. *Polym. Sci. Ser. A.*
- Thanh, C. N., Chaiwat, R., and Yupaporn, R. (2017) Biocomposites of poly (Lactic Acid) and cellulose nanofibers from cassava pulp. In: Vol. 753 KEM. *Key Eng. Mater.* (pp. 13-17).
- Toniatto, T. V., Rodrigues, B. V. M., Marsi, T. C. O., Ricci, R., Marciano, F. R., Webster, T. J., and Lobo, A. O. (2017). Nanostructured poly (lactic acid) electrospun fiber with high loadings of TiO₂ nanoparticles: Insights into bactericidal activity and cell viability. *Mater. Sci. Eng. C.* 71: 381-385.
- Torma, V., Peterlik, H., Bauer, U., Rupp, W., Hüsing, N., Bernstorff, S., Steinhart, M., Goerigk, G., and Schubert, U. (2005). Mixed silica titania materials prepared from a single-source sol-gel precursor: a time-resolved SAXS study of the gelation, aging, supercritical drying, and calcination processes. *Chem. Mater.* 17(12): 3146-3153.
- Ullattil, S. G., and Periyat, P. (2017). Sol-Gel Synthesis of Titanium Dioxide. In S. C. Pillai & S. Hehir (Eds.), *Sol-Gel Materials for Energy, Environment and Electronic Applications* (pp. 271-283). Cham: Springer International Publishing.
- Van Grieken, R., Aguado, J., López-Muñoz, M. J., and Marugán, J. (2010). Sol-gel titania and titania-silica mixed oxides photocatalysts. *Solid State Phenom.* 162: 221-238.
- Vepari, C., and Kaplan, D. L. (2007). Silk as a biomaterial. *Prog. Polym. Sci.* 32(8-9): 991-1007.

- Vestena, M., Grossa, I. P., Müllerc, C. M. O., and Piresa, A. T. N. (2016). Nanocomposite of poly (lactic acid)/cellulose nanocrystals: effect of CNC content on the polymer crystallization kinetics. *J. Braz. Chem. Soc.* 27(5): 905-911.
- Vijatović, M.M., Bobić, J.D., and Stojanović, B. D. (2008). History and challenges of barium titanate: Part I. *Sci. Sinter.* 40(2): 155-165.
- Vishwanath, V., Pramanik, K., and Biswas, A. (2016). Optimization and evaluation of silk fibroin-chitosan freeze-dried porous scaffolds for cartilage tissue engineering application. *J. Biomater. Sci.* 27(7): 657-674.
- Vives, S., and Meunier, C. (2008). Influence of the synthesis route on sol-gel $\text{SiO}_2\text{-TiO}_2$ (1:1) xerogels and powders. *Ceram. Int.* 34(1): 37-44.
- Vollrath, F., and Knight, D. P. (2001). Liquid crystalline spinning of spider silk. *Nature.* 410(6828): 541-548.
- Vp, S., Mohanty, S., and Nayak, S. K. (2016). Effect of poly (lactic acid)-graft-glycidyl methacrylate as a compatibilizer on properties of poly (lactic acid)/banana fiber biocomposites. *Polym. Adv. Technol.* 27:515-524.
- Wang, F., Liu, X., Yuan, J., Yang, S., Li, Y., and Gao, Q. (2016). Synthesis and characterization of poly (lactic acid-co-glycolic acid) complex microspheres as drug carriers. *J. Biomater. Appl.* 31(4): 544-552.
- Wang, F., Wu, H., Venkataraman, V., and Hu, X. (2019). Silk fibroin-poly (lactic acid) biocomposites: Effect of protein-synthetic polymer interactions and miscibility on material properties and biological responses. *Mater. Sci. Eng., C.* 104: 109890.
- Wang, H., Liu, H., Chu, C., She, Y., Jiang, S., Zhai, L., Jiang, S., and Li, X. (2015). Diffusion and antibacterial properties of nisin-loaded chitosan/poly (l-lactic acid) towards development of active food packaging film. *Food Bioprocess Technol.* 8(8): 1657-1667.
- Wellenreuther, G., Parthasarathy, V., and Meyer-Klaucke, W. (2010). Towards a black-box for biological EXAFS data analysis. II. Automatic BioXAS Refinement and Analysis (ABRA). *J. Synchrotron Radiat.* 17(1): 25-35.

- Whitehouse, C. M., Dreyer, R. N., Yamashita, M., and Fenn, J. B. (1985). Electrospray interface for liquid chromatographs and mass spectrometers. *Anal. Chem.* 57(3): 675-679.
- Wist, J., Sanabria, J., Dierolf, C., Torres, W., and Pulgarin, C. (2002). Evaluation of photocatalytic disinfection of crude water for drinking-water production. *J. Photochem. Photobiol., A.* 147(3): 241-246.
- Wu, D., Zhang, Y., Yuan, L., Zhang, M., and Zhou, W. (2010). Viscoelastic interfacial properties of compatibilized poly(ϵ -caprolactone)/polylactide blend. *J. Polym. Sci., Part B: Polym. Phys.* 48(7): 756-765.
- Wu, F., Lan, X., Ji, D., Liu, Z., Yang, W., and Yang, M. (2013). Grafting polymerization of polylactic acid on the surface of nano-SiO₂ and properties of PLA/PLA-grafted-SiO₂ nanocomposites. *J. Appl. Polym. Sci.* 129(5): 3019-3027.
- Wu, G., Liu, S., Jia, H., and Dai, J. (2016). Preparation and properties of heat resistant polylactic acid (PLA)/Nano-SiO₂ composite filament. *J. Wuhan Univ. Technol. Mater. Sci. Ed.* 31(1): 164-171.
- Wu, L., Wu, Y., and Lü, Y. (2006). Self-assembly of small ZnO nanoparticles toward flake-like single crystals. *Mater. Res. Bull.* 41(1): 128-133.
- Wu, Y., Li, M., and Gao, H. (2009). Polymeric micelle composed of PLA and chitosan as a drug carrier. *J. Polym. Res.* 16(1): 11-18.
- Xiao, H., Guo, D., and Bao, J. (2015). Synergistic effects of N, N'-bis (benzoyl) sebacic acid dihydrazide and talc on the physical and mechanical behaviors of poly (l-lactic acid). *J. Appl. Polym. Sci.* 132(7): n/a-n/a.
- Xiu, H., Qi, X., Bai, H., Zhang, Q., and Fu, Q. (2017). Simultaneously improving toughness and UV-resistance of polylactide/titanium dioxide nanocomposites by adding poly(ether)urethane. *Polym. Degrad. Stab.* 143: 136-144.
- Xu, T., Zhang, A., Zhao, Y., Han, Z., and Xue, L. (2015). Crystallization kinetics and morphology of biodegradable poly (lactic acid) with a hydrazide nucleating agent. *Polym. Test.* 45: 101-106.
- Yamada, N., Yoshinaga, I., and Katayama, S. (1998). Processing and properties of inorganic-organic hybrids containing various inorganic components. *J. Sol-Gel Sci. Technol.* 13(1): 445-449.

- Yamashita, H., Kawasaki, S., Ichihashi, Y., Harada, M., Takeuchi, M., Anpo, M., Stewart, G., Fox, M. A., Louis, C., and Che, M. (1998). Characterization of titanium–silicon binary oxide catalysts prepared by the sol–gel method and their photocatalytic reactivity for the liquid-phase oxidation of 1-octanol. *J. Phys. Chem. B.* 102(30): 5870-5875.
- Yaowalak, S., Wilaiwan, S., and Prasong, S. (2009). Preparation and characterization of Eri (philosamia ricini) silk fibroin powder. *J. Appl. Polym. Sci.* 9: 2992-2995.
- Yeh, J. T., Huang, C. Y., Chai, W. L., and Chen, K. N. (2009). Plasticized properties of poly (lactic acid) and triacetine blends. *J. Appl. Polym. Sci.* 112(5): 2757-2763.
- Yew, G. H., Mohd Yusof, A. M., Mohd Ishak, Z. A., and Ishiaku, U. S. (2005). Water absorption and enzymatic degradation of poly (lactic acid)/rice starch composites. *Polym. Degrad. Stab.* 90(3): 488-500.
- Yoldas, B. E. (1980). Formation of titania-silica glasses by low temperature chemical polymerization. *Non-Cryst. Solids.* 38(Part 1): 81-86.
- Yu, H.-F., and Wang, S.-M. (2000). Effects of water content and pH on gel-derived TiO₂-SiO₂. *J. Non. Cryst. Solids.* 261(1): 260-267.
- Yuan, X., Mak, A. F. T., and Yao, K. (2002). In vitro degradation of poly (L- lactic acid) fibers in phosphate buffered saline. *J. Appl. Polym. Sci.* 85(5): 936-943.
- Zapata, P. A., Palza, H., Cruz, L. S., Lieberwirth, I., Catalina, F., Corrales, T., and Rabagliati, F. M. (2013). Polyethylene and poly(ethylene-co-1-octadecene) composites with TiO₂ based nanoparticles by metallocenic “in situ” polymerization. *Polymer.* 54(11): 2690-2698.
- Zhang, H., Huang, J., Yang, L., Chen, R., Zou, W., Lin, X., and Qu, J. (2015). Preparation, characterization and properties of PLA/TiO₂ nanocomposites based on a novel vane extruder. *RSC Adv.* 5(6): 4639-4647.
- Zhang, Y.-Q., Shen, W.-D., Xiang, R.-L., Zhuge, L.-J., Gao, W.-J., and Wang, W.-B. (2007). Formation of silk fibroin nanoparticles in water-miscible organic solvent and their characterization. *J. Nanopart. Res.* 9(5): 885-900.
- Zhao, Y. Q., Cheung, H. Y., Lau, K. T., Xu, C. L., Zhao, D. D., and Li, H. L. (2010). Silkworm silk/poly (lactic acid) biocomposites: Dynamic mechanical, thermal and biodegradable properties. *Polym. Degrad. Stab.* 95(10): 1978-1987.

Zhu, H., Feng, X., Zhang, H., Guo, Y., Zhang, J., and Chen, J. (2009). Structural characteristics and properties of silk fibroin/poly (lactic acid) blend films. *J. Biomater. Sci., Polym. Ed.* 20(9): 1259-1274.





APPENDIX A
PUBLICATIONS

List of publications

- Teamsinsungvon, A., Ruksakulpiwat, C., Sutapan, W., and Ruksakulpiwat, Y. (2017). Preparation of titanium-silica binary mixed oxide to use as a filler in poly (lactic acid). In **Abstract of The First Materials Research Society of Thailand International Conference (MRS-Thailand 2017)**. 31 October –3 November 2017, Chiang Mai, Thailand.
- Teamsinsungvon, A., Ruksakulpiwat, C., and Ruksakulpiwat, Y. (2017). Preparation, characterization and properties of titanium-silica binary mixed oxide with different Ti/Si ratios using a filler for poly (lactic acid). In **Abstract of International Conference on Advanced and Applied Petroleum Petrochemicals, and Polymer 2018 (ICAPPP2018)**. 18-20 December 2017, Bangkok, Thailand.
- Teamsinsungvon, A., Ruksakulpiwat, C., and Ruksakulpiwat, Y. (2019). Preparation and characterization of nano-titania-silica binary mixed oxide and PLA composite on mechanical, thermal and morphological properties. In **Abstract of at The Second Materials Research Society of Thailand International Conference (2nd MRS Thailand International Conference)**, 10–12 July 2019, Pattaya, Thailand.
- Teamsinsungvon, A., Ruksakulpiwat, C., Sutapan, W., and Ruksakulpiwat, Y. (2019). Preparation of titanium-silica binary mixed oxide to use as a filler in poly (lactic acid). *Suranaree Journal of Science and Technology*. 26(1): 31-36.
- Teamsinsungvon, A., Ruksakulpiwat, C., and Ruksakulpiwat, Y. (2021). Preparation and characterization of nano-titania-silica binary mixed oxide and PLA composite on mechanical, thermal and morphological properties. *Suranaree Journal of Science and Technology*. 28(3): 1-8.

- Teamsinsungvon, A., Ruksakulpiwat, C., Amonpattaratkit, P., and Ruksakulpiwat, Y. (2022). Structural Characterization of Titanium–Silica Oxide Using Synchrotron Radiation X-ray Absorption Spectroscopy. *Polymers* **14**(13): 2729.
- Teamsinsungvon, A., Ruksakulpiwat, C., and Ruksakulpiwat, Y. (2022). Effects of Titanium–Silica Oxide on Degradation Behavior and Antimicrobial Activity of Poly (Lactic Acid) Composites. *Polymers* **14**(16): 3310.
- Teamsinsungvon, A., Ruksakulpiwat, C., and Ruksakulpiwat, Y. Material for UV absorber from biopolymer and Titanium-Silica Mixed oxide. **Patent pending:** 2103000626.
- Teamsinsungvon, A., Ruksakulpiwat, C., and Ruksakulpiwat, Y. Method for preparing Titanium-Silicon mixed oxide to use as a filler in polymer. **Patent pending:** 2101001184.
- Teamsinsungvon, A., Ruksakulpiwat, C., and Ruksakulpiwat, Y. Material of absorber and photocatalytic degradation of dyes prepared from biopolymer and Titanium-Silica Mixed oxide. **Patent pending:** 2103000627
- . Teamsinsungvon, A., Ruksakulpiwat, C., and Ruksakulpiwat, Y. Material of antibacterial from biopolymer and Titanium-Silicon Mixed oxide. **Patent pending:** 2101001185.

The First Materials Research Society of Thailand International Conference
(1st MRS Thailand International Conference)
October 31 - November 3, 2017
The Empress Convention Center, Chiang Mai, Thailand

Preparation of titanium-silica binary mixed oxide to use as a filler in poly (lactic acid)

Arpaporn Teamsinsungvon^{a,b}, Wimonlak Sutapun^a, ChaiwatRuksakulpiwat^{a,b}
And YupapornRuksakulpiwat^{a,b*}

^aSchool of Polymer Engineering, Institute of Engineering, Suranaree University of Technology,
Nakhon Ratchasima 30000, Thailand

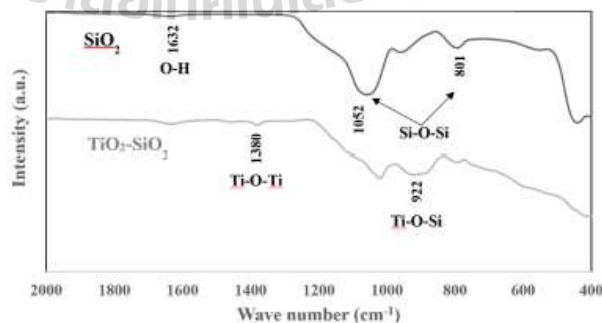
^bCenter for Petroleum, Petrochemicals, and Advanced Materials,
Chulalongkorn University, Bangkok 10330, Thailand

*Corresponding Authors Email: yupa@sut.ac.th

Abstract

Poly (lactic acid) (PLA), a biodegradable polyester, derived from renewable resources has been widely used in biomedical and packaging applications due to its good strength and high stiffness. However, its slow crystallization rate lead to several drawbacks during large-scale production. Titanium-silica binary mixed oxide ($\text{TiO}_2\text{-SiO}_2$), an environmental benign material, has good chemical resistance, high chemical stability, antimicrobial biomaterials and non-toxic using for biomedical applications such as drug delivery. In this study, $\text{TiO}_2\text{-SiO}_2$ mixed oxide was prepared to use as nucleating agent for PLA. $\text{TiO}_2\text{-SiO}_2$ has been synthesized via sol-gel method using tetraethyl orthosilicate (TEOS) and tetraisopropoxide (TTIP) as the silicon and titanium precursors, respectively. The structural and chemical properties of $\text{TiO}_2\text{-SiO}_2$ mixed oxide were characterized by FT-IR spectroscopy, X-ray diffraction, scanning electron microscopy with energy dispersive X-ray spectroscopy (SEM-EDS) and X-Rays Fluorescence. The FTIR spectrashowedtwo strong bands at 1,052 and 801 cm^{-1} associated with asymmetric and symmetric Si-O-Si stretching vibrations. Moreover, $\text{TiO}_2\text{-SiO}_2$ mixed oxide obtained the band at 922 cm^{-1} associated to Ti-O-Si vibration. This confirmed that the interaction between TiO_2 and SiO_2 was formed.

Keywords: Mixed oxide; Sol-gel method; Titania; silica



9_54

P-BIP-1: Preparation, characterization and properties of titanium-silica binary mixed oxide with different Ti/Si ratios using a filler for poly(lactic acid)

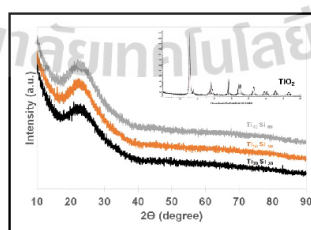
Arpaporn Teamsinsungvon^{a,b}, Chaiwat Ruksakulpiwat^{a,b}, Yupaporn Ruksakulpiwat^{a,b*}

^a*School of Polymer Engineering, Institute of Engineering, Suranaree University of Technology, Nakhon Ratchasima 30000, Thailand*

^b*Center for Petroleum, Petrochemicals, and Advanced Materials, Chulalongkorn University, Bangkok 10330, Thailand*

Poly (lactic acid) (PLA), a biodegradable polyester, has been widely used in biomedical and packaging applications due to its good strength and high stiffness. However, its slow crystallization rate limits its applications. Titanium-silica binary mixed oxide ($\text{TiO}_2\text{-SiO}_2$) is an environmental benign material and antimicrobial biomaterial. In addition, it has good chemical resistance, high chemical stability, and non-toxicity which is suitable for biomedical applications such as wound dressing and drug delivery. In this study, $\text{TiO}_2\text{-SiO}_2$ was prepared via sol-gel method to use as nucleating agent for PLA with three different molar ratio of Ti/Si. Titanium(IV) isopropoxide (TTIP) and tetraethylorthosilicate (TEOS) were used as Ti and Si precursor, respectively. The structural and chemical properties of $\text{TiO}_2\text{-SiO}_2$ were characterized by Fourier transform infrared spectroscopy (FT-IR), scanning electron microscope (SEM), powder X-ray diffraction (XRD) and X-ray absorption spectroscopy (XAS). In addition, the chemical compositions were analyzed by energy dispersive X-ray fluorescence (EDX). The XRD patterns of the mixed oxides with different Ti/Si ratio exhibited a broad diffraction peak within the 2θ range 10-40, characteristic of amorphous silica. This indicates that the titanium is dispersed in the silica and does not exist as crystals of size sufficient to be detected by XRD.

Corresponding author e-mail: yupa@sut.ac.th



XRD patterns of $\text{TiO}_2\text{-SiO}_2$ mixed oxides with various Ti/Si ratios

Author Biography: Miss Arpaporn Teamsinsungvon was born on May 1, 1983.

She graduated in 2004 with a Bachelor's degree of Science (Chemistry) from Khon Kaen University (KKU). She then pursued her Master's degree in Polymer Engineering at School of Polymer Engineering, Institute of Engineering, Suranaree University of Technology (SUT).

Her research was about poly (lactic acid)/poly (butylene adipate-co-terephthalate) blends and their composites. In the present, she is a Ph.D candidate in Polymer Engineering at School of Polymer Engineering, Institute of Engineering, Suranaree University of Technology (SUT).

Name: Arpaporn Teamsinsungvon
University/Institute: Suranaree University of
Technology Research Interest: Biomedical and Bio-
based Polymers



The Second Materials Research Society of Thailand International Conference
(2nd MRS Thailand International Conference)
10-12 July 2019
The Zign Hotel, Pattaya, Thailand

SYM7_P3

Preparation and characterization of nano-titania-silica binary mixed oxide and PLA composite on mechanical, thermal and morphological properties

Arpaporn Teamsinsungvon^{a,b}, Chaiwat Ruksakulpiwat^{a,b} And Yupaporn Ruksakulpiwat^{a,b}

^a*School of Polymer Engineering, Institute of Engineering, Suranaree University of Technology,
Nakhon Ratchasima 30000, Thailand*

^b*Center of Excellence on Petrochemical and Materials Technology,
Chulalongkorn University, Bangkok 10330, Thailand*

*Corresponding Author's E-mail: yupa@sut.ac.th

Abstract

Poly (lactic acid) (PLA), as one of the most promising biopolymer, has been widely used in biomedical and packaging applications because of its good strength, high stiffness and biocompatibility. However, its application is limited by its slow crystallization rate and lack of crystallinity after fast processing. Titanium-silica binary mixed oxide (TiO₂-SiO₂) is an environmental benign material and antimicrobial biomaterial. In addition, it has good chemical resistance, high chemical stability, and non-toxicity which is suitable for biomedical applications such as wound dressing and drug delivery. In this study, TiO₂-SiO₂ was prepared via sol-gel method to use as nucleating agent for PLA with 1:1 molar ratio of Ti/Si. Titanium(IV) isopropoxide (TTIP) and tetraethylorthosilicate (TEOS) were used as Ti and Si precursor, respectively. The structural and chemical properties of TiO₂-SiO₂ were characterized by Fourier transform infrared spectroscopy (FT-IR), field emission scanning electron microscope (FE-SEM) and powder X-ray diffraction (XRD). In addition, the chemical compositions were analyzed by energy dispersive X-ray fluorescence (XRF). The FTIR spectra showed two strong bands at 1,052 and 801 cm⁻¹ associated with asymmetric and symmetric Si-O-Si stretching vibrations. Moreover, the band at 949 cm⁻¹ of TiO₂-SiO₂ mixed oxide associated with Ti-O-Si vibration indicating the forming of chemical bond between TiO₂ and SiO₂. PLA nanocomposite films were prepared by solvent film casting method with at different percentages of mixed oxide (1, 3, and 5 wt%). Mechanical and thermal properties of the composites were investigated. In addition, morphological properties was also investigated.

Keywords: Mixed oxide; Sol-gel method; Titania; silica; nanocomposites; antimicrobial activity

Poster
Presentation

Symposium

01

02

03

04

05

06

07

08

09

10

11

12

13

14

15

16

17

PREPARATION OF TITANIUM-SILICA BINARY MIXED OXIDE TO USE AS A FILLER IN POLY (LACTIC ACID)

Arpaporn Teamsinsungvon^{1,2}, Wimonlak Sutapun¹, Chaiwat Ruksakulpiwat^{1,2}, and Yupaporn Ruksakulpiwat^{1,2*}

Received: November 01, 2017; Revised: February 27, 2018; Accepted: March 02, 2018

Abstract

Poly(lactic acid) (PLA), a biodegradable polyester, derived from renewable resources has been widely used in biomedical and packaging applications due to its good strength and high stiffness. However, one of the main drawbacks of PLA is its slow crystallization rate leading to several problems during large-scale production. Titanium-silica binary mixed oxide (TiO₂-SiO₂) is an environmentally benign and antimicrobial biomaterial. In addition, it has good chemical resistance, high chemical stability, and non-toxicity which is suitable for biomedical applications such as wound dressing and drug delivery. In this study, TiO₂-SiO₂ mixed oxide was prepared for use as a nucleating agent for PLA. The TiO₂-SiO₂ was synthesized via the sol-gel method using tetraethyl orthosilicate and tetraisopropoxide as silicon and titanium precursors, respectively. The structural and chemical properties of the TiO₂-SiO₂ mixed oxide were characterized by powder X-ray diffraction, X-ray fluorescence, Fourier transform infrared (FTIR) spectroscopy, and scanning electron microscopy with energy dispersive X-Ray spectroscopy. The FTIR spectra showed 2 strong bands at 1,052 and 801 cm⁻¹ associated with asymmetric and symmetric Si-O-Si stretching vibrations. Moreover, the band at 949 cm⁻¹ of the TiO₂-SiO₂ mixed oxide associated with Ti-O-Si vibration indicated the forming of a chemical bond between the TiO₂ and SiO₂.

Keywords: Mixed oxide, sol-gel method, titania, silica

¹ School of Polymer Engineering, Institute of Engineering, Suranaree University of Technology, Nakhon Ratchasima 30000, Thailand. Tel: 0-4422-4433; Fax: 0-4422-4605;

² Center for Petroleum, Petrochemicals, and Advanced Materials, Chulalongkorn University, Bangkok 10330, Thailand. E-mail: yupa@sut.ac.th

* Corresponding author

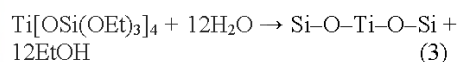
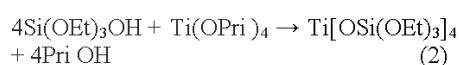
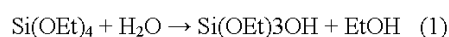
Introduction

Titanium dioxide (TiO₂) or titania, is an important substance. It is well recognized as a valuable material used in applications such as paints or as a filler in paper, polymer, textiles or photocatalysis, etc. Nano- TiO₂ particles hold many positive properties such as good chemical resistance, high chemical stability (Zapata *et al.*, 2013), attractive photocatalytic activity, excellent photostability, biocompatibility, and antimicrobial activity (Fonseca *et al.*, 2015).

Silicon dioxide (SiO₂) or silica, is a chemical compound that contains oxygen and silicon. It has a good thermal stability, low cost, and high density of silanol groups (Si-OH) on the surface. As a result, it has been widely used in many applications. For example, poly(lactic acid)/SiO₂ hybrid microspheres (PLAHs) have been used in the controlled release of drugs by embedding the drugs in the holes of the PLAHs. The drug loading amount can be controlled by the size and number of holes in the PLAHs (Wang *et al.*, 2006). Moreover, the crystallization properties of PLA can be improved by SiO₂ (Ge *et al.*, 2014).

Titanium-silicon binary mixed oxide (TiO₂-SiO₂) represents a novel class of materials that has attracted much attention in recent years. The mixed oxide can be generated via a sol-gel process to obtain a controllable combination of the beneficial mixed oxide (Kim *et al.*, 2000). This is due to the interaction of TiO₂ with SiO₂ and chemical bonds between the 2 materials. The sol-gel process is an adaptable method that has been successfully used in commercial applications because of its ability to form pure and homogenous products in mild conditions. The synthesis usually includes the hydrolysis of titania and silica alkoxide precursors and their condensation processes that leads to branched polymeric gels. The most common procedure was proposed by Yoldas (1980) in which Si-alkoxide was pre-hydrolyzed in an alcohol solution of concentrated acid and water under magnetic stirring to create silanol groups (Ismail and Vejayakumaran, 2012). The Ti-alkoxide was

added dropwise to the solution to prevent instant precipitation of the TiO₂ species. The reactions are shown as follows (Kibombo *et al.*, 2012):



The goal of this work is to determine the synthesis and structural characterization with different molar ratios of the Ti and Si. In addition, the effect of pre-hydrolysis of tetraethyl orthosilicate (TEOS) was investigated. The mixed oxide was characterized by powder X-ray diffraction (XRD), X-ray fluorescence (XRF), Fourier transform infrared (FTIR) spectroscopy, and scanning electron microscopy (SEM) with energy dispersive X-ray spectroscopy (EDS). The mixed oxide will be used as a filler in a PLA composite in our future work.

Materials and Methods

Materials

Tetraethyl orthosilicate (TEOS, 98%, AR grade) and titanium (IV) isopropoxide (TTIP, 98%, AR grade) were purchased from Acros Organics BVBA, Geel, Belgium. Absolute ethanol (C₂H₅OH, AR grade) and hydrochloric acid (HCl, AR grade) were supplied from Carlo Erba Reagents S.A.S., Val de Reuil, France.

Experimental Procedures

Titania-silica mixed oxide was prepared using the sol-gel method (Kim *et al.*, 2000). The TEOS and TTIP were used without purification. Hydrochloric acid was added to the alkoxide (TEOS and TTIP) solution to catalyze the sol-gel process. The mixture of 0.11 mole of alkoxides and 25 cm³ ethanol was added into a reactor containing 75 cm³ ethanol. A condenser was attached to prevent the

solvent from vaporizing. The reactor temperature was increased to 75°C while stirring. A solution of HCl was slowly added to the reactor drop by drop for 1 h. An additional 0.22 mole of distilled water was added into the sol and aged at 80°C for 24 h in an oven. During this period, ethanol was removed and the aged gel was almost dry in appearance. The aged gel was further dried under a reduced pressure in a rotary evaporator at 80°C for 2 h and calcined in the reactor at 550°C for 4 h. The compositions of the sol-gel liquid solution used for the preparation of TiO₂-SiO₂ are shown in Table 1.

Characterization Techniques

The crystal structures of the SiO₂ and TiO₂-SiO₂ were determined by XRD using a Model D2 phaser (Bruker Corporation, Billerica, MA, USA), with CuK α radiations scanning from 10-60° at a rate of 0.05°/s with the current at 35 mA. The chemical compositions were analyzed by XRF using an ED 2000 EDS analyser (Oxford Instruments, Abingdon, UK)

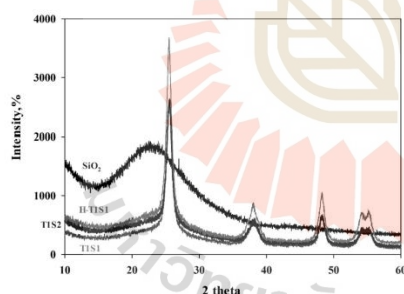


Figure 1. XRD pattern of SiO₂, T1S1, T1S2, and H-T1S1

with a Rh X-ray tube and a vacuum medium. The infrared spectra of the TiO₂-SiO₂ were determined by FTIR spectroscopy using attenuated total reflectance (FTIR-ATR) with a TENSOR 27 spectrometer (Bruker Corporation, Billerica, MA, USA). The spectra were recorded within the wavenumber of 400-4,000 cm⁻¹ with 4 cm⁻¹ resolution through the accumulation of 64 scans. A JSM-6380LV scanning electron microscope (JEOL Ltd., Tokyo, Japan) and an EDAX Genesis 2000 energy dispersive spectrometer (AMETEK, Inc., Berwyn, PA, USA) were applied to determine the morphology and composition of the SiO₂ and TiO₂-SiO₂.

Results and Discussion

The X-ray diffraction patterns of the synthesized SiO₂ and TiO₂-SiO₂ mixed oxides are shown in Figure 1. The SiO₂ showed the only diffraction peak at 23° attributed to a typical pattern of amorphous silica (Pabón *et al.*, 2007). The TiO₂-SiO₂ nanoparticles showed the diffraction peaks at 25° (101) and 48° (200) corresponding to the crystalline phase (anatase) of the TiO₂ (Yamashita *et al.*, 1998; Sahu *et al.*, 2009). The crystal structure of the TiO₂ was tetragonal; a = b = 3.782 Å, c = 9.502 Å (Etacheri *et al.*, 2015). However, no rutile phase was detected in any case according to the absence of the (110) diffraction peak at 27.4°. The crystal structures of the anatase and rutile are shown in Figure 2. The molar content of the metal oxides of the SiO₂ and TiO₂-SiO₂ mixed oxides by XRF are shown in Table 2. From the XRF analysis, pre-hydrolyzed TiO₂-SiO₂ mixed oxides (H-T1S1) showed a higher content of SiO₂ (32.64%) than the T1S1(24.36%) because TTIP can be hydrolyzed faster than the TEOS.

Table 1. Compositions of sol-gel liquid solution used for the preparation of TiO₂-SiO₂ mixed oxide

Compound	TTIP (mol)	TEOS (mol)	HCl (mol)	Mole ratio of Ti:Si
SiO ₂	-	0.11	0.055	0:1
T1S1	0.055	0.055	0.055	1:1
T1S2	0.037	0.073	0.055	1:2
*H-T1S1	0.055	0.055	0.055	1:1

*Hydrolysis TEOS for 1h before reaction

Moreover, the content of the SiO_2 in the T1S2 increased with increasing the molar ratio of the Ti/Si (43.72%). The FTIR technique was utilized to analyze the stretching and bending vibration frequencies in the mixed oxide materials. The FTIR spectrum of the TiO_2 - SiO_2 mixed oxides showed 3 main peaks with the wavenumbers of 801, 949, and 1052 cm^{-1} as depicted in Figure 3. The peaks at the wavenumbers of $1,052$ and 801 cm^{-1} were assigned to the symmetric and asymmetric stretching vibration of the Si-O-Si of silica, respectively (Sahu *et al.*, 2009). The peak with the wavenumber of 949 cm^{-1} was commonly attributed to the Ti-O-Si vibrations. Thus, the appearance can be used to infer the presence of Ti-O-Si linkages (Yamashita *et al.*, 1998). In addition, the Ti-O-Ti bond of the mixed oxides was too weak to be detected at $1,400 \text{ cm}^{-1}$ (Huang *et al.*, 2012).

The images of the SEM, the corresponding EDS spectra, and the mapping of the synthesized SiO_2 and TiO_2 - SiO_2 mixed oxide

for the Si, Ti, and O elements are shown in Figure 4. The mixed oxide exhibited a morphology containing a flat surface without porosity in the magnification used ($\times 5000$), together with a uniform dispersion of mixed oxides. Maps of different elements over the same area showed the absence of the phase's segregation or islands on the sample. In addition, the element maps showed the spatial distribution of the Si, Ti, and O elements in a T1S1 sample, as shown in Figure 5. The distribution of Si and Ti in the particles was relatively uniform in the case of the T1S1.

Conclusions

In this study, TiO_2 - SiO_2 mixed oxide was synthesized using TTIP and TEOS as precursors. The XRD pattern showed the diffraction peaks at 25° and 48° , which were attributed to the crystalline phase (anatase) of TiO_2 . The FTIR spectra showed 2 strong bands

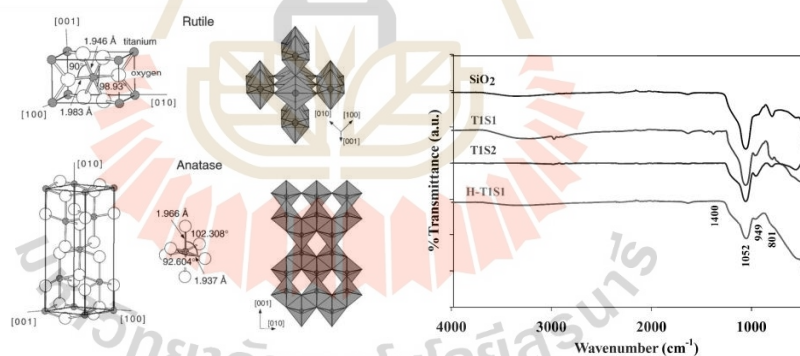


Figure 2. Crystal structures of rutile and anatase phases (Diebold, 2003) **Figure 3. FTIR transmission spectra of SiO_2 , T1S1, T1S2, and H-T1S1**

Table 2. Molar content of metal oxides of SiO_2 and TiO_2 - SiO_2 mixed oxides by XRF

Compound	TiO_2 (mol.%)	SiO_2 (mol.%)
SiO_2	-	99.94
T1S1	75.64	24.36
T1S2	56.28	43.72
H-T1S1	67.36	32.64

at 1,052 and 801 cm^{-1} associated with asymmetric and symmetric Si-O-Si stretching vibrations. Additionally, the Ti-O-Si vibration of the TiO_2 - SiO_2 mixed oxide was confirmed by the band at 949 cm^{-1} indicating the forming of a chemical bond between the TiO_2 and SiO_2 . Furthermore, SEM images exhibited a morphology containing a flat surface and a uniform dispersion of mixed oxides without porosity. Additionally, the absence of the phase's

segregation or islands was demonstrated in the EDS elemental mapping.

Acknowledgement

The authors wish to acknowledge Suranaree University of Technology and the Center for Petroleum, Petrochemicals and Advanced Materials for their financial support.

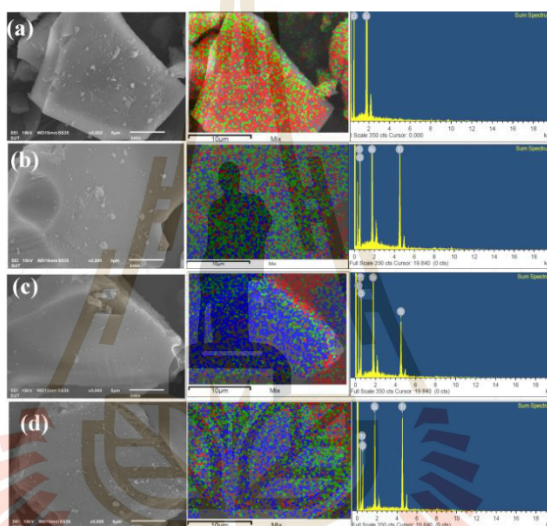


Figure 4. SEM images (x5000, 15 kV), EDS spectra, and mapping of SiO_2 and TiO_2 - SiO_2 mixed oxides; (a) SiO_2 , (b) T1S1, (c) T1S2, and (d) H-T1S1

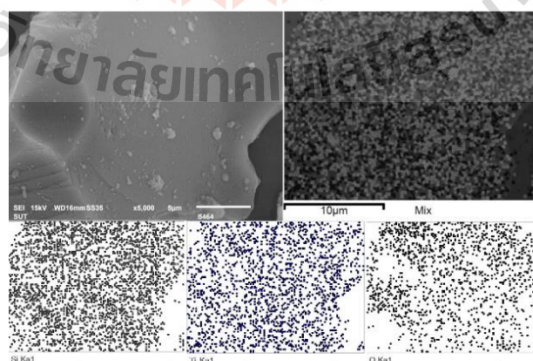


Figure. 5 EDS mapping of T1S1

References

- Diebold, U. (2003). The surface science of titanium dioxide. *Surf. Sci. Rep.*, 48(5):53-229.
- Etacheri, V., Di Valentin, C., Schneider, J., Bahnemann, D., and Pillai, S.C. (2015). Visible-light activation of TiO₂ photocatalysts: Advances in theory and experiments. *J. Photoch. Photobio. C.*, 25:1-29.
- Fonseca, C., Ochoa, A., Ulloa, M.T., Alvarez, E., Canales, D., and Zapata, P.A. (2015). Poly(lactic acid)/TiO₂ nanocomposites as alternative biocidal and antifungal materials. *Mater. Sci. Eng. C.*, 57:314-320.
- Ge, H., Zhu, Z., Yin, H., Zhang, X., and Wang, R. (2014). Fabrication and properties of sc- PLA/ SiO₂ composites. *IOP Conf. Ser. Mat. Sci.*, 62:012031.
- Huang, C., Bai, H., Huang, Y., Liu, S., Yen, S., and Tseng, Y. (2012). Synthesis of neutral SiO₂/TiO₂ hydrosol and its application as antireflective self-cleaning thin film. *Int. J. Photoenergy*, 2012:ID 6207464 1-8.
- Ismail, A.R. and Vejayakumaran, P. (2012). Synthesis of silica nanoparticles by sol-gel: size-dependent properties, surface modification, and applications in silica-polymer nanocomposites - a review. *J. Nanomaterials*, 2012:ID 132424 1-15.
- Kibombo, H.S., Peng, R., Rasalingam, S., and Koodali, R.T. (2012). Versatility of heterogeneous photocatalysis: synthetic methodologies epitomizing the role of silica support in TiO₂ based mixed oxides. *Catal. Sci. Technol.*, 2:1,737-1,766.
- Kim, W.B., Choi, S.H., and Lee, J.S. (2000). Quantitative analysis of Ti-O-Si and Ti-O-Ti bonds in Ti-Si binary oxides by the linear combination of XANES. *J. Phys. Chem. B.*, 104(36):8,670-8,678.
- Pabón, E., Retuert, J., and Quijada, R. (2007). Synthesis of mixed silica-titania by the sol-gel method using polyethylenimine: porosity and catalytic properties. *J. Porous Mat.*, 14(2):151-158.
- Sahu, D.R., Hong, L.Y., Wang, S.-C., and Huang, J.-L. (2009). Synthesis, analysis and characterization of ordered mesoporous TiO₂/SBA-15 matrix: Effect of calcination temperature. *Micropor. Mesopor. Mat.*, 117(3):640-649.
- Wang, H., Fang, M., Shi, T., Zhai, L., and Tang, C. (2006). Preparation of porous poly(lactic acid)/SiO₂ hybrid microspheres. *J. Appl. Polym. Sci.* 102(1):679-683.
- Yamashita, H., Kawasaki, S., Ichihashi, Y., Harada, M., Takeuchi, M., Anpo, M., Stewart, G., Fox, M. A., Louis, C., and Che, M. (1998). Characterization of titanium-silicon binary oxide catalysts prepared by the sol-gel method and their photocatalytic reactivity for the liquid-phase oxidation of 1-octanol. *J. Phys. Chem. B*, 102(30):5,870-5,875.
- Yoldas, B.E. (1980). Formation of titania-silica glasses by low temperature chemical polymerization. *J. Non-Cryst. Solids*, 38-39(1):81-86.
- Zapata, P. A., Palza, H., Cruz, L. S., Lieberwirth, I., Catalina, F., Corrales, T., and Rabagliati, F.M. (2013). Polyethylene and poly(ethylene-co-1-octadecene) composites with TiO₂ based nanoparticles by metallocenic "in situ" polymerization. *Polymer*, 54(11):2,690-2,698.





Acceptance Letter

22 March 2020

Dear **Miss Arpaporn Teamsinsungvon**

On behalf of the MRS-Thailand 2019 academic committee, I am pleased to inform you that your manuscript has been accepted for publication in the proceeding/journal designated below. The details of your manuscript are as follows:

Manuscript title: **PREPARATION AND CHARACTERIZATION OF NANO-TITANIA-SILICA BINARY MIXED OXIDE AND PLA COMPOSITE ON MECHANICAL, THERMAL AND MORPHOLOGICAL PROPERTIES**

Proceeding/Journal : **Suranaree Journal of Science and Technology (Scopus indexed, Accepted up to 10 papers from all symposia)**

Please kindly be reminded that your accepted manuscript will be transferred to the production department of the respective proceeding/journal. The publication date is estimated to be around July 2020 but the actual date will depend on the processing schedule of each proceeding/journal.

Sincerely yours,

A handwritten signature in blue ink, appearing to read 'Santi Maensiri', is written over a large, faint watermark of a university emblem.

(Prof. Dr. Santi Maensiri, Ph.D.)
President
Materials Research Society of
Thailand

PREPARATION AND CHARACTERIZATION OF NANO-TITANIA-SILICA BINARY MIXED OXIDE AND PLA COMPOSITE ON MECHANICAL, THERMAL AND MORPHOLOGICAL PROPERTIES

Arpaporn Teamsinsungvon^{1,2}, Chaiwat Ruksakulpiwat^{1,2} and Yupaporn Ruksakulpiwat^{1,2,*}

Received: July 10, 2019; Revised: January 08, 2020; Accepted: January 15, 2020

Abstract

This paper presents the preparation and characterization of titania-silica binary mixed oxide (Ti_xSi_y) and PLA composite on mechanical, thermal and morphological properties. Ti_xSi_y was prepared via sol-gel method to be used as nucleating agent for PLA with 1:1 molar ratio of Ti/Si. Ti_x-Si_y Titanium(IV) isopropoxide (TTIP) and tetraethylorthosilicate (TEOS) were used as Ti and Si precursor, respectively. The structural and chemical properties of TiO_2-SiO_2 were characterized by Fourier transform infrared spectroscopy (FTIR), field emission scanning electron microscope (FE-SEM) and powder X-ray diffraction (XRD). In addition, the chemical compositions were analyzed by energy dispersive X-ray fluorescence (XRF). The FTIR spectra showed the band at 949 cm^{-1} of $Ti_{50}Si_{50}$ mixed oxide associated with Ti-O-Si vibration indicating the forming of chemical bond between TiO_2 and SiO_2 . PLA nanocomposite films were prepared by solvent film casting method at various contents of mixed oxide (1, 3, and 5 wt%). The incorporation of $Ti_{50}Si_{50}$ decreased cold crystallization temperature (T_{cc}) of PLA and increased degree of crystallinity of neat PLA. Thermal stability of PLA was enhanced with the incorporating of TiO_2 and SiO_2 . The addition of 3wt% of $Ti_{50}Si_{50}$ into PLA film exhibited the best tensile strength and Young's modulus comparing to PLA and other PLA composites but low %elongation at break.

Keywords: Mixed oxide, Sol-gel method, Titania, silica, nanocomposites

Introduction

Over the last decade, there has been a continuous research interest on environmental friendly polymers derived from renewable sources as one of the solution to moderate the plastic pollution problem (Lim *et al.*, 2008). Poly (lactic acid) (PLA) is one of the most important biocompatible and biodegradable polymers and it is a sustainable

alternative to petrochemical-derived products. It could be used as the traditional commodity plastic aliphatic polyester that can derived from renewable resources like corn and sugar cane and decomposes through simple hydrolysis into water and carbon dioxide (Chandra and Rustgi, 1998; Madhavan Nampoothiri *et al.*, 2010). PLA has been viewed as

¹ School of Polymer Engineering, Institute of Engineering, Suranaree University of Technology, Nakhon Ratchasima 30000, Thailand. E-mail: yupa@sut.ac.th

² Center of Excellence on Petrochemical and Materials Technology, Chulalongkorn University, Bangkok 10330, Thailand.

* Corresponding author

one of the most promising materials because of its excellent biodegradability, biocompatibility, compostability, renewability, transparency, high strength, and high modulus. Hence, PLA has attracted more attention in various applications especially biomedical applications (Athanasios *et al.*, 1996). However, its brittleness, poor toughness, slow crystallization rate, low degree of crystallinity, poor thermal stability, low degradation rate, and hydrophobicity are major drawbacks of PLA and limit its application (Burg *et al.*, 1999; Yeh *et al.*, 2009; Rasal *et al.*, 2010). Several modifications such as copolymerization, plasticization, polymer blending and polymer composites have been applied for improving some PLA properties. Nowadays, the addition of selected nanofillers into PLA such as organomodified layered silicates (OMLS) (Huang *et al.*, 2010), carbon nanotubes (CNTs) (Tang *et al.*, 2012), zinc oxide (Murariu *et al.*, 2015), silica nanofillers (SiO₂) (Wu *et al.*, 2016; Hakim *et al.*, 2017), titanium dioxide (TiO₂) (Xiu *et al.*, 2017), can improve PLA characteristic features. TiO₂ or titania is well recognized as a valuable material used in applications such as paints or as filler in paper, polymer, textile, photocatalysis, etc. Nano-TiO₂ particles hold many good properties such as good chemical resistance, high chemical stability (Zapata *et al.*, 2013), attractive photocatalytic activity, excellent photostability, biocompatibility, antimicrobial activity (Fonseca *et al.*, 2015). Another interesting filler is silicon dioxide (SiO₂) or silica, is a chemical compound that contains oxygen and silicon. It has good thermal stability, low cost and high density of silanol groups (Si-OH) on the surface. As a result, it has been widely used in wide applications such as drug delivery (Wang *et al.*, 2006). Moreover, the crystallization properties of PLA can be improved by SiO₂ (Ge *et al.*, 2014). The binary oxides are prepared for many purposes: to expand the chemical properties, to develop a specific textural properties, or to produce a particle with a personalized composition that known to present unique characteristics (large surface areas, thermal stability, etc.) (Galindo *et al.*, 2007). The use of nano-titania-silica binary mixed oxide (Ti_x-Si_y) as a nucleating agent for PLA composites was studied in this work. Moreover, the effect of Ti_xSi_y, TiO₂, SiO₂ and TiO₂-SiO₂ on mechanical, thermal and morphological properties of PLA composites were investigated.

Experimental

Materials

Poly (lactic acid) (PLA, grade 4043D) was supplied from Nature Works LLC. This PLA is the

commercial grade for 3D printing and film applications. Tetraethylorthosilicate (TEOS, 98%, AR grade) and Titanium(IV) isopropoxide (TTIP, 98%, AR grade) were purchased from Acros. Absolute ethanol (C₂H₅OH, AR grade) and ammonium hydroxide (NH₄OH, AR grade), and hydrochloric acid (HCl, AR grade) were supplied from Carlo Erba Reagents.

Synthesis of Titania-Silica Binary Mixed Oxide (Ti₅₀Si₅₀)

Titania-silica mixed oxide was prepared using sol-gel methods (Kim *et al.*, 2000). TEOS and TTIP were used without purification. The mole ratio of alkoxide precursors: NH₄OH: C₂H₅OH: H₂O was 2:1:31:8. Total moles of the two alkoxide precursors were fixed at 0.22 mol. The mixture of two alkoxides was added into a 500 cm³ five-neck flask containing 150 cm³ ethanol for 1h for pre-hydrolysis. A condenser was attached to prevent the solvent from vaporizing. The reactor temperature was increased to 75-80°C while stirring. TTIP and ethanol (25 ml) was slowly added to reactor drop by drop for 1h and then yellowish transparent sol was obtained after an hour of further mixing. Additional distilled water was added in the sol and aged at 80°C for 2 h at room temperature. Then, the aged gel was further refined for 6,000 rpm for 10 min in centrifugal separator. Finally, the obtained solid particles was calcined at 550°C for 4h. A referenced pure SiO₂ sample was prepared in NH₄OH with the same way described above without the addition of TTIP (Kim *et al.*, 2017). In addition, referenced pure TiO₂ was prepared in acid condition at the same way with mixed oxide (Karkare, 2014).

Preparation of PLA Nanocomposite Films

PLA and nanocomposites were prepared by solvent film casting method. Ti₅₀Si₅₀, SiO₂, and TiO₂ was dispersed in chloroform and then PLA were added into this solution. The suspensions were stirred and dispersed for 3 days with ultrasound for 30 min so that the particles could disperse in PLA solution uniformly. At last, the nanocomposites were casted on glass petri dishes. Then the prepared films were kept at room temperature for 12 h and kept in oven at 40°C for 4 h.

Characterization of Titania-Silica Binary Mixed Oxide

Infrared spectra of TiO₂, SiO₂, and Ti₅₀Si₅₀ was determined by Fourier transform infrared spectroscopy using attenuated total reflectance (FTIR-ATR, Bruker, TENSOR 27). The spectra were recorded within the wavenumber of 400-4,000 cm⁻¹ with 4 cm⁻¹ resolution through the accumulation of 64 scans. Field-emission scanning electron

microscope (FESEM-EDS, Carl Zeiss Auriga) was applied to determine the morphologies of TiO₂, SiO₂, and Ti₅₀Si₅₀. The crystal structure of TiO₂, SiO₂, and Ti₅₀Si₅₀ was determined by powder X-ray diffraction (Bruker, Model D2 phaser, Germany), with CuK α radiations scanning from 10-80° at a rate of 0.05°/s with current 35 mA and powder X-ray diffraction (XRD). In addition, the chemical compositions were analyzed by energy dispersive X-ray fluorescence (XRF) (EDS Oxford Instrument ED 2000) with Rh X-ray tube and a vacuum medium.

Characterization of PLA and PLA Nanocomposites

The tensile properties of PLA and PLA nanocomposites films were obtained using an Instron universal testing machine (UTM, model 5565) with a load cell of 5 kN according to the ASTM standard method D882-88. Initial grip separation and crosshead speed were set at 10 cm and 50 cm/min, respectively.

Thermal properties of PLA and PLA nanocomposites films were carried out using a differential scanning calorimeter (DSC204F1, Netzsch) equipped with a liquid nitrogen cooling system. The sample was heated from room temperature to 200°C at a heating rate of 10°C, and kept for 5 min to erase the thermal history. Then it was cooled to room temperature (25°C) at a cooling rate of 10°C/min. Finally, it was heated again to 200°C at heating rate 10°C/min. The degree of crystallinity (X_c) of PLA and PLA nanocomposites was estimated using the following equation:

$$X_c = \frac{\Delta H_m}{\Delta H_m^0 \left(1 - \frac{\%wt \text{ filler}}{100}\right)} \times 100$$

where ΔH_m are the melting enthalpy in the second heating process and ΔH_m^0 , which is the melting enthalpy of an infinitely large crystal, was taken as 93.6 J/g (Tang *et al.*, 2012).

Thermogravimetric analysis of PLA and PLA nanocomposite films were examined using thermogravimetric analyzer (TGA/DSC1, Mettler Toledo). The temperature was raised from the room temperature to 650°C under nitrogen and then heated to 800°C under air atmosphere at heating rate of 10°C/min. The weight change was recorded as a function of temperature.

Morphological properties of the film were examined by a scanning electron microscope (JEOL, JSM-6010LV). Acceleration voltage 9-12 kV was used to collect SEM images of sample. The cross-sections of the films after tensile test and the

freeze-fractured films in liquid nitrogen were sputtered with gold.

Results and Discussion

Characteristics of Ti₅₀Si₅₀ mixed oxides, TiO₂, and SiO₂

Fourier transform infrared (FTIR) spectrum of the Ti₅₀Si₅₀ mixed oxides, TiO₂, and SiO₂ nanoparticles were shown in Figure 1. The FTIR spectrum of the Ti₅₀Si₅₀ mixed oxides showed three main peaks with the wavenumbers of 801, 949, and 1,052 cm⁻¹. The peak with the wavenumber of 801 and 1,052 were assigned to the symmetric and asymmetric stretching vibration of Si-O-Si of silica, respectively (Sahu *et al.*, 2009). The peak with the wavenumber of 949 cm⁻¹ was commonly attributed to Ti-O-Si vibrations indicating the existence of Ti-O-Si linkages (Yamashita *et al.*, 1998). The Ti-O-Ti bond of the mixed oxides may be too weak to be detected at 1,400 cm⁻¹ (Chiahung *et al.*, 2012). The FE-SEM images of Ti₅₀Si₅₀ mixed oxides, TiO₂, and SiO₂ were shown in Figure 2. The powders of Ti₅₀Si₅₀ mixed oxides, TiO₂, and SiO₂ show a homogeneous spherical morphology with size of 20-250 nm. The chemical compositions of Ti₅₀Si₅₀

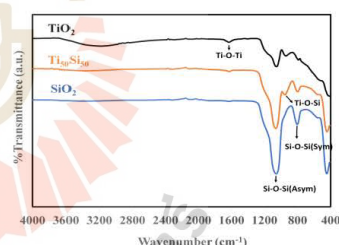


Figure 1. FTIR spectra of Ti₅₀Si₅₀, TiO₂, and SiO₂

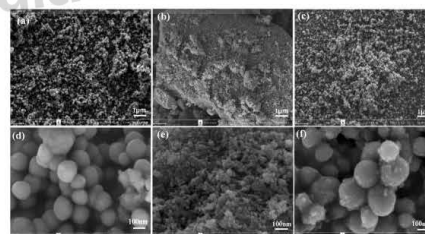


Figure 2. FE-SEM image of (a) Ti₅₀Si₅₀ (×10k), (b) TiO₂ (×10k), (c) SiO₂ (×10k), (d) Ti₅₀Si₅₀ (×100k), (e) TiO₂ (×100k), (f) SiO₂ (×100k)

Table 1. The molar content of metal oxides Ti₅₀Si₅₀, TiO₂, and SiO₂ by XRF

Compound	TiO ₂ (mol.%)	SiO ₂ (mol.%)
Ti ₅₀ Si ₅₀	50.19	49.80
TiO ₂	99.91	-
SiO ₂	-	99.94

Table 2. Tensile properties of PLA and PLA nanocomposites

Sample	Tensile strength (MPa)	Elongation at break (%)	Young's Modulus (GPa)
PLA	33.94±1.38	19.62±8.64	0.98±0.23
99PLA/1Ti ₅₀ Si ₅₀	29.16±1.78	9.08±2.75	1.13±0.10
97PLA/3Ti ₅₀ Si ₅₀	35.64±3.21	9.61±2.57	1.29±0.12
95PLA/5Ti ₅₀ Si ₅₀	34.25±0.61	7.44±2.19	1.21±0.10
97PLA/3TiO ₂	28.22±1.47	18.1±4.24	1.01±0.04
97PLA/3SiO ₂	29.75±1.38	11.8±4.96	1.07±0.10
97PLA/3TiO ₂ :SiO ₂	29.00±1.42	58.37±5.00	0.96±0.07

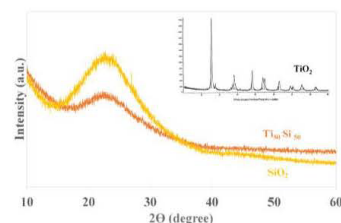
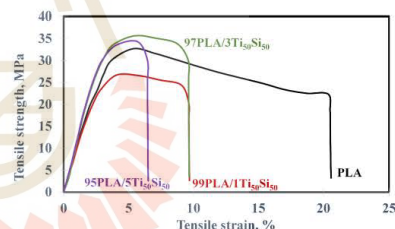
mixed oxide, TiO₂, and SiO₂ were analyzed by XRF as shown in Table 1. The XRF analysis showed the content of TiO₂ and SiO₂ were 50.19% and 49.80%, respectively. This result confirmed the content of Ti and Si in Ti₅₀Si₅₀ mixed oxide.

The crystalline structure of Ti₅₀Si₅₀ mixed oxides, TiO₂, and SiO₂ was determined by X-ray diffraction (XRD) analysis. The X-ray diffraction patterns of Ti₅₀Si₅₀ mixed oxides, TiO₂, and SiO₂ were shown in Figure 3. TiO₂ showed the diffraction peak at 25° (101) and 48° (200), which correspond to the crystalline phase (anatase) of TiO₂ (Sahu *et al.*, 2009; Yamashita *et al.*, 1998). SiO₂ showed only diffraction peak at 23°, which was attributed to a typical pattern of amorphous silica (Pabón *et al.*, 2007). Ti₅₀Si₅₀ mixed oxides exhibited a broad diffraction peak within 2θ range of 10–40 corresponding to the characteristic of amorphous silica. This indicates that titanium is highly dispersed in silica matrix. However, its crystal size may be too small to be detected by XRD (Ren *et al.*, 2008).

Characterization of PLA nanocomposites

From Figure 4, all of the composite films showed lower transparency than PLA. The transparency of PLA/Ti₅₀Si₅₀ decreased with increasing Ti₅₀Si₅₀ content. The film of 97PLA/3SiO₂ showed the highest transparency compared with 97PLA/3Ti₅₀Si₅₀, 97PLA/3TiO₂SiO₂ and 97PLA/3TiO₂.

Tensile stress-strain curves of pure PLA and PLA/Ti₅₀Si₅₀ were shown in Figure 5. Tensile properties of PLA and PLA nanocomposites were listed in Table 2 and Figure 6. The addition of 3wt%

**Figure 3. XRD pattern of Ti₅₀Si₅₀, TiO₂, and SiO₂****Figure 4. Photographs of films prepared from PLA and PLAnanocomposites (250-300 μm thickness)****Figure 5. Stress-strain curves of PLA and PLA nanocomposites**

of Ti₅₀Si₅₀ slightly increased tensile strength and Young's modulus and decreased %elongation at break of nanocomposites films compared to neat PLA (Figure 6(a)). The addition of nanoparticles to polymer matrix was also found to result in a decrease in ductile properties (Chu *et al.*, 2017). With increasing Ti₅₀Si₅₀ content from 3 to 5wt%, the tensile strength and Young's modulus slightly decreased. This may be due to the agglomeration of Ti₅₀Si₅₀ mixed oxide. This result was corresponded to SEM observation. The agglomeration of nanoparticle may act as stress concentrating center in the matrix and adversely affect the mechanical properties of PLA (Shirkavand and Moslehifard, 2014). With the different nanoparticle, 97PLA/3Ti₅₀Si₅₀ exhibited higher tensile strength, Young's modulus and lower %elongation at break than

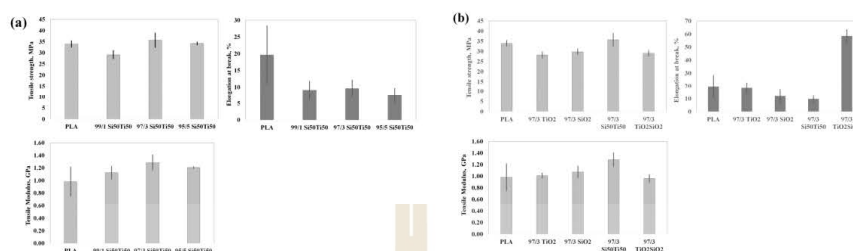


Figure 6. Tensile properties of PLA and PLA nanocomposites (a) various $Ti_{50}Si_{50}$ contents (b) different types of nanoparticles

Table 3. Thermal characteristics of PLA and PLA nanocomposites (the second heating, heating rate $10^{\circ}C/min$)

Samples	$T_g, ^{\circ}C$	$T_{cc}, ^{\circ}C$	$\Delta H_c, J/g$	$T_{m1}, ^{\circ}C$	$T_{m2}, ^{\circ}C$	$\Delta H_m, J/g$	$X_c, \%$
PLA	46.6	103.1	30.14	137.3	146.3	28.59	30.50
99PLA/1 $Ti_{50}Si_{50}$	46.4	100.6	31.93	135.8	145.0	32.99	35.56
97PLA/3 $Ti_{50}Si_{50}$	46.3	95.2	32.37	133.8	145.0	34.11	37.53
95PLA/5 $Ti_{50}Si_{50}$	46.7	95.4	32.16	135.8	145.0	32.75	36.79
97PLA/3 TiO_2	46.8	106.5	24.08	140.0	147.2	28.17	30.99
97PLA/3 SiO_2	46.8	105.0	28.78	138.8	146.7	29.03	31.94
97PLA/3 TiO_2SiO_2	46.7	104.2	24.43	138.9	146.9	23.71	26.09

97PLA/3 TiO_2 , 97PLA/3 SiO_2 , and 97PLA/3 TiO_2SiO_2 as shown in Figure 6(b). This may be due to better dispersion of 3 $Ti_{50}Si_{50}$ in PLA than the others.

DSC thermograms of PLA and PLA nanocomposites were shown in Figure 7. Thermal properties of all samples were listed in Table 3. Glass transition temperature (T_g), cold crystallization temperature (T_{cc}), and melting temperature (T_m) of PLA nanocomposites were observed. The double melting endotherms of neat PLA was explained by the melting and recrystallization. The peak at low temperature was attributed to the melting of the crystals formed during the nonisothermal melt crystallization, while the peak at high temperature was corresponded to re-melting of newly formed crystallite during melting and recrystallization during DSC heating scans (Sarasua *et al.*, 1998).

T_g of PLA/ $Ti_{50}Si_{50}$ nanocomposites did not change with varying $Ti_{50}Si_{50}$ content. In this work, the T_{cc} of the nanocomposites composites shifted to lower temperature approximately $3-8^{\circ}C$ with increasing $Ti_{50}Si_{50}$ mixed oxide contents up to 5 wt%. This indicated that crystallization ability of composite was enhanced. While 97PLA/3 TiO_2 , 97PLA/3 SiO_2 , and 97PLA/3 TiO_2SiO_2 composites showed an increase of the T_{cc} of PLA. This result can be explained by the agglomeration of TiO_2 and SiO_2 . The T_m of nanocomposites was decreased with addition of $Ti_{50}Si_{50}$. This may be due to the heterogeneous nucleation effect of $Ti_{50}Si_{50}$

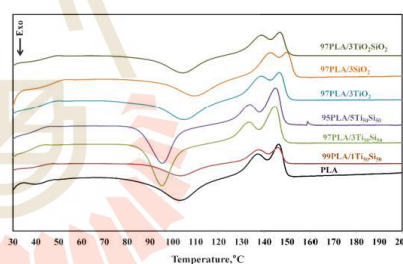


Figure 7. DSC thermograms of PLA and PLA nanocomposites (the second heating, heating rate $10^{\circ}C/min$)

nanoparticles on PLA during the crystallization process. The lamella formation of PLA was hindered by $Ti_{50}Si_{50}$ nanoparticles and led to less perfect crystals of PLA (Chen *et al.*, 2014). The degree of crystallinity (X_c), of neat PLA significant increases with increasing $Ti_{50}Si_{50}$ content. This implies that $Ti_{50}Si_{50}$ nanoparticles can act as a nucleating agent for PLA. However, adding TiO_2 , SiO_2 and TiO_2SiO_2 at 3wt% into PLA showed insignificant effect on T_g and X_c .

TGA curves of neat PLA and PLA nanocomposites were shown in Figure 8. The presence of $Ti_{50}Si_{50}$, TiO_2 , SiO_2 and TiO_2SiO_2 did not change the thermal decomposition behavior of PLA. First, there was an initial mass loss between

80-170°C, attributed to the loss of water and moisture. After that, a significantly mass loss between 250-360°C was observed, which corresponded to the decomposition of PLA. Finally, from 360 to 600°C thermal analysis curves slow down to complete the decomposition of PLA matrix until a constant mass was reached. The constant mass remaining at the end of each TGA experiment corresponded to the amount of nanoparticles in PLA nanocomposites. The onset decomposition temperature (T_{onset}), decomposition temperature (T_d) and final decomposition temperature (T_f) were listed in Table 4. With the addition of nanoparticles, the degradation begins at slightly higher temperature. This suggested that thermal stability of PLA was slightly enhanced with the incorporating of TiO_2 and SiO_2 . Moreover, when 1, 3, and 5 wt% Ti_50Si_50 mixed oxides were added into PLA, the composites left the char residual of nanoparticle at 1.61, 3.67, and 5.22%, respectively for PLA/ Ti_50Si_50 . The char residual generally depends on the amount of added nanoparticles (Buzarovska, 2013).

The surface morphology of prepared films was investigated by SEM analysis. The cross-section of PLA and PLA composites films were presented in Figure 9. PLA showed relative brittle and smooth fracture surface morphology. At low Ti_50Si_50 content, well dispersion of nanoparticles in PLA matrix was observed. Moreover, 97PLA/3 SiO_2 and PLA/3 TiO_2SiO_2 showed more agglomeration of SiO_2 , and TiO_2SiO_2 leading to PLA composites with poor mechanical properties. In addition, the micrographs of the fracture surface after tensile tests for PLA and PLA nanocomposites films with a magnification of 1500x were shown in Figure 10. PLA/ Ti_50Si_50 nanocomposite showed many small cavities on the fracture surface of the nanocomposite due to the removal of agglomerate of nanoparticles during the tensile test. However, PLA/ TiO_2 , PLA/ SiO_2 , and PLA/ TiO_2SiO_2 nanocomposites presented more cavities and fibril on the fracture surface than PLA/ Ti_50Si_50 nanocomposite indicating poor interfacial interaction between particles of TiO_2 or SiO_2 and PLA matrix.

Table 4. Thermal degradation of PLA and PLA nanocomposites

Samples	T_{onset} , °C	T_d , °C	T_f , °C	Residual, %
PLA	344.86	358.83	424.64	0.7053
99PLA/1 Ti_50Si_50	345.30	350.26	420.69	1.6108
97PLA/3 Ti_50Si_50	346.24	356.67	425.49	3.6729
95PLA/5 Ti_50Si_50	347.09	356.33	418.93	5.2243
97PLA/3 TiO_2	351.16	362.17	429.22	4.0747
97PLA/3 SiO_2	346.04	359.50	427.27	4.1432
97PLA/3 TiO_2SiO_2	348.66	360.17	418.69	3.7922

Conclusions

In this study, Ti_50Si_50 mixed oxide was synthesized using TTIP and TEOS as precursors. A combination of FTIR, FE-SEM, XRD and XRF have been used to characterize morphologies and structures of the mixed oxide. Ti-O-Si vibration of Ti_50Si_50 mixed oxide was confirmed by FTIR at 949 cm^{-1} indicating the forming of chemical bond between TiO_2 and SiO_2 . The powders of Ti_50Si_50 mixed oxides, TiO_2 , and SiO_2 show a homogeneous spherical morphology with size of 20-250 nm. XRD results of Ti_50Si_50 mixed oxides presented a broad diffraction peak within the 2θ range 10-40 corresponding to

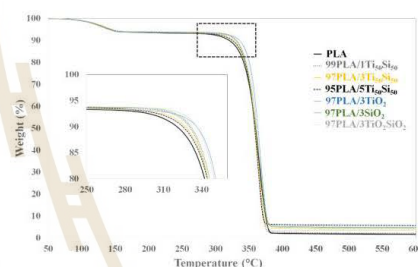


Figure 8. TGA curves of PLA and PLA nanocomposites at a heating rate of 10°C/min

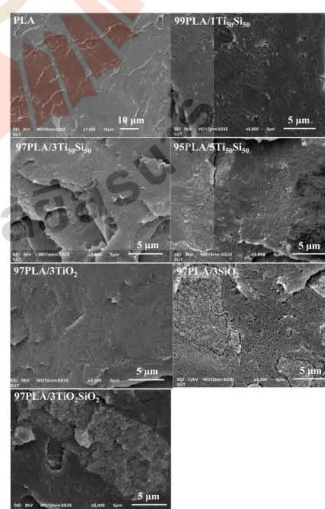


Figure 9. SEM micrographs at 5000x magnification of PLA and PLA nanocomposites

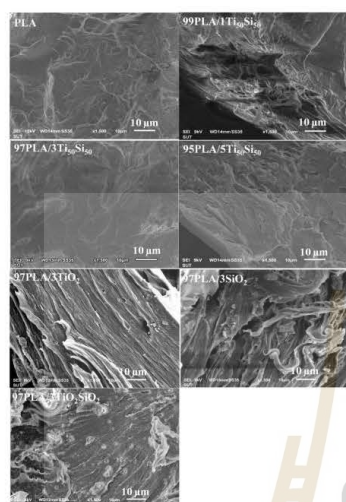


Figure 10. SEM micrographs after tensile testing at 1,500x magnification of PLA and PLA nanocomposites

characteristic of amorphous silica. This indicates that the titanium is highly dispersed in the silica matrix. The addition of 3 wt% of $Ti_{50}Si_{50}$ into PLA film improved the tensile strength and Young's modulus of PLA. The incorporation of $Ti_{50}Si_{50}$ decreased the cold crystallization temperature and increased degree of crystallinity of PLA. It may be concluded that $Ti_{50}Si_{50}$ nanoparticles can act as a nucleating agent for PLA. Thermal stability of PLA was enhanced with the incorporation of TiO_2 and SiO_2 .

Acknowledgments

The authors wish to acknowledge Suranaree University of Technology and Center of Excellence on Petrochemical and Materials Technology for their financial support.

References

- Athanasou, K.A., Niederauer, G.G., and Agrawal, C.M. (1996). Sterilization, toxicity, biocompatibility and clinical applications of polylactic acid/polyglycolic acid copolymers. *Biomater.*, 17:93-102.
- Burg, K.J.L., Holder, W.D., Culberson, C.R., Beiler, R.J., Greene, K.G., Loebbeck, A.B., Roland, W.D., Mooney, D.J., and Halberstadt, C.R. (1999). Parameters affecting cellular adhesion to polylactide films. *J. Biomater. Sci., Polym. Ed.*, 10:147-161.
- Buzarovska, A. (2013). PLA Nanocomposites with functionalized TiO_2 nanoparticles. *Polym. Plast. Technol. Eng.*, 52:280-286.
- Chandra, R. and Rustgi, R. (1998). Biodegradable polymers. *Progress in Polymer Science*, 23:1,273-1,335.
- Chen, R.-y., Zou, W., Wu, C.-r., Jia, S.-k., Huang, Z., Zhang, G.-z., Yang, Z.-t., and Qu, J.-p., (2014). Poly (lactic acid)/poly (butylene succinate)/calcium sulfate whiskers biodegradable blends prepared by vane extruder: Analysis of mechanical properties, morphology, and crystallization behavior. *Polym. Test.*, 34:1-9.
- Chiahung, H., Hsunling, B., Yaoling, H., Shuling, L., Shaoi, Y., and Yaohsuan, T., (2012). Synthesis of neutral SiO_2/TiO_2 hydrosol and its application as antireflective self-cleaning thin film. *Int. J. Photoenergy*, p. 1-8.
- Chu, Z., Zhao, T., Li, L., Fan, J., Qin, Y. (2017). Characterization of antimicrobial poly (lactic acid)/nano-composite films with silver and zinc oxide nanoparticles. *Materials*, 10(6):659.
- Fonseca, C., Ochoa, A., Ulloa, M.T., Alvarez, E., Canales, D., and Zapata, P.A. (2015). Poly(lactic acid)/ TiO_2 nanocomposites as alternative biocidal and antifungal materials. *Mater. Sci. Eng. C.*, 57:314-320.
- Galindo, I.R., Viveros, T., and Chadwick, D. (2007). Synthesis and characterization of titania-based ternary and binary mixed oxides prepared by the sol-gel method and their activity in 2-propanol dehydration. *Ind. Eng. Chem. Res.*, 46(4):1,138-1,147.
- Huang, S.-M., Hwang, J.-J., Liu, H.-J., and Lin, L.-H. (2010). Crystallization behavior of poly(L-lactic acid)/montmorillonite nanocomposites. *J. Appl. Polym. Sci.*, 117(1):434-442.
- Karkare, M.M. (2014). Choice of precursor not affecting the size of anatase TiO_2 nanoparticles but affecting morphology under broader view. *Int. Nano Lett.*, 4(3):111.
- Kim, T.G., An, G.S., Han, J.S., Hur, J.U., Park, B.G., Choi, S.-C. (2017). Synthesis of size controlled spherical silica nanoparticles via sol-gel process within hydrophilic solvent. *J. Korean Ceram. Soc.*, 54:49-54.
- Kim, W.B., Choi, S.H., and Lee, J.S. (2000). Quantitative analysis of Ti-O-Si and Ti-O-Ti bonds in Ti-Si binary oxides by the linear combination of XANES. *J. Phys. Chem. B*, 104:8,670-8,678.
- Lim, L.T., Auras, R., and Rubino, M. (2008). Processing technologies for poly (lactic acid). *Prog. Polym. Sci.*, 33:820-852.
- Madhavan Nampoothiri, K., Nair, N.R., and John, R.P. (2010). An overview of the recent developments in polylactide (PLA) research. *Bioresour. Technol.*, 101:8,493-8,501.
- Murariu, M., Paint, Y., Murariu, O., Raquez, J.-M., Bonnaud, L., and Dubois, P. (2015). Current progress in the production of PLA-ZnO nanocomposites: Beneficial effects of chain extender addition on key properties. *J. Appl. Polym. Sci.*, 132(48):42480
- Pabón, E., Retuert, J., and Quijada, R. (2007). Synthesis of mixed silica-titania by the sol-gel method using polyethylenimine: porosity and catalytic properties. *J. Porous Mater.*, 14:151-158.
- Rasal, R.M., Janorkar, A.V., and Hirt, D.E. (2010). Poly (lactic acid) modifications. *Prog. Polym. Sci.*, 35:338-356.
- Ren, J., Li, Z., Liu, S., Xing, Y., and Xie, K. (2008). Silica-titania mixed oxides: Si-O-Ti connectivity, coordination of titanium, and surface acidic properties. *Catal. Lett.*, 124:185-194.
- Sahu, D.R., Hong, L.Y., Wang, S.-C., and Huang, J.-L. (2009). Synthesis, analysis and characterization of ordered mesoporous $TiO_2/SBA-15$ matrix: Effect of calcination temperature. *Microporous Mesoporous Mater.*, 117:640-649.
- Sarasua, J.-R., Prud'homme, R.E., Wisniewski, M., Le Borgne, A., and Spassky, N. (1998). Crystallization and melting

- behavior of polylactides. *Macromolecules*, 31:3,895-3,905.
- Shirkavand, S. and Moslehifard, E. (2014). Effect of TiO₂ nanoparticles on tensile strength of dental acrylic resins. *J. Dent. Res. Dent. Clin. Dent. Prospect*, 8(4):197-203.
- Tang, Z., Zhang, C., Liu, X., and Zhu, J. (2012). The crystallization behavior and mechanical properties of polylactic acid in the presence of a crystal nucleating agent. *J. Appl. Polym. Sci.*, 125:1,108-1,115.
- Wang, H., Fang, M., Shi, T., Zhai, L., and Tang, C. (2006) Preparation of porous poly(lactic acid)/SiO₂ hybrid microspheres. *J. Appl. Polym. Sci.*, 102:679-683.
- Wu, G., Liu, S., Jia, H., and Dai, J. (2016). Preparation and properties of heat resistant polylactic acid (PLA)/Nano-SiO₂ composite filament. *J. Wuhan Univ. Technol. Mat. Sci. Edit.*, 31(1):164-171
- Xiu, H., Qi, X., Bai, H., Zhang, Q., and Fu, Q. (2017). Simultaneously improving toughness and UV-resistance of polylactide/titanium dioxide nanocomposites by adding poly(ether)urethane. *Polym. Degrad. Stab.*, 143:136-144.
- Yamashita, H., Kawasaki, S., Ichihashi, Y., Harada, M., Takeuchi, M., Anpo, M., Stewart, G., Fox, M.A., Louis, C., and Che, M. (1998). Characterization of titanium-silicon binary oxide catalysts prepared by the sol-gel method and their photocatalytic reactivity for the liquid-phase oxidation of 1-Octanol. *J. Phys. Chem. B*, 102:5,870-5,875.
- Yeh, J.T., Huang, C.Y., Chai, W.J., and Chen, K.N. (2009). Plasticized properties of poly (lactic acid) and triacetine blends. *J. Appl. Polym. Sci.*, 112:2,757-2,763.



Article

Structural Characterization of Titanium–Silica Oxide Using Synchrotron Radiation X-ray Absorption Spectroscopy

Arpaporn Teamsinsungvon ^{1,2,3}, Chaiwat Ruksakulpiwat ^{1,2,3,*}, Penphittha Amonpattaratkit ⁴ and Yupaporn Ruksakulpiwat ^{1,2,3,*}

¹ School of Polymer Engineering, Institute of Engineering, Suranaree University of Technology, Nakhon Ratchasima 30000, Thailand; arpaporn.te@gmail.com (A.T.); charuk@sut.ac.th (C.R.)

² Center of Excellence on Petrochemical and Materials Technology, Chulalongkorn University, Bangkok 10330, Thailand

³ Research Center for Biocomposite Materials for Medical Industry and Agricultural and Food Industry, Nakhon Ratchasima 30000, Thailand

⁴ Synchrotron Light Research Institute (SLRI), 111 University Avenue, Muang District, Nakhon Ratchasima 30000, Thailand; penphittha@slri.or.th

* Correspondence: yupa@sut.ac.th; Tel.: +66-44-22-3033



Citation: Teamsinsungvon, A.; Ruksakulpiwat, C.; Amonpattaratkit, P.; Ruksakulpiwat, Y. Structural Characterization of Titanium–Silica Oxide Using Synchrotron Radiation X-ray Absorption Spectroscopy. *Polymers* **2022**, *14*, 2729. <https://doi.org/10.3390/polym14132729>

Academic Editors: Wei Jiang and Yubing Hu

Received: 8 June 2022

Accepted: 30 June 2022

Published: 3 July 2022

Publisher's Note: MDPI stays neutral with regard to jurisdictional claims in published maps and institutional affiliations.



Copyright: © 2022 by the authors. Licensee MDPI, Basel, Switzerland. This article is an open access article distributed under the terms and conditions of the Creative Commons Attribution (CC BY) license (<https://creativecommons.org/licenses/by/4.0/>).

Abstract: In this study, titania–silica oxides (Ti_xSi_y oxides) were successfully prepared via the sol–gel technique. The Ti and Si precursors were titanium (IV), isopropoxide (TIP), and tetraethylorthosilicate (TEOS), respectively. In this work, the effects of pH and the Ti/Si atomic ratio of titanium–silicon binary oxide (Ti_xSi_y) on the structural characteristics of Ti_xSi_y oxide are reported. ^{29}Si solid-state NMR and FTIR were used to validate the chemical structure of Ti_xSi_y oxide. The structural characteristics of Ti_xSi_y oxide were investigated using X-ray diffraction, XRF, Fe-SEM, diffraction particle size analysis, and nitrogen adsorption measurements. By applying X-ray absorption spectroscopy (XAS) obtained from synchrotron light sources, the qualitative characterization of the Ti–O–Si and Ti–O–Ti bonds in Ti–Si oxides was proposed. Some Si atoms in the SiO_2 network were replaced by Ti atoms, suggesting that Si–O–Ti bonds were formed as a result of the synthesis accomplished using the sol–gel technique described in this article. Upon increasing the pH to alkaline conditions (pH 9.0 and 10.0), the nanoparticles acquired a more spherical shape, and their size distribution became more uniform, resulting in an acceptable nanostructure. Ti_xSi_y oxide nanoparticles were largely spherical in shape, and agglomeration was minimized. However, the $Ti_{50}Si_{50}$ oxide particles at pH 10.0 become nano-sized and agglomerated. The presence of a significant pre-edge feature in the spectra of $Ti_{50}Si_{50}$ oxide samples implied that a higher fraction of Ti atoms occupied tetrahedral symmetry locations, as predicted in samples where Ti directly substituted Si. The proportion of Ti atoms in a tetrahedral environment agreed with the value of 1.83 given for the Ti–O bond distance in Ti_xSi_y oxides produced at pH 9.0 using extended X-ray absorption fine structure (EXAFS) analysis. Photocatalysis was improved by adding 3% wt TiO_2 , SiO_2 , and Ti_xSi_y oxide to the PLA film matrix. TiO_2 was more effective than $Ti_{50}Si_{50}$ pH 9.0, $Ti_{50}Si_{50}$ pH 10.0, $Ti_{50}Si_{50}$ pH 8.0, and SiO_2 in degrading methylene blue (MB). The most effective method to degrade MB was $TiO_2 > Ti_{70}Si_{30} > Ti_{50}Si_{50} > Ti_{40}Si_{60} > SiO_2$. Under these conditions, PLA/ $Ti_{70}Si_{30}$ improved the effectiveness of the photocatalytic activity of PLA.

Keywords: mixed oxide; sol–gel method; titania; silica; XAS

1. Introduction

In recent years, binary oxides of Ti and Si have gained a great deal of attention in a wide range of applications, including TiO_2 – SiO_2 [1], Ag– TiO_2 – SiO_2 [2], and the ordered mesoporous TiO_2 /SBA-15 matrix [3]. Sol–gel processing is an adjustable method that has attained commercial success because it allows for the control of the desired properties of a material during the preparation process. As a result, the sol–gel method has become one of the most preferred methods to produce oxide materials. Titanium dioxide (TiO_2),

often known as titania, is an important substance. This multifunctional material may be used in coatings [4,5], biomaterials [6], photocatalysts [7], food packaging [8], and chemical sensors [9], to mention a few applications. It possesses a number of desirable characteristics, including chemical resistance, chemical stability [10], photocatalytic activity, outstanding photostability, biocompatibility, and antibacterial activity [11]. Furthermore, titanium dioxide (TiO_2) is widely recognized as a large-bandgap semiconductor with photocatalytic activity, whereas silicon dioxide (SiO_2), often known as silica, has a well-defined ordered structure, a large surface area, is cost-effective to produce, and is easy to modify [12].

Adding SiO_2 to the formulation of a polymer is also known to increase its modulus of elasticity, strength, heat and fire resistance, wear resistance, insulating properties, and other properties [13]. In addition to drug delivery, bioimaging, gene transport, and engineering, SiO_2 is employed as a food ingredient. Moreover, the FDA has classified silica as a “generally recognized as safe” (GRAS) substance, making it an attractive candidate for biological activities [14].

Titanium–silicon oxide (Ti_xSi_y) is a fascinating material family that has gained a great deal of attention in recent years. The oxide has been widely employed as a catalyst and support for a variety of processes. It is constructed of TiO_2 and SiO_2 , and it not only possesses the advantages of both TiO_2 (photocatalytic properties and antimicrobial biomaterials) and SiO_2 (high thermal stability and excellent mechanical strength), but it also expands their applications by developing additional catalytic active sites, owing to the chemical link between the two materials [15]. There are several techniques for manufacturing Ti_xSi_y oxide, but sol–gel approaches appear to be the most cost-effective. These methods do not necessitate the use of costly solvents. Titanium alkoxide (e.g., titanium isopropoxide) is frequently utilized in sol–gel techniques.

One of the most prevalent methods for producing oxide materials is the sol–gel method. This method allows for the management of textural characteristics, as well as a high degree of mixing in bulk mixed oxides while retaining the oxide material anion-free. Furthermore, the materials produced using this method are not microstructurally ordered, have a large surface area, and show pore size variation [16,17].

The powerful technique of synchrotron X-ray absorption spectroscopy (XAS) using tunable, very intense X-rays from a high-energy electron storage ring has been applied to investigate the structural properties of materials. XAS is particularly attractive because of its ability to deliver electronic structure as well as geometric information. A typical K-edge absorption spectrum is divided into two sections: (i) the X-ray absorption near-edge structure (XANES) (<50 eV) contains bond lengths and angles, as well as information about the three-dimensional structure around the absorbing atom; (ii) the extended X-ray absorption fine structure (EXAFS) region (typically > 50 eV) provides information on the initial coordination shell around the absorbing atom, including coordination numbers and bond lengths [18].

In most of the previous reports, XAS has been employed to determine information on the coordination environment of tetravalent Ti [Ti(IV)] in structurally complex oxide materials and bond distances between Ti–O and Ti–Si atoms. Niltharach et al. [19] used XANES methods to investigate the structural details of sol–gel-produced TiO_2 samples with and without the inclusion of Ce. The XANES results also showed that the sample produced under the low hydrolysis condition had a significant number of Ti atoms in forms other than anatase and rutile TiO_2 . Won Bae Kim et al. [20] used the linear combination of two reference XANES spectra to estimate the pre-edge of the Ti K-edge in order to quantitatively analyze the percentages of Ti–O–Si and Ti–O–Ti bonds. The findings of pre-edge fitting in conjunction with XRD and XPS suggested that monolayer coverage was attained at around 7–10 wt.% Ti loading, where the concentration of Ti in Ti–O–Si was saturated to 0.56 mmol-Ti/g material. Shuji Matsuo et al. [21] determined the local Ti environments in the sol, gel, and xerogels of titanium oxide prepared by a sol–gel method using titanium K-edge XANES. All of the samples could be divided into three groups: the anatase group, the anatase-like structure group, and the weak Ti–Ti interaction group.

A variety of materials were produced by changing the composition of the primary sol and/or the thermal treatment. The nature of the precursor, the molar ratio between silicon and titanium alkoxide, the type of solvent, and the use of modifying agents all had an influence on the final material's microstructure and hence its properties. Furthermore, while manufacturing Ti_xSi_y oxide via sol-gel, the pH of the solution is one of the most essential factors determining Ti_xSi_y oxide's properties. The hydrolysis and condensation behavior of a solution during gel formation, as well as the structure of the binary oxide, is influenced by its pH [22]. In order to maintain the sample in a powder morphology with a large surface area, the gel must be stabilized. The goal of this study was to evaluate the effects of pH and Ti/Si atomic ratio on Ti_xSi_y oxide using the sol-gel technique (Stöber method). XANES and EXAFS were used to evaluate Ti–O–Si and Ti–O–Ti connectivity in Ti_xSi_y oxides, the local atomic structure, the bond distances between Ti–O and Ti–Si atoms, the coordination number, and the valence state of titanium atoms TiO_2 and all mixed oxide samples. In addition, the photocatalytic behavior of all samples was investigated by comparing their degradation of methylene blue (MB) solutions exposed to UV radiation.

2. Materials and Methods

2.1. Materials

Tetraethylorthosilicate (TEOS, 98%, AR-grade) and titanium (IV) isopropoxide (TTIP, 98%, AR-grade) were purchased from Acros (Geel, Belgium). Absolute ethanol (C_2H_5OH , AR-grade), hydrochloric acid (HCl, AR-grade), and ammonium hydroxide (NH_4OH , AR-grade) were supplied by Carlo Erba Reagents (Emmendingen, Germany). PLA4043D was provided by NatureWorks LLC (Minnetonka, MN, USA).

2.2. Synthesis of Titania–Silica Binary Oxide (Ti_xSi_y Oxide), Silica, and Titanium Dioxide

Sol-gel techniques were used to prepare titanium–silicon oxide (Ti_xSi_y) utilizing a modified Stöber procedure, including the simultaneous hydrolysis and condensation of TEOS [20]. Figure 1 illustrates the experimental technique for producing Ti_xSi_y oxide particles. TEOS and TTIP were used without purification.

The total moles of Ti-alkoxide and Si-alkoxide were determined to be 0.12 mol. For the pre-hydrolysis step, the mixture of two alkoxides was added into a five-neck round-bottom flask containing 150 cm^3 of ethanol for 1 h. A condenser was used in the condensation step to prevent the solvent from vaporizing out of the process. Stirring raised the temperature of the reactor to $75\text{--}80\text{ }^\circ\text{C}$. After an hour of mixing, a yellowish translucent sol was observed after adding TTIP and 25 ml of ethanol to the reactor drop by drop for 1 h. DI water was added to the sol, which was then aged at room temperature for 2 h at $80\text{ }^\circ\text{C}$. The aged gel was then refined in a centrifugal separator for 10 min at 6000 rpm. Finally, the solid particles were calcined for 3 h at $450\text{ }^\circ\text{C}$. A reference pure SiO_2 sample was prepared in NH_4OH in the same manner as described above but without the addition of TTIP [23]. In addition, reference pure TiO_2 was generated in the same manner as Ti_xSi_y oxide in acid [24]. Tables 1 and 2 reveal the composition of the sol-gel liquid solution used to produce Ti_xSi_y oxide.

Table 1. Moles of components in the preparation of $Ti_{50}Si_{50}$ oxide synthesized at various pH values.

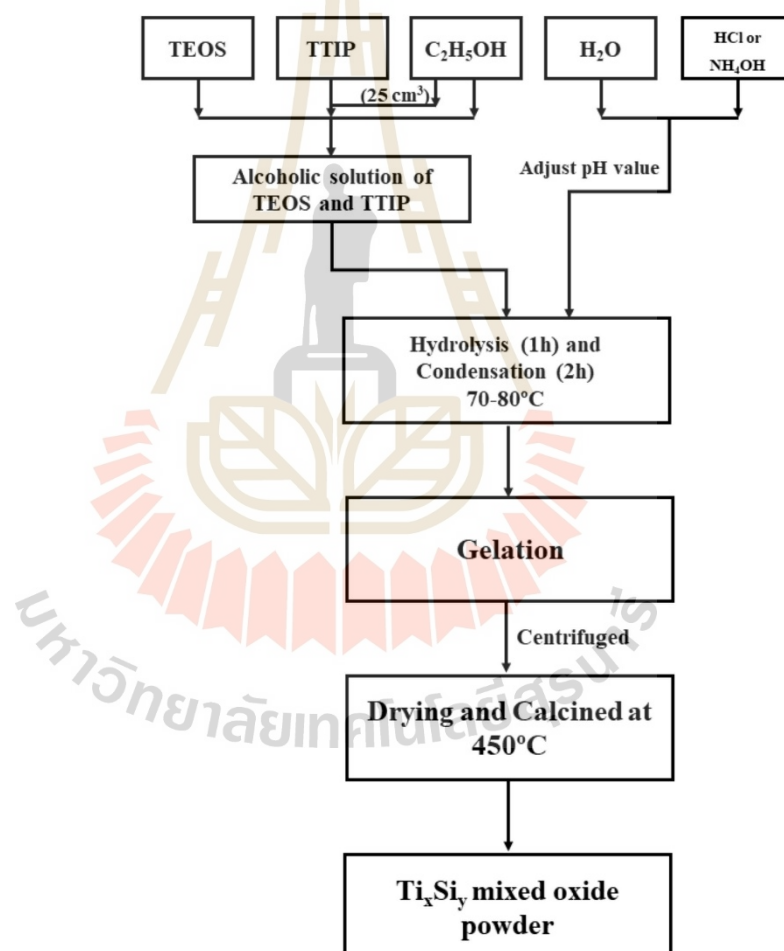
Samples	TTIP (mol)	TEOS (mol)	C_2H_5OH (mol)	HCl/ NH_4OH (mol)	H_2O (mol)
SiO_2	-	0.120	1.889	0.060 ^b	0.440
$Ti_{50}Si_{50}$ pH 8.0	0.011	0.109	1.889	0.025 ^b	0.440
$Ti_{50}Si_{50}$ pH 9.0	0.011	0.109	1.889	0.060 ^b	0.440
$Ti_{50}Si_{50}$ pH 10.0	0.011	0.109	1.889	0.075 ^b	0.440
TiO_2	0.120	-	4.293	0.081 ^a	0.702

^a moles of HCl, ^b moles of NH_4OH .

Table 2. Moles of components in Ti_xSi_y oxide synthesized at pH 9.0 with different Ti/Si ratios.

Samples	TTIP (mol)	TEOS (mol)	C_2H_5OH (mol)	NH_4OH/HCl (mol)	H_2O (mol)
SiO_2	-	0.120	1.889	0.060 ^b	0.440
$Ti_{70}Si_{30}$	0.020	0.100	1.889	0.060 ^b	0.440
$Ti_{50}Si_{50}$	0.011	0.109	1.889	0.060 ^b	0.440
$Ti_{40}Si_{60}$	0.008	0.112	1.889	0.060 ^b	0.440
TiO_2	0.120	-	4.293	0.081 ^a	0.702

^a moles of HCl, ^b moles of NH_4OH .

**Figure 1.** Experimental procedures for preparing Ti_xSi_y oxide particles.

2.3. Characterization of Titanium–Silicon Oxide

2.3.1. ^{29}Si Solid-State Nuclear Magnetic Resonance Spectroscopy (^{29}Si Solid-State NMR)

The ^{29}Si solid-state NMR spectra were used to evaluate the structure of the silicate phase in SiO_2 and Ti_xSi_y oxide. ^{29}Si NMR spectra were recorded on a Bruker Avance III HD 500 MHz spectrometer (Billerica, MA, USA).

2.3.2. Fourier Transform Infrared Spectroscopy (FT-IR)

Infrared spectra of Ti_xSi_y oxide, TiO_2 , and SiO_2 were recorded by Fourier transform infrared spectroscopy (FTIR) (Bruker, Tensor 27, Billerica, MA, USA) using attenuated total reflectance (ATR) equipped with a platinum diamond crystal (TYPE A225/QL). The spectra were recorded at wavenumbers from 400 to 4000 cm^{-1} with 4 cm^{-1} resolution through the accumulation of 64 scans. All samples of Ti_xSi_y oxide, TiO_2 , and SiO_2 were dried in an oven at 70 °C for 4 h before testing.

2.3.3. Field Emission Scanning Electron Microscopy (FE-SEM)

FE-SEM images of Ti_xSi_y oxide, TiO_2 , and SiO_2 were examined by a field-emission scanning electron microscope (FESEM-EDS, Carl Zeiss Auriga, Oberkochen, Germany). The film specimens were coated with carbon prior to the investigation. An acceleration voltage of 3 kV was used to collect SEM images of the samples.

2.3.4. X-ray Diffraction (XRD)

The diffractograms of Ti_xSi_y oxide, TiO_2 , and SiO_2 were recorded via powder X-ray diffraction (Bruker, Model D2 phaser, Billerica, MA, USA), with $\text{CuK}\alpha$ radiation, scanning from 10° to 90° at a rate of 0.05°/s, with a current of 35 mA and 35 mA.

2.3.5. X-ray Absorption Near-Edge Structure Spectroscopy (XANES) and Extended X-ray Absorption Fine Structure Spectroscopy (EXAFS)

All TiO_2 and SiO_2 standard compounds and Ti_xSi_y oxide samples were analyzed by XANES and EXAFS spectroscopy at the Ti K-edge at beamline 8 of the electron storage ring (using an electron energy of 1.2 GeV, a bending magnet, beam current of 80–150 mA, and 1.1 to 1.7 $\times 10^{11}$ photons s^{-1}) at the Synchrotron Light Research Institute (SLRI), Nakhon Ratchasima, Thailand [25]. Finely ground, homogenized powder of each sample was spread as a thin film (area 2.0 cm \times 0.5 cm) and carefully dispersed with a spatula to yield a homogeneous particle distribution and to avoid hole effects on Kapton tape (Lanmar Inc., Northbrook, IL, USA) mounted on a sample holder. At least five spectra were obtained for each standard compound and oxide sample. All XANES and EXAFS spectra were measured in the transmission mode with ionization chamber detectors. For the acquisition of all spectra, a Ge (220) double crystal monochromator with an energy resolution ($\Delta E/E$) of 2×10^{-4} was used. An energy range of 4936–5824 eV with an energy step of 2, 0.2, 0.05k eV was used for Ti K-edge spectra. The photon energy was calibrated against the K-edge of Ti foil at 4966 \pm 0.2 eV. Finally, the normalized XANES and EXAFS data were processed and analyzed after background subtraction in the pre-edge and post-edge regions using a software package including (i) ATHENA (Chicago, IL, USA) for XAS data processing, (ii) ARTEMIS (Chicago, IL, USA) for EXAFS data analysis using theoretical standards from FEFF, and (iii) HEPHAESTUS (Chicago, IL, USA) software for a collection of beamline utilities based on tables of atomic absorption data. This package is based on the IFEFFIT library of numerical and XAS algorithms and is written in the Perl programming language using the Perl/Tk graphics toolkit [26].

2.3.6. X-ray Fluorescence (XRF)

The chemical compositions of Ti_xSi_y oxide, TiO_2 , and SiO_2 were investigated by energy-dispersive XRF (EDS Oxford Instrument ED 2000, Abingdon, UK) with a Rh X-ray tube with a vacuum medium.

2.3.7. Particle Size Distribution

The particle size distribution of Ti_xSi_y oxide, TiO_2 , and SiO_2 was evaluated by a diffraction particle size analyzer (DPSA) (Malvern Instruments, model Mastersizer 2000, Great Malvern, England). The Ti_xSi_y oxide, TiO_2 , and SiO_2 were dispersed in absolute ethanol and analyzed by a He-Ne laser. The average particle size distribution was investigated from the standard volume percentiles at 10, 50, and 90%. The average volume-weighted diameter was used to define the average particle size.

2.3.8. Specific Surface Area (BET)

The specific surface areas of Ti_xSi_y oxide, TiO_2 , and SiO_2 were investigated by a nitrogen adsorption analyzer (BELSORP MINI II, model Bel-Japan, Osaka, Japan). The samples of Ti_xSi_y oxide, TiO_2 , and SiO_2 were degassed at 300 °C for 3 h before measurement. The Brunauer, Emmett, Teller (BET) and Barrett, Joyner, Halenda (BJH) methods were used to calculate the specific surface area and pore size distribution, respectively.

2.3.9. Photocatalytic Activity Characterization

PLA, PLA/ TiO_2 , PLA/ SiO_2 , and PLA/ Ti_xSi_y oxide composites with 3 wt.% of Ti_xSi_y oxide were prepared by the solvent-casting method. The polymer was dissolved in solvent (10% w/v) by stirring. Firstly, Ti_xSi_y oxide was dispersed in chloroform with ultrasonic treatment for 1 day. After this, PLA was added to the Ti_xSi_y oxide and strictly stirred for 4 days. The dispersions of PLA composites were additionally ultrasonically treated for 1 h using a frequency of 42 kHz, four times per day. The treated dispersions were gently poured onto Petri dishes, and the solvent was evaporated at room temperature. The films were dried to a constant mass, dried at room temperature for 24 h, and kept in the oven at 40 °C for 4 h. Film thickness was measured by using a micrometer in eight replicates for each sample, from which an average value was attained. Pure PLA and nanocomposite films had a uniform thickness of 200–250 μm .

The photocatalytic activity of PLA composite films was evaluated in terms of the degradation of methylene blue (MB) under UV light according to Chinese standard GB/T 23762-2009. PLA composite films were placed in a flask and then 200 mL of MB solution (10 mg/L) was added. The flask was placed on a mechanical shaker at 50 rpm in a UV chamber with 4 UV lamps (LP Hg lamps, 8 watts, main light emission at 245 nm). The schematic design of the investigational setup for the photocatalytic process is presented in Figure 2. Then, 4 mL MB solution was collected every 60 min and analyzed using a UV-vis spectrophotometer (Cary300, Agilent Technology, CA, USA). In order to maintain the volume of MB solution in the flask, the samples were returned after each measurement. The maximum absorbance of MB occurred at 664 nm (Figure 3). The spectrometer was calibrated with a solution of MB at 1mg/L, 3mg/L, 5mg/L, 7mg/L, and 10mg/L concentrations, respectively. The calibration curve of methylene blue aqueous solutions is shown in Figure 4. In order to precisely predict the decomposition of MB under UV light, the PLA and composite films, as well as the solution, were stored in a black box without any photocatalyst. The concentration of MB was also collected every 60 min to estimate the absorption of MB.

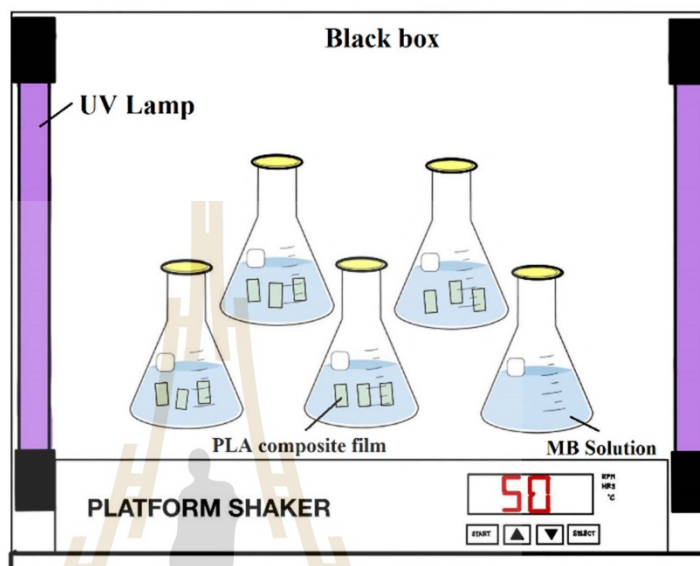


Figure 2. Schematic illustration of the experimental setup for photocatalytic process.

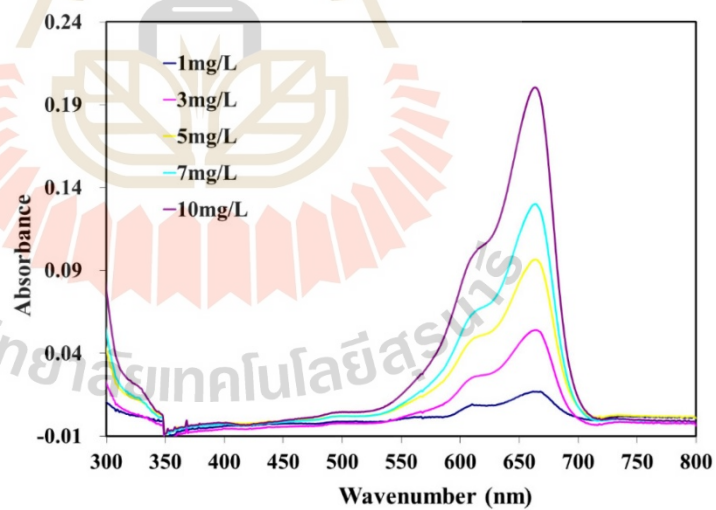


Figure 3. Wavelength-absorbance curves of methylene blue (MB) aqueous solutions.

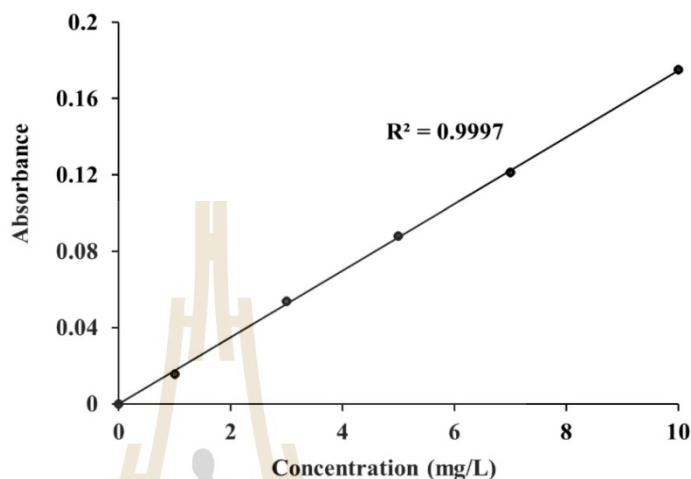


Figure 4. Calibration curve of methylene blue (MB) aqueous solutions.

3. Results

3.1. Effect of pH

^{29}Si Solid-state NMR spectroscopy was used to investigate the structures of Ti_xSi_y oxide (particularly for 1:1 atomic ratio) and SiO_2 in order to determine the development of the framework of silicon atoms in these materials. The structural analysis of ^{29}Si NMR is illustrated in Figure 5, which presents the spectra of the silica and the $\text{Ti}_{50}\text{Si}_{50}$ oxide. In general, the ^{29}Si NMR spectra of oxides show three peaks for different environments for Si: isolated silanol groups ($\text{SiO}_3\text{Si-OH}$, Q^3 ; geminal silanols ($\text{SiO}_2\text{Si-(OH)}_2$, Q^2 ; and silicon in the siloxane binding environment without hydroxyl groups (SiO_4Si , Q^4 (Q^n represents a SiO_4 unit, with n being the number of bridging oxygen atoms) [27,28]. According to related references, the three resonance signals of pure SiO_2 (synthesized by sol-gel method) appearing at -93.9 , -103.3 , and -110.2 ppm can be attributed to the configurations of Q^2 , Q^3 , and Q^4 , respectively. The spectrum of silica (Figure 5a) exhibits a chemical shift of -110 ppm, which is attributed to the Q^4 units, and a minor peak appears at -103 ppm that would conform to the Q^3 units corresponding to the siloxane (Si-O-Si) and silanol ($=\text{Si-OH}$) groups of silica. The strength of Q^4 structural units [$\text{Si}(\text{SiO})_4$] represents a three-dimensional network of silica, as evidenced by the intensity of the peaks in Figure 5a. There would also be a very small proportion of Si nuclei directly bonded to the hydroxyl groups, influenced by the chemical shift of the Q^3 structural unit [$\text{Si}(\text{SiO})_3\text{OH}$] [17]. Additionally, Figure 5b indicates that silica was chemically combined with titanium oxide for the formation of the $\text{Ti}_{50}\text{Si}_{50}$ oxide, causing Ti atoms to be disrupted in the three-dimensional silica network and the microstructure surrounding the silicon atoms. When comparing the peak at approximately -103 ppm to the quantity of siloxane (Si-O-Si) and silanol ($=\text{Si-OH}$) groups in pure SiO_2 , a very substantial increase in Q^3 units (mono-substitution) is detected, which might be due to the existence of significant Si-O-Ti bonds in this sample, signaling atomic mixing. The presence of Ti-O-Si-O-Ti-O groups may have caused the appearance of Q^2 units, which might be linked to disubstituted silica in tetrahedra [29]. A similar observation was reported by Pabón, Retuert, and Quijada (2007) [17]. Obviously, Ti atoms replaced some Si atoms in the SiO_2 network, indicating that, as a consequence of the synthesis performed by the sol-gel method defined in this work, a large number of Si-O-Ti bonds were created, in agreement with the results of the FTIR and XRD.

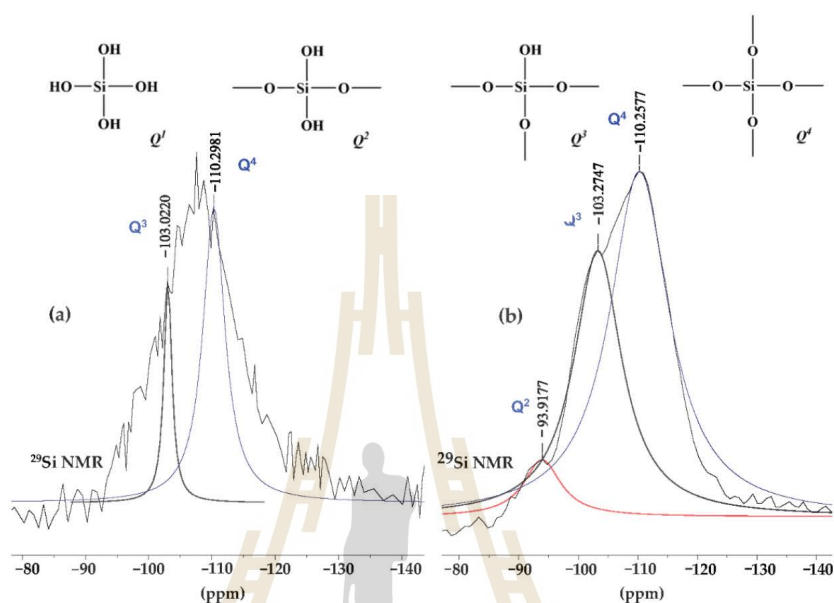


Figure 5. ^{29}Si -NMR patterns of (a) SiO_2 and (b) $\text{Ti}_{50}\text{Si}_{50}$ oxide.

FTIR spectra of TiO_2 , SiO_2 , and $\text{Ti}_{50}\text{Si}_{50}$ oxides synthesized at various pH values are shown in Figure 6. TiO_2 and all $\text{Ti}_{50}\text{Si}_{50}$ oxides displayed a prominent band at 400 to 700 cm^{-1} in their FTIR spectra, which corresponded to the bending and stretching mode of Ti-O-Ti and was characteristic of well-ordered TiO_6 octahedrons [30].

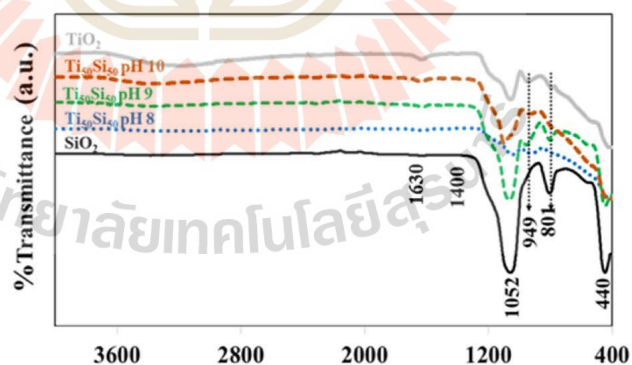


Figure 6. FTIR spectra of TiO_2 , SiO_2 , and Ti_xSi_y oxides synthesized at pH 8.0, 9.0, and 10.0.

Strong bands near 3440 and 1630 cm^{-1} can be seen in Figure 6, which are assigned to the stretching and deformation vibration of the hydroxyl groups present ($\text{TiO}_2\text{-OH}$) on the surfaces of TiO_2 and all mixed oxide samples. The intensive band of OH-group asymmetrical and symmetrical stretching vibrations at 3440 cm^{-1} and O-H deformation

vibration at 1630 cm^{-1} could confirm the large amount of water molecules [31]. However, the OH-group vibration bands were substantially weaker as the calcination temperatures increased [32]. The peaks at 440 , 801 , and 1052 cm^{-1} corresponded to the rocking, symmetric, and asymmetric stretching vibrations of Si–O–Si of silica, respectively [3]. However, TiO_2 also presents a peak at $1000\text{--}1200\text{ cm}^{-1}$, which is assigned to the deformation vibration of Ti–O–Ti of TiO_2 [33]. The peak at 949 cm^{-1} was commonly attributed to Ti–O–Si vibrations by various authors, indicating the existence of Ti–O–Si linkages [34]. This band can also be attributed to the Si–OH bond, which should be attributed to Si–OH bonding. However, this absorption band disappeared after the SiO_2 particles were calcined at $450\text{ }^\circ\text{C}$. On the other hand, the 949 cm^{-1} absorption band was still observed for all Ti_xSi_y oxide samples that had been calcined at a temperature of $450\text{ }^\circ\text{C}$. Accordingly, the 949 cm^{-1} peak in the FTIR spectra for Ti_xSi_y oxide particles should not be attributed to Si–OH bonds but rather be associated with Si–O–Ti bonding [35,36]. This indicated titanium being combined into the framework of silica. Therefore, the influence of pH on the FTIR of the $\text{Ti}_{50}\text{Si}_{50}$ oxide was not observed. Based on the evidence from NMR and FTIR, the probable mechanism for the synthesized Ti_xSi_y oxides based on results of earlier studies [37] is suggested in Figure 7.

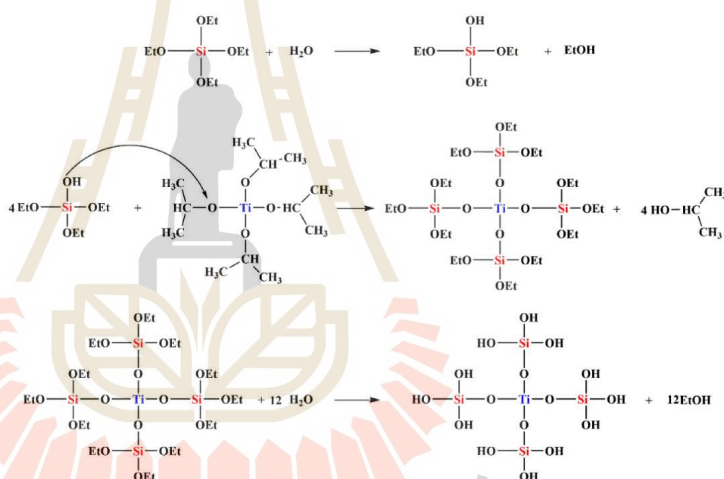


Figure 7. Proposed probable mechanism for synthesized Ti_xSi_y oxides.

Figure 8 shows FE-SEM images of SiO_2 and $\text{Ti}_{50}\text{Si}_{50}$ oxide powder nanoparticles synthesized at various pH values. SiO_2 particles were mostly spherical in shape, with low agglomeration (Figure 8a). Meanwhile, large bulk particles with high agglomeration of $\text{Ti}_{50}\text{Si}_{50}$ oxides are shown in Figure 8b. This agglomeration with an irregular shape was a result of the Ti and Si precursors in the sol solution during the processing, synthesized due to the absence of appropriate hydroxide ions (OH^- ions) at pH 8.0 [38]. Figure 8c,d show that the nanoparticles were spherical in shape and the size distribution of particles became more uniform, with a respectable nanostructure, upon increasing the pH to alkaline conditions (pH 9.0 and 10.0). In this work, Ti_xSi_y oxide nanoparticles were essentially spherical in form, with low agglomeration. However, the size of the $\text{Ti}_{50}\text{Si}_{50}$ oxide particles at pH 10.0 was nano-sized, with the appearance of agglomeration (Figure 8d). Wu, Wu, and Lü, (2006) claimed that the colloidal sol–gel technique can generate large particles composed of agglomerated nanoparticles and either condensed or porous polycrystalline microparticles [39]. Therefore, pH 9.0 was selected to achieve the compositionally controlled synthesis of Ti_xSi_y oxide particles that are spherical in shape.

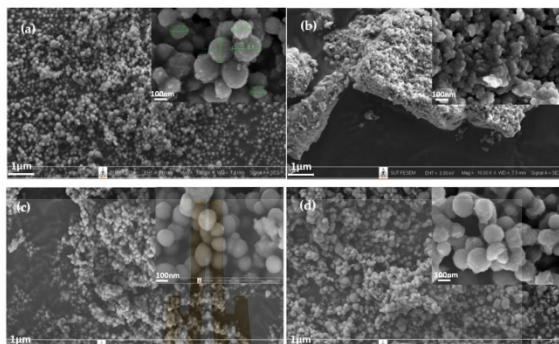


Figure 8. Low ($\times 10k$ WD = 7.0–7.5 mm EHT = 3.00 kV) and high ($\times 100k$ WD = 6.9–7.3 mm EHT = 3.00 kV) magnification SEM images of $Ti_{50}Si_{50}$ oxides synthesized at various pH values: (a) SiO_2 , (b) $Ti_{50}Si_{50}$ pH 8.0, (c) $Ti_{50}Si_{50}$ pH 9.0, (d) $Ti_{50}Si_{50}$ pH 10.0.

XRD patterns of $Ti_{50}Si_{50}$ oxide powders synthesized at various pH values (8.0, 9.0, and 10.0) are shown in Figure 9. Silica showed one amorphous peak located at 2θ angles at 23° . In most of the $Ti_{50}Si_{50}$ oxide powders prepared at pH 8.0 and 9.0 (Figure 9), XRD patterns exhibited a broad amorphous peak because of the existence of silica. Furthermore, the formation of the $Ti_{50}Si_{50}$ oxides suggests that titanium oxide was combined with the silica by atomic mixing, and consequently the distribution of Ti atoms occurred in the microstructure around the silicon atoms and the three-dimensional silica network. However, the $Ti_{50}Si_{50}$ oxide powders prepared at pH 10.0 exhibited an intense TiO_2 anatase peak, suggesting that the formation of higher crystallites of anatase occurred in $Ti_{50}Si_{50}$ oxides when the high pH of the sol–gel solution was applied during hydrolysis [38]. It can be clearly seen that the crystallinity of anatase in $Ti_{50}Si_{50}$ oxide samples is enhanced by adjusting the pH value of the sol.

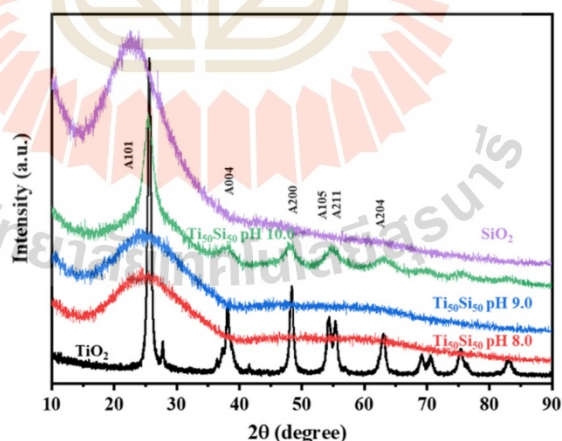


Figure 9. XRD patterns of $Ti_{50}Si_{50}$ oxide synthesized with pH 8.0, 9.0, and 10.0.

Furthermore, the XRD peaks for $Ti_{50}Si_{50}$ oxide powder with pH > 9 present a crystalline nature with 2θ angles at 25° (101) and 48° (200), which correspond to the crystalline

phase (anatase) of TiO_2 [3,34], due to the presence of a sufficient amount of OH^- to form TiO_2 . It is possible that the pH influences the particle size and crystallinity of $\text{Ti}_{50}\text{Si}_{50}$ oxides. The crystal structure of TiO_2 was tetragonal; $a = b = 3.782 \text{ \AA}$, $c = 9.502 \text{ \AA}$ [40]. However, no rutile phase was detected in any case, according to the absence of (110) diffraction peak at 27.4° .

Titanium K-edge X-ray-absorption near-edge structure (XANES) spectroscopy is widely used to derive information on the coordination environment of tetravalent Ti[Ti(IV)] in structurally complex oxide materials. Normalized Ti K-edge XANES spectra of anatase TiO_2 standards, synthesized TiO_2 materials, and $\text{Ti}_{50}\text{Si}_{50}$ oxides synthesized at various pH values were collected and are presented in Figure 10. The spectrum is mostly separated into two regions: (i) the pre-edge region (4940 to 4990 eV) and (ii) the post-edge region (4990 to 5010 eV) [41]. The anatase is composed of pre-edge features A_1 – A_3 and a characteristic shoulder B [42,43]. The origin of these features was described by Farges et al. The first pre-edge (A_1) is mainly attributed to quadrupolar transitions to t_{2g} levels of the TiO_6 octahedron. The second pre-edge (A_2) and the third pre-edge (A_3) are attributed to 1s to 3d dipolar transitions [43]. The B features may be attributed to the interactions of the central Ti 4p orbital hybridized with the near Ti or O atom (Wu et al., 1997). The intensive absorbance of the B feature may be due the local structures of the Ti orbital hybridized for the TiO_2 – SiO_2 photocatalyst [41]. Both TiO_2 anatase and synthesized TiO_2 display three minor pre-edge peaks, which are attributed to transitions from the 1s level of Ti to $1t_{1g}$, $2t_{2g}$, and $3e_g$ molecular orbitals (in sequence of increasing energy) [44]. The three minor pre-edge peaks for TiO_2 anatase are outstanding fingerprints for the crystalline phase of titanium dioxide materials. Thus, the formation of anatase is specified by the near-edge region of TiO_2 .

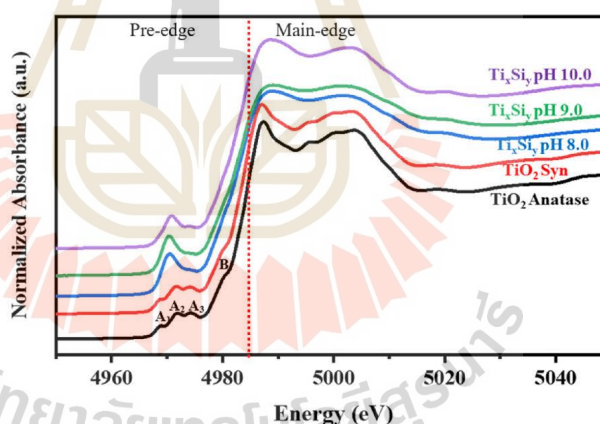


Figure 10. Ti K-edge XANES spectra of $\text{Ti}_{50}\text{Si}_{50}$ oxide synthesized with pH 8.0, 9.0, and 10.0.

As silicon merged into the $\text{Ti}_{50}\text{Si}_{50}$ oxide, a large single pre-edge feature was observed to dominate the other weaker feature. From Figure 10, the significant pre-edge feature in $\text{Ti}_{50}\text{Si}_{50}$ oxide samples indicates that a larger proportion of Ti atoms occupy tetrahedral symmetry positions, as expected for samples where Ti directly replaces Si in the oxide sample. Moreover, the pre-edge area of $\text{Ti}_{50}\text{Si}_{50}$ oxides was not affected by the various pH values applied during synthesis. Furthermore, the XANES spectra of the $\text{Ti}_{50}\text{Si}_{50}$ oxides have a higher intensity of pre-edge peaks than TiO_2 anatase, indicating that Ti is no longer entirely confined to octahedral sites when combined with Si. Therefore, the results of the XANES spectra of mixed oxide samples are in reasonable agreement with the XRD results.

The EXAFS analysis at the Ti K-edge was used to investigate the coordination number of Ti atoms and bond distances between Ti-O and Ti-Si atoms. The program package of ATHENA-ARTEMIS was used to perform the background noise correction and the normalization of the raw data [26]. The EXAFS data were FT to the R-space to define the local atom structure and relative bond length with respect to the absorbing atom. The ATOM and FEFF codes were used to simulate the FT data (in R-space) by creating a systematic theoretical structure of SiO₂ [45]. The range of data reserved for the transformation was 3–9 Å⁻¹ in k-space. Structural parameters were attained, without the phase corrections, by fitting the data in R-space, within the intermission of 1.1–3 Å (Figure 11). The shell parameters, such as Ti-O and Ti-Si bond distances (R), coordination number (CN), Debye-Waller factor (σ^2), and R-factor, are presented in Table 3. Note that the amplitude reduction factor (S_0^2) was preliminarily determined to be 0.52 by fitting the EXAFS spectrum of SiO₂.

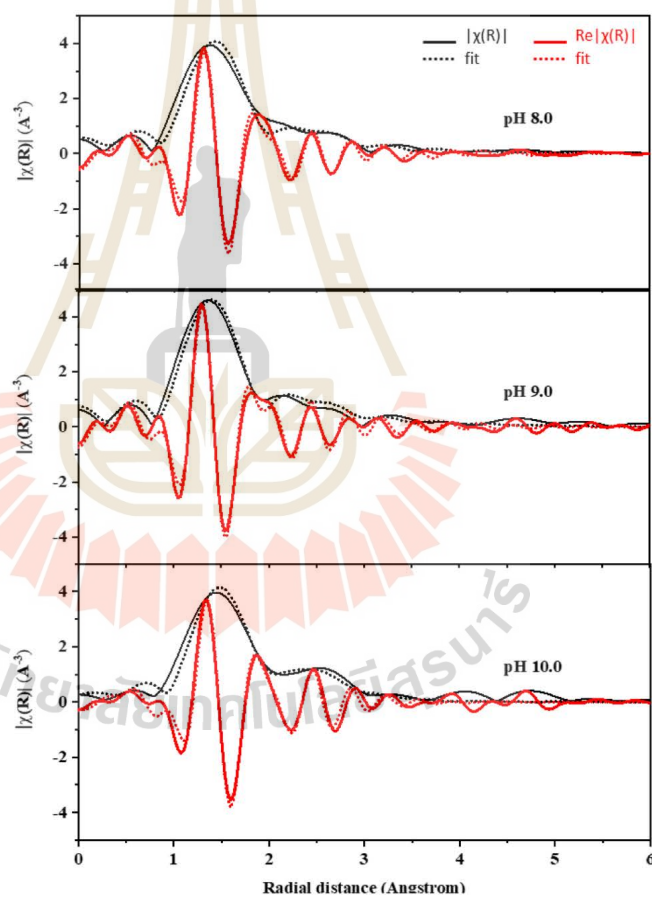


Figure 11. Ti K-edge XANES spectra of Ti₅₀Si₅₀ oxide synthesized at pH 8.0, 9.0, and 10.0.

Table 3. Structural parameters (obtained from fittings of Ti *K*-edge EXAFS data) of first two coordination shells around Ti atom of Ti and Si in $\text{Ti}_{50}\text{Si}_{50}$ oxide synthesized at various pH values and Ti_xSi_y oxide synthesized at pH 9.0 with different Ti/Si ratios.

Sample	Shell	Bond	ΔE (eV)	CN	R(Å)	σ^2	R-Factor
$\text{Ti}_{50}\text{Si}_{50}$ pH 8.0	1	Ti-O	4.11 ± 3.34	4.14 ± 0.18	1.99 ± 0.02	0.0053 ± 0.0013	0.0176
	2	Ti-Si		1.27 ± 0.44	2.79 ± 0.03	0.0018 ± 0.0019	
$\text{Ti}_{50}\text{Si}_{50}$ pH 9.0	1	Ti-O	2.72 ± 2.03	4.07 ± 0.12	1.83 ± 0.01	0.0042 ± 0.0008	0.0082
	2	Ti-Si		1.00 ± 0.13	2.77 ± 0.02	0.0020 ± 0.0020	
$\text{Ti}_{50}\text{Si}_{50}$ pH 10.0	1	Ti-O	6.70 ± 3.29	4.08 ± 0.19	1.94 ± 0.02	0.0049 ± 0.0024	0.0158
	2	Ti-Si		1.52 ± 0.22	2.81 ± 0.03	0.0013 ± 0.0031	
$\text{Ti}_{70}\text{Si}_{30}$	1	Ti-O	6.68 ± 3.23	4.15 ± 0.19	1.90 ± 0.02	0.0051 ± 0.0014	0.0198
	2	Ti-Si		0.97 ± 0.21	2.800 ± 0.04	0.0006 ± 0.0050	
$\text{Ti}_{50}\text{Si}_{50}$	1	Ti-O	2.72 ± 2.03	4.07 ± 0.12	1.83 ± 0.01	0.0042 ± 0.0008	0.0082
	2	Ti-Si		1.00 ± 0.13	2.77 ± 0.02	0.0020 ± 0.0020	
$\text{Ti}_{40}\text{Si}_{60}$	1	Ti-O	6.54 ± 2.27	4.09 ± 0.13	1.82 ± 0.01	0.0048 ± 0.0010	0.0103
	2	Ti-Si		1.19 ± 0.03	2.79 ± 0.03	0.0023 ± 0.0017	

The first and second shells in the FTs arise from the single scattering paths of cation–oxygen and cation–cation, respectively [46]. In this study, we first focus on the Ti–O and Ti–Si shells of all Ti_xSi_y oxide samples. TiO_2 anatase has an average Ti–O bond distance of 1.95 Å. The results from curve fitting of the EXAFS provide an interatomic distance of 1.99, 1.82, and 1.94 Å for Ti atom dilute silica of $\text{Ti}_{50}\text{Si}_{50}$ oxides synthesized at various pH levels of 8.0, 9.0, and 10.0, respectively. This result can be compared favorably with the bond distance of Ti–O in the titanium silicalite molecular sieve of 1.80 Å, corresponding to the cation existing in a tetrahedral environment [47,48]. Neurock and Manzer (1996) calculated the Ti–O bond distance using density functional methods, obtaining a value of 1.81 Å, suggesting Ti in a tetrahedral cluster [49]. On the other hand, we found that there is evidence of a longer Ti–O distance at 1.99 at pH 8.0, indicating a six-fold Ti site (octahedral), which agrees with Loshmanov et al. [47], who investigated TiO_2 in SiO_2 with neutron diffraction and attempted to isolate the Ti–O bond by subtracting their radial distribution functions from that of pure SiO_2 . They assigned a value of 1.95 Å. By analogy with the Ti–O distance in its octahedrally bonded oxides (1.91–2.01 Å), they inferred an octahedral coordination for Ti in SiO_2 . This may be due to the effect of pH on the reaction of the Ti_xSi_y oxides synthesized. Obviously, the value of 1.83 Å described for the Ti–O bond distance in Ti_xSi_y oxides synthesized at pH 9.0 is agreeable with the absolute value of the Ti atoms occupied in a tetrahedral environment, which supports the comparable assumption from XANES. Furthermore, all of the $\text{Ti}_{50}\text{Si}_{50}$ oxides presented a small value for the Debye–Waller factor, corresponding to the structural disturbance in the materials [45]. The Debye–Waller factor is used to describe the influence of static and thermal disorder on the EXAFS spectrum. A large value for the σ^2 can be caused by a variance in the ligand distances (static disorder), whereas small Debye–Waller factors artificially increase the ligand contribution [50,51].

The chemical compositions of TiO_2 , SiO_2 , and $\text{Ti}_{50}\text{Si}_{50}$ oxide synthesized at various pH values by XRF are shown in Table 4. The XRF analysis showed that $\text{Ti}_{50}\text{Si}_{50}$ oxide synthesized at pH 8.0 showed a higher percentage of Si (54.39%) than those synthesized at pH 9.0 (47.87%) and pH 10.0 (9.82%) because TTIP can be hydrolyzed more quickly than TEOS in a solution at a high pH. In contrast, the atomic content of Ti in $\text{Ti}_{50}\text{Si}_{50}$ oxide synthesized at various pH values increased with the increasing pH value of the sol (43.72%).

Table 4. Percentage of atomic and atomic ratio of Ti and Si in TiO₂, SiO₂, and Ti₅₀Si₅₀ oxide synthesized at various pH values and Ti_xSi_y oxide synthesized at pH 9.0 with different Ti/Si ratios.

Sample	Atomic (%)		Atomic Ratio of Ti/Si
	Si	Ti	
SiO ₂	100	0	-
Ti ₅₀ Si ₅₀ pH 8.0	54.39	45.61	0.84
Ti ₅₀ Si ₅₀ pH 9.0	47.87	52.13	1.09
Ti ₅₀ Si ₅₀ pH 10.0	9.82	93.18	9.49
Ti ₇₀ Si ₃₀	29.79	70.21	2.36
Ti ₅₀ Si ₅₀	47.87	52.13	1.09
Ti ₄₀ Si ₆₀	60.19	39.81	0.66
TiO ₂	0	100	-

The particle sizes of TiO₂, SiO₂, and Ti₅₀Si₅₀ oxides synthesized at various pH values as determined by the Zetasizer Nano ZS and SEM micrographs are shown in Table 5 and Figure 12. The mean particle size distributions of TiO₂ and SiO₂ were 40.3 and 147.8 nm, while Ti₅₀Si₅₀ oxide synthesized at pH 9.0 presented a mean particle size distribution of 136.2 nm. However, the mean particle size distribution of Ti₅₀Si₅₀ oxide synthesized at pH 8.0 and 10.0 covered a range of 350–650 nm due to the tendency towards agglomeration.

Table 5. Particle sizes of SiO₂, TiO₂, and Ti₅₀Si₅₀ oxide synthesized at various pH values, and Ti_xSi_y oxide synthesized at pH 9.0 with different Ti/Si ratios.

Sample	Zetasizer Nano ZS		SEM
	Particle Size, d (nm)	Polydispersity Index, PDI	Value of Average Diameter, d _n (nm)
SiO ₂	147.8	0.248	144.2 ± 11.3
Ti ₅₀ Si ₅₀ pH 8.0	639.3	0.627	41.5 ± 16.7
Ti ₅₀ Si ₅₀ pH 9.0	136.2	0.239	135.4 ± 12.3
Ti ₅₀ Si ₅₀ pH 10.0	397.0	0.322	114.2 ± 24.2
Ti ₇₀ Si ₃₀	573.1	0.630	149.3 ± 15.5
Ti ₅₀ Si ₅₀	136.2	0.239	135.4 ± 12.3
Ti ₄₀ Si ₆₀	825.5	0.907	131.8 ± 13.3
TiO ₂	40.3	0.490	27.8 ± 6.3

To determine the correct diameter of TiO₂, SiO₂, and Ti_xSi_y oxide, SEM micrographs (Figure 8) were used for measurement with ImageJ. The number average diameter, d_n, was calculated from a minimum of 200 particles according to the following equations [52]:

$$d_n = \frac{\sum_i n_i d_i}{\sum_i n_i} \quad (1)$$

$$SD = \sqrt{\frac{\sum_i n_i (d_i - d_n)^2}{N}} \quad (2)$$

where d_i is the diameter of a particle and n_i is the total number of particles having diameter, d_i.

It can be observed that the number average diameter of the sample increased with the increasing pH value of the synthesis.

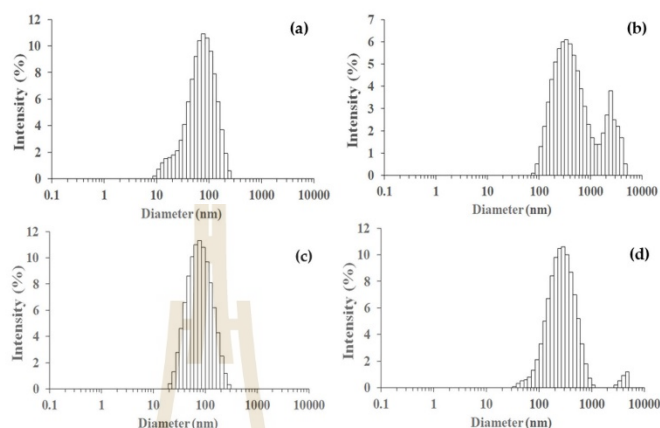


Figure 12. Particle size distributions measured on a Zetasizer Nano ZS of SiO_2 and $\text{Ti}_{50}\text{Si}_{50}$ oxide synthesized at various pH values: (a) SiO_2 , (b) $\text{Ti}_{50}\text{Si}_{50}$ pH 8.0, (c) $\text{Ti}_{50}\text{Si}_{50}$ pH 9.0, (d) $\text{Ti}_{50}\text{Si}_{50}$ pH 10.0.

The textural properties of the SiO_2 , TiO_2 , and $\text{Ti}_{50}\text{Si}_{50}$ oxides synthesized at various pH values are shown in Table 6. It can be observed that the surface areas (S_{BET}) of the oxides were 177.02, 225.68, and $62.75 \text{ m}^2\text{g}^{-1}$ for $\text{Ti}_{50}\text{Si}_{50}$ synthesized at pH 8.0, 9.0, and 10.0, respectively. In addition, the mean pore diameter of the $\text{Ti}_{50}\text{Si}_{50}$ oxides was 2.56, 5.85, and 27.31 nm. Meanwhile, the S_{BET} of SiO_2 and TiO_2 was 116.90 and $74.07 \text{ m}^2\text{g}^{-1}$, with an average pore size of 37.08 and 12.75 nm.

Table 6. Specific surface area, pore volume, and mean pore size of TiO_2 , SiO_2 , and $\text{Ti}_{50}\text{Si}_{50}$ oxide synthesized at various pH values, and Ti_xSi_y oxide synthesized at pH 9.0 with different Ti/Si ratios.

Sample	Specific Surface Area, S_{BET} (m^2g^{-1})	Pore Volume, V_p (cm^3g^{-1})	Mean Pore Diameter, d_p (nm)
SiO_2	116.90	1.06	51.08
Ti_xSi_y pH 8.0	177.02	0.11	2.56
Ti_xSi_y pH 9.0	225.68	0.33	5.85
Ti_xSi_y pH 10.0	62.75	0.42	27.31
$\text{Ti}_{70}\text{Si}_{30}$	569.07	1.42	10.96
$\text{Ti}_{50}\text{Si}_{50}$	225.68	0.33	5.85
$\text{Ti}_{40}\text{Si}_{60}$	68.34	0.36	21.97
TiO_2	74.07	0.23	12.75

A typical nitrogen adsorption–desorption isotherm of the SiO_2 , TiO_2 , and $\text{Ti}_{50}\text{Si}_{50}$ oxides synthesized at various pH values is presented in Figure 13. The isotherm of SiO_2 is a type II curve according to the IUPAC isotherm classification, indicating that the obtained SiO_2 particles contain macropores. An inflection point occurs near the completion of the first adsorbed monolayer, which is typical for non-porous or macroporous materials with a pore size of >50 nm. In addition, all $\text{Ti}_{50}\text{Si}_{50}$ oxides exhibited type II isotherms with pore diameters of 2.56, 5.85, and 27.31 nm. However, the isotherm of TiO_2 is a type IV curve according to the IUPAC isotherm classification. An abrupt hysteric loop is detected from this curve, which is typical for mesoporous materials with pores in the range of 2 to 50 nm that show capillary condensation and evaporation [53,54].

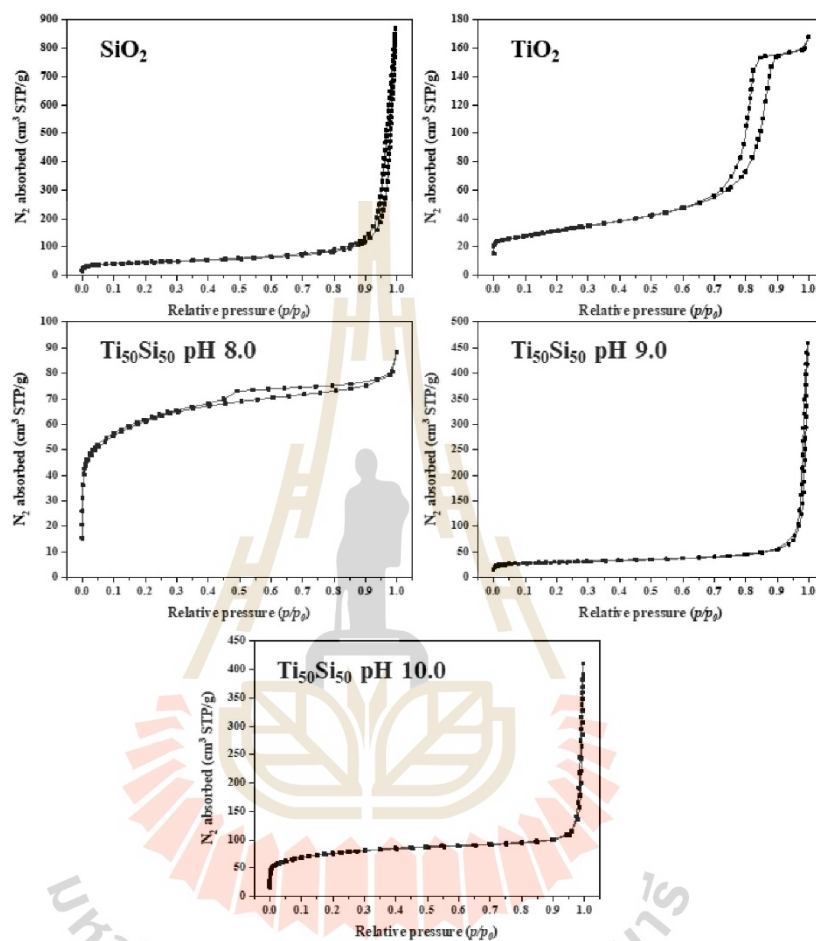


Figure 13. Nitrogen adsorption–desorption isotherms of SiO₂, TiO₂, and Ti₅₀Si₅₀ oxide synthesized at various pH values.

3.2. Effect of Ti/Si Ratio

FTIR spectra of TiO₂, SiO₂, and Ti_xSi_y oxide synthesized at pH 9.0 with different Ti/Si ratios are shown in Figure 14. All Ti_xSi_y oxides have three major peaks in their FTIR spectra, with wavenumbers of 801, 949, and 1052 cm^{-1} . The peaks at 801 and 1052 cm^{-1} corresponded to symmetric and asymmetric stretching vibrations of Si–O–Si of silica, while the peak at 949 cm^{-1} was commonly attributed to Ti–O–Si vibrations, indicating the existence of Ti–O–Si linkages [34]. This suggested that titanium had been incorporated into the silica framework. Therefore, there was no effect of the Ti/Si atomic ratio on the FTIR of Ti_xSi_y oxide.

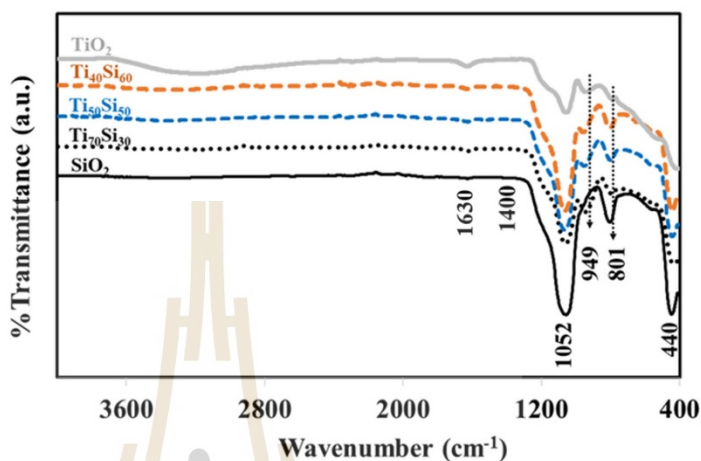


Figure 14. FTIR spectra of TiO_2 , SiO_2 , and Ti_xSi_y oxide synthesized at pH 9.0 with different Ti/Si ratios.

The FE-SEM image of TiO_2 exhibits a large majority of particles with high agglomeration, as shown in Figure 15a. $\text{Ti}_{70}\text{Si}_{30}$ and $\text{Ti}_{50}\text{Si}_{50}$ oxides show particles that are homogeneous with a good nanostructure and mostly spherical in shape when Ti/Si is more than 1 (Figure 15b,c). However, the size of $\text{Ti}_{40}\text{Si}_{60}$ oxide particles becomes gradually aggregated with increasing moles of Si (Figure 15d).

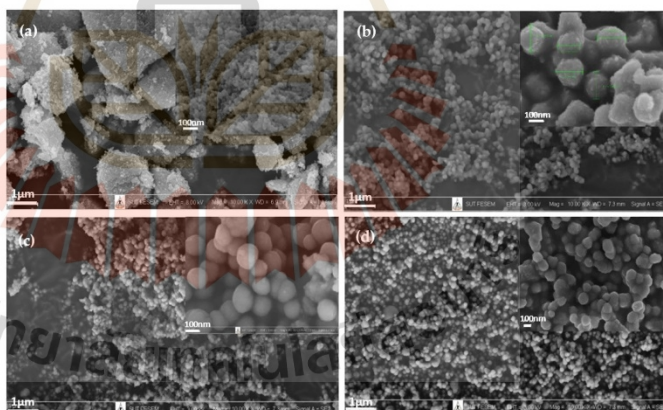


Figure 15. Low ($\times 10\text{k}$ WD = 7.3 mm EHT = 3.00 kV) and high ($\times 100\text{k}$ WD = 6.9–7.3 mm EHT = 3.00 kV) magnification SEM images of TiO_2 and Ti_xSi_y oxide synthesized at pH 9.0 with different Ti/Si ratios: (a) TiO_2 , (b) $\text{Ti}_{70}\text{Si}_{30}$, (c) $\text{Ti}_{50}\text{Si}_{50}$, (d) $\text{Ti}_{40}\text{Si}_{60}$.

From the XRD patterns, only broad-range signals due to the uniform dispersion of titanium atoms onto the SiO_2 network can be seen in the XRD patterns of $\text{Ti}_{70}\text{Si}_{30}$, $\text{Ti}_{50}\text{Si}_{50}$, and $\text{Ti}_{40}\text{Si}_{60}$ oxides (Figure 16). As a result, the absence of XRD diffraction signals suggests that anatase crystallization is still hindered by the titania aggregate's segregation from the silica network [55].

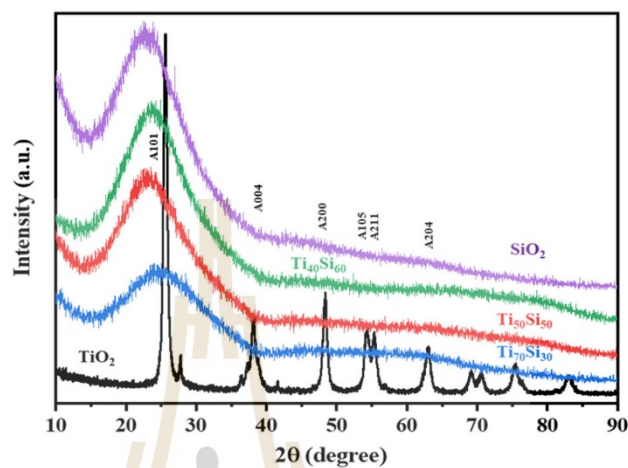


Figure 16. XRD patterns of SiO_2 , TiO_2 , and Ti_xSi_y oxide synthesized at pH 9.0 with different Ti/Si ratios.

Ti K-edge XANES spectra of standard TiO_2 anatase, synthesized TiO_2 materials, and Ti_xSi_y oxides synthesized with different Ti/Si ratios were collected and are presented in Figure 17. Ti is expected to readily replace Si in the tetrahedral SiO_2 framework at low Ti concentrations in $\text{Ti}_{40}\text{Si}_{60}$. The features and position in the rising edge of the B shoulders are clearer and the positions are lower. This suggests that the Ti–O–Ti linkages in Ti_xSi_y oxides increase and are incomplete in anatase [21].

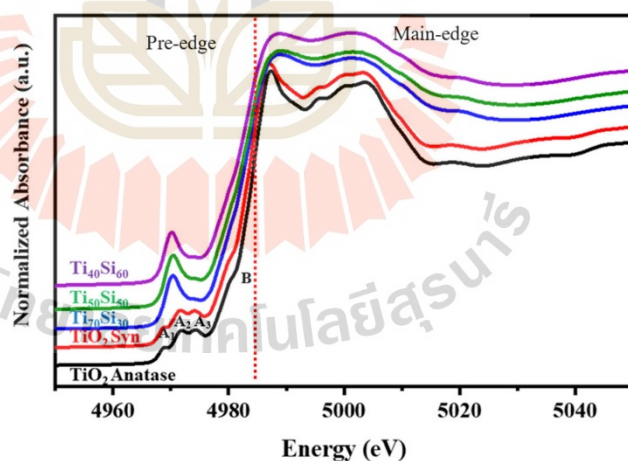


Figure 17. Ti K-edge XANES spectra of TiO_2 and Ti_xSi_y oxide synthesized at pH 9.0 with different Ti/Si ratios.

The structural parameters of Ti_xSi_y oxide synthesized at pH 9.0 with varying Ti/Si ratios were attained without phase corrections by fitting the data in R-space within the intermission of 1.1–3 Å (Figure 18). The shell parameters, such as Ti–O and Ti–Si bond

distances (R), coordination number (CN), Debye–Waller factor (σ^2), and R -factor, are presented in Table 3. The amplitude reduction factor (S_0^2) was estimated to be 0.52 based on the EXAFS spectra of SiO_2 . According to the EXAFS curve fitting findings, the interatomic distances for Ti atom dilute silica of $\text{Ti}_{70}\text{Si}_{30}$, $\text{Ti}_{50}\text{Si}_{50}$, and $\text{Ti}_{40}\text{Si}_{60}$ oxide are 1.90, 1.83, and 1.82, respectively. The average Ti–O bond distance dropped from 1.90 to 1.82 when Ti in Ti_xSi_y oxide increased. Furthermore, the 1.83 and 1.82 Ti–O bond lengths found for $\text{Ti}_{50}\text{Si}_{50}$ and $\text{Ti}_{40}\text{Si}_{60}$ oxide correspond with the absolute value of the Ti atoms occupied in a tetrahedral environment, validating the comparable assumption from XANES.

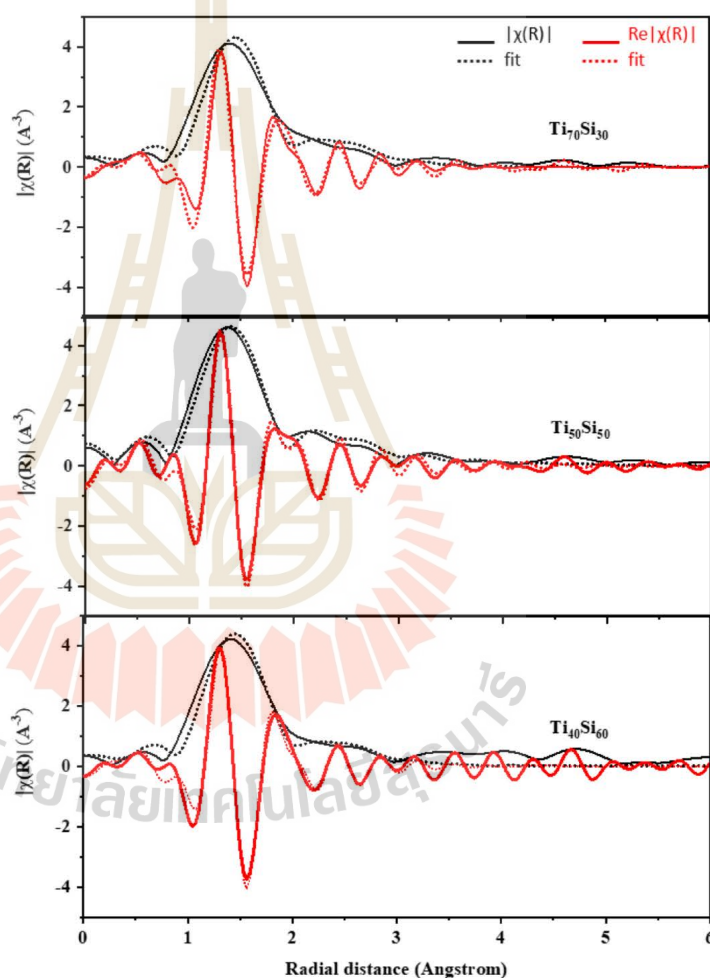


Figure 18. The experimental EXAFS data of Ti_xSi_y oxide synthesized at pH 9.0 with different Ti/Si ratios in R-space within the intermission of 1.1–3 Å.

The proportion of Si atoms in $\text{Ti}_{70}\text{Si}_{30}$, $\text{Ti}_{50}\text{Si}_{50}$, and $\text{Ti}_{40}\text{Si}_{60}$ oxide was verified by XRF analysis to be 29.79, 47.87, and 60.19%, respectively. Ti content was 70.21, 52.13, and 39.81% in $\text{Ti}_{70}\text{Si}_{30}$, $\text{Ti}_{50}\text{Si}_{50}$, and $\text{Ti}_{40}\text{Si}_{60}$ oxide, respectively (Table 4).

Table 5 and Figure 19 display the particle sizes of TiO_2 , SiO_2 , and Ti_xSi_y oxides synthesized at various Ti/Si ratios, as measured by the Zetasizer Nano ZS and SEM micrographs. The mean particle size distribution of $\text{Ti}_{70}\text{Si}_{30}$, $\text{Ti}_{50}\text{Si}_{50}$, and $\text{Ti}_{40}\text{Si}_{60}$ oxide was 573.1, 136.1, and 825.5 nm, respectively. In addition, SEM micrographs (Figure 15) were used to measure the correct diameter of TiO_2 , SiO_2 , and Ti_xSi_y oxide by ImageJ. The number average diameter, d_n , was estimated using Equations (1) and (2) from the minimum value given in [52]. $\text{Ti}_{70}\text{Si}_{30}$, $\text{Ti}_{50}\text{Si}_{50}$, and $\text{Ti}_{40}\text{Si}_{60}$ oxide had an average diameter of 149.3, 135.4, and 131.8 nm, respectively, as reported in Table 6. As the amount of Ti incorporated into the silica network increased, the number average diameter decreased.

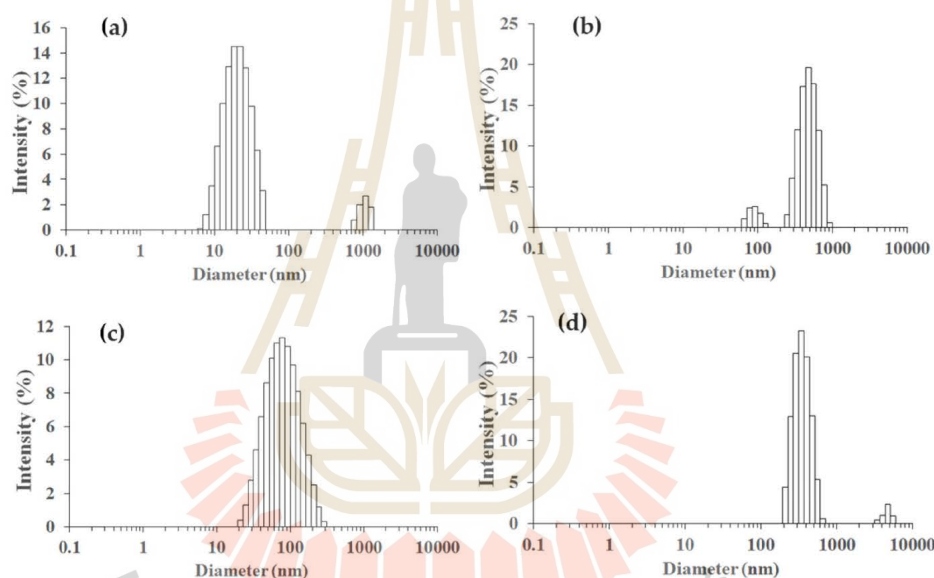


Figure 19. Particle size distributions measured on a Zetasizer Nano ZS of TiO_2 and Ti_xSi_y oxide synthesized at pH 9.0 with different Ti/Si ratios: (a) TiO_2 , (b) $\text{Ti}_{70}\text{Si}_{30}$, (c) $\text{Ti}_{50}\text{Si}_{50}$, (d) $\text{Ti}_{40}\text{Si}_{60}$.

The $\text{Ti}_{70}\text{Si}_{30}$, $\text{Ti}_{50}\text{Si}_{50}$, and $\text{Ti}_{40}\text{Si}_{60}$ oxides had surface areas (S_{BET}) of 569.07, 225.68, and 68.34 m^2g^{-1} , respectively. The S_{BET} displayed an upward trend as the Ti content increased. According to a prior study, the S_{BET} of the Ti_xSi_y oxide was enhanced as the Ti concentration in the silica network increased [56].

A typical nitrogen adsorption–desorption isotherm of the SiO_2 , TiO_2 , and $\text{Ti}_{70}\text{Si}_{30}$, $\text{Ti}_{50}\text{Si}_{50}$, and $\text{Ti}_{40}\text{Si}_{60}$ oxides is presented in Figure 20. Type II isotherms with pore diameters of 10.96, 5.85, and 21.97 nm were found in $\text{Ti}_{70}\text{Si}_{30}$, $\text{Ti}_{50}\text{Si}_{50}$, and $\text{Ti}_{40}\text{Si}_{60}$ oxides, corresponding to mesoporous materials with pore sizes ranging from 2 to 50 nm. However, the TiO_2 isotherm is classified as a type IV curve according to the IUPAC. This curve shows an abrupt hysteric loop, which is common in mesoporous materials with pores between 2 and 50 nm that exhibit capillary condensation and evaporation [53,54].

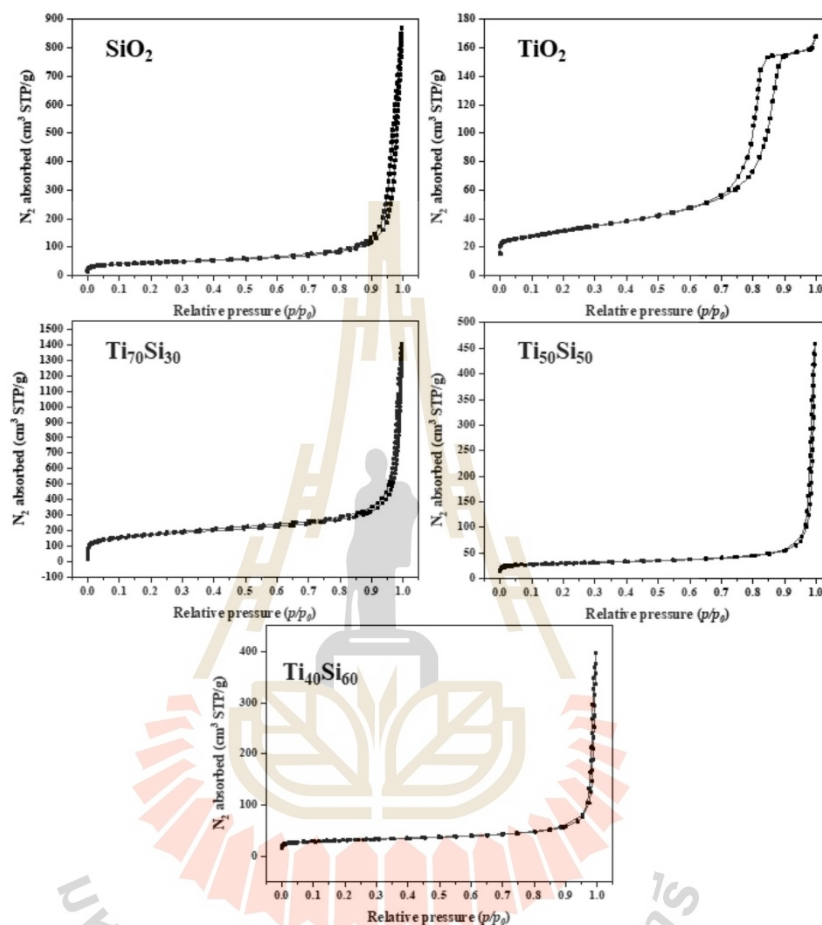


Figure 20. Nitrogen adsorption–desorption isotherms of SiO_2 , TiO_2 , and Ti_xSi_y oxide synthesized at pH 9.0 with different Ti/Si ratios.

3.3. Photocatalytic Degradation of Methylene Blue (MB)

The degradation of methylene blue (MB) was used to study the photocatalytic activity of PLA and PLA/ Ti_xSi_y oxide composite films. In addition, UV irradiation may also lead to the decomposition of MB without the presence of any photocatalyst. The degradation of MB on PLA and PLA/ Ti_xSi_y oxide composite films was caused by a change in MB concentration in aqueous solution under UV irradiation, as illustrated in Figures 21 and 22. The addition of 3%wt TiO_2 , SiO_2 , and Ti_xSi_y oxide to the PLA film matrix increased the effectiveness of photocatalysis in the degradation of MB. TiO_2 is more effective at degrading MB than $\text{Ti}_{50}\text{Si}_{50}$ pH 9.0, $\text{Ti}_{50}\text{Si}_{50}$ pH 10.0, $\text{Ti}_{50}\text{Si}_{50}$ pH 8.0, and SiO_2 . In the degradation of MB, the efficiency of the materials was of the following order: $\text{TiO}_2 > \text{Ti}_{70}\text{Si}_{30} > \text{Ti}_{50}\text{Si}_{50} > \text{Ti}_{40}\text{Si}_{60} > \text{SiO}_2$.

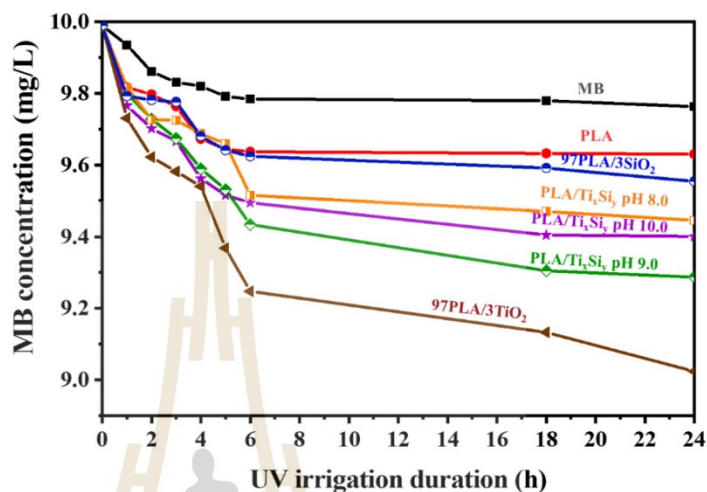


Figure 21. Concentration of methylene blue (MB) due to absorption of PLA film and PLA/Ti₅₀Si₅₀ oxide (synthesized at pH 8.0, 9.0, and 10.0) films under UV irradiation.

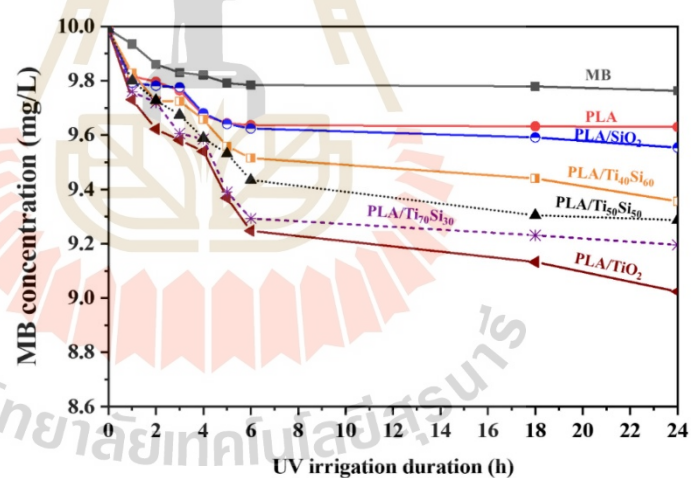
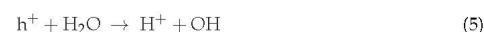
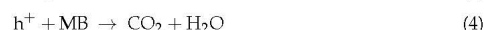


Figure 22. Concentration of methylene blue (MB) due to absorption of PLA film and PLA/Ti_xSi_y oxide (synthesized at pH 9.0 with different Ti/Si ratios) films under UV irradiation.

Photocatalytic activity is generally accepted to occur at the surface of a photocatalyst. As a result, the surface area of PLA nanocomposite film, which is dependent on the size of nanoparticles, film morphology, and thickness, influences photocatalytic reactivity [7]. The PLA nanocomposite film including TiO₂ degrades MB more efficiently than employing only photocatalysis because of the two mechanisms of degradation. The first is that in which UVC directly degrades MB, while the second occurs when TiO₂ receives light energy greater than the bandgap energy, and electrons in the valence band (VB) are excited into

the conduction band (CB), resulting in the generation of a hole (h^+) (Equation (3)). This hole can oxidize MB (Equation (4)) or oxidize H_2O to produce OH (Equation (5)). The e^- in CB can reduce O_2 at the surface of TiO_2 to generate O_2^- (Equation (6)). Radicals (OH, O_2^-) and h^+ interact with MB to create peroxide derivatives and hydroxylate or completely degrade to CO_2 and H_2O [7]. The photodegradation pathway can be summarized by Equations (3)–(6).



4. Conclusions

Titania–silica oxides (Ti_xSi_y oxides) can be prepared by the sol–gel technique. The effect of pH and the Ti/Si atomic ratio of titanium–silicon binary oxide (Ti_xSi_y) on the structural characteristics of Ti_xSi_y oxide were investigated by using the sol–gel technique. ^{29}Si solid-state NMR and FTIR measurements indicated that certain Si atoms in the SiO_2 network had been replaced by Ti atoms, implying the formation of Si–O–Ti connections. As the pH was elevated to alkaline conditions (pH 9.0 and 10.0), the nanoparticles of $Ti_{50}Si_{50}$ oxide acquired a more spherical shape and their size distribution became more uniform, resulting in an acceptable nanostructure. Agglomeration was reduced in $Ti_{50}Si_{50}$ oxide nanoparticles, which were mostly spherical in form. However, the $Ti_{50}Si_{50}$ oxide particles at pH 10.0 become nano-sized and agglomerated. In $Ti_{50}Si_{50}$ oxide samples, the existence of a large pre-edge feature indicated that a higher percentage of Ti atoms occupied tetrahedral symmetry positions, as expected in samples where Ti directly substitutes Si. The result of 1.83 Å for the Ti–O bond distance in Ti_xSi_y oxides generated at pH 9.0 accords with the fraction of Ti atoms occupied in a tetrahedral environment. The average diameter of the sample increased with the increasing pH of the sol. In addition, $Ti_{70}Si_{30}$, $Ti_{50}Si_{50}$, and $Ti_{40}Si_{60}$ oxide had an average diameter of 149.3, 135.4, and 131.8 nm, respectively. As the amount of Ti incorporated into the silica network increased, the average diameter decreased. The S_{BET} displayed an upward trend as the Ti content increased. Type II isotherms with pore diameters of 10.96, 5.85, and 21.97 nm were found in $Ti_{70}Si_{30}$, $Ti_{50}Si_{50}$, and $Ti_{40}Si_{60}$ oxides, corresponding to mesoporous materials with pore sizes ranging from 2 to 50 nm, which is common in mesoporous materials. However, the TiO_2 isotherm was classified as a type IV curve. The addition of 3%wt TiO_2 , SiO_2 , and Ti_xSi_y oxide to the PLA film matrix increased the effectiveness of photocatalysis in the degradation of MB. TiO_2 was more effective at degrading MB than $Ti_{50}Si_{50}$ pH 9.0, $Ti_{50}Si_{50}$ pH 10.0, $Ti_{50}Si_{50}$ pH 8.0, and SiO_2 . In the degradation of MB, the order of efficiency is $TiO_2 > Ti_{70}Si_{30} > Ti_{50}Si_{50} > Ti_{40}Si_{60} > SiO_2$. Moreover, PLA/ $Ti_{70}Si_{30}$ also increased the effectiveness of the photocatalytic activity of PLA. Finally, PLA/ $Ti_{70}Si_{30}$ improved the efficiency of the photocatalytic activity of PLA.

Author Contributions: Conceptualization, Y.R.; methodology, A.T., C.R., P.A. and Y.R.; validation, A.T., C.R., P.A. and Y.R.; formal analysis, A.T. and P.A.; investigation, A.T., C.R., P.A. and Y.R.; resources, A.T., C.R. and Y.R.; data curation, A.T.; writing—original draft preparation, A.T.; writing—review and editing, A.T., C.R., P.A. and Y.R.; visualization, C.R. and Y.R.; supervision, C.R. and Y.R.; project administration, C.R. and Y.R.; funding acquisition, C.R. and Y.R. All authors have read and agreed to the published version of the manuscript.

Funding: This research was funded by Thailand Science Research and Innovation (TSRI), grant number 42853.

Institutional Review Board Statement: Not applicable.

Informed Consent Statement: Not applicable.

Data Availability Statement: Not applicable.

Acknowledgments: The authors are grateful to Suranaree University of Technology (SUT); to the Center of Excellence on Petrochemical and Materials Technology (PETROMAT); to the Science, Research and Innovation Promotion Fund from Thailand Science Research and Innovation (TSRI); and to the Research Center for Biocomposite Materials for Medical Industry and Agricultural and Food Industry for the financial support. In addition, we would like to express our gratitude to the Synchrotron Light Research Institute (Public Organization) for the XAS experiment.

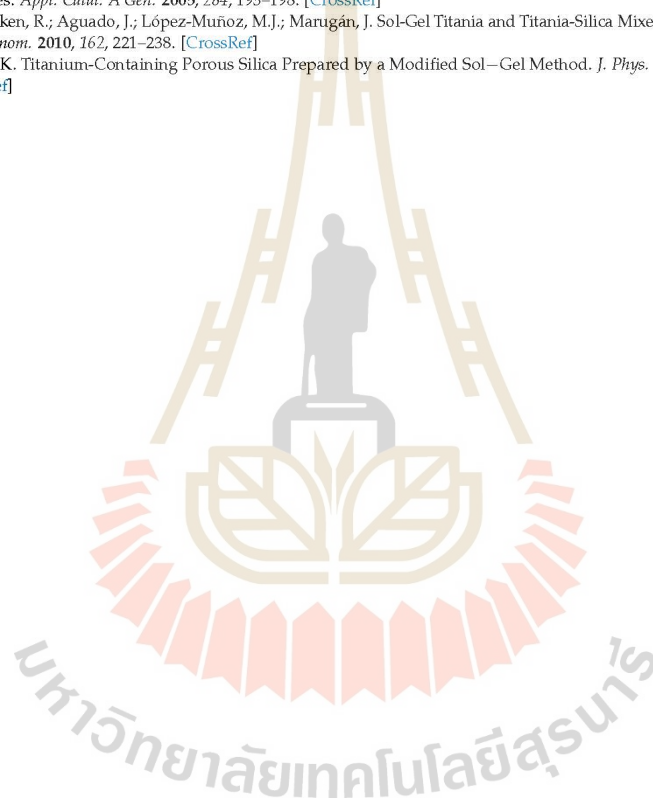
Conflicts of Interest: The authors declare no conflict of interest.

References

- Rasalingam, S.; Peng, R.; Koodali, R.T. Review Article: Removal of Hazardous Pollutants from Wastewaters: Applications of TiO₂-SiO₂ Mixed Oxide Materials. *J. Nanomater.* **2014**, *2014*, 1–42. [\[CrossRef\]](#)
- Wang, X.; Xue, J.; Wang, X.; Liu, X. Heterogeneous Ag-TiO₂-SiO₂ composite materials as novel catalytic systems for selective epoxidation of cyclohexene by H₂O₂. *PLoS ONE* **2017**, *12*, e0176332. [\[CrossRef\]](#)
- Sahu, D.R.; Hong, L.Y.; Wang, S.-C.; Huang, J.-L. Synthesis, analysis and characterization of ordered mesoporous TiO₂/SBA-15 matrix: Effect of calcination temperature. *Microporous Mesoporous Mater.* **2009**, *117*, 640–649. [\[CrossRef\]](#)
- Petronella, F.; Pagliarulo, A.; Truppi, A.; Lettieri, M.; Masieri, M.; Calia, A.; Curri, M.L.; Comparelli, R. TiO₂ Nanocrystal Based Coatings for the Protection of Architectural Stone: The Effect of Solvents in the Spray-Coating Application for a Self-Cleaning Surfaces. *Coatings* **2018**, *8*, 356. [\[CrossRef\]](#)
- Zhu, Y.; Buonocore, G.G.; Lavorgna, M. Photocatalytic activity of PLA/TiO₂ nanocomposites and TiO₂-active multilayered hybrid coatings. *Ital. J. Food Sci.* **2012**, *24*, 102–106.
- Tiainen, H.D.; Wiedmer, H.; Haugen, J. Processing of highly porous TiO₂ bone scaffolds with improved compressive strength. *J. Eur. Ceram. Soc.* **2013**, *33*, 15–24. [\[CrossRef\]](#)
- Chen, L.; Zheng, K.; Liu, Y. Geopolymer-supported photocatalytic TiO₂ film: Preparation and characterization. *Constr. Build. Mater.* **2017**, *151*, 63–70. [\[CrossRef\]](#)
- Allodi, V.; Brutti, S.; Giarola, M.; Sgambetterra, M.; Navarra, M.A.; Panero, S.; Mariotto, G. Structural and Spectroscopic Characterization of a Nanosized Sulfated TiO₂ Filler and of Nanocomposite Nafion Membranes. *Polymers* **2016**, *8*, 68. [\[CrossRef\]](#)
- Bertuna, A.; Comini, E.; Poli, N.; Zappa, D.; Sberveglieri, G. Titanium Dioxide Nanostructures Chemical Sensor. *Procedia Eng.* **2016**, *168*, 313–316. [\[CrossRef\]](#)
- Zapata, P.A.; Palza, H.; Cruz, L.S.; Lieberwirth, I.; Catalina, F.; Corrales, T.; Rabagliati, F.M. Polyethylene and poly(ethylene-co-1-octadecene) composites with TiO₂ based nanoparticles by metalocenic “in situ” polymerization. *Polymer* **2013**, *54*, 2690–2698. [\[CrossRef\]](#)
- Fonseca, C.; Ochoa, A.; Ulloa, M.T.; Alvarez, E.; Canales, D.; Zapata, P.A. Poly(lactic acid)/TiO₂ nanocomposites as alternative biocidal and antifungal materials. *Mater. Sci. Eng. C* **2015**, *57*, 314–320. [\[CrossRef\]](#)
- Wu, F.; Lan, X.; Ji, D.; Liu, Z.; Yang, W.; Yang, M. Grafting polymerization of polylactic acid on the surface of nano-SiO₂ and properties of PLA/PLA-grafted-SiO₂ nanocomposites. *J. Appl. Polym. Sci.* **2013**, *129*, 3019–3027. [\[CrossRef\]](#)
- Serenko, O.A.; Muzafarov, A.M. Polymer composites with surface modified SiO₂ nanoparticles: Structures, properties, and promising applications. *Polym. Sci. Ser. C* **2016**, *58*, 93–101. [\[CrossRef\]](#)
- Ha, S.-W.; Weitzmann, M.N.; Beck, G.R., Jr. Chapter 4—Dental and Skeletal Applications of Silica-Based Nanomaterials A2—Subramani, Karthikeyan. In *Nanobiomaterials in Clinical Dentistry*; Ahmed, W., Hartsfield, J.K., Eds.; William Andrew Publishing: Norwich, NY, USA, 2013; pp. 69–91.
- Gao, X.; Wachs, I.E. Titania-silica as catalysts: Molecular structural characteristics and physico-chemical properties. *Catal. Today* **1999**, *51*, 233–254. [\[CrossRef\]](#)
- Pabón, E.; Retuert, J.; Quijada, R.; Zarate, A. TiO₂-SiO₂ mixed oxides prepared by a combined sol-gel and polymer inclusion method. *Microporous Mesoporous Mater.* **2004**, *67*, 195–203. [\[CrossRef\]](#)
- Pabón, E.; Retuert, J.; Quijada, R. Synthesis of mixed silica-titania by the sol-gel method using polyethylenimine: Porosity and catalytic properties. *J. Porous Mater.* **2007**, *14*, 151–158.
- Milne, C.J.; Penfold, T.J.; Chergui, M. Recent experimental and theoretical developments in time-resolved X-ray spectroscopies. *Coord. Chem. Rev.* **2014**, *277–278*, 44–68.
- Niltharach, A.; Kityakam, S.; Worayingyong, A.; Thienprasert, J.T.; Klysubun, W.; Songsiririthigul, P.; Limpijumng, S. Structural characterizations of sol-gel synthesized TiO₂ and Ce/TiO₂ nanostructures. *Phys. B Condens. Matter* **2012**, *407*, 2915–2918. [\[CrossRef\]](#)
- Kim, W.B.; Choi, S.H.; Lee, J.S. Quantitative Analysis of Ti–O–Si and Ti–O–Ti Bonds in Ti–Si Binary Oxides by the Linear Combination of XANES. *J. Phys. Chem. B* **2000**, *104*, 8670–8678. [\[CrossRef\]](#)
- Matsuo, S.; Sakaguchi, N.; Wakita, H. Pre-edge features of Ti K-edge X-ray absorption near-edge structure for the local structure of sol-gel titanium oxides. *Anal. Sci.* **2005**, *21*, 805–809. [\[CrossRef\]](#)
- Alias, S.S.; Mohamad, A.A. ZnO: Effect of pH on the Sol-Gel Process. In *Synthesis of Zinc Oxide by Sol-Gel Method for Photoelectrochemical Cells*; SpringerBriefs in Materials; Springer: Singapore, 2014; pp. 9–25.

23. Kim, T.G.; An, G.S.; Han, J.S.; Hur, J.U.; Park, B.G.; Choi, S.-C. Synthesis of Size Controlled Spherical Silica Nanoparticles via Sol-Gel Process within Hydrophilic Solvent. *J. Korean Ceram. Soc.* **2017**, *54*, 49–54. [[CrossRef](#)]
24. Karkare, M.M. Choice of precursor not affecting the size of anatase TiO₂ nanoparticles but affecting morphology under broader view. *Int. Nano Lett.* **2014**, *4*, 111. [[CrossRef](#)]
25. Klysubun, W.; Tarawarakarn, P.; Thamsanong, N.; Amonpattaratkit, P.; Cholsuk, C.; Lapboonrueng, S.; Chaichuay, S.; Wongtepa, W. Upgrade of SLRI BLS beamline for XAFS spectroscopy in a photon energy range of 1–13 keV. *Radiat. Phys. Chem.* **2020**, *175*, 108145. [[CrossRef](#)]
26. Ravel, B.; Newville, M. THENA, ARTEMIS, HEPHAESTUS: Data analysis for X-ray absorption spectroscopy using IFEFFIT. *J. Synchrotron Radiat.* **2005**, *12*, 537–541. [[CrossRef](#)]
27. Schraml-Marth, M.; Walther, K.L.; Wokaun, A.; Handy, B.E.; Baiker, A. Porous silica gels and TiO₂/SiO₂ mixed oxides prepared via the sol-gel process: Characterization by spectroscopic techniques. *J. Non-Cryst. Solids* **1992**, *143*, 93–111. [[CrossRef](#)]
28. Degirmenci, V.; Erdem, Ö.F.; Ergun, O.; Yilmaz, A.; Michel, D.; Uner, D. Synthesis and NMR Characterization of Titanium and Zirconium Oxides Incorporated in SBA-15. *Top. Catal.* **2008**, *49*, 204–208. [[CrossRef](#)]
29. Dirken, P.J.; Smith, M.E.; Whitfield, H.J. ¹⁷O and ²⁹Si Solid State NMR Study of Atomic Scale Structure in Sol-Gel-Prepared TiO₂-SiO₂ Materials. *J. Phys. Chem.* **1995**, *99*, 395–401. [[CrossRef](#)]
30. Zeitler, V.A.; Brown, C.A. The Infrared Spectra of Some Ti–O–Si, Ti–O–Ti and Si–O–Si Compounds. *J. Phys. Chem.* **1957**, *61*, 1174–1177. [[CrossRef](#)]
31. Praveen, P. Structural, Functional and Optical Characters of TiO₂ Nanocrystallites: Anatase and Rutile Phases. *St. Joseph's J. Humanit. Sci.* **2019**, *6*, 43–53.
32. Chen, Y.-F.; Lee, C.-Y.; Yeng, M.-Y.; Chiu, H.-T. The effect of calcination temperature on the crystallinity of TiO₂ nanopowders. *J. Cryst. Growth* **2003**, *247*, 363–370. [[CrossRef](#)]
33. Vasquez, J.; Lozano, H.; Lavayen, V.; Lira-Cantú, M.; Gómez-Romero, P.; Santa Ana, M.A.; Benavente, E.; Gonzalez, G. High-yield preparation of titanium dioxide nanostructures by hydrothermal conditions. *J. Nanosci. Nanotechnol.* **2009**, *9*, 1103–1107. [[CrossRef](#)]
34. Yamashita, H.; Kawasaki, S.; Ichihashi, Y.; Harada, M.; Takeuchi, M.; Anpo, M.; Stewart, G.; Fox, M.A.; Louis, C.; Che, M. Characterization of Titanium–Silicon Binary Oxide Catalysts Prepared by the Sol–Gel Method and Their Photocatalytic Reactivity for the Liquid-Phase Oxidation of 1-Octanol. *J. Phys. Chem. B* **1998**, *102*, 5870–5875. [[CrossRef](#)]
35. Vives, S.; Meunier, C. Influence of the synthesis route on sol-gel SiO₂-TiO₂ (1:1) xerogels and powders. *Ceram. Int.* **2008**, *34*, 37–44. [[CrossRef](#)]
36. Yu, H.-F.; Wang, S.-M. Effects of water content and pH on gel-derived TiO₂-SiO₂. *J. Non-Cryst. Solids* **2000**, *261*, 260–267. [[CrossRef](#)]
37. Yoldas, B.E. Formation of titania-silica glasses by low temperature chemical polymerization. *J. Non-Cryst. Solids* **1980**, *38*, 81–86. [[CrossRef](#)]
38. Alias, S.S.; Ismail, A.B.; Mohamad, A.A. Effect of pH on ZnO nanoparticle properties synthesized by sol-gel centrifugation. *J. Alloys Compd.* **2010**, *499*, 231–237. [[CrossRef](#)]
39. Wu, L.; Wu, Y.; Lü, Y. Self-assembly of small ZnO nanoparticles toward flake-like single crystals. *Mater. Res. Bull.* **2006**, *41*, 128–133. [[CrossRef](#)]
40. Etacheri, V.; Di Valentin, C.; Schneider, J.; Bahnemann, D.; Pillai, S.C. Visible-light activation of TiO₂ photocatalysts: Advances in theory and experiments. *J. Photochem. Photobiol. C Photochem. Rev.* **2015**, *25*, 1–29. [[CrossRef](#)]
41. Li Hsiung, T.; Paul Wang, H.; Wang, H.C. XANES studies of photocatalytic active species in nano TiO₂-SiO₂. *Radiat. Phys. Chem.* **2006**, *75*, 2042–2045. [[CrossRef](#)]
42. Rossi, T.C.; Grölimund, D.; Nachtegaal, M.; Cannelli, O.; Mancini, G.F.; Bacellar, C.; Kinschel, D.; Rouxel, J.R.; Ohannessian, N.; Pergolesi, D.; et al. X-ray absorption linear dichroism at the Ti K-edge of anatase TiO₂ single crystals. *Phys. Rev. B* **2019**, *100*, 245207. [[CrossRef](#)]
43. Farges, F.; Brown, G.E.; Rehr, J.J. Ti K-edge XANES studies of Ti coordination and disorder in oxide compounds: Comparison between theory and experiment. *Phys. Rev. B* **1997**, *56*, 1809–1819. [[CrossRef](#)]
44. Davis, R.J.; Liu, Z. Titania–Silica: A Model Binary Oxide Catalyst System. *Chem. Mater.* **1987**, *9*, 2311–2324. [[CrossRef](#)]
45. Sharma, A.; Varshney, M.; Park, J.; Ha, T.-K.; Chae, K.-H.; Shin, H.-J. XANES, EXAFS and photocatalytic investigations on copper oxide nanoparticles and nanocomposites. *RSC Adv.* **2015**, *5*, 21762–21771. [[CrossRef](#)]
46. Khemthong, P.; Photai, P.; Grisdanurak, N. Structural properties of CuO/TiO₂ nanorod in relation to their catalytic activity for simultaneous hydrogen production under solar light. *Int. J. Hydrogen Energy* **2013**, *38*, 15992–16001. [[CrossRef](#)]
47. Loshmanov, A.A.; Sigaev, V.N.; Khodakovskaya, R.Y.; Pavlushkin, N.M.; Yamzin, I.I. Small-angle neutron scattering on silica glasses containing titania. *J. Appl. Crystallogr.* **1974**, *7*, 207–210. [[CrossRef](#)]
48. Sandstrom, D.R.; Lytle, F.W.; Wei, P.S.P.; Greeger, R.B.; Wong, J.; Schultz, P. Coordination of Ti in TiO₂-SiO₂ glass by X-ray absorption spectroscopy. *J. Non-Cryst. Solids* **1980**, *41*, 201–207. [[CrossRef](#)]
49. Neurock, M.; Manzer, L.E. Theoretical insights on the mechanism of alkene epoxidation by H₂O₂ with titanium silicalite. *Chem. Commun.* **1996**, *10*, 1133–1134. [[CrossRef](#)]

50. Scherk, C.G.; Ostermann, A.; Achterhold, K.; Iakovleva, O.; Nazikkol, C.; Krebs, B.; Knapp, E.W.; Meyer-Klaucke, W.; Parak, F.G. The X-ray absorption spectroscopy Debye-Waller factors of an iron compound and of met-myoglobin as a function of temperature. *Eur. Biophys. J.* **2001**, *30*, 393–403.
51. Wellenreuther, G.; Parthasarathy, V.; Meyer-Klaucke, W. Towards a black-box for biological EXAFS data analysis. II. Automatic BioXAS Refinement and Analysis (ABRA). *J. Synchrotron Radiat.* **2010**, *17*, 25–35. [[CrossRef](#)]
52. Wu, D.; Zhang, Y.; Yuan, L.; Zhang, M.; Zhou, W. Viscoelastic interfacial properties of compatibilized poly(ϵ -caprolactone)/ polylactide blend. *J. Polym. Sci. Part B Polym. Phys.* **2010**, *48*, 756–765. [[CrossRef](#)]
53. Gregg, S.J.; Sing, K.S.W. *Adsorption, Surface Area and Porosity Auflage*, 2nd ed.; John Wiley & Sons, Ltd: Hoboken, NJ, USA; Academic Press: London, UK, 1982.
54. Zhang, X.; Zhang, F.; Chan, K.-Y. Synthesis of titania–silica mixed oxide mesoporous materials, characterization and photocatalytic properties. *Appl. Catal. A Gen.* **2005**, *284*, 193–198. [[CrossRef](#)]
55. Van Grieken, R.; Aguado, J.; López-Muñoz, M.J.; Marugán, J. Sol-Gel Titania and Titania-Silica Mixed Oxides Photocatalysts. *Solid State Phenom.* **2010**, *162*, 221–238. [[CrossRef](#)]
56. Kosuge, K. Titanium-Containing Porous Silica Prepared by a Modified Sol–Gel Method. *J. Phys. Chem. B* **1999**, *103*, 3563–3569. [[CrossRef](#)]



Article

Effects of Titanium–Silica Oxide on Degradation Behavior and Antimicrobial Activity of Poly (Lactic Acid) Composites

 Arporn Teamsinsungvon ^{1,2,3} , Chaiwat Ruksakulpiwat ^{1,2,3} and Yupaporn Ruksakulpiwat ^{1,2,3,*} 
¹ School of Polymer Engineering, Institute of Engineering, Suranaree University of Technology, Nakhon Ratchasima 30000, Thailand

² Center of Excellence on Petrochemical and Materials Technology, Chulalongkorn University, Bangkok 10330, Thailand

³ Research Center for Biocomposite Materials for Medical Industry and Agricultural and Food Industry, Nakhon Ratchasima 30000, Thailand

* Correspondence: yupa@sut.ac.th; Tel.: +66-44-22-3033

Abstract: A mixed oxide of titania–silica oxides (Ti_xSi_y oxides) was successfully prepared via the sol-gel technique from our previous work. The use of Ti_xSi_y oxides to improve the mechanical properties, photocatalytic efficiency, antibacterial property, permeability tests, and biodegradability of polylactic acid (PLA) was demonstrated in this study. The influence of different types and contents of Ti_xSi_y oxides on crystallization behavior, mechanical properties, thermal properties, and morphological properties was presented. In addition, the effect of using Ti_xSi_y oxides as a filler in PLA composites on these properties was compared with the use of titanium dioxide (TiO_2), silicon dioxide (SiO_2), and TiO_2SiO_2 . Among the prepared biocomposite films, the PLA/ Ti_xSi_y films showed an improvement in the tensile strength and Young's modulus (up to 5% and 31%, respectively) in comparison to neat PLA films. Photocatalytic efficiency to degrade methylene blue (MB), hydrolytic degradation, and in vitro degradation of PLA are significantly improved with the addition of Ti_xSi_y oxides. Furthermore, PLA with the addition of Ti_xSi_y oxides exhibited an excellent antibacterial effect on Gram-negative bacteria (*Escherichia coli* or *E. coli*) and Gram-positive bacteria (*Staphylococcus aureus* or *S. aureus*), indicating the improved antimicrobial effectiveness of PLA composites. Importantly, up to 5% Ti_xSi_y loading could promote more PLA degradation via the water absorption ability of mixed oxides. According to the research results, the PLA composite films produced with Ti_xSi_y oxide were transparent, capable of screening UV radiation, and exhibited superior antibacterial efficacy, making them an excellent food packaging material.

Keywords: titanium silicon oxide; hydrolytic degradation; titania; silica; antimicrobial activity; photocatalytic degradation



Citation: Teamsinsungvon, A.; Ruksakulpiwat, C.; Ruksakulpiwat, Y. Effects of Titanium–Silica Oxide on Degradation Behavior and Antimicrobial Activity of Poly (Lactic Acid) Composites. *Polymers* **2022**, *14*, 3310. <https://doi.org/10.3390/polym14163310>

Academic Editors: Alexandre Vetcher and Alexey Iordanskii

Received: 18 July 2022

Accepted: 11 August 2022

Published: 14 August 2022

Publisher's Note: MDPI stays neutral with regard to jurisdictional claims in published maps and institutional affiliations.



Copyright: © 2022 by the authors. Licensee MDPI, Basel, Switzerland. This article is an open access article distributed under the terms and conditions of the Creative Commons Attribution (CC BY) license (<https://creativecommons.org/licenses/by/4.0/>).

1. Introduction

Higher usage rates of plastics all over the world are causing an increasing rate of disposal of this petroleum-based product. In addition, the limited obtainability of petrochemical resources has become a major global concern [1,2]. Poly (lactic acid) (PLA) is one of the most important biocompatible and biodegradable polymers, and it is a sustainable alternative to petrochemical-derived products [3]. PLA is a synthetic biodegradable polymer, made up of a repeated monomer unit: lactic acid (LA). It is derived from renewable and degradable resources such as corn and rice, and decomposes through simple hydrolysis into water and carbon dioxide. PLA has been viewed as one of the most promising materials because of its excellent biodegradability, biocompatibility, composability, renewability, transparency, high strength, and high modulus [4,5]. Moreover, PLA degradation products are non-toxic (at a lower composition) making it a natural choice for biomedical applications [5,6]. Therefore, this polymer has attracted a wide range of attention in various

applications. However, PLA has a slow degradation rate and hydrophobicity, so it does not decompose fast enough for industrial decomposers [7–9].

To overcome such shortcoming, extra materials are added to fulfill the essential properties such as improved mechanical, heat stability, and barrier properties, and controlled degradation. In addition, the critical hydrolytic degradation rate often limits its application. The rate of degradation could be controlled by adding plasticizers and additives [10]. Although PLA can be degraded with microorganisms in the ground, it takes over two months to decompose, and does not degrade in air [11]. One method to solve this drawback is to add photodegradability filler into PLA, which helps improve degradability under any conditions [12].

Numerous modifications such as copolymerization, plasticization, polymer blends, and polymer composites have been applied to improve some PLA properties. An example of such modifications is to incorporate nanoparticles into the PLA matrix to enhance PLA properties and control the degradation process in various media [13]. The addition of selected nanofillers into PLA, such as organomodified layered silicates (OMLS) [14], carbon nanotubes (CNTs) [15], zinc oxide [16], silica nanofillers (SiO₂) [17,18], and titanium dioxide (TiO₂) [19], can enhance PLA's characteristic features. However, among the nanofillers mentioned above, TiO₂ is the most widely used. TiO₂ or titania is well recognized as a valuable material used in applications such as paints or filler in paper, polymers, textiles, photocatalysis, etc. Nano-TiO₂ particles hold many good properties such as good chemical resistance, high chemical stability [20], attractive photocatalytic activity, excellent photostability, biocompatibility, and antimicrobial activity [21]. Another most-popular nanofiller is silicon dioxide (SiO₂) or silica, a chemical compound that contains oxygen and silicon. Within inorganic oxide fillers, SiO₂ admits much concentration because of its well-defined ordered structure, the easy surface modification, high surface area, and cost-effective production [22]. SiO₂ helps improve the strength, modulus of elasticity, wear resistance, heat and fire resistances, and insulation of properties of polymer materials [23]. Moreover, SiO₂ has been widely applied in food additives, drug delivery, bioimaging, gene delivery, and engineering. Additionally, SiO₂ is classified by the FDA as a “generally regarded as safe” (GRAS) agent, thus making it an ultimate candidate for biomedical applications [24]. The binary oxides are prepared for many purposes: to expand the chemical properties, to develop specific textural properties, or to produce a particle with a personalized composition that is known to present unique characteristics (large surface areas, thermal stability, etc.) [25].

Furthermore, the antimicrobial activity of PLA is usually obtained by adding several metal particles and metal oxides such as silver (Ag) particles [26], zinc oxide (ZnO) [27,28], titanium dioxide (TiO₂) [29,30], and magnesium oxide (MgO) [31] as antibacterial agents.

The objective of the present research was to study PLA composites incorporated with Ti_xSi_y oxide of different concentrations in PLA. We have inspected the influence of TiO₂, SiO₂, and Ti_xSi_y oxide on the mechanical properties, thermal properties, morphological properties, and degradation of PLA in various media. In addition, the antimicrobial activity of the PLA composite was investigated. Furthermore, the addition of Ti₇₀Si₃₀ oxides into PLA significantly improved the photocatalytic efficiency of degrading methylene blue (MB), hydrolytic degradation, and the *in vitro* degradation of PLA. In addition, PLA, with the addition of Ti₇₀Si₃₀ oxides, exhibited an excellent antibacterial effect on Gram-negative bacteria (*E. coli*) and Gram-positive bacteria (*S. aureus*), indicating the improved antimicrobial effectiveness of PLA composites. As a result, Ti₇₀Si₃₀ oxide was used to study the influence of the contents of Ti_xSi_y oxides on the mechanical properties, thermal properties, morphological properties, and degradation of PLA in various media, and the antimicrobial activity of PLA.

2. Materials and Methods

2.1. Materials

Poly (lactic acid) (PLA, grade 4043D) was supplied from Nature Works LLC (Minnetonka, MN, USA), a commercial grade for 3D printing and film applications. Tetraethy-

lorthosilicate (TEOS, 98%, AR grade) and Titanium (IV) isopropoxide (TTIP, 98%, AR grade) were purchased from Acros (Geel, Belgium). Absolute ethanol (C_2H_5OH , AR grade), hydrochloric acid (HCl, AR grade), and ammonium hydroxide (NH_4OH , AR grade) were supplied from Carlo Erba Reagents (Emmendingen, Germany). TiO_2 , SiO_2 , and Ti_xSi_y oxide prepared in-house were used as filler [32,33]. Particle size of SiO_2 , $Ti_{70}Si_{30}$, $Ti_{50}Si_{50}$, and $Ti_{40}Si_{60}$ oxide used in this study were in the range of 130–150 nm. TiO_2 can be generally synthesized under high acid conditions to obtain a uniform spherical shape and small nanoparticles in the range of 25–50 nm [34]. However, the author could synthesise Ti_xSi_y under alkali conditions to control hydrolysis step of Ti-precursor to obtain a uniform shape and size in the range of 130–150 nm because Ti-precursor decreased the reactivity of the alkoxide, hence low concentration of Ti-precursor decreased reactivity of the alkoxide with the lower hydrolysis rate [35].

2.2. Preparation of PLA Composite Films

PLA and PLA composites were prepared by solvent film casting method. First, $Ti_{70}Si_{30}$, $Ti_{50}Si_{50}$, $Ti_{40}Si_{60}$, SiO_2 , and TiO_2 were dispersed in chloroform with ultrasonic treatment for 1 day. After that, PLA was added to the Ti_xSi_y oxide and strictly stirred for 4 days. The dispersions of PLA composites were additionally ultrasonically treated for 1 h with frequency of 42 kHz for four times per day. Then, the treated dispersions were slightly poured onto Petri dishes, and the solvent was evaporated under room temperature. The films were dried to constant mass at room temperature for ~24 h and stored in oven at 40 °C for 4 h. Pure PLA and PLA composite films had uniform thickness of $250 \pm 4.68 \mu m$. After that, Ti_xSi_y oxides were synthesized using a modified Stöber method involving simultaneous hydrolysis and condensation of TEOS, and Ti_xSi_y mixed oxides' preparation was reported in details in Teamsinsungvon et al. [32].

2.3. Mechanical Properties

The tensile properties of PLA and PLA composites films were obtained in accordance with the ASTM standard method D882-18 using an Instron universal testing machine (UTM, model 5565, Norwood, MA, USA) with a load cell of 5 kN. Specimen samples were 10 cm \times 2.54 cm. Crosshead speed was set at 50 cm/min. The values were presented as the average of seven measurements.

2.4. Thermal Properties

Thermal properties of PLA and PLA composites films were carried out using a differential scanning calorimeter (DSC204F1, Netzsch, Selb, Germany) equipped with a liquid nitrogen cooling system. The samples were heated from room temperature to 180 °C with a heating rate of 5 °C/min (1st heating scan) and stored for 5 min to erase previous thermal history. Then it was cooled to room temperature (25 °C) with a cooling rate of 5 °C/min. Finally, it was heated again to 180 °C with heating rate 5 °C/min (2nd heating scan). The degree of crystallinity (X_c) of PLA and PLA composites was estimated using Equation (1) [36,37]:

$$X_c = \frac{\Delta H_m}{\Delta H_m^0 \cdot (\phi_{PLA})} \cdot 100 \quad (1)$$

where ΔH_m are the melting enthalpy in the second heating process, ΔH_m^0 , which is the melting enthalpy of an infinitely large crystal, was taken as 93.6 J/g [38], and ϕ_{PLA} is the PLA weight fraction in the composites.

Thermogravimetric analysis of PLA and PLA composite films were examined using thermogravimetric analyzer (TGA/DSC1, Mettler Toledo, Columbus, OH, USA). The temperature was raised from the room temperature to 650 °C under nitrogen and then heated to 800 °C under air atmosphere at heating rate of 10 °C/min. The weight change was recorded as a function of temperature.

as reference. The opacity of the film specimens was determined with well-controlled thicknesses. Equation (3) was used to calculate the *Opacity* ($\text{AU}\cdot\text{nm}\cdot\text{mm}^{-1}$) of the films:

$$\text{Opacity} = \frac{\text{Abs}_{600}}{b} \quad (3)$$

where Abs_{600} = the absorbance at 600 nm; the transmittance values were converted to absorbance values using the Lambert–Beer equation and b = the film thickness (mm). This test was triplicated for each type of film [41].

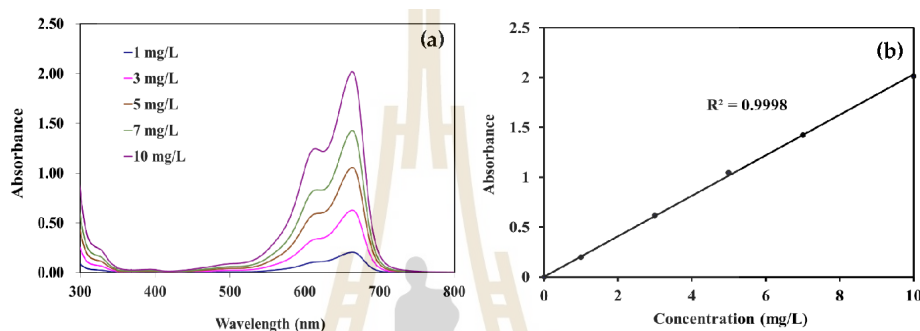


Figure 1. (a) Wavelength–absorbance curves and (b) calibration curve of methylene blue aqueous solutions.

2.9. Hydrolytic Degradation

Hydrolytic degradation of PLA and PLA composite films ($10 \times 10 \text{ mm}^2$) were carried out at 37°C in small bottles containing $1 \text{ mol}\cdot\text{dm}^{-3}$ NaOH solutions (pH 13). Following the incubation for a given time (0, 60, 120, 180, 240, 300, 360, and 420 min), the films were periodically removed, washed with distilled water, and dried in oven at 40°C for 48 h. The weight loss (W_{loss}) was estimated using following Equation (4):

$$W_{\text{loss}}(\%) = \frac{W_0 - W_t}{W_0} \cdot 100 \quad (4)$$

where W_0 = the initial weight of polymer film, and W_t = the weight of degraded sample measured at time t after drying in oven for 48 h [12].

2.10. In Vitro Degradation

The study of degradation of PLA and its composite was carried out following the standards specified by BS EN ISO 10993-13:2010 [42] and ASTM F1635-11 [43]. Each of PLA and PLA composite samples of (0.4–0.5 g) was accurately weighed. The samples were then immersed separately in 0.01 M phosphate-buffered saline (PBS) ($\text{pH} = 7.4 \pm 0.2$) solution and maintained at 37°C with different soaking times from 1 to 8 weeks (0, 2, 4, 6, 8). At various time points, the specimens were washed with deionized water to remove the salts, then oven dried at 40°C for 48 h. Later, dry weights of the samples were recorded. The percentage mass change was determined using the following Equation (5):

$$W_{\text{loss}}(\%) = \frac{W_t - W_0}{W_0} \cdot 100 \quad (5)$$

where W_t = mass of degraded sample measured at time t after drying at 40°C in oven for 48 h, and W_0 = the initial mass of the sample. At each time point, every sample was weighed and mechanically tested, allowing the degradation pathway of each individual sample to be followed with time.

as reference. The opacity of the film specimens was determined with well-controlled thicknesses. Equation (3) was used to calculate the *Opacity* ($\text{AU}\cdot\text{nm}\cdot\text{mm}^{-1}$) of the films:

$$\text{Opacity} = \frac{\text{Abs}_{600}}{b} \quad (3)$$

where Abs_{600} = the absorbance at 600 nm; the transmittance values were converted to absorbance values using the Lambert–Beer equation and b = the film thickness (mm). This test was triplicated for each type of film [41].

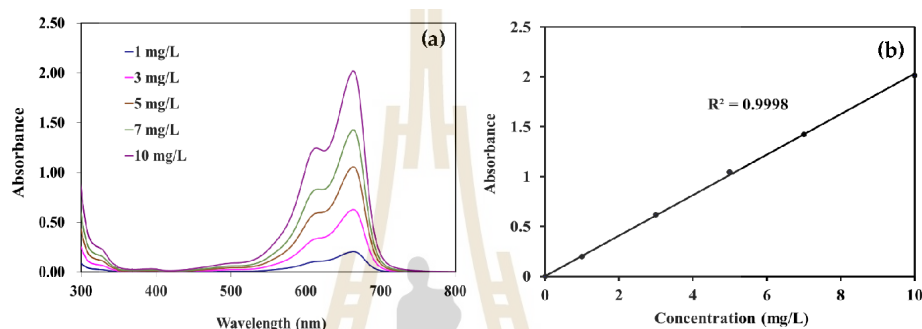


Figure 1. (a) Wavelength–absorbance curves and (b) calibration curve of methylene blue aqueous solutions.

2.9. Hydrolytic Degradation

Hydrolytic degradation of PLA and PLA composite films ($10 \times 10 \text{ mm}^2$) were carried out at 37°C in small bottles containing $1 \text{ mol}\cdot\text{dm}^{-3}$ NaOH solutions (pH 13). Following the incubation for a given time (0, 60, 120, 180, 240, 300, 360, and 420 min), the films were periodically removed, washed with distilled water, and dried in oven at 40°C for 48 h. The weight loss (W_{loss}) was estimated using following Equation (4):

$$W_{\text{loss}}(\%) = \frac{W_0 - W_t}{W_0} \cdot 100 \quad (4)$$

where W_0 = the initial weight of polymer film, and W_t = the weight of degraded sample measured at time t after drying in oven for 48 h [12].

2.10. In Vitro Degradation

The study of degradation of PLA and its composite was carried out following the standards specified by BS EN ISO 10993-13:2010 [42] and ASTM F1635-11 [43]. Each of PLA and PLA composite samples of (0.4–0.5 g) was accurately weighed. The samples were then immersed separately in 0.01 M phosphate-buffered saline (PBS) ($\text{pH} = 7.4 \pm 0.2$) solution and maintained at 37°C with different soaking times from 1 to 8 weeks (0, 2, 4, 6, 8). At various time points, the specimens were washed with deionized water to remove the salts, then oven dried at 40°C for 48 h. Later, dry weights of the samples were recorded. The percentage mass change was determined using the following Equation (5):

$$W_{\text{loss}}(\%) = \frac{W_t - W_0}{W_0} \cdot 100 \quad (5)$$

where W_t = mass of degraded sample measured at time t after drying at 40°C in oven for 48 h, and W_0 = the initial mass of the sample. At each time point, every sample was weighed and mechanically tested, allowing the degradation pathway of each individual sample to be followed with time.

The tensile properties of each specimen were measured by an Instron universal testing machine (UTM, model 5565) with a load cell of 5 kN and crosshead speed of 50 cm/min. The values were presented as the average of five measurements.

2.11. Antimicrobial Activity

Antimicrobial effects of the different samples were determined using the JIS Z 2801:2006 method. The ability of PLA and PLA composite films to restrain the growth of *Escherichia coli* and *Staphylococcus aureus* were investigated. The bacteria were incubated at 37 °C for 24 h. A plate containing a test sample was inoculated with 0.2 mL of an overnight culture of *Escherichia coli* and *Staphylococcus aureus*, while bacterial culture concentration was adjusted to 10⁶ CFU/mL. All petri dishes were incubated at 37 °C for 24 h and colony-forming units (CFU) were counted. Percentage reduction of the colonies was calculated using Equations (6) and (7) below, which relates the number of colonies of neat PLA with that of the composites.

$$\% \text{ Reduction} = \frac{(\text{Log CFU at 0 h} - \text{Log CFU at 24 h})}{\text{Log CFU at 0 h}} \cdot 100 \quad (6)$$

$$\text{Antimicrobial activity}(R) = U_t - A_t \quad (7)$$

where U_t = average of CFU per milliliter after inoculation on untreated test pieces after 24 h; A_t = average of CFU per milliliter after inoculation on antibacterial test pieces after 24 h.

3. Results and Discussion

3.1. Mechanical Properties

The tensile properties of PLA and PLA composites with various Ti₇₀Si₃₀ oxide contents and different types of nanoparticles are listed in Table 1.

Table 1. Tensile properties of PLA, PLA/TiO₂, PLA/SiO₂, PLA/Ti_xSi_y, and PLA/TiO₂SiO₂ composites.

Sample	Tensile Strength (MPa)	Elongation at Break (%)	Young's Modulus (GPa)
PLA	33.94 ± 1.38	19.62 ± 8.64	0.98 ± 0.23
97PLA/3TiO ₂	28.22 ± 1.47	18.1 ± 4.24	1.01 ± 0.04
97PLA/3SiO ₂	29.75 ± 1.38	11.8 ± 4.96	1.07 ± 0.10
97PLA/3Ti ₇₀ Si ₃₀	35.64 ± 3.21	11.12 ± 1.81	1.18 ± 0.06
95PLA/5Ti ₇₀ Si ₃₀	32.06 ± 2.29	9.88 ± 2.81	1.01 ± 0.10
97PLA/3Ti ₅₀ Si ₅₀	35.31 ± 2.01	9.61 ± 2.57	1.29 ± 0.12
97PLA/3Ti ₄₀ Si ₆₀	30.67 ± 1.74	22.30 ± 2.53	1.02 ± 0.05
97PLA/3TiO ₂ SiO ₂	29.00 ± 1.42	58.37 ± 5.00	0.96 ± 0.07

The addition of 3 wt.% of Ti₇₀Si₃₀ and Ti₅₀Si₅₀ slightly increased the tensile strength and Young's modulus and decreased the elongation at break of the PLA composite films compared to neat PLA (Figure 2). This may be due to higher interfacial adhesion between the oxide filler and the PLA matrix by the Van der Waals force or induction interactions, which decreased thereafter when adding a mixed oxide content of up to 5 wt.%, however, it was slightly higher than pure PLA. The result could be attributed to the increased filler quantity leading to a weaker filler–matrix interface and the agglomeration of filler particles, which consequently decreases the tensile strength. The Young's modulus of the composites insignificantly varied in correspondence with Ti_xSi_y oxide (Figure 2c). However, elongation at the break decreased with the addition of Ti_xSi_y oxide (Figure 2b) as a result of the addition of a rigid phase in the PLA composite, which contributed to a reduction of the PLA ductility. Nevertheless, the addition of TiO₂SiO₂ and Ti₄₀Si₆₀ in the PLA matrix increased elongation at the break of PLA.

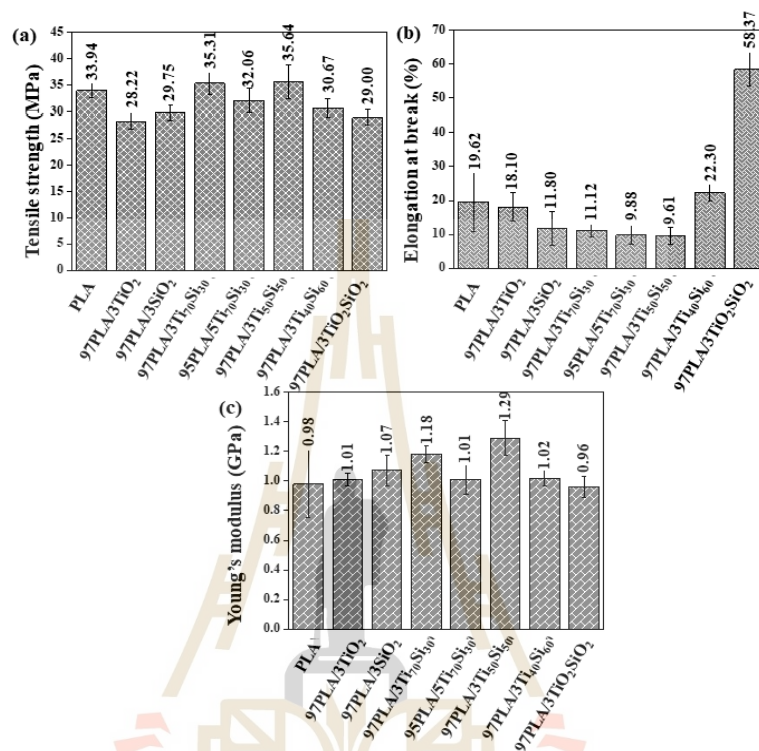


Figure 2. Comparison of the (a) Tensile strength, (b) Elongation at break, and (c) Young's modulus of PLA, PLA/TiO₂, PLA/SiO₂, PLA/Ti_xSi_y, and PLA/TiO₂SiO₂ composites.

During tensile testing, it was observed that the fracture behavior of the film changed for PLA, PLA/TiO₂, PLA/SiO₂, PLA/Ti_xSi_y, and PLA/TiO₂SiO₂ composites. This was demonstrated in the tensile stress–strain curves, as shown in Figure 3. With the addition of filler to the PLA matrix, the composite exhibits elastic behavior, enhancing the toughness of PLA. Furthermore, it was shown that the addition of Ti₇₀Si₃₀ oxide to the PLA polymer matrix resulted in a decrease in the ductile characteristics, while slightly increasing the tensile strength and decreasing elongation at the break. However, the addition of TiO₂SiO₂ and Ti₄₀Si₆₀ oxide increased elongation at the break of PLA. This may be due to the particles of TiO₂SiO₂ in the formulation being homogeneously distributed in the polymer matrix, contributing to the occurrence of plastic deformations in the whole sample, allowing a higher elongation than that of the pure PLA.

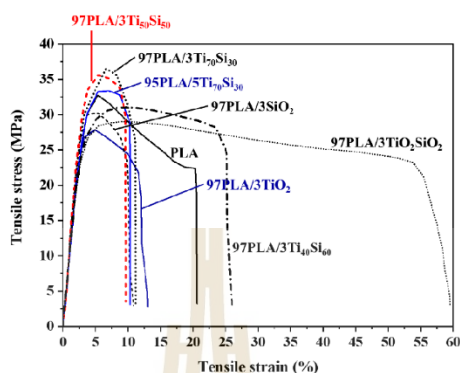


Figure 3. Stress–strain curves of PLA, PLA/TiO₂, PLA/SiO₂, PLA/Ti_xSi_y, and PLA/TiO₂SiO₂ composites.

3.2. Thermal Properties

Thermal behaviors of pure PLA and PLA composites with TiO₂, SiO₂, Ti₇₀Si₃₀, Ti₅₀Si₅₀, Ti₄₀Si₆₀, and TiO₂SiO₂ were investigated using differential scanning calorimetry (DSC), in which first heating scans (1st heating scans), cooling scans, and second heating scans (2nd heating scans) of PLA and PLA composites were performed. DSC thermograms of PLA and PLA composites are shown in Figure 4. The thermal properties of all samples are listed in Table 2. The glass transition temperature (T_g), cold crystallization temperature (T_{cc}), and melting temperature (T_m) of the PLA composites were observed.

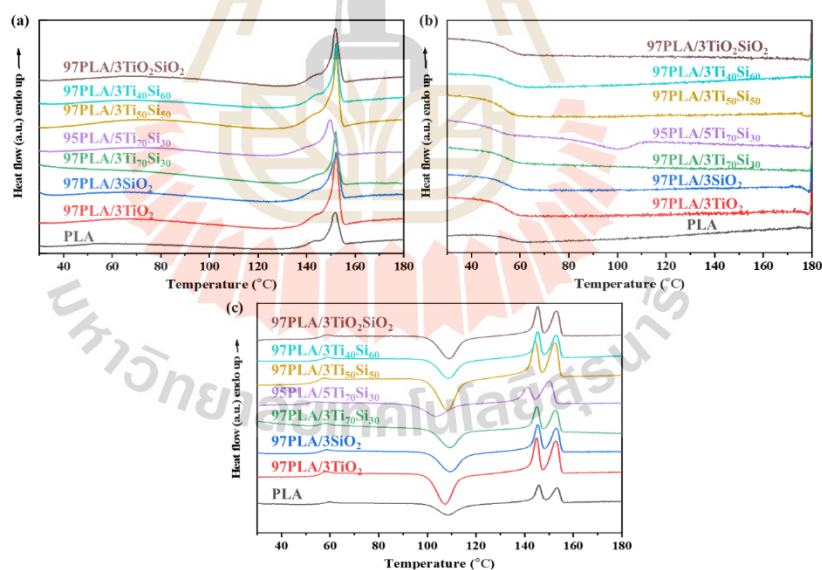


Figure 4. DSC thermogram of (a) first heating, heating rate 5 °C/min, (b) cooling, cooling rate 5 °C/min, (c) second heating, heating rate 5 °C/min of PLA, PLA/TiO₂, PLA/SiO₂, PLA/Ti_xSi_y, and PLA/TiO₂SiO₂ composites.

Table 2. Thermal characteristics of PLA, PLA/TiO₂, PLA/SiO₂, PLA/Ti_xSi_y, and PLA/TiO₂SiO₂ composites (the second heating, heating rate 5 °C/min).

Samples	T _{gr} °C	T _{ccr} °C	ΔH _c J/g	T _{m1} °C	T _{m2} °C	ΔH _m J/g	X _c %
PLA	58.87	109.47	36.15	145.84	153.35	31.73	33.86
97PLA/3TiO ₂	56.86	107.36	33.61	144.89	152.72	33.17	36.50
97PLA/3SiO ₂	56.64	108.22	33.06	145.39	145.33	33.31	36.65
97PLA/3Ti ₇₀ Si ₃₀	54.81	107.3	34.41	145.07	152.75	32.71	35.99
95PLA/5Ti ₇₀ Si ₃₀	51.84	103.09	26.80	141.29	150.22	32.18	36.15
97PLA/3Ti ₅₀ Si ₅₀	55.96	107.14	33.06	144.41	152.50	34.44	37.89
97PLA/3Ti ₄₀ Si ₆₀	57.40	107.72	34.16	145.33	153.01	33.38	36.73
97PLA/3TiO ₂ SiO ₂	57.46	107.79	30.54	145.39	153.07	32.31	35.55

T_g and T_{cc} of neat PLA occur at 58.87 °C and 109.47 °C, respectively, while T_m appeared at 145.84 °C and 152.35 °C, respectively. The double melting endotherms of neat PLA were explained by the melting and recrystallization. The peak at a low temperature was attributed to the melting of the crystals formed during the non-isothermal melt crystallization, while the peak at a high temperature corresponded to the re-melting of the newly-formed crystallite during melting, and recrystallization during the DSC heating scans [44]. However, T_c of the neat PLA did not appear in the cooling cycle. The addition of TiO₂, SiO₂, Ti₇₀Si₃₀, Ti₅₀Si₅₀, Ti₄₀Si₆₀, and TiO₂SiO₂ in the PLA matrix showed insignificant effects on the glass transition temp (T_g), cold crystallization temp (T_{cc}), and melting temp (T_m) of PLA. After the cooling scan (Figure 4b), no crystallization temperatures (T_c) were observed in all composites in the cooling cycle. However, by adding 5wt.% of Ti₇₀Si₃₀ oxide into PLA, T_c was only observed at 101 °C when cooling the sample in the DSC measurement at a cooling rate of 5 °C/min.

Cold crystallization is a phenomena that occurs from re-crystallization during the heating process of polymers [45]. Cold crystallization behaviors (Figure 4c) of PLA films containing 3 wt.% of TiO₂, SiO₂, Ti₇₀Si₃₀, Ti₅₀Si₅₀, Ti₄₀Si₆₀, and TiO₂SiO₂ nanoparticles and 5 wt.% of Ti₇₀Si₃₀ were observed. For neat PLA, there is a slightly cold crystallization peak around 109.47 °C. While adding 3 wt.% of TiO₂, SiO₂, Ti₇₀Si₃₀, Ti₅₀Si₅₀, Ti₄₀Si₆₀, and TiO₂SiO₂ into PLA, the cold crystallization peak of PLA composites shifted to a lower temperature by approximately 1–2 °C. Moreover, the T_{cc} of the PLA composite shifted to 103.09 °C with Ti₇₀Si₃₀-loading rising to 5 wt.%, showing that a 5 wt.% Ti₇₀Si₃₀ addition can promote PLA crystallization. This might be attributed to the increase of the chain mobility of PLA, and the Ti_xSi_y oxide could act as an efficient cold crystal nuclei site, which consequently increased the crystallinity of PLA. These results suggest that Ti₇₀Si₃₀ oxide had a positive effect on the promotion of the crystallization of PLA and could act as a nucleating agent. Similar to other results, Chen et al. [45] found that by incorporating a composite nucleating agent (CNA) to PLA, the polymer could decrease T_{cc}, indicating that the crystallization ability of the PLA composite can be enhanced in such a way.

The addition of 5 wt.% Ti₇₀Si₃₀ is found to be able to enhance the T_m of PLA composites. This is possibly a result of the heterogeneous nucleation effects of Ti₇₀Si₃₀ nanoparticles on PLA during the crystallization process. The lamella formation of PLA was hindered by Ti₇₀Si₃₀ and led to less perfect crystals of PLA [46]. While the addition of a 3 wt.% of TiO₂, SiO₂, Ti₇₀Si₃₀, Ti₅₀Si₅₀, Ti₄₀Si₆₀, and TiO₂SiO₂ did not significantly affect the T_m of PLA, the degree of crystallinity (X_c) of neat PLA significantly increased with incorporating TiO₂, SiO₂, Ti₇₀Si₃₀, Ti₅₀Si₅₀, Ti₄₀Si₆₀, and TiO₂SiO₂, indicating that TiO₂, SiO₂, Ti₇₀Si₃₀, Ti₅₀Si₅₀, Ti₄₀Si₆₀, and TiO₂SiO₂ can act as nucleating agents for PLA.

Thermal degradation at 5% weight loss (T_{0.05}), 50% weight loss (T_{0.5}), final degradation (T_f), and the char formation at 800 °C of PLA and PLA composites are listed in Table 3, respectively. TGA and DTG curves of PLA and PLA composites at a heating rate of 10 °C/min are shown in Figure S1a,b, respectively. The presence of TiO₂, SiO₂, Ti₇₀Si₃₀, Ti₅₀Si₅₀, Ti₄₀Si₆₀, and TiO₂SiO₂ did not change the thermal decomposition behavior of PLA, while the mass loss between 250–365 °C was observed, which corresponded to the

decomposition of PLA. Then from 365 to 600 °C thermal analysis curves slowed down to complete the decomposition of the PLA matrix until a constant mass was reached. The constant mass remaining at the end of each TGA experiment corresponded to amounts of nanoparticles in PLA composites. In this study, the temperature at 5% weight loss ($T_{0.05}$) was defined as the onset degradation temperature for the evaluation of the TiO_2 , SiO_2 , and Ti_xSi_y oxide effects on the thermal stability of the PLA composites.

Table 3. Thermal degradation temperature of PLA, PLA/ TiO_2 , PLA/ SiO_2 , PLA/ Ti_xSi_y , and PLA/ TiO_2SiO_2 composites.

Samples	$T_{0.05}$, °C	$T_{0.5}$, °C	T_d , °C	T_f , °C	Residual, %
PLA	321.67	360.33	358.83	424.64	1.20
97PLA/3 TiO_2	336.17	363.67	363.17	429.22	4.07
97PLA/3 SiO_2	331.17	361.17	359.33	427.27	4.14
97PLA/3 $\text{Ti}_{70}\text{Si}_{30}$	304.00	351.83	350.17	408.68	3.91
95PLA/5 $\text{Ti}_{70}\text{Si}_{30}$	284.50	347.33	346.33	407.16	5.46
97PLA/3 $\text{Ti}_{50}\text{Si}_{50}$	324.50	358.36	356.50	425.49	4.22
97PLA/3 $\text{Ti}_{40}\text{Si}_{60}$	326.50	358.67	356.83	416.83	3.53
97PLA/3 TiO_2SiO_2	330.67	362.33	361.33	418.69	4.50

It is obvious that the T_{onset} of the PLA composites shifted to a higher temperature with the presence of 3 wt.% of TiO_2 , SiO_2 , $\text{Ti}_{50}\text{Si}_{50}$, $\text{Ti}_{40}\text{Si}_{60}$, and TiO_2SiO_2 . Consequently, the thermal stability of the PLA composites was improved. A possible reason to explain this behavior is that TiO_2 , SiO_2 , $\text{Ti}_{50}\text{Si}_{50}$, $\text{Ti}_{40}\text{Si}_{60}$, and TiO_2SiO_2 particles may act as a heat barrier in the early stage of thermal decomposition [12]. Similar data have been reported by Zhang et al., who studied PLA composites obtained by adding TiO_2 to poly (lactic acid) [47]. However, PLA with the addition of 3 wt.% of $\text{Ti}_{70}\text{Si}_{30}$ oxide was found to present a lower onset temperature than that of pure PLA, which resulted in a decrease in the PLA thermal stability. Moreover, it was found that the onset degradation temperature of the composites shifted to a lower temperature with increasing $\text{Ti}_{70}\text{Si}_{30}$ oxide nanoparticles loading from 3 to 5 wt.%. This suggests that there might be degradation due to the water absorption of the filler that would be associated with the cleavage of the chain of PLA at the ester group ($-\text{C}-\text{O}-$) by water molecules due to hydrolysis leading to decreased the thermal stability of PLA.

Moreover, the peak in the DTG curves represented the temperature maximum degradation rate (Figure S1b). PLA/3 TiO_2 exhibited the fastest degradation rate at the highest temperature, compared to neat PLA and other PLA composites. However, the degradation temperature of the PLA/ $\text{Ti}_{70}\text{Si}_{30}$ composite shifted to a lower temperature. This suggested that the thermal stability of PLA decreased with the incorporation of $\text{Ti}_{70}\text{Si}_{30}$ loading. In addition, when 3 wt.% TiO_2 , SiO_2 , $\text{Ti}_{70}\text{Si}_{30}$, $\text{Ti}_{50}\text{Si}_{50}$, $\text{Ti}_{40}\text{Si}_{60}$, and TiO_2SiO_2 , and 5 wt.% $\text{Ti}_{70}\text{Si}_{30}$ mixed oxides were added to PLA, the composites left the char residual of fillers at 4.07, 4.14, 3.91, 4.22, 3.53, 4.50, and 5.46%, respectively, for the PLA composites. The char residual generally depended on the amount of added nanoparticles [48].

3.3. Morphological Properties

In order to investigate the dispersion and distribution of TiO_2 , SiO_2 , $\text{Ti}_{70}\text{Si}_{30}$, $\text{Ti}_{50}\text{Si}_{50}$, $\text{Ti}_{40}\text{Si}_{60}$, and TiO_2SiO_2 in the PLA composites films, SEM analysis was performed. SEM micrographs of the fracture surface of PLA and PLA adding 3 wt.% of TiO_2 , SiO_2 , $\text{Ti}_{70}\text{Si}_{30}$, $\text{Ti}_{50}\text{Si}_{50}$, $\text{Ti}_{40}\text{Si}_{60}$, and TiO_2SiO_2 , and 5 wt.% of $\text{Ti}_{70}\text{Si}_{30}$ are shown in Figure 5a, and the surface of the PLA and PLA composites films after the tensile test is shown in Figure 5b.

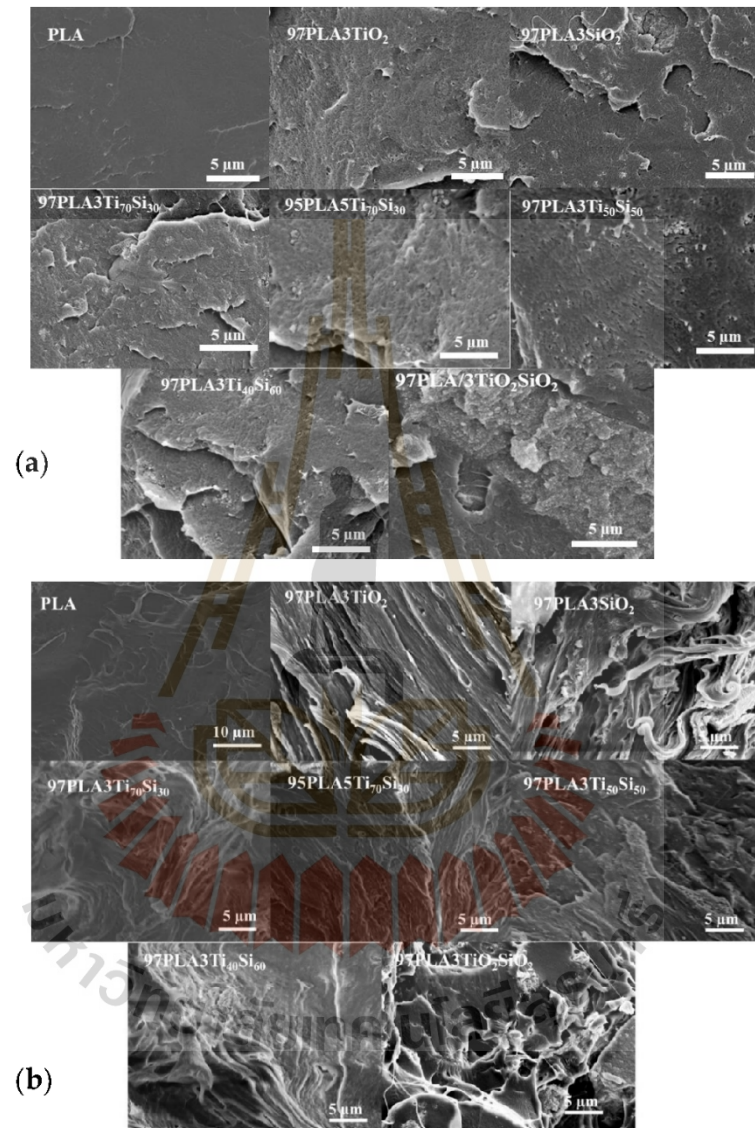


Figure 5. SEM micrographs ($\times 2.5$ k, WD = 13–15 mm, acceleration voltage 9–12 kV) of (a) the fracture surface and (b) after tensile testing of PLA, PLA/TiO₂, PLA/SiO₂, PLA/Ti_xSi_y, and PLA/TiO₂SiO₂ composites.

The SEM results showed that a relatively brittle and comparatively flat surface without holes and air bubbles was found on the fracture surface of the pure PLA films. Meanwhile, SEM images of all PLA composites exhibited roughness caused by adding 3 wt.% of TiO_2 , SiO_2 , $\text{Ti}_{70}\text{Si}_{30}$, $\text{Ti}_{50}\text{Si}_{50}$, $\text{Ti}_{40}\text{Si}_{60}$, and TiO_2SiO_2 nanoparticles, particularly at 3 wt.% of TiO_2SiO_2 (Figure 5a). The enhancement of the mechanical properties depended on the absence of voids, undamaged position of fillers, interfacial bonding between the fillers and matrix, and the absence of an agglomerate of fillers [49]. However, the white spots in the PLA composites micrographs illustrates the agglomerates of TiO_2 , SiO_2 , $\text{Ti}_{70}\text{Si}_{30}$, $\text{Ti}_{50}\text{Si}_{50}$, $\text{Ti}_{40}\text{Si}_{60}$, and TiO_2SiO_2 in the PLA matrix, leading to poor mechanical properties. In this work, although some agglomerations could be observed in all PLA composite films, 3wt.% of $\text{Ti}_{70}\text{Si}_{30}$ and $\text{Ti}_{50}\text{Si}_{50}$ was still kept intact within the PLA matrix (Figure 5b). As $\text{Ti}_{70}\text{Si}_{30}$ -loading was increased to 5 wt.%, the position of $\text{Ti}_{70}\text{Si}_{30}$ in PLA was displaced, leading to the formation of a gap between the filler surface and PLA matrix. Therefore, it is an indication of poor interfacial adhesion between $\text{Ti}_{70}\text{Si}_{30}$ and PLA at high loading [50].

The EDX elemental mapping results (Figure 6b–e) suggested the existence of Ti_xSi_y mixed oxides in the PLA composites. Furthermore, EDX elemental analysis results (Figure 6f) of the selected area also confirmed the spatial distribution of the Si, Ti, and O elements of the Ti_xSi_y mixed oxide in the PLA composite. The distribution of Si and Ti in the particles was relatively uniform in the case of the PLA/3 $\text{Ti}_{70}\text{Si}_{30}$ composite.

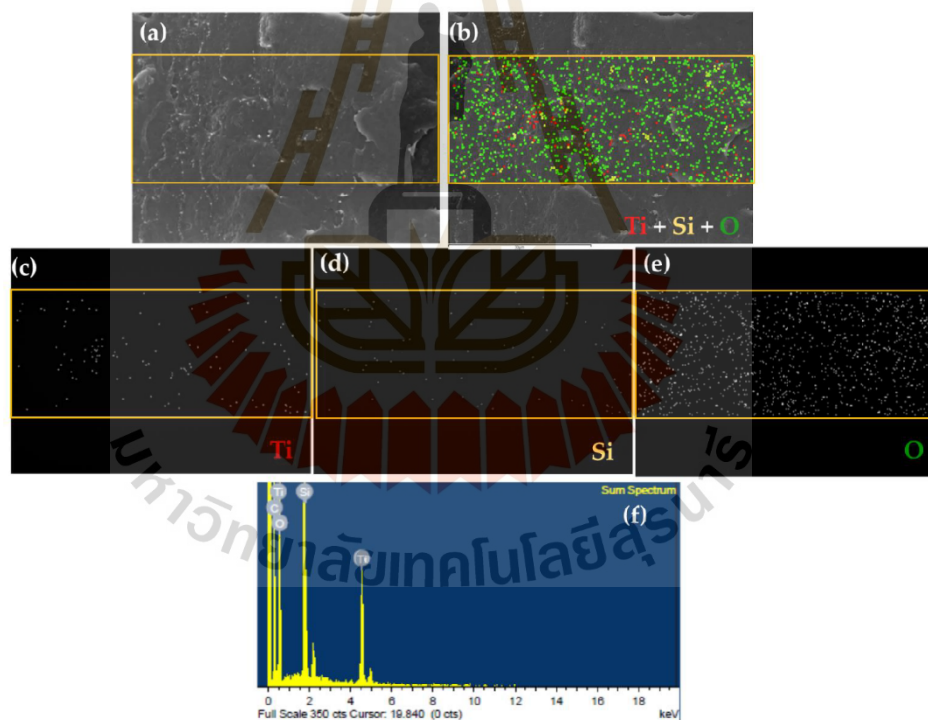


Figure 6. (a) SEM images (b) over all elements in the PLA/ $\text{Ti}_{70}\text{Si}_{30}$ composite and the corresponding elemental mapping analysis of (c) Ti, (d) Si, (e) O, and (f) EDX spectra.

3.4. Water Vapor Transmission Rate (WVTR)

One of the most important properties of bio-based composites films is the ability to evaluate the moisture transfer from the environment to the product. The WVTR of the PLA and PLA composite films is shown in Figure 7. The WVTR of the PLA films was $0.316 \text{ g m}^{-2} \text{ day}^{-1}$ which was lower than the PLA films incorporated with 3wt.% of SiO_2 , $\text{Ti}_{70}\text{Si}_{30}$, and $\text{Ti}_{50}\text{Si}_{50}$, which were 1.000, 1.023, and $0.523 \text{ g m}^{-2} \text{ day}^{-1}$. In addition, the WVTR of the PLA/ $\text{Ti}_{70}\text{Si}_{30}$ composite film increased with increasing $\text{Ti}_{70}\text{Si}_{30}$ content to 5 wt.%. It is common that, for a solid polymer, the water vapor transmission follows a simple mechanism including adsorbing at the entering face, dissolving, and rapidly creating equilibrium, diffusing through the film, and desorbing at the exit face [51]. The smaller the particle diameter of the nanoparticles is, the more the indirect pathway reducing the diffusion coefficient is produced [52,53]. In other words, the particle diameter is indirectly proportional to the diffusion coefficient. Consequently, the hydrophilicity of the PLA composite incorporating SiO_2 , $\text{Ti}_{70}\text{Si}_{30}$, and $\text{Ti}_{50}\text{Si}_{50}$ was improved.

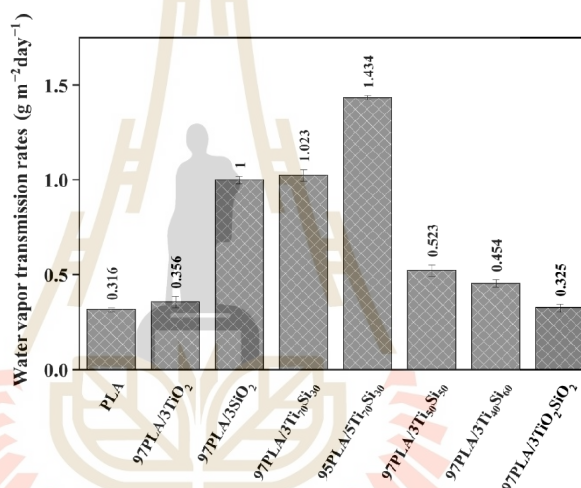


Figure 7. Water vapor transmission rate (WVTR) of PLA, PLA/ TiO_2 , PLA/ SiO_2 , PLA/ Ti_xSi_y , and PLA/ TiO_2SiO_2 composites.

3.5. Photocatalytic Degradation of Methylene Blue (MB)

In this study, the photocatalytic activity of PLA and PLA composite films were investigated by degrading methylene blue (MB). The decomposition of MB might be caused by UV irradiation without the presence of any photocatalyst.

Figure 8 shows changes in the concentration of MB in an aqueous solution under UV irradiation, which was a result of MB decomposition. The presence of 3 wt.% TiO_2 , SiO_2 , $\text{Ti}_{70}\text{Si}_{30}$, $\text{Ti}_{50}\text{Si}_{50}$, $\text{Ti}_{40}\text{Si}_{60}$, and TiO_2SiO_2 in the PLA film matrix exhibited MB degradation more efficiently than using photocatalysis solely. The efficiency to degrade MB was $\text{TiO}_2 > \text{Ti}_{70}\text{Si}_{30} > \text{TiO}_2\text{SiO}_2 > \text{Ti}_{50}\text{Si}_{50} > \text{Ti}_{40}\text{Si}_{60} > \text{SiO}_2$, respectively. It was also found that an increase in $\text{Ti}_{70}\text{Si}_{30}$ -loading to 5wt.% improved the efficiency of the photocatalytic activity of PLA. The photo-activity of the mixed oxide was evidently increased because the high content of the mixed oxide's increasing surface area of the filler effectively concentrated MB around the nanoparticle and produced high concentrations of organic compounds for the photocatalysis, which consequently improved the photocatalytic activity of PLA. It is known that photocatalytic activity occurs at the surface of the photocatalyst. Therefore, the

surface area of PLA composite film, which in turn depends on the size of the nanoparticles, film morphology, and thickness, has an effect on photocatalytic reactivity [54]. The PLA composite film containing TiO_2 can degrade MB more effectively than that containing only photocatalysis. This may be due to two reasons. Firstly, MB was degraded directly by UVC. Secondly, TiO_2 received light energy more than band-gap energy and then the electron in the valence band (VB) was excited to the conduction band (CB), resulting in a generated hole (h^+) (Equation (8)). This hole could oxidize MB (Equation (9)) or oxidized H_2O to produce OH (Equation (10)). The e^- in CB could reduce O_2 at the surface of TiO_2 to generate O_2^- (Equation (11)). The appearance of radical (OH , O_2^-) and h^+ reacted with MB to generate a peroxide derivative and hydroxylate or degrade completely to CO_2 and H_2O [54]. The photodegradation mechanism can be summarized by Equations (8)–(11).

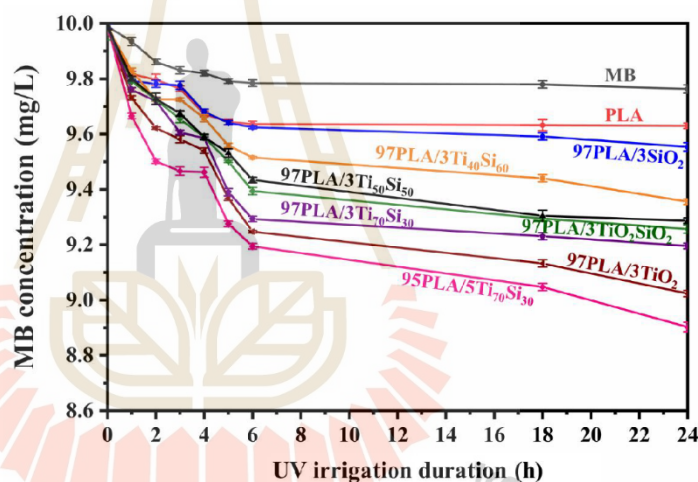
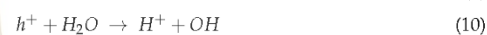


Figure 8. Concentration of methylene blue (MB) due to absorption of PLA, PLA/ TiO_2 , PLA/ SiO_2 , PLA/ Ti_xSi_y , and PLA/ TiO_2SiO_2 composite films under UV irradiation.

The presence of filler in the PLA film matrix shows more efficiency to degrading MB than using only photocatalysis. The enhanced photocatalytic properties of the PLA composites could be mainly attributed to promoted surface adsorption and mass transfer/diffusion, increased light absorption and utilization efficiency, and especially, the higher charge transfer and separation rate by the filler, increased light-harvesting ability, and promoting photoexcitation charge separation, which were the main reasons for improving photocatalytic activity [55,56]. In addition, the photocatalytic activity is influenced by the crystal structure, particle size, specific surface area, and porosity of nanoparticles. So, ultrafine powders of mixed oxide show good catalytic activity. However, agglomeration often takes place, resulting in the reduction or even complete loss of photocatalytic activity.

Due to its photocatalytic activity, $\text{Ti}_{70}\text{Si}_{30}$ nanoparticles with a high specific surface area ($569 \text{ m}^2 \text{ g}^{-1}$) [33] can degrade MB, making it a suitable material for photocatalytic application.

3.6. Light Transmittance and Opacity Measurements

UV light can create free radicals in products by a photochemical reaction, leading to a negative effect for food. Some of the unfriendly effects include the deterioration of antioxidants, destruction to vitamins and proteins, and a change in color. UV radiation is classified into UV-A (wavelength 320–400 nm), UVB (280–320 nm), and UV-C (200–280 nm) [57,58]. For good optical properties, the optical transmittance should exceed 90% in the visible range (measured from 400 to 800 nm). So, the optical transmittance was measured using a light source with a 600 nm wavelength, which is the central wavelength of the visible range. So, a lot of research uses this wavelength to evaluate opacity [41,59,60]. The addition of TiO_2 , SiO_2 , $\text{Ti}_{70}\text{Si}_{30}$, $\text{Ti}_{50}\text{Si}_{50}$, $\text{Ti}_{40}\text{Si}_{60}$, and TiO_2SiO_2 into the PLA matrix caused a significant decrease of transmittance in all UV regions (Table 4). The results show that the addition of filler into the PLA matrix caused a significantly decrease of transmittance in all UV regions. The presence of 3wt.% $\text{Ti}_{70}\text{Si}_{30}$ in the PLA film matrix succeeded in blocking more than 99.6% of the 240, 300, and 360 nm wavelengths, as representatives of UV-C, UV-B, and UV-A radiation, respectively, with a low opacity for the composite film. Moreover, the increase of $\text{Ti}_{70}\text{Si}_{30}$ oxide-loading up to 5wt.% into PLA improved the UV-blocking efficiency.

Table 4. Transmittance (%) and opacity values of PLA, PLA/ TiO_2 , PLA/ SiO_2 , PLA/ Ti_xSi_y , and PLA/ TiO_2SiO_2 composite films in the visible, UV-A, UV-B, and UV-C regions.

Sample	Transmittance, %				Opacity ($\text{AU}\cdot\text{nm}\cdot\text{mm}^{-1}$)
	UV-C (240 nm)	UV-B (300 nm)	UV-A (360 nm)	Visible (600 nm)	
PLA	1.24	24.47	34.77	51.39	1.16
97PLA/3 TiO_2	0.00	0.12	0.41	1.98	6.81
97 PLA/3 SiO_2	0.04	9.48	18.03	38.37	2.31
97 PLA/3 $\text{Ti}_{70}\text{Si}_{30}$	0.00	0.28	0.75	14.00	3.42
95 PLA/5 $\text{Ti}_{70}\text{Si}_{30}$	0.00	0.00	0.36	4.06	6.33
97 PLA/3 $\text{Ti}_{50}\text{Si}_{50}$	0.00	0.32	2.37	15.65	3.22
97 PLA/3 $\text{Ti}_{40}\text{Si}_{60}$	0.00	0.03	0.81	10.48	3.92
97 PLA/3 TiO_2SiO_2	0.00	0.19	1.43	7.30	4.74

The PLA films were transparent and colorless, and the addition of SiO_2 to PLA remained transparent, while other PLA composite films showed higher opacity than the pure PLA film. However, the transparency changes related to the increasing $\text{Ti}_{70}\text{Si}_{30}$ oxide contents from 3 up to 5 wt.% provided totally opaque films by more than two orders of magnitude in the opacity films, but this was still lower than the composite film of PLA with TiO_2 . Similarly, the addition of TiO_2 and $\text{Ti}_{70}\text{Si}_{30}$ made the PLA composites' color appear whiter because of the characteristic whiteness of the TiO_2 and $\text{Ti}_{70}\text{Si}_{30}$ nanoparticles. Photographs of PLA, PLA/ TiO_2 , PLA/ SiO_2 , PLA/ Ti_xSi_y , and PLA/ TiO_2SiO_2 composites films are shown in Figure 9. These results suggest that the PLA composite produced with $\text{Ti}_{70}\text{Si}_{30}$ oxide was suitably applied to transparency packaging with good UV-blocking efficiency.



Figure 9. Photographs of films prepared from PLA, PLA/TiO₂, PLA/SiO₂, PLA/Ti_xSi_y, and PLA/TiO₂SiO₂ composites (250 ± 4.68 μm thickness).

3.7. Hydrolytic Degradation

Figure 10 shows the percentage weight loss of PLA and PLA composite films as a function of hydrolytic degradation time. Complete degradation of PLA was achieved at about 1200 min, while all of the PLA composite films were hydrolyzed faster than neat PLA. Interestingly, the incorporation of 3 wt.% of TiO₂, SiO₂, Ti₇₀Si₃₀, Ti₅₀Si₅₀, Ti₄₀Si₆₀, and TiO₂SiO₂ exhibited a much higher weight loss as a function of time than neat PLA. The presence of filler induced a much more apparent change of weight loss of hydrolytic degradation, which indicates the enhancement of a hydrolytic degradation ability of the PLA matrix. This was attributed by the addition of nanoparticles, which helped accelerate the hydrolytic degradation of the PLA matrix. Furthermore, 97PLA/3TiO₂, 97PLA/3SiO₂, 97PLA/3Ti₇₀Si₃₀, 97PLA/3Ti₅₀Si₅₀, 97PLA/3Ti₄₀Si₆₀, and 97PLA/3TiO₂SiO₂ were fully degraded at 840, 300, 420, 420, and 560 min, respectively. Moreover, the PLA composite containing 5 wt.% of Ti₇₀Si₃₀ degraded faster than all the composites and it was fully degraded in approximately 240 min. Consequently, it could be concluded that the rate of the hydrolytic degradation of PLA composite films can be controlled by the filler content. This result is in agreement with Buzarovka and Grozdanov (2012) [12].

3.8. In Vitro Degradation

The degradation of PLA in PLA composites involves several processes such as water uptake, ester cleavage and formation of oligomer fragments, the dissolution of the oligomer fragment, etc., [61]; as a result, factors affecting the hydrolysis tendency of PLA would control the degradation of PLA. The long-term hydrolytic degradation of PLA and PLA composite films in a phosphate buffered saline (PBS) (pH = 7.4 ± 0.2) solution at 37 °C was evaluated by mass loss in 56 days. Figure 11 illustrates the mass loss of the PLA and PLA composite with the degradation time. From 0 to 14 days, all of the samples exhibited a dramatic increase in mass loss with increasing immersion time. After this period, the mass loss of all samples accelerated gradually. PLA incorporating with 3 wt.% of TiO₂, SiO₂, Ti₇₀Si₃₀, Ti₅₀Si₅₀, Ti₄₀Si₆₀, and TiO₂SiO₂ exhibited higher weight loss as a function of immersion time than neat PLA. In this case, TiO₂, SiO₂, Ti₇₀Si₃₀, Ti₅₀Si₅₀, Ti₄₀Si₆₀, and TiO₂SiO₂ dispersed in the PLA matrix, the water molecules penetrated easier

within the samples to generate the degradation process and might have been absorbed into the gap between the conglomeration of the nanoparticles due to the agglomeration of the nanofiller. Consequently, a long time is spent on diffusion into the PLA matrix. Therefore, the degradation rate increased in the first period and reached its maximum [62]. In addition, the mass loss of the PLA composite was also found to increase with an increasing amount of $Ti_{70}Si_{30}$ to 5 wt.%. Consequently, it could be concluded that the rate of the long-term degradation of the PLA composite films depended upon the content of the mixed oxide loading. This result was connected to the hydrophilicity of TiO_2 , SiO_2 , $Ti_{70}Si_{30}$, $Ti_{50}Si_{50}$, $Ti_{40}Si_{60}$, and TiO_2SiO_2 , as well as the high-water absorption of the composites [63]. Regarding changes in the tensile strength, elongation at the break and Young's modulus of the PLA and PLA composite films are shown in Table 5. This table shows that the tensile strength and elongation at the break of the PLA and all of the PLA composite films decreased significantly after 28 days of in vitro degradation. The result suggests that the PLA and PLA composite films were mechanically stable during 28 days of in vitro degradation. The tensile strengths of the PLA and PLA composites decreased after 28 days of degradation with microcracks appearing on part of their surfaces. It was supposed that the PLA composites would lose their mechanical strengths quickly after the microcracks developed over the whole area of the fibers [64].

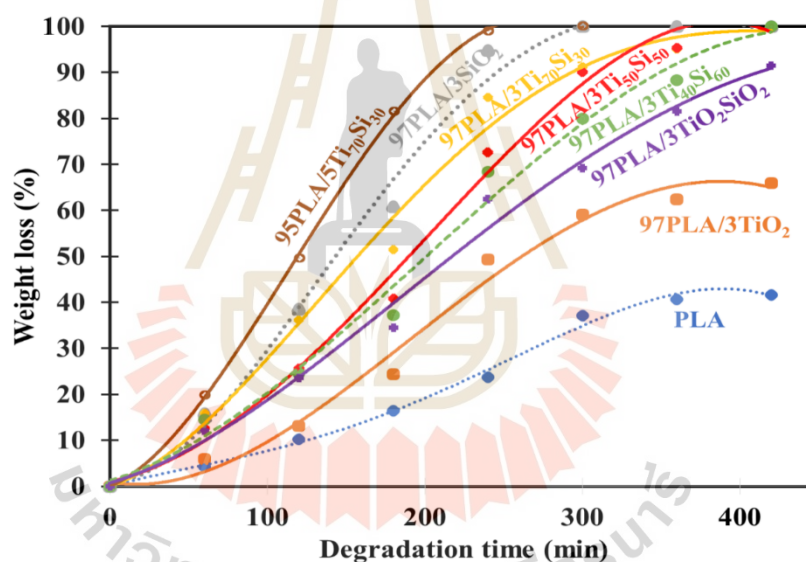


Figure 10. Weight loss of hydrolytic degradation of PLA, PLA/ TiO_2 , PLA/ SiO_2 , and PLA/ Ti_xSi_y composite films as functions of degradation time.

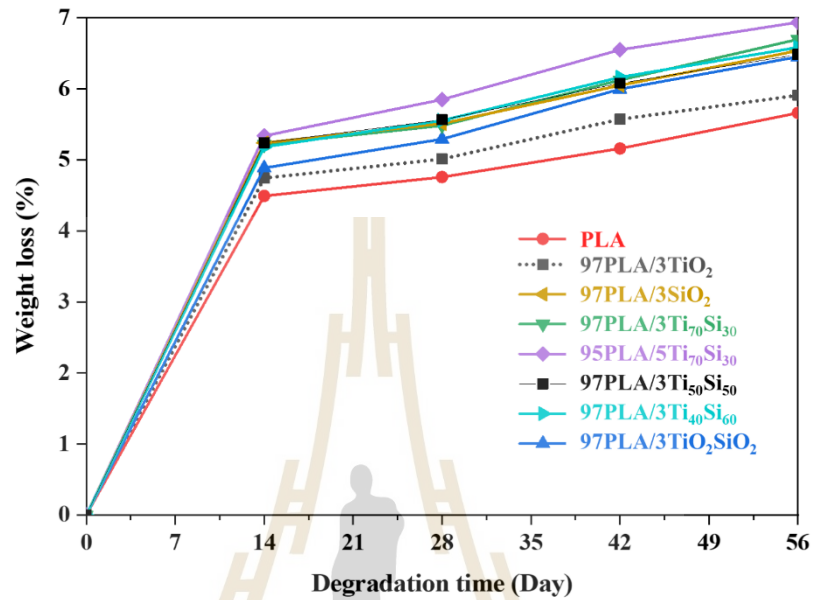


Figure 11. Weight loss of PLA, PLA/TiO₂, PLA/SiO₂, PLA/Ti_xSi_y, and PLA/TiO₂SiO₂ composite films after different periods of in vitro degradation.

Table 5. Tensile properties of properties of PLA, PLA/TiO₂, PLA/SiO₂, and PLA/Ti_xSi_y composite films after different period of in vitro degradation.

Time (Day)	Sample	Tensile Strength (MPa)	Elongation at Break (%)	Young's Modulus (GPa)
0	PLA	33.94 ± 1.38	19.62 ± 8.64	0.98 ± 0.23
	97PLA/3TiO ₂	28.22 ± 1.47	18.1 ± 4.24	1.01 ± 0.04
	97PLA/3SiO ₂	29.75 ± 1.38	11.8 ± 4.96	1.07 ± 0.10
	97PLA/3Ti ₇₀ Si ₃₀	35.64 ± 3.21	11.12 ± 1.81	1.18 ± 0.06
	95PLA/5Ti ₇₀ Si ₃₀	32.06 ± 2.29	9.88 ± 2.81	1.01 ± 0.10
	97PLA/3Ti ₅₀ Si ₅₀	35.31 ± 2.01	9.61 ± 2.57	1.29 ± 0.12
	97PLA/3Ti ₄₀ Si ₆₀	30.67 ± 1.74	22.30 ± 2.53	1.02 ± 0.05
	97PLA/3TiO ₂ SiO ₂	29.00 ± 1.42	58.37 ± 5.00	0.96 ± 0.07
14	PLA	29.43 ± 3.02	3.81 ± 1.61	1.51 ± 0.14
	97PLA/3TiO ₂	23.05 ± 2.87	2.58 ± 0.54	1.46 ± 0.31
	97PLA/3SiO ₂	23.53 ± 2.07	2.78 ± 0.27	1.39 ± 0.40
	97PLA/3Ti ₇₀ Si ₃₀	33.56 ± 3.45	3.69 ± 0.61	1.74 ± 0.14
	95PLA/5Ti ₇₀ Si ₃₀	31.75 ± 2.31	3.55 ± 0.70	1.49 ± 0.03
	97PLA/3Ti ₅₀ Si ₅₀	30.75 ± 2.51	3.45 ± 0.80	1.29 ± 0.04
	97PLA/3Ti ₄₀ Si ₆₀	27.99 ± 1.18	4.46 ± 0.95	1.21 ± 0.44
	97PLA/3TiO ₂ SiO ₂	24.83 ± 2.35	3.25 ± 0.38	1.44 ± 0.56

Table 5. Cont.

Time (Day)	Sample	Tensile Strength (MPa)	Elongation at Break (%)	Young's Modulus (GPa)
28	PLA	19.95 ± 2.45	2.06 ± 0.38	1.75 ± 0.25
	97PLA/3TiO ₂	18.69 ± 2.02	1.98 ± 0.23	2.02 ± 0.00
	97PLA/3SiO ₂	n/a *	n/a	n/a
	97PLA/3Ti ₇₀ Si ₃₀	29.35 ± 2.07	2.56 ± 0.12	1.91 ± 0.39
	95PLA/5Ti ₇₀ Si ₃₀	10.03 ± 2.40	1.11 ± 0.33	n/a
	97PLA/3Ti ₅₀ Si ₅₀	18.03 ± 2.80	2.11 ± 0.23	n/a
	97PLA/3Ti ₄₀ Si ₆₀	17.56 ± 2.01	2.08 ± 0.13	n/a
	97PLA/3TiO ₂ SiO ₂	17.39 ± 2.46	1.79 ± 0.35	n/a
42	PLA	6.95 ± 2.49	1.33 ± 0.19	n/a
	97PLA/3TiO ₂	0.26 ± 0.11	0.81 ± 0.10	n/a
	97PLA/3SiO ₂	n/a	n/a	n/a
	97PLA/3Ti ₇₀ Si ₃₀	15.97 ± 2.62	1.52 ± 0.11	n/a
	95PLA/5Ti ₇₀ Si ₃₀	n/a	n/a	n/a
	97PLA/3Ti ₅₀ Si ₅₀	5.97 ± 2.63	0.62 ± 0.52	n/a
	97PLA/3Ti ₄₀ Si ₆₀	n/a	n/a	n/a
	97PLA/3TiO ₂ SiO ₂	3.24 ± 1.79	1.12 ± 0.64	n/a

* n/a = not available.

3.9. Antimicrobial Activity

Metal oxides hold greater antibacterial efficiency, and their reinforcement in polymer composites expressively expands the antimicrobial properties of the film, which is desired in biomedical and food packaging applications. Bacteria are generally characterized by the cell membrane, which is composed mostly of a homogeneous peptidoglycan layer (which consists of amino acids and sugar). Gram-positive bacteria such as *Staphylococcus aureus* have one cytoplasm membrane with multilayers of the peptidoglycan polymer and a thicker cell wall (20–80 nm) [65], whereas in Gram-negative bacteria such as *Escherichia coli*, the bacteria wall is composed of two cell membranes, and an outer membrane and a plasma membrane with a thin layer of peptidoglycan with a thickness of 7–8 nm [65].

TiO₂ nanoparticles are known for their antibacterial activity, and recent studies have confirmed their efficiency as antibacterial agents [65,66]. As a result, the antibacterial activity of PLA incorporated with 3 wt.% of Ti₇₀Si₃₀, Ti₅₀Si₅₀, and TiO₂SiO₂, and 5 wt.% of Ti₇₀Si₃₀, to form composites was compared to the antibacterial activity of PLA adding 3 wt.% of TiO₂. The results of the antimicrobial activity of the Gram-negative bacteria (*Escherichia coli* or *E. coli*) and Gram-positive bacteria (*Staphylococcus aureus* or *S. aureus*) of the PLA and PLA composites are shown in Tables 6 and 7, respectively. The number of bacteria *Escherichia coli* and bacteria *Staphylococcus aureus* on the PLA and PLA composite films at time 0 h (at dilution 10⁻³) and 24 h (at dilution 10⁰) are shown in Figure 12.

Table 6. Antimicrobial activity of Gram-negative bacteria (*Escherichia coli*) of PLA, PLA/TiO₂, PLA/Ti_xSi_y, and PLA/TiO₂SiO₂ composites.

Samples	Blank (U) (t = 24 h)		Sample (A) (t = 24 h)		Antimicrobial Activity ^a (R)
	Log CFU/mL		Log CFU/mL		
PLA	5.96 ± 0.01		5.87 ± 0.02		0.09
97PLA/3TiO ₂	5.96 ± 0.01		0.00 ± 0.00		5.96
97PLA/3Ti ₇₀ Si ₃₀	5.96 ± 0.01		0.00 ± 0.00		5.96
95PLA/5Ti ₇₀ Si ₃₀	5.96 ± 0.01		0.00 ± 0.00		5.96
97PLA/3Ti ₅₀ Si ₅₀	5.96 ± 0.01		3.21 ± 0.04		2.75
97PLA/3TiO ₂ SiO ₂	5.96 ± 0.01		2.53 ± 0.04		3.43

^a Antimicrobial activity (R) ≥ 2 = antimicrobial effectiveness.

Table 7. Antimicrobial activity of Gram-positive bacteria (*Staphylococcus aureus*) of PLA, PLA/TiO₂, PLA/Ti_xSi_y, and PLA/TiO₂SiO₂ composites.

Samples	Blank (U) (f = 24 h)	Sample (At) (f = 24 h)	Antimicrobial Activity ^a (R)
	Log CFU/mL	Log CFU/mL	
PLA	4.35 ± 0.04	4.35 ± 0.04	0
PLA/3TiO ₂	4.35 ± 0.04	0.00 ± 0.00	4.35
PLA/3Ti ₇₀ Si ₃₀	4.35 ± 0.04	2.96 ± 0.01	2.04
PLA/5Ti ₇₀ Si ₃₀	4.35 ± 0.04	0.00 ± 0.00	4.35
PLA/3Ti ₅₀ Si ₅₀	4.35 ± 0.04	3.17 ± 0.08	1.83
PLA/3TiO ₂ SiO ₂	4.35 ± 0.04	3.21 ± 0.01	1.79

^a Antibacterial activity (R) ≥ 2 = antimicrobial effectiveness.

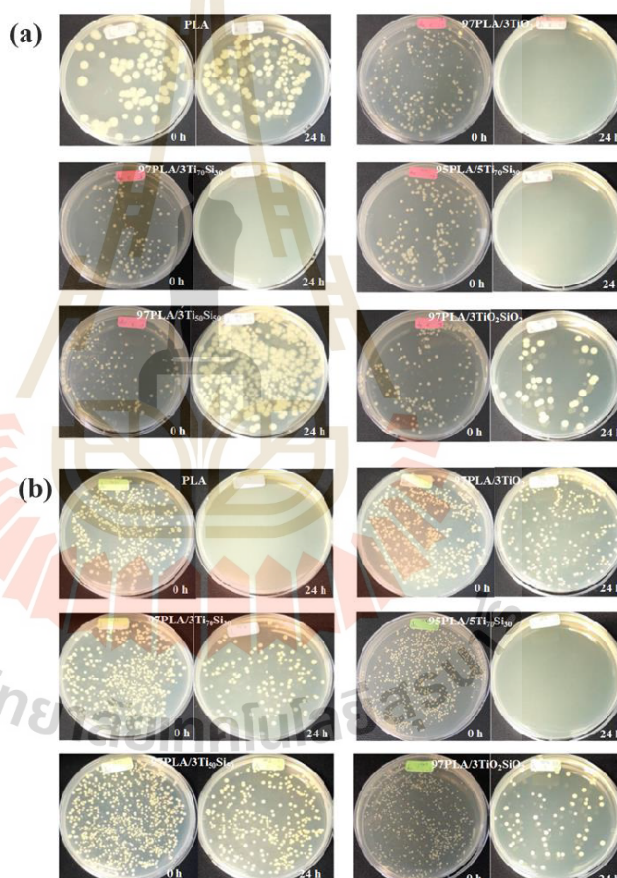


Figure 12. The number of (a) bacteria *Escherichia coli* and (b) bacteria *Staphylococcus aureus* on PLA and PLA composite films at time 0 h (at dilution 10⁻³) and 24 h (at dilution 10⁰).

The antimicrobial activity (R) values of Neat PLA film against *E. coli* and *S. aureus* were 0.09 and 0, respectively. This result shows that PLA has no significant antibacterial effects on *E. coli* and *S. aureus*. However, the 97PLA/3TiO₂ composite film exhibited the highest antimicrobial activity (R = 5.96 against *E. coli* and R = 4.35 against *S. aureus*). As shown in Table 6, all of PLA composites exhibited an antimicrobial activity agent against *E. coli* (if R ≥ 2 antimicrobial effectiveness). Moreover, the results confirm that PLA incorporated with 3wt.% of Ti₇₀Si₃₀ has sufficient antimicrobial effectiveness. Likewise, PLA with the addition of 3 wt.% of TiO₂ and Ti₇₀Si₃₀ exhibited an antibacterial effect on *S. aureus*. This was due to TiO₂ and Ti_xSi_y oxide utilizing a similar mechanism against bacterial growth by directly damaging the bacterial surface. Adding TiO₂ and Ti_xSi_y oxide into PLA could lead to reduced soluble protein expression by suppressing the synthesis of nucleic acids. Thus, TiO₂ and Ti_xSi_y oxide antibacterial action against *S. aureus* was probably through inhibiting the synthesis of nucleic acid, thereby reducing protein synthesis against bacterial growth [67]. The mechanism referred to as the antimicrobial action of TiO₂ is commonly associated with reactive oxygen species (ROS) with high oxidative potentials produced under a band-gap irradiation photo-induced charge in the presence of O₂ [68]. Pleskova et al. investigated the bactericidal activity of the TiO₂ film and discovered that *S. aureus* is swelled by TiO₂ through damaging the cell membrane [69]. In addition, the increment of Ti₇₀Si₃₀ loading to 5 wt.% improved the antimicrobial effectiveness of the PLA composites. However, 97PLA/3Ti₃₀Si₅₀ and 97PLA/3TiO₂SiO₂ exhibited low antimicrobial activity (R = 2.75, 3.43 against *E. coli* and R = 1.83, 1.79 against *S. aureus*). This was due to a higher SiO₂ content in Ti₅₀Si₅₀ and TiO₂SiO₂, resulting in a lower efficiency of antimicrobial activity. In addition, the variation in the microorganism structure between the Gram-negative (*E. coli*) and Gram-positive (*S. aureus*) bacteria may explain the difference in the antibacterial effect of samples against *E. coli* and *S. aureus*. Both bacteria have similar internal, but different external structures. The peptidoglycan layer of Gram-positive bacteria is thick and includes teichoic and lipoteichoic acids. A Gram-negative bacterium has a thin peptidoglycan layer and an outer membrane made up of proteins, phospholipids, and lipopolysaccharides. Therefore, *S. aureus* needs longer contact time or higher catalyst concentrations to achieve the same effect as *E. coli* [70].

4. Conclusions

The aim of this study was to examine the influence of 3wt.% of TiO₂, SiO₂, Ti₇₀Si₃₀, Ti₅₀Si₅₀, Ti₄₀Si₆₀, and TiO₂SiO₂, and 5 wt.% of Ti₇₀Si₃₀ on the mechanical properties, thermal properties, morphological properties, degradation behavior, and antimicrobial activity of PLA. The PLA and PLA composites films were obtained by the solvent casting method. The addition of Ti₇₀Si₃₀ and Ti₅₀Si₅₀ into the PLA film slightly improved the tensile strength and Young's modulus of PLA. The incorporation of 5 wt.% of Ti₇₀Si₃₀ was found to decrease the cold crystallization temperature and increased the degree of crystallinity of PLA. It can be concluded that Ti₇₀Si₃₀ nanoparticles can act as a good nucleating agents for PLA. The thermal stability of PLA was enhanced with the incorporation of TiO₂ and SiO₂. The water vapor transmission rate (WVTR) of PLA was significantly increased by the incorporation of SiO₂, Ti₇₀Si₃₀, and Ti₅₀Si₅₀ nanoparticles. This is due to the hydrophilicity of the nanoparticles. In addition, efficiency of degrading MB is TiO₂ > Ti₇₀Si₃₀ > TiO₂SiO₂ > Ti₅₀Si₅₀ > Ti₄₀Si₆₀ > SiO₂, respectively. Moreover, the increase in Ti₇₀Si₃₀ loading to 5 wt.% improved the efficiency of the photocatalytic activity of PLA. All of the nanoparticles were able to remove UV light and, in particular, TiO₂ and Ti₇₀Si₃₀ enhanced a stronger higher UV-shielding potential. The hydrolytic degradation and in vitro degradation of PLA are important properties of the variety of application such as biomedical application and food packaging. PLA incorporated with 3wt.% of SiO₂, Ti₇₀Si₃₀, Ti₅₀Si₅₀, Ti₄₀Si₆₀, and TiO₂SiO₂ exhibited much higher weight loss as a function of time than neat PLA. The weight loss of the PLA composite was also found to increase with increasing Ti₇₀Si₃₀ to 5 wt.%. Furthermore, PLA with the addition of TiO₂ and Ti₇₀Si₃₀ exhibited an excellent

antibacterial effect on Gram-negative bacteria (*E. coli*) and Gram-positive bacteria (*S. aureus*), indicating the improved antimicrobial effectiveness of PLA composites.

Supplementary Materials: The following supporting information can be downloaded at: <https://www.mdpi.com/article/10.3390/polym14163310/s1>, Figure S1: Curve of (a) TGA thermogram, (b) DTG Thermogram of PLA, PLA/TiO₂, PLA/SiO₂, PLA/Ti_xSi_y, and PLA/TiO₂SiO₂ composites.; Figure S2: The changes in tensile properties of PLA, PLA/TiO₂, PLA/SiO₂, and PLA/Ti_xSi_y composite films after different periods of in vitro degradation.

Author Contributions: Conceptualization, Y.R.; methodology, A.T., C.R. and Y.R.; validation, A.T., C.R. and Y.R.; formal analysis, A.T.; investigation, A.T., C.R. and Y.R.; resources, A.T., C.R. and Y.R.; data curation, A.T.; writing—original draft preparation, A.T.; writing—review and editing, A.T., C.R. and Y.R.; visualization, C.R. and Y.R.; supervision, C.R. and Y.R.; project administration, C.R. and Y.R.; funding acquisition, C.R. and Y.R. All authors have read and agreed to the published version of the manuscript.

Funding: This research was funded by Thailand Science Research and Innovation (TSRI), grant number 42853.

Institutional Review Board Statement: Not applicable.

Informed Consent Statement: Not applicable.

Data Availability Statement: Not applicable.

Acknowledgments: The authors are grateful to Suranaree University of Technology (SUT); to the Center of Excellence on Petrochemical and Materials Technology (PETROMAT); to the Science, Research and Innovation Promotion Fund from Thailand Science Research and Innovation (TSRI); and to the Research Center for Biocomposite Materials for the Medical Industry and Agricultural and Food Industry for the financial support.

Conflicts of Interest: The authors declare no conflict of interest.

References

1. Cadar, O.; Paul, M.; Roman, C.; Miclean, M.; Majdik, C. Biodegradation behaviour of poly(lactic acid) and (lactic acid-ethylene glycol-malonic or succinic acid) copolymers under controlled composting conditions in a laboratory test system. *Polym. Degrad. Stab.* **2012**, *97*, 354–357. [[CrossRef](#)]
2. Lim, L.T.; Auras, R.; Rubino, M. Processing technologies for poly(lactic acid). *Prog. Polym. Sci.* **2008**, *33*, 820–852. [[CrossRef](#)]
3. Deroine, M.; Le Duigou, A.; Corre, Y.M.; Le Gac, P.Y.; Davies, P.; César, G.; Bruzard, S. Accelerated ageing of polylactide in aqueous environments: Comparative study between distilled water and seawater. *Polym. Degrad. Stab.* **2014**, *108*, 319–329. [[CrossRef](#)]
4. Wang, Y.; Kong, Y.; Zhao, Y.; Feng, Q.; Wu, Y.; Tang, X.; Gu, X.; Yang, Y. Electrospun, reinforcing network-containing, silk fibroin-based nerve guidance conduits for peripheral nerve repair. *J. Biomater. Tissue Eng.* **2016**, *6*, 53–60. [[CrossRef](#)]
5. Athanasiou, K.A.; Niederauer, G.G.; Agrawal, C.M. Sterilization, toxicity, biocompatibility and clinical applications of poly(lactic acid)/polyglycolic acid copolymers. *Biomaterials* **1996**, *17*, 93–102. [[CrossRef](#)]
6. Cheung, H.Y.; Lau, K.T. Study on a silkworm silk fiber/biodegradable polymer biocomposite. In Proceedings of the ICCM International Conferences on Composite Materials, Kyoto, Japan, 8–13 July 2007.
7. Yeh, J.T.; Huang, C.Y.; Chai, W.L.; Chen, K.N. Plasticized properties of poly(lactic acid) and triacetone blends. *J. Appl. Polym. Sci.* **2009**, *112*, 2757–2763. [[CrossRef](#)]
8. Burg, K.J.L.; Holder, W.D.; Culberson, C.R.; Beiler, R.J.; Greene, K.G.; Loebbeck, A.B.; Roland, W.D.; Mooney, D.J.; Halberstadt, C.R. Parameters affecting cellular adhesion to polylactide films. *J. Biomater. Sci. Polym. Ed.* **1999**, *10*, 147–161. [[CrossRef](#)]
9. Rasal, R.M.; Janorkar, A.V.; Hirt, D.E. Poly(lactic acid) modifications. *Prog. Polym. Sci.* **2010**, *35*, 338–356. [[CrossRef](#)]
10. Paul, M.A.; Delcourt, C.; Alexandre, M.; Degée, P.; Monteverde, F.; Dubois, P. Polylactide/montmorillonite nanocomposites: Study of the hydrolytic degradation. *Polym. Degrad. Stab.* **2005**, *87*, 535–542. [[CrossRef](#)]
11. Shogren, R.L.; Doane, W.M.; Garlotta, D.; Lawton, J.W.; Willett, J.L. Biodegradation of starch/polylactic acid/poly(hydroxyester-ether) composite bars in soil. *Polym. Degrad. Stab.* **2003**, *79*, 405–411. [[CrossRef](#)]
12. Buzarovska, A.; Grozdanov, A. Biodegradable poly(L-lactic acid)/TiO₂ nanocomposites: Thermal properties and degradation. *J. Appl. Polym. Sci.* **2012**, *123*, 2187–2193. [[CrossRef](#)]
13. Yang, K.K.; Wang, X.L.; Wang, Y.Z. Progress in nanocomposite of biodegradable polymer. *J. Ind. Eng. Chem.* **2007**, *13*, 485–500.
14. Huang, S.M.; Hwang, J.J.; Liu, H.J.; Lin, L.H. Crystallization behavior of poly(L-lactic acid)/montmorillonite nanocomposites. *J. Appl. Polym. Sci.* **2010**, *117*, 434–442. [[CrossRef](#)]

15. Tang, H.; Chen, J.B.; Wang, Y.; Xu, J.Z.; Hsiao, B.S.; Zhong, G.J.; Li, Z.M. Shear flow and carbon nanotubes synergistically Induced nonisothermal crystallization of poly(lactic acid) and its application in injection molding. *Biomacromolecules* **2012**, *13*, 3858–3867. [[CrossRef](#)]
16. Murariu, M.; Paint, Y.; Murariu, O.; Raquez, J.-M.; Bonnaud, L.; Dubois, P. Current progress in the production of PLA–ZnO nanocomposites: Beneficial effects of chain extender addition on key properties. *J. Appl. Polym. Sci.* **2015**, *132*, 42480. [[CrossRef](#)]
17. Hakim, R.H.; Cailloux, J.; Santana, O.O.; Bou, J.; Sánchez-Soto, M.; Odent, J.; Raquez, J.M.; Dubois, P.; Carrasco, F.; MasPOCH, M.L. PLA/SiO₂ composites: Influence of the filler modifications on the morphology, crystallization behavior, and mechanical properties. *J. Appl. Polym. Sci.* **2017**, *134*, 45367. [[CrossRef](#)]
18. Wu, G.; Liu, S.; Jia, H.; Dai, J. Preparation and properties of heat resistant polylactic acid (PLA)/Nano-SiO₂ composite filament. *J. Wuhan Univ. Technol. Mater. Sci. Ed.* **2016**, *31*, 164–171. [[CrossRef](#)]
19. Xiu, H.; Qi, X.; Bai, H.; Zhang, Q.; Fu, Q. Simultaneously improving toughness and UV-resistance of polylactide/titanium dioxide nanocomposites by adding poly(ether)urethane. *Polym. Degrad. Stab.* **2017**, *143*, 136–144. [[CrossRef](#)]
20. Zapata, P.A.; Palza, H.; Cruz, L.S.; Lieberwirth, I.; Catalina, F.; Corrales, T.; Rabagliati, F.M. Polyethylene and poly(ethylene-co-1-octadecene) composites with TiO₂ based nanoparticles by metallocenic “in situ” polymerization. *Polymer* **2013**, *54*, 2690–2698. [[CrossRef](#)]
21. Fonseca, C.; Ochoa, A.; Ulloa, M.T.; Alvarez, E.; Canales, D.; Zapata, P.A. Poly(lactic acid)/TiO₂ nanocomposites as alternative biocidal and antifungal materials. *Mater. Sci. Eng. C* **2015**, *57*, 314–320. [[CrossRef](#)]
22. Wu, F.; Lan, X.; Ji, D.; Liu, Z.; Yang, W.; Yang, M. Grafting polymerization of polylactic acid on the surface of nano-SiO₂ and properties of PLA/PLA-grafted-SiO₂ nanocomposites. *J. Appl. Polym. Sci.* **2013**, *129*, 3019–3027. [[CrossRef](#)]
23. Serenko, O.A.; Muzafarov, A.M. Polymer composites with surface modified SiO₂ nanoparticles: Structures, properties, and promising applications. *Polym. Sci. Ser. C* **2016**, *58*, 93–101. [[CrossRef](#)]
24. Ha, S.W.; Weitzmann, M.N.; Beck, G.R., Jr. Applications of silica-based nanomaterials in dental and skeletal biology. In *Nanobiomaterials in Clinical Dentistry*; Karthikeyan, W., Ahmed, J.K., Eds.; Elsevier: Amsterdam, The Netherlands, 2013; pp. 69–91.
25. Galindo, I.R.; Viveros, T.; Chadwick, D. Synthesis and characterization of titania-based ternary and binary mixed oxides prepared by the sol–gel method and their activity in 2-propanol dehydration. *Ind. Eng. Chem. Res.* **2007**, *46*, 1138–1147. [[CrossRef](#)]
26. Liao, S.Y.; Read, D.C.; Pugh, W.J.; Furr, J.; Russell, A.D. Interaction of silver nitrate with readily identifiable groups: Relationship to the antibacterial activity of silver ions. *Letts. Appl. Microbiol.* **1997**, *25*, 279–283. [[CrossRef](#)]
27. Marra, A.; Silvestre, C.; Duraccio, D.; Cimmino, S. Polylactic acid/zinc oxide biocomposite films for food packaging application. *Int. J. Biol. Macromol.* **2016**, *88*, 254–262. [[CrossRef](#)]
28. Sirelkhatim, A.; Mahmud, S.; Seeni, A.; Kaus, N.H.M.; Ann, L.C.; Bakhori, S.K.M.; Hasan, H.; Mohamad, D. Review on zinc oxide nanoparticles: Antibacterial activity and toxicity mechanism. *Nano-Micro Lett.* **2015**, *7*, 219–242. [[CrossRef](#)]
29. Li, W.; Zhang, C.; Chi, H.; Li, L.; Lan, T.; Han, P.; Chen, H.; Qin, Y. Development of antimicrobial packaging film made from poly(lactic acid) incorporating titanium dioxide and silver nanoparticles. *Molecules* **2017**, *22*, 1170. [[CrossRef](#)]
30. Shebi, A.; Lisa, S. Evaluation of biocompatibility and bactericidal activity of hierarchically porous PLA-TiO₂ nanocomposite films fabricated by breath-figure method. *Mater. Chem. Phys.* **2019**, *230*, 308–318. [[CrossRef](#)]
31. Swaroop, C.; Shukla, M. Polylactic acid/magnesium oxide nanocomposite films for food packaging applications. In Proceedings of the 21st International Conference on Composite Materials, Xi’an, China, 20–25 August 2017.
32. Teamsinsungvon, A.; Sutapun, W.; Ruksakulpiwat, C.; Ruksakulpiwat, Y. Preparation of titanium-silica binary mixed oxide to use as a filler in poly (lactic acid). *Suranaree J. Sci. Technol.* **2019**, *26*, 31–36.
33. Teamsinsungvon, A.; Ruksakulpiwat, C.; Amonpattaratkit, P.; Ruksakulpiwat, Y. Structural Characterization of Titanium–Silica Oxide Using Synchrotron Radiation X-ray Absorption Spectroscopy. *Polymers* **2022**, *14*, 2729. [[CrossRef](#)]
34. Matijević, E.; Budnik, M.; Meites, L. Preparation and mechanism of formation of titanium dioxide hydrosols of narrow size distribution. *J. Colloid Interface Sci.* **1977**, *61*, 302–311. [[CrossRef](#)]
35. Vorkapic, D.; Matsoukas, T. Effect of Temperature and Alcohols in the Preparation of Titania Nanoparticles from Alkoxides. *J. Am. Ceram. Soc.* **1998**, *81*, 2815–2820. [[CrossRef](#)]
36. Cheung, H.Y.; Lau, K.T.; Tao, X.M.; Hui, D. A potential material for tissue engineering; Silkworm silk/PLA biocomposite. *Compos. Part B Eng.* **2008**, *39*, 1026–1033. [[CrossRef](#)]
37. Boonying, S.; Sutapun, W.; Suppakarn, N.; Ruksakulpiwat, Y. Crystallization Behavior of Vetiver Grass Fiber-Polylactic Acid Composite. *Adv. Mater. Res.* **2012**, *410*, 55–58. [[CrossRef](#)]
38. Tang, Z.; Zhang, C.; Liu, X.; Zhu, J. The crystallization behavior and mechanical properties of polylactic acid in the presence of a crystal nucleating agent. *J. Appl. Polym. Sci.* **2012**, *125*, 1108–1115. [[CrossRef](#)]
39. Elsner, J.; Shefy-Peleg, A.; Zilberman, M. Novel biodegradable composite wound dressings with controlled release of antibiotics: Microstructure, mechanical and physical properties. *J. Biomed. Mater. Res. Part B Appl. Biomater.* **2010**, *93*, 425–435. [[CrossRef](#)]
40. Teo, P.S.; Chow, W.S. Water vapour permeability of poly(lactic acid)/chitosan binary and ternary blends. *Appl. Sci. Eng. Prog.* **2014**, *7*, 23–27.
41. Feng, S.; Zhang, F.; Ahmed, S.; Liu, Y. Physico-mechanical and antibacterial properties of PLA/TiO₂ composite materials synthesized via electrospinning and solution casting processes. *Coatings* **2019**, *9*, 525. [[CrossRef](#)]

42. Felfel, R.M.; Leander, P.; Miquel, G.F.; Tobias, M.; Gerhard, H.; Ifty, A.; Colin, S.; Virginie, S.; David, M.G.; Klaus, L. In vitro degradation and mechanical properties of PLA-PCL copolymer unit cell scaffolds generated by two-photon polymerization. *Biomed. Mater.* **2016**, *11*, 015011. [[CrossRef](#)]
43. Racksanti, A.; Janhom, S.; Punyanitya, S.; Wataneski, R.; Wataneski, S. An approach for preparing an absorbable porous film of silk fibroin–rice starch modified with trisodium trimetaphosphate. *J. Appl. Polym. Sci.* **2015**, *132*, 41517. [[CrossRef](#)]
44. Sarasua, J.R.; Prud'homme, R.E.; Wisniewski, M.; Le Borgne, A.; Spassky, N. Crystallization and melting behavior of polylactides. *Macromolecules* **1998**, *31*, 3895–3905. [[CrossRef](#)]
45. Chen, P.; Zhou, H.; Liu, W.; Zhang, M.; Du, Z.; Wang, X. The synergistic effect of zinc oxide and phenylphosphonic acid zinc salt on the crystallization behavior of poly (lactic acid). *Polym. Degrad. Stab.* **2015**, *122*, 25–35. [[CrossRef](#)]
46. Chen, R.Y.; Zou, W.; Wu, C.R.; Jia, S.K.; Huang, Z.; Zhang, G.Z.; Yang, Z.T.; Qu, J.P. Poly(lactic acid)/poly(butylene succinate)/calcium sulfate whiskers biodegradable blends prepared by vane extruder: Analysis of mechanical properties, morphology, and crystallization behavior. *Polym. Test.* **2014**, *34*, 1–9. [[CrossRef](#)]
47. Zhang, H.; Huang, J.; Yang, L.; Chen, R.; Zou, W.; Lin, X.; Qu, J. Preparation, characterization and properties of PLA/TiO₂ nanocomposites based on a novel vane extruder. *RSC Adv.* **2015**, *5*, 4639–4647. [[CrossRef](#)]
48. Buzarovska, A. PLA nanocomposites with functionalized TiO₂ nanoparticles. *Polym. Plast. Technol. Eng.* **2013**, *52*, 280–286. [[CrossRef](#)]
49. Garlotta, D.; Doane, W.; Shogren, R.; Lawton, J.; Willett, J.L. Mechanical and thermal properties of starch-filled poly(D,L-lactic acid)/poly(hydroxy ester ether) biodegradable blends. *J. Appl. Polym. Sci.* **2003**, *88*, 1775–1786. [[CrossRef](#)]
50. Yew, G.H.; Mohd Yusof, A.M.; Mohd Ishak, Z.A.; Ishiaku, U.S. Water absorption and enzymatic degradation of poly(lactic acid)/rice starch composites. *Polym. Degrad. Stab.* **2005**, *90*, 488–500. [[CrossRef](#)]
51. Hu, Y.; Topolkarav, V.; Hiltner, A.; Baer, E. Measurement of water vapor transmission rate in highly permeable films. *J. Appl. Polym. Sci.* **2001**, *81*, 1624–1633. [[CrossRef](#)]
52. Choudalakis, G.; Gotsis, A.D. Permeability of polymer/clay nanocomposites: A review. *Eur. Polym. J.* **2009**, *45*, 967–984. [[CrossRef](#)]
53. Tantekin-Ersolmaz, Ş.B.; Atalay-Oral, Ç.; Tather, M.; Erdem-Şenatalar, A.; Schoeman, B.; Sterte, J. Effect of zeolite particle size on the performance of polymer–zeolite mixed matrix membranes. *J. Membr. Sci.* **2000**, *175*, 285–288. [[CrossRef](#)]
54. Chen, L.; Zheng, K.; Liu, Y. Geopolymer-supported photocatalytic TiO₂ film: Preparation and characterization. *Constr. Build. Mater.* **2017**, *151*, 63–70. [[CrossRef](#)]
55. Zhuang, J.; Zhang, B.; Wang, Q.; Guan, S.; Li, B. Construction of novel ZnTiO₃/g-C₃N₄ heterostructures with enhanced visible light photocatalytic activity for dye wastewater treatment. *J. Mater. Sci. Mater. Electron.* **2019**, *30*, 6322–6334. [[CrossRef](#)]
56. Wang, Q.; Zhang, L.; Guo, Y.; Shen, M.; Wang, M.; Li, B.; Shi, J. Multifunctional 2D porous g-C₃N₄ nanosheets hybridized with 3D hierarchical TiO₂ microflowers for selective dye adsorption, antibiotic degradation and CO₂ reduction. *Chem. Eng. J.* **2020**, *396*, 125347. [[CrossRef](#)]
57. Asmatulu, R.; Mahmud, G.A.; Hille, C.; Misak, H.E. Effects of UV degradation on surface hydrophobicity, crack, and thickness of MWCNT-based nanocomposite coatings. *Prog. Org. Coat.* **2011**, *72*, 553–561. [[CrossRef](#)]
58. Oleyaei, S.A.; Zahedi, Y.; Ghanbarzadeh, B.; Moayedi, A.A. Modification of physicochemical and thermal properties of starch films by incorporation of TiO₂ nanoparticles. *Int. J. Biol. Macromol.* **2016**, *89*, 256–264. [[CrossRef](#)] [[PubMed](#)]
59. Cui, R.; Jiang, K.; Yuan, M.; Cao, J.; Li, L.; Tang, Z.; Qin, Y. Antimicrobial film based on polylactic acid and carbon nanotube for controlled cinnamaldehyde release. *J. Mater. Res. Technol.* **2020**, *9*, 10130–10138. [[CrossRef](#)]
60. Chu, Z.; Zhao, T.; Li, L.; Fan, J.; Qin, Y. Characterization of Antimicrobial Poly (Lactic Acid)/Nano-Composite Films with Silver and Zinc Oxide Nanoparticles. *Materials* **2017**, *10*, 659. [[CrossRef](#)]
61. Sinha Ray, S.; Yamada, K.; Okamoto, M.; Ueda, K. Polylactide-layered silicate nanocomposite: a novel biodegradable material. *Nano Lett.* **2002**, *2*, 1093–1096. [[CrossRef](#)]
62. Luo, Y.B.; Wang, X.L.; Wang, Y.Z. Effect of TiO₂ nanoparticles on the long-term hydrolytic degradation behavior of PLA. *Polym. Degrad. Stab.* **2012**, *97*, 721–728. [[CrossRef](#)]
63. Kaseem, M.; Hamad, K.; Ur Rehman, Z. Review of recent advances in polylactic acid/TiO₂ Composites. *Materials* **2019**, *12*, 3659. [[CrossRef](#)]
64. Yuan, X.; Mak, A.F.T.; Yao, K. In vitro degradation of poly(L-lactic acid) fibers in phosphate buffered saline. *J. Appl. Polym. Sci.* **2002**, *85*, 936–943. [[CrossRef](#)]
65. Fu, G.; Vary, P.S.; Lin, C.T. Anatase TiO₂ nanocomposites for antimicrobial coatings. *J. Phys. Chem. B* **2005**, *109*, 8889–8898. [[CrossRef](#)]
66. Joost, U.; Juganson, K.; Visnapuu, M.; Mortimer, M.; Kahru, A.; Nömmiste, E.; Joost, U.; Kisand, V.; Ivask, A. Photocatalytic antibacterial activity of nano-TiO₂ (anatase)-based thin films: Effects on *Escherichia coli* cells and fatty acids. *J. Photochem. Photobiol. B Biol.* **2015**, *142*, 178–185. [[CrossRef](#)]
67. Jiang, X.; Lv, B.; Wang, Y.; Shen, Q.; Wang, X. Bactericidal mechanisms and effector targets of TiO₂ and Ag-TiO₂ against *Staphylococcus aureus*. *J. Med. Microbiol.* **2017**, *66*, 440–446. [[CrossRef](#)] [[PubMed](#)]
68. Verdier, T.; Coutand, M.; Bertron, A.; Roques, C. Antibacterial Activity of TiO₂ Photocatalyst Alone or in Coatings on *E. coli*: The Influence of Methodological Aspects. *Coatings* **2014**, *4*, 670–686. [[CrossRef](#)]

69. Pleskova, S.N.; Golubeva, I.S.; Verevkin, Y.K. Bactericidal activity of titanium dioxide ultraviolet-induced films. *Mater. Sci. Eng. C* **2016**, *59*, 807–817. [[CrossRef](#)] [[PubMed](#)]
70. Talebian, N.; Zare, E. Structure and antibacterial property of nano-SiO₂ supported oxide ceramic. *Ceram. Int.* **2014**, *40*, 281–287. [[CrossRef](#)]



BIOGRAPHY

Miss Arpaporn Teamsinsungvon was born on May 1, 1983 in Udonthani Province, Thailand. She attended Khon Kaen University (KKU) and graduated in 2004 with Bachelor's degree of science (Chemistry). Her senior project was physical and chemical properties of polymer blends of natural rubber cassava starch and glycerol. After graduation, she has been employed as a research analyst at Research and Development (R&D) department, Advance Agro Public company limited for 3 years. She then pursued her Master's Degree in School of Polymer Engineering at Suranaree University of Technology (SUT) and earned her Master's Degree in Polymer Engineering in 2012. Her research was about poly (lactic acid)/poly (butylene adipate-co-terephthalate) blends and their composites. During her graduate study, she got a research assistant scholarship from the Center of Excellence for Petroleum, Petrochemical and Advanced Materials, Chulalongkorn University, Thailand and National Innovation Agency (NIA). In 2014, she started her Ph.D. studying in Polymer Engineering, Institute of Engineering, Suranaree University of Technology, Nakhon Ratchasima. Her Ph.D. study was entitled "Biocomposite from poly (lactic acid) and natural fiber" which was under the supervision of Assoc. Prof. Dr. Yupaporn Ruksakulpiwat and Assoc. Prof. Dr. Chaiwat Ruksakulpiwat. Her Ph.D. study was supported by Suranaree University of Technology and the Center of Excellence for Petroleum, Petrochemical and Advanced Materials, Chulalongkorn University, Thailand. In the period of her study, several parts of her work were presented at The First Materials Research Society of Thailand International Conference in Chiang Mai, Thailand (MRS-Thailand 2017), and published in Suranaree Journal of Science and Technology. International Conference on Advanced and Applied Petroleum Petrochemicals, and Polymer 2018 (ICAPPP2018) in Bangkok, Thailand. The Second Materials Research Society of Thailand International Conference in Pattaya, Thailand (2nd MRS Thailand International Conference) and published in Suranaree Journal of Science and Technology.